Assessment of CO_2 storage capacity in the Sureste Basin in Mexico

By

JESSICA ARELLANO SANCHEZ

School of Earth Sciences
UNIVERSITY OF BRISTOL

A dissertation submitted to the University of Bristol in accordance with the requirements of the degree of DOCTOR OF PHILOSOPHY in the Faculty of Science.

FEBRUARY 2022

Word count: 41,758

ABSTRACT

Carbon Capture and Storage (CCS) provides a technology to reduce greenhouse gas emissions and combat global warming. Many countries have adopted and implemented CCS projects. CO_2- Enhanced Oil Recovery (EOR) has been used for about five decades, with the development of pipelines and CO_2 subsurface injection. More recently, dedicated projects for CO_2 sequestration have been developed. However, this type of project has been limited to developed countries so far. For this reason, it is crucial that nations like Mexico, with substantial potential for CCS, take action to contribute to efforts to stabilise the global average temperature rise.

CCS has to be undertaken in specific areas that meet geological and petrophysical criteria and specifications, such as being close to emission sources and at a reasonable distance from urban developments. The Sureste Basin, in the Southeast of Mexico, is the most prolific hydrocarbon basin in the country. It has numerous mature oil and gas fields that could be utilised for CCS, and there are many industry emission sources. This thesis aims to study the Ogarrio field, which is a mature oil field in the Sureste Basin. In this thesis, I carry out three different analyses that complement each other to cover the transport and storage phases of CCS.

I begin by applying a storage capacity assessment methodology to estimate the probable CO_2 storage capacity in the target geological formations of the field (Upper Concepcion, Lower Concepcion, and Encanto). I create a database to characterise the stratigraphy and subsurface structures, using well log information, lithology, depth, location, and 2D seismic data from the field. I also use this data to produce a detailed assessment of storage capacity. I then compare the total storage capacity with the volume of hydrocarbons produced from the field to obtain an acceptable constraint on the fluid volumes that could be removed from or injected into the field. Via an uncertainty analysis, I determine that the minimum, total, and maximum storage potential capacities are 0.4, 36, and 131 megatonnes (Mt) of CO_2. I also performed a Monte Carlo analysis where I obtained the minimum (3.4 Mt), most likely (32.3 Mt), and maximum (275 Mt) capacity values. The range of potential storage capacities at the upper and lower ends highlights the challenges of estimating capacities even when subsurface data is abundant.

Since storing CO_2 at specific depths implies changes in the subsurface that can generate induced seismicity, I go on to analyse fault stability for the faults located in the basin. Such analysis is helpful to assess whether CO_2 injection is likely to trigger induced seismicity. I produce a risk assessment, comparing the hazard of induced seismicity relative to that generated by natural earthquakes in the region. Based on this analysis, I obtain the suggested largest allowable magnitude of induced events in the area of M_w 4.5. To meet this requirement, I provide recommendations to mitigate the induced seismicity by introducing a Traffic Light System set at a M_w 2.5. Meeting this criterion would require deploying dedicated seismic monitoring networks in the basin.

I conclude by matching the potential storage capacity of the Ogarrio field with the

largest emission sources closest to the previously selected injection sites. I create various cost-effective pipeline routes that connect sources and storage sites through a “Least Cost Path Analysis”. Furthermore, I consider the possible obstacles present in the area (i.e., terrain, vegetation, water bodies, buildings, existing pipelines, roads, and geological faults). Finally, I calculate the potential average capital costs of the routes, which vary from 7,000,000 USD to 31,700,000 USD.

The significance of this study is that the Ogarrio Field and the analyses mentioned above could potentially be applied as a prototype methodology in other fields within the Sureste Basin, assuming that similar conditions and characteristics can be found in them.

To this day, this kind of assessment has not been carried out yet in Mexico, and there are no official records of matching Mexican CO_2 sources to possible injection sites.

DEDICATION AND ACKNOWLEDGEMENTS

Never in my life did I think I would do a PhD; it seemed like something unreachable and not in my life path, and yet here I am. It was only possible partly thanks to the Consejo Nacional de Ciencia y Tecnología (CONACyT) and the Secretaría de Energía (Sener) of Mexico, that awarded me with a scholarship to carry out my PhD research. And thank you to the Comisión Nacional de Hidrocarburos (CNH) for providing me with the information and data needed for my project.

I would also like to thank my two supervisors, Dr. James Verdon and Prof. Matt Watson, it has been a bumpy road, full of situations and challenges, and I am happy that you taught me, supported me, and guided me in your particular way. Also, thank you for your patience.

To the Earth Sciences people and fellow PhDs, it was nice to share time with you, I always found you very interesting, and I learnt a lot from your conversations. Especially thanks to Adam K, Melody, Bob, and Dave for being my friends all these years.

To the Mexican Society of Bristol, thank you for making me feel welcome from the beginning and for all the support you have given me; I am glad I got to be part of the society and make good friends.

Thanks to my friends back home for the encouragement and pep talks you always gave me.

To the people who became my Bristol family: Daniel, thank you for letting me be part of your PhD journey and for being there; I could not have asked for a better friend. To Iskra, Ale, Marco, and Bere, thanks for all the laughs and entire days of fun.

Finally, I cannot thank enough my family: my mom, sister, granny, and dad; the unconditional love and support that I have received from you are what keep me going every day; without you, I would not be here. Gracias por creer en mi, los quiero.

AUTHOR'S DECLARATION

I declare that the work in this dissertation was carried out in accordance with the requirements of the University's Regulations and Code of Practice for Research Degree Programmes and that it has not been submitted for any other academic award. Except where indicated by specific reference in the text, the work is the candidate's own work. Work done in collaboration with, or with the assistance of, others, is indicated as such. Any views expressed in the dissertation are those of the author.

SIGNED: ..... DATE: .....

TABLE OF CONTENTS

List of Tables

LIST OF FIGURES

FIGURE **Page**

CHAPTER 1

INTRODUCTION

1.1 Motivation of the study

1.1.1 Carbon Capture and Storage

Since the industrial revolution, vast CO_2 emissions from different sources around the globe have been one of the main factors that have contributed to climate warming (Mortezaei and Vahedifard, 2015). Nowadays, around 80% of the primary energy in the world is supplied by fossil fuels. Hence, to combat climate change, there is a great acceptance that preventive and mitigation actions must be carried out worldwide. Therefore, to limit the temperature rise, worldwide greenhouse gas (GHG) emissions should reach net-zero emission by 2050 (IPCC et al., 2018). Net-zero emissions mean that greenhouse gases emissions by then should be balanced with a proportional amount of removal out of the atmosphere.

One of the most effective ways to achieve this is through a process known as Carbon Capture and Storage (CCS). This technology prevents anthropogenic carbon dioxide (CO_2) from being released into the atmosphere. According to the International Energy Agency (IEA, 2012), the CCS can contribute between 9 to 14% of the reduction of global emissions. The overall CCS process consists of four stages:

1. Capture and purification of CO_2, usually from combustion of fossil fuels. Capture can be applied to different industries such as gas, oil, steel, and cement, followed by the compression of the CO_2 (Mortezaei and Vahedifard, 2015).

2. Transportation from the CO_2 source to the storage site, this could be through pipelines, shipping, trucks or rail.

3. Injection and geological storage of CO_2 into a subsurface formation with suitable conditions.

4. Monitoring the site to ensure the injected CO_2 remains permanently stored in the subsurface (Global CCS Institute, 2019).

1.1.2 CO_2 Capture

The utilisation of carbon capture in industrial processes dates from the 1930s, when CO_2 absorption with chemical solvents was used to separate CO_2 from methane in the natural gas industry. Currently, second-generation technologies are being developed and could significantly reduce costs. (Kearns et al., 2021).

The most commonly-applied capture technologies include (IEA, 2021):

- Chemical absorption, based on the reaction between CO_2 and a chemical solvent that absorbs the CO_2; a high-purity CO_2 stream is then released by applying heat. This technology is capable of capturing up to 99% of emitted CO_2 (Danaci et al., 2021).

- Oxyfuel combustion uses almost pure oxygen for fuel combustion, producing an exhaust stream composed mainly of water vapour and CO_2, making the CO_2 separation and capture easier. More than 90% of the emission can be captured with this technology (Danaci et al., 2021).

Other technologies include membrane separation, direct separation, and supercritical CO_2 power cycles, among others (IEA, 2021).

Industries where the CO_2 can be captured include power generation, natural gas processing, oil refineries, chemical production, waste-to-energy, hydrogen production, ethanol production, cement, fertiliser production, iron and steel, and direct air capture.

1.1.3 CO_2 Transportation

Transportation is a crucial phase in the CCS chain; pipelines and ships are the most reliable options for transporting CO_2 from the emission sources to a storage site.

Transportation via pipeline is the cheapest method for a large-scale project, and pipelines can cover long distances onshore and offshore (Kearns et al., 2021). Large-scale shipping of gases has taken place for over 30 years, mainly in Europe, and its utilisation in CCS has been increasing in the last years. Trucks have been used for small projects covering short distances; however, transportation via trucks is not a viable option in the long term because of the quantity of CO_2 and the prices they imply. Rail transportation has not been used actively in the CCS so far (Global CCS Institute, 2018; ITJ, 2019).

1.1.4 CO_2 Storage and Enhanced Oil Recovery

For the storage process, the CO_2 is injected into sites that are located underground, typically at more than 800 m depth. Geological storage targets high porosity formations, where large pore volumes enables the storage of large amounts of CO_2. High porosities and permeabilities allow the CO_2 to flow according to the injection rate, filling the pore space (SENER, 2014). The porous storage targets must be overlain by impermeable rocks that seal the reservoir and prevent further upward migration of CO_2. Reservoirs targeted for CCS include deep saline aquifers, as well as depleted oil and gas reservoirs.

CO_2 storage sites can be associated with Enhanced Oil Recovery (EOR). CO_2-EOR has been a common practice in depleted oil and gas fields. The objective is to maximise oil recovery while the injected CO_2 remains stored in the pore space where the oil and gas used to be trapped (Kearns et al., 2021). However, since the CO_2 may be highly miscible with the oil and/or gas, only a proportion of the CO_2 injected may remain in the reservoir with the remainder coming back to the surface with the recovered hydrocarbons (Gozalpour et al., 2005). Nevertheless, storage conditions and behaviour of CO_2 in the subsurface are well-comprehended thanks to the years of injection experience of CO_2-EOR (IEA, 2021).

1.1.5 Monitoring

Ensuring the long-term geological CO_2 storage requires monitoring prior, during, and even after injection operations stop to prevent leakage to the surface, contamination of fresh-water aquifers, and induced seismicity (SENER, 2014). Various geophysical monitoring methods have been applied in CCS projects, including reflection seismic imaging (Blackford et al., 2015), passive seismic monitoring (Verdon et al., 2012), InSAR measurements of surface deformation (Yang et al., 2015), and near-surface measurements of groundwater properties and gas fluxes (Spangler et al., 2010).

1.2 Risk associated with CO_2 storage

One of the obstacles in executing the CCS projects is the security of geological CO_2 storage. CO_2 can induce seismicity, displacements, and leakages when injected into the subsurface.

Induced seismicity is the seismic activity caused by anthropogenic operations such as CO_2 injection; displacements could occur due to changes in pressures and reactivate faults and fractures in the subsurface and surface. Injection of CO_2 can also cause a displacement of the brine when the brine flows to other formations and aquifers (Damen et al., 2006). The leakage is the migration of CO_2 out of the storage formations, and it moves around in overlaying formations to leak on the surface and the atmosphere.

CO_2 can be damaging when exposed at high concentrations to living beings, ecosystems, and the atmosphere (Koornneef et al., 2009). If the exposure is too elevated, it could cause death, and CO_2 leaked in an aquatic environment such as aquifers can compromise the

potable water quality. In addition, it could alter the composition of the soils, affecting nutrients and plant growth (Damen et al., 2006).

The leakage depends on the type of reservoir, caprock, trapping mechanisms, and well integrity (Damen et al., 2006). The knowledge and leaking data are scarce because there is no accurate comprehension of the CO_2 behaviour in the underground in terms of thousand years, nor of the behaviour of the CO_2 leaked (Alcalde et al., 2018). However, global analyses have determined that to provide adequate storage; an acceptable leakage rate must be between 0.01% and 1.0% per year, which means that 99.9% of CO_2 must remain in the reservoir for more than 10,000 years (Alcalde et al., 2018; Lindeberg and Bergmo, 2003; Hepple and Benson, 2003; Nordbotten et al., 2005).

1.2.1 Abandoned wells

Generally, geological storage CO_2 uses technology, infrastructure, and methodologies from the oil and gas industries (Alcalde et al., 2018). The primary sources of leakage are natural pathways and abandoned wells from the hydrocarbon industry.

Hydrocarbon reservoirs are usually perforated by hundreds of wells, which are often abandoned without a proper assessment to establish their integrity and risk of leakage (Damen et al., 2006). Different reasons could compromise the integrity of a well, such as faulty cementation, defective plugging, corrosion, and overpressure (Ide et al., 2006). Furthermore, leaking could occur between cement and rock formations through cement, casing, and damaged cement plugs (Nordbotten et al., 2005).

These wells penetrate the caprock and formation, generating conduits for buoyant CO_2, causing its migration to the surface, aquifers or the atmosphere; therefore, abandoned wells represent the main leakage risk in any storage site (Ide et al., 2006).

In order to reduce this type of risk, there must be regulations to address the well abandonment all over the world and in the specific regions where CCS projects are planned to be carried out. Stakeholders responsible for the deployment of such projects must locate, identify, characterise, screen, and monitor all wells in the area before, during, and after injection of CO_2 (Koornneef et al., 2009; Sy et al., 2012).

1.3 CCS worldwide

The costs of implementing CCS vary according to the application, location, and amount of CO_2 transported and stored. The future of CCS projects is expected to rely on hubs and clusters of CCS projects linked by their infrastructure to different storage sites, as this will minimise the economic costs for projects of a range of sizes (Global CCS Institute, 2021).

The IEA set the goal of keeping the global average temperature rise below 1.5° C. However, at this point, this goal seems unattainable because around 5,600 megatonnes per annum (Mtpa) of CO_2 must be stored by 2050 (Loria and Bright, 2021), whereas present

volumes of CO_2 being captured and stored amount to approximately 40 Mtpa (Global CCS Institute, 2021). This means that 70 to 100 new facilities should be developed every year (Townsend and Gillespie, 2020).

Clearly, the potential for CCS has not yet been taken advantage of. In part, this may stem from issues with legal and regulatory frameworks, which change from one country to another. In many places, the public is still unaware of what this technology entails (Mortezaei and Vahedifard, 2015).

The first CO_2 underground injection project at a commercial scale, SACROC, started operations in Texas in 1972 (Hill et al., 2013); it stores around 0.4 Mtpa and is used for EOR. Since then, around 300 megatonnes (Mt) of CO_2 emissions from different fossil-derived fuels such as steel, cement, and oil and gas industries have already been captured and injected around the globe (see Figure 1.1). According to the Global CCS Institute, in 2021, approximately 36 Mt of CO_2 capture will have been dedicated to geological storage, with the remaining 90 Mt being associated with EOR activities.

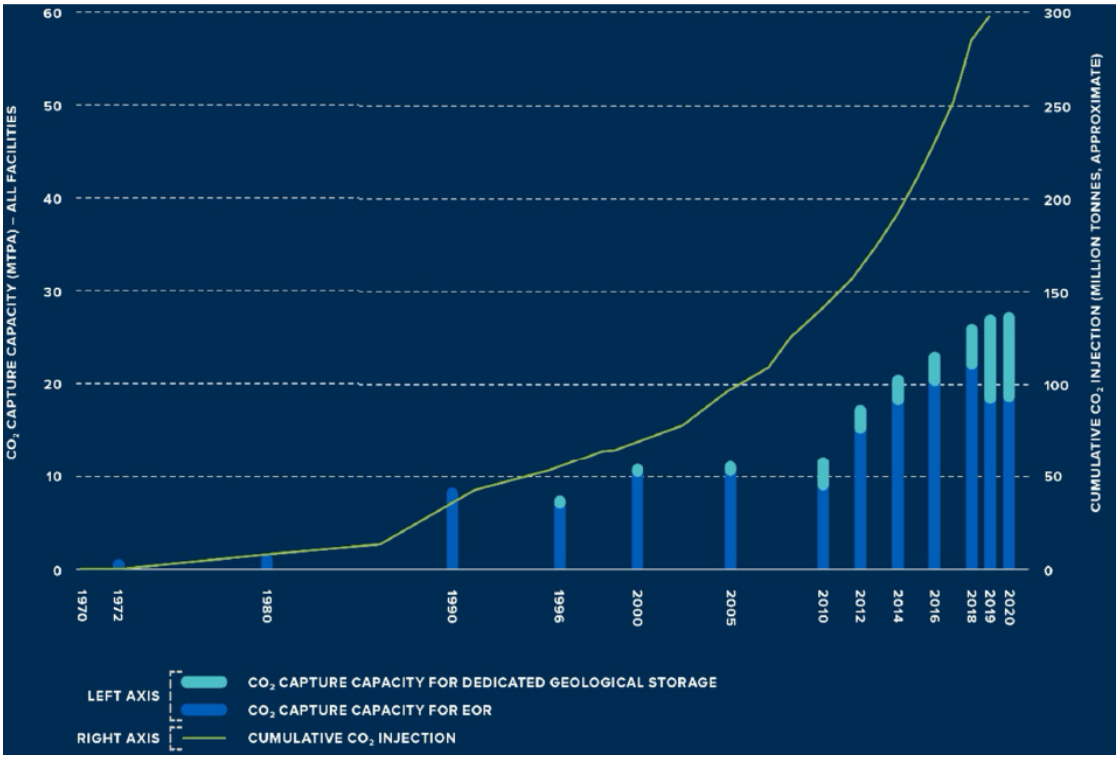

Figure 1.1: Cumulative CO_2 injection worldwide for all full-chain CCS projects. Taken from Loria and Bright (2021).

The Alberta Carbon Trunk Line (ACTL) with the Northwest Redwater Partnership's Sturgeon Refinery CO_2 Stream and the Nutrien Fertiliser Plant in Canada (2020), the CNOOC South China Sea Offshore CCS in China (2021), and the Orca project in Iceland (2021) are the most recent operational CCS projects in the world, and they are planned to store 1.9 Mtpa (Global CCS Institute, 2020).

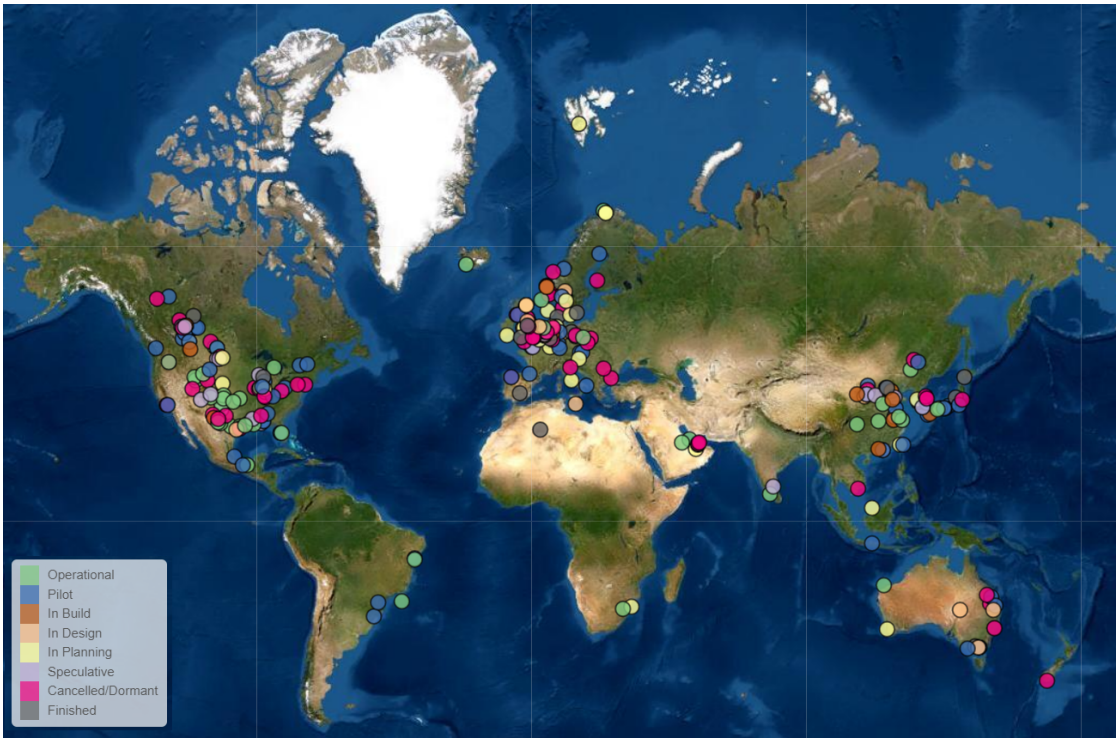

Figure 1.2: Status of the CCS projects worldwide. Taken from SCCS (2021).

Currently, there are 135 commercial CCS facilities worldwide; 29 are active, and 106 are under development (see Figure 1.2). The United States has 12 fully operational projects. Canada and China have four each, the Gulf Cooperation Council (GCC) has three, Norway has two, whereas Hungary, Brazil, Australia and Iceland have one each (Global CCS Institute, 2020).

One of the largest projects is at Sleipner in Norway, which has stored 19 Mt since 1996. This site was the first in the world to sequester the CO_2 geologically. Another significant project is the Archer-Daniels-Midland (ADM) site in the USA; it captures and stores CO_2 from ethanol, making it the first project that does not use fossil energy. In Canada, the Quest project is projected to store 27 Mt, using only 5-7% of the total storage capacity of the sequestration area for the next 25 years (Loria and Bright, 2021).

1.4 CCS in Mexico

In 2020, Mexico contributed 1.13% to global CO_2 emissions, ranking 16th internationally with 407 Mt of CO_2 emitted (Crippa; M. et al., 2021). The country relies mainly on fossil fuels in the transportation and electrical generation industries (see Figure 1.3). Mexico must develop and use CCS technology as it is one of the biggest and most populated countries globally, and the use of fossil fuels generates over 75% of the CO_2 in the country.

The first steps towards developing CCS technology in Mexico started in 2012. At that

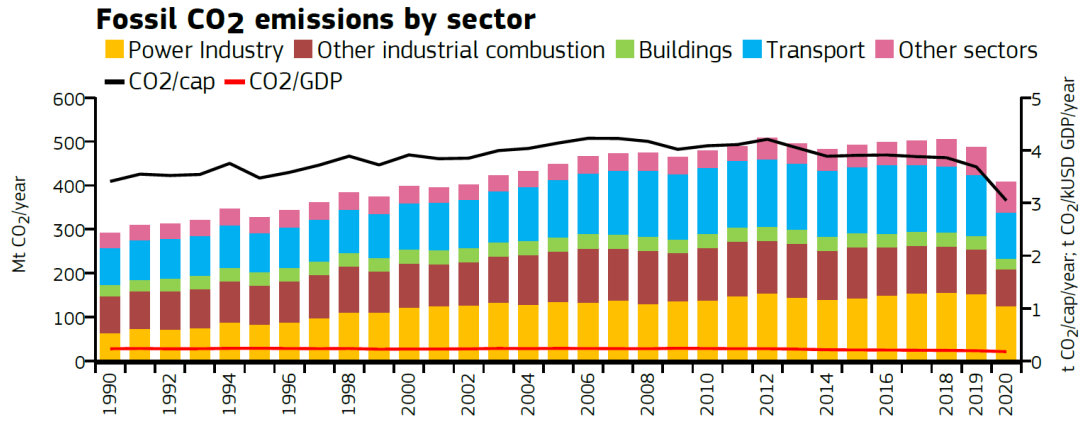

Figure 1.3: CO_2 emissions by sector in Mexico from 1990 to 2018. Taken from (Crippa; M. et al., 2021).

time, the country only had information about the emission points and the amount of CO_2 emitted per year by industry. In addition to this, other studies, such as the Atlas of Geological Storage in Mexico (SENER, 2012), made by the SENER (Ministry of Energy in Mexico) along with the Federal Electricity Commission (CFE in Spanish), published estimates of the geological storage capacities in Mexico, emission points on a map and potential locations to store CO_2. These estimates were based on the study carried out by Dávila et al. (2010), which divided the country into seven zones of geological CO_2 storage potential according to their geology, seismicity and volcanic activity. These zones were used in the North American Carbon Storage Atlas (USDOE et al., 2012) to divide Mexico into two zones: the inclusion zone and the exclusion zone. The inclusion zone is a stable area with saline formations and gas and oil reservoirs surrounding the Gulf of Mexico. The exclusion zone, along the Pacific coast, has high tectonic and volcanic activity and is therefore not recommended for CO_2 storage (see Figure 1.4).

It should be noted that the SENER (2012) storage Atlas is based on a broad-brush approach to large areas; it did not take into account the actual subsurface structures where the CO_2 could accumulate, and as such, likely produces an overestimated potential storage volume.

Furthermore, in 2018, SENER developed the Technology Route Map of Carbon Capture, Use and Storage (CCUS) in Mexico (SENER, 2018a), showing the plans to store the CO_2 produced in Mexico, including activities such as public policy, planning, and pilot programmes (González-Díaz et al., 2017). Following that document, in the same year, SENER launched the National Inventory of Emission Sources and Sites for the Use and Storage of CO_2 in Mexico online (SENER, 2018b), which contains open data on the planning and development of CCS projects in the country.

A climate change law was established in 2012, aiming to reduce GHG emissions from 2000 by 30% by 2020 and 50% by 2050 (Mota and Heras, 2018). The storage of 50 Mtpa of CO_2 is necessary to achieve this goal by 2050. Therefore, it is essential to identify power

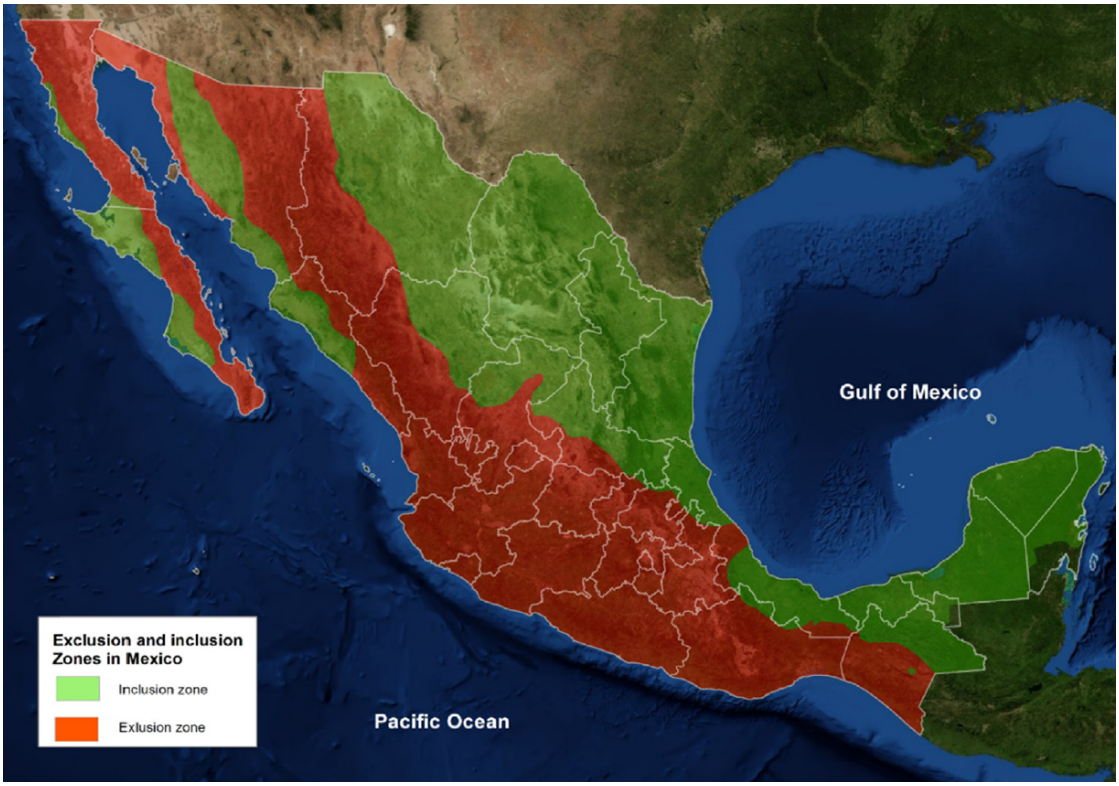

Figure 1.4: Inclusion and Exclusion CO_2 storage zones in Mexico Taken from Lacy et al. (2013).

plants and industries where CCS activities can be carried out. An advantage is that Mexico can develop CCS industrial clusters in regions near the oil fields, and the existing plants can be adapted for capture, transportation, injection, and storage of CO_2. Moreover, there has been an increase in depleted and less productive oil and gas fields in recent years which could present attractive storage targets, with CO_2-EOR being used to offset some of the high costs involved in CCS.

The Gulf of Mexico region is the largest industrial CO_2 emitter in the country, with approximately 20.1 Mtpa, from which 13 Mtpa are emitted by natural gas combined cycle (NGCC). Other industries with the potential to capture CO_2 are coal-fired power, cement, iron, and steel. A fuel oil-fired power plant, "Adolfo Lopez Mateos", located in Veracruz, is the largest emitter in Mexico, releasing 4 Mtpa (Lacy et al., 2013). Other large CO_2 sources in the country are the Mexican Petroleum (Pemex in Spanish) and CFE facilities; both run by the Mexican Government.

There are currently plans for two pilot projects whose purpose is to evaluate the implementation of CCS on a commercial scale, the socioeconomic and environmental impacts, and to analyse the technical and political barriers of a CCS project. One project is planned for an NGCC natural gas-fired, combined-cycle generating station in Poza Rica, Veracruz. The other will be CO_2-EOR to store CO_2 in a 2 km depth reservoir in the Brillante Field in the south of Veracruz (Mota and Heras, 2018). According to the Technology Route

Map, these projects should be finished and marketed in Mexico by 2024. However, after the feasibility studies in both projects, there has been no further development as they have been delayed due to political issues (BEIS, 2020).

Due to the fact that since 2018 there have been no significant advances in the work done by SENER and on the subject of CCS in Mexico, this thesis proposes a methodology that selects the most suitable places to inject and store CO_2 into depleted and mature oil and gas fields, calculates their storage capacity according to their characteristics, and also analyses and suggests mitigation measures for potential hazards such as induced seismicity, to finally connect emission sources such as PEMEX power plants to the injection and storage places. Therefore, the application of this methodology will result in a practical and functional approach to start developing CCS projects in the country.

1.5 Estimation of storage volumes

A CCS project requires prior study of the target geological formations in which the CO_2 will be sequestrated, analysis of how the CO_2 will be transported from the emission sources, and how it will behave in the different environments to which it will be exposed during the process (e.g., pipelines, subsurface). For that reason, it is essential to know and understand the properties of CO_2 at different temperatures and pressures.

1.5.1 CO_2 properties

At ambient pressure and temperature, CO_2 is a colourless, odourless and incombustible gas that constitutes 0.038% of the volume of the atmosphere and is heavier than air. At temperatures between -56.5°C and 31.1°C, the CO_2 changes from vapour to liquid if compressed at adequate liquefaction pressure. It is solid at temperatures lower than 31.1°C. Figure 1.5 displays the phase behaviour of CO_2, including the triple point, which is the point at which the gas, liquid and solid phases coexist in thermodynamic equilibrium. Above the critical point, CO_2 exists in a supercritical fluid phase, where separate gas and liquid phases do not exist. In its supercritical phase, CO_2 has the density of a liquid and the viscosity of a gas. Changes in temperature or pressure very close to the critical point could drastically change the density of CO_2, and also changes the phase and fluid velocity (Serpa et al., 2011).

In order to prevent such phase changes affecting the transport and storage processes, the supercritical CO_2 needs to be compressed to a pressure higher than 7.38 bar and a temperature higher than 31.1°C. For this reason, CO_2 transportation should have constant monitoring. Storage in the supercritical phase maximises the CO_2 mass in a given volume, and so is optimum for CCS. The CO_2 density is directly affected by the temperature and depth, and it ranges from 150 to 800 kg/m^3, which also affects the buoyancy forces moving

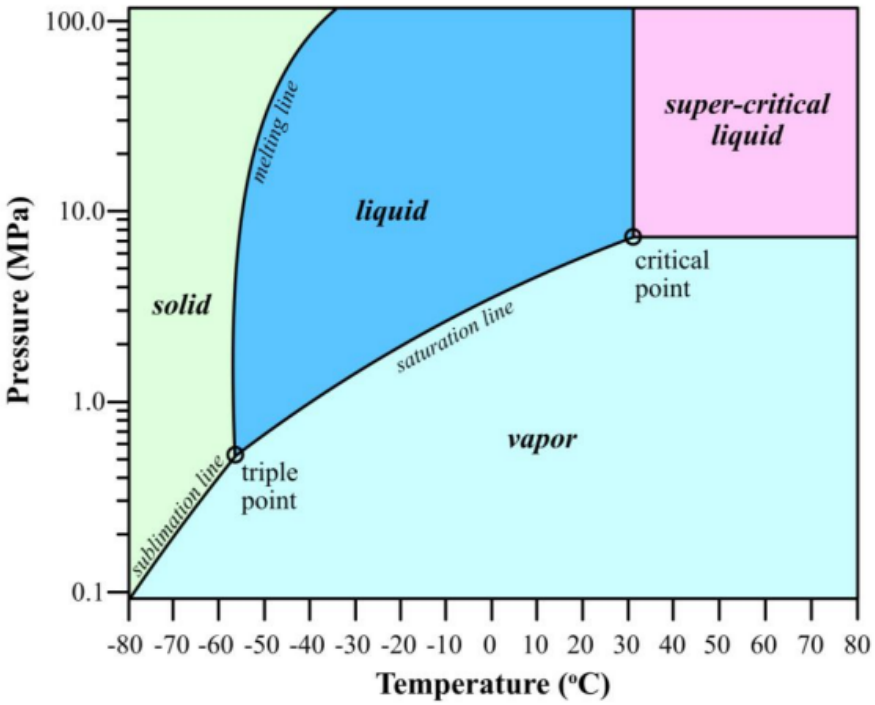

Figure 1.5: CO_2 phase diagram. Taken from Gierzynski (2016).

the CO_2 towards the ground surface (Bachu, 2003). Therefore, impermeable caprocks are required to store CO_2 to secure and prevent CO_2 motion toward the surface (Lacy 2013).

1.5.2 CO_2 trapping mechanisms

Due to its characteristics, it is possible to store CO_2 at various sites, such as coal beds, oil and gas reservoirs, salt caverns, and deep saline aquifers; see Figure 1.6 (Bachu, 2015). CO_2 can be kept at the sequestration site because it can be stored in four different trapping mechanisms: 1) "structural and stratigraphical trapping", where the supercritical CO_2 in a mobile phase is contained under an impermeable layer of rock, caprock, which acts as an obstruction for CO_2 to migrate to the surface Alcalde et al. (2018); Cao et al. (2020). 2) In "residual trapping", the injected supercritical CO_2 displaces the formation fluid and this fluid traps the residual CO_2 in the pores of rocks due to capillary forces (Hosseininoosheri et al., 2018). 3) In "solubility trapping", CO_2 can be dissolved in solution in the reservoir fluid entering an immobile phase (Cao et al., 2020). 4) The "mineral trapping" is when the dissolution of CO_2 changes the pH of the reservoir fluid and dissolute the formation rock, causing the precipitation of carbonate minerals; it is a slow process that can take up to 1000 years (Han, 2008; Hosseininoosheri et al., 2018).

Furthermore, when CO_2-EOR is applied, CO_2 flows through the rock fractures of the oil reservoir in its supercritical CO_2 phase and permeates into the rock. The CO_2 solubility decreases the density and viscosity of the oil in the rock, leading to the migration of the

oil through rock fractures to the production well, enhancing the recovery of the oil and allowing CO_2 to remain stored in the reservoir Cao et al. (2020).

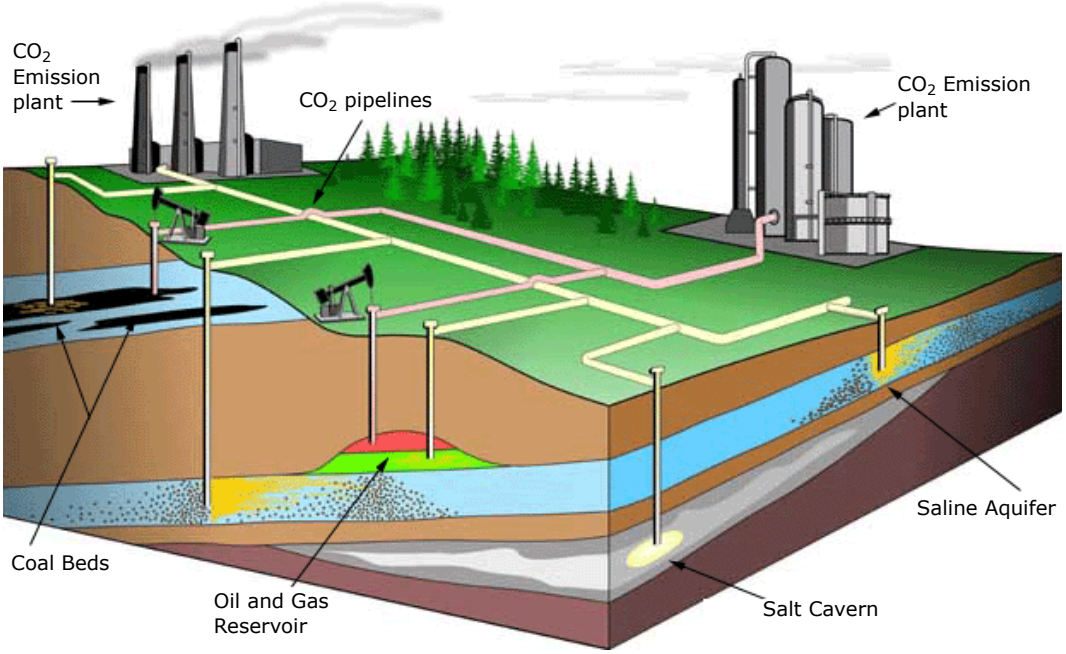

Figure 1.6: CO_2 storage and sequestration options in a geological environment. Modified from Bachu (2003).

Typically, sedimentary basins contain the pore space and injectivity necessary for the sequestration of CO_2. Adequate structural and solubility trapping can be found in oil and gas reservoirs. Mineral trapping is found in the deep sandstone and carbonate aquifers. Coal beds are suitable for absorption trapping. Salt beds and domes are suitable for cavern trapping. These environments have the porosity, permeability, and capacity to contain CO_2 for significant amounts of time, preventing it from being released back into the atmosphere (Bachu, 2003).

1.6 CO_2 storage assessment scale

From a general point of view, Bachu (2003) classified the criteria to locate the most feasible sedimentary basins for CO_2 storage as:

1. The invariable characteristics or “hard criteria” include tectonism, geology, geothermal regimes. It also includes depth, lithology, mineralogy, geometry, and petrophysical characterisation of the basin, and an analysis of the fluid properties.
2. The “semi-hard” criteria or the criteria that might change (i.e., basin resources, hydrocarbons, coal).
3. The “soft” criteria are the socio-economic and political situation in the location of the basin.

In addition, the methodology applied to estimate the storage capacity depends on the scale of the assessment, affecting the level of detail needed. Bachu et al. (2007) described an assessment scale, which consists of five levels (Figure 1.7):

1. **Country-Scale**, the requirements of this assessment are minimal, and it includes all basins within a country.
2. **Basin-Scale**, this assessment studies a specific sedimentary basin and attempts to determine the best sites for storage, considering the emission sources nearby.
3. **Regional-Scale**, the difference between this assessment and the above is that a region could include a portion of a basin or several basins, with more details in the assessment and large CO_2 sources already targeted.
4. **Local-Scale**, this assessment is carried out to select the best option from different storage sites; it is very detailed and includes economic and engineering assessments.
5. **Site-Scale** has a target storage unit, which is modelled to analyse and assess the behaviour of the CO_2 injected for long periods.

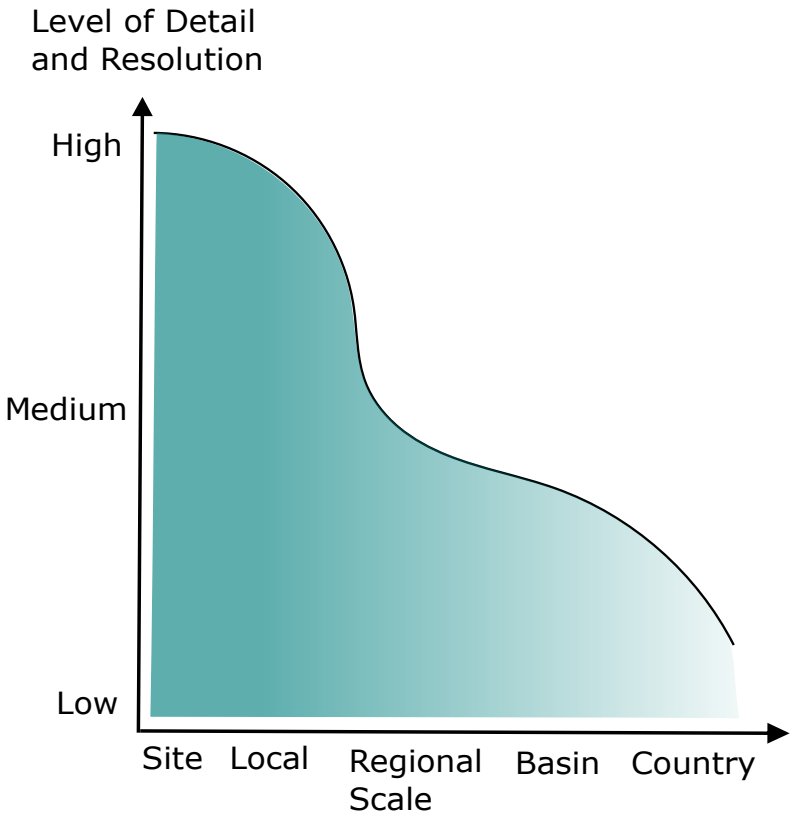

Figure 1.7: Assessment scale for the estimated storage capacity of the CO_2, modified from Bachu et al. (2007).

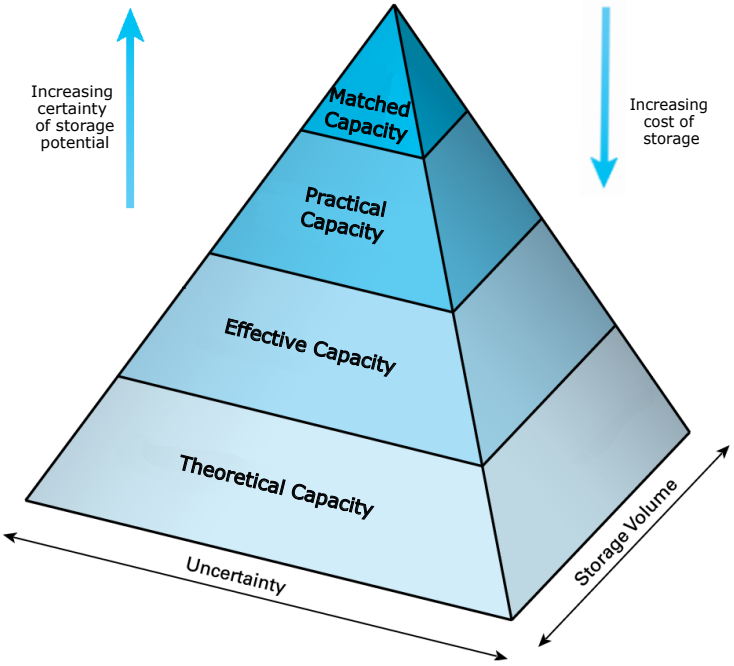

Figure 1.8: Techno-economic resource pyramid, modified from Bachu et al. (2007); CSLF (2008).

Another way to standardise the storage capacity assessment is according to the resources and reserves available at four different levels (CSLF, 2008); this is represented by the Techno-Economic Resource Pyramid for CO_2 Storage Capacity (see Figure 1.8).

1. **The theoretical storage capacity** assumes that the maximum physical capacity of the geological media can store CO_2 in its entirety.
2. **The effective storage capacity** considers that part of the theoretical capacity can be analysed to determine if it meets the required geological and technology criteria.
3. **The practical storage capacity** is related to the legal, political, and infrastructure regulations and frameworks.
4. **The matched storage capacity** is the one that links the storage capacity of the CO_2 sources with the storage sites, according to the CO_2 rate capture, transported and stored. This capacity is at the top of the pyramid.

1.7 CO_2 storage in oil and gas reservoirs

One of the advantages of storage in oil and gas reservoirs, specifically depleted fields, is that oil and gas companies have already explored geophysically and geologically analysed sites

with the data obtained from their wells. Appropriate sites can then be selected considering their petrophysical characteristics, capacity, structural conditions, faults, and fractures to maximise storage potential and prevent leaking. The presence of the wells makes it easier to monitor storage sites in order to constantly review their integrity and safety (Loria and Bright, 2021).

The Carbon Sequestration Leadership Forum (CSLF) 2008 stated that the sum of capacities in a hydrocarbon reservoir gives the CO_2 storage capacity, regardless of the region or scale. The capacity is measured based on the petrophysical characteristics of the reservoir and the volume of oil and gas formerly occupied since it is assumed that this volume could be available for CO_2 storage. For instance, if the trapping structure in a reservoir is not filled with oil and gas, the space not occupied could be used to store CO_2. However, it is not possible to use the total pore space of the reservoirs to store CO_2 as this substance cannot fill the entire pore space. When the hydrocarbon production stops, and if the reservoir is in contact with an aquifer, some water could penetrate it as the pressure decreases. Due to capillarity and gravity effects, this water could take up some pore space, decreasing the availability of CO_2 (Bachu et al., 2007). Thus, only a limited volume of CO_2 can be stored before the accumulated pore fluid pressure of the reservoir is surpassed (Gammer et al., 2011).

In the last decades, static and dynamic storage capacity assessment methodologies have been developed. They depend on the scale, type, amount, and characteristics of the data. The static methods are unrelated to time. Whereas the dynamic methods are related to time, and they include numerical and analytical simulations. The most used static methods are the volumetric and compressibility methods, and the dynamic methods are the semi-closed, reservoir simulation and reservoir simulation (Jin et al., 2010).

This thesis will mainly focus on the static volumetric method. The volumetric method could be applied from a country to a basin-scale capacity estimates (CSLF, 2008). It estimates the total pore volume and the storage efficiency, which is the part of the volume that is available for CO_2 to be stored (Pickup, 2013).

In 2007, the CSLF for Review and Development of Standard Methodology for Storage Capacity Estimation reported a set of volumetric methodologies for CO_2 storage capacity estimation in oil and gas reservoirs based on published hydrocarbon reserves. This methodology could be used to calculate the theoretical and effective capacities, using an equation based on the area extent and thickness of the reservoir:

$$MCO_2 = \rho CO_2 r \times [R_f \times A \times h \times \phi \times (1 - S_w)] \times C_e \quad , \tag{1.1}$$

where $\rho CO_2 r$ is the CO_2 density at reservoir conditions, R_f is the recovery factor, A, h, and ϕ and S_w are reservoir area, thickness, porosity, and water saturation, respectively. C_e is the capacity or storage coefficient, which relates the total available volume to that actually used for CO_2 storage.

The recovery factor R_f is the average amount of hydrocarbon predicted to be extracted or recovered from a field or reservoir, and it depends on the geological heterogeneity, diagenesis process, structural complexity, proximity of aquifers, oil viscosity, and the number of wells in the hydrocarbon field (Shepherd, 2009).

The water saturation is the portion of the pore space that contains water and has not been removed by oil and gas because it is trapped in the rock pores (Pickup, 2013). The irreducible water saturation in the pore space cannot be removed or replaced by the water saturated with CO_2 (Gammer et al., 2011).

In 2008, the United States Department of Energy (USDOE) created a storage capacity estimation method for their Carbon Sequestration Atlas of the United States and Canada. It considers the whole aquifer and could estimate the effective storage capacity. Their equation is:

$$MCO_2 = \rho CO_2 r \times A \times h \times \phi \times (1 - S_w) \times E \quad , \tag{1.2}$$

where E is a CO_2 storage efficiency factor that indicates the portion that could be filled with CO_2 of the reservoir pore volume that had oil and gas production. In effect, the efficiency factor E in the USDOE equation combines the recovery factor and capacity coefficients of the CLSF equation.

This approach is one of the most commonly used methodologies to evaluate the prospective CO_2 geological storage volumes and select sequestration sites (CSLF, 2008). The USDOE stated that field-scale estimates could be added to obtain the basin or region-scale.

Other parameters play an essential role in these estimates, such as the wettability, the effect of salinity, and residual trapping. The wettability impacts the fluid dispersion and adherence in the reservoir. Any change in the wettability of the formation rocks increments the CO_2 possibility of wetting and filling the pores of the formation rocks (Farokhpoor et al., 2013). Effects on salinity such as salt precipitation could damage and reduce the CO_2 storage and, therefore, should be analysed to prevent drying and fractures (Sokama-Neuyam et al., 2020). When injected, the CO_2 displaces through the porous rock, removing the existing fluid. However, as it displaces, the fluid recovers its position and some CO_2 or residual CO_2 is left in the pores and becomes immobile; this process occurs relatively fast, and thus remains trapped for millions of years (Burnside and Naylor, 2014).

1.8 Induced Seismicity

One crucial thing to consider when developing CCS projects is the risks of this activity, such as leakage and induced seismicity. The concern around the induced earthquakes is that they may be felt, damaging housing and infrastructures in populated areas.

There is a relation between the injection of significant fluid volumes into the subsurface and induced seismicity (Ellsworth, 2013). Also, the risk of leakage is possible if the rock is fractured, generating permeable pathways through the caprocks, causing the upward

migration of CO_2, and contaminating the drinking water. Due to its density, the CO_2 could migrate to the surface if an active fault crosses a sealed overburden layer. Existing wells could also represent a leakage risk if the induced seismic activity damages their integrity (Verdon, 2014).

There are similitudes between CO_2 injection and storage and other fluid injection activities such as wastewater reinjection that have helped understand the behaviour of the subsurface when a substance is injected. Wastewater injection has been shown to have increased the probability of having an earthquake in and around target reservoirs, and that the earthquakes could damage the hydraulic integrity of the caprock. Most of the seismic events are located within 20 km of injection wells, showing the lateral extent of influence that such activities can create. To date, most induced events have been related to faults closer to the basement than in overburden layers (Verdon, 2014). Studies have shown that injection pressures, volumes, and depths can influence the occurrence of induced seismicity (Lee et al., 2016) .

The largest events attributed to wastewater disposal were M_w 5.3 to 5.7 in the United States (White and Foxall, 2016). In addition, the increase in pore pressure because of CO_2 injection caused seismic activity at the In Salah CCS project, around 9000 microseismic events per year, with the largest magnitude reaching M_w 1.6 (Stork et al., 2015). Natural gas injection in the Castor natural gas storage facility caused seismic events with magnitudes M > 4.0 (del Potro and Diez, 2015).

Fluid injection into an aquifer or reservoir will increase the pore pressure, with the pressure pulse expanding from the injection point to the formation, reducing the effective normal stress in a plane. This means that reduced normal stress could potentially cause failure or reactivation of a fault, inducing seismicity and changing the permeability (Mortezaei and Vahedifard, 2015).

The increase of pore fluid pressure (P_f) leads to low effective stress $\sigma' = \sigma - P_f$. Positive effective normal stresses ($\sigma_n - P_f$) press opposing fault blocks and resist sliding motion parallel to the fault surface generated by shear stress (τ), see Figure 1.9 a . Therefore, the resistance to sliding is reduced by an increment in fluid pressure that also reduces the effective normal stress (Streit and Hillis, 2004). These parameters can be represented in a Mohr diagram (Figure 1.9 b), which depicts the consequences of changes in pore fluid pressure on fault stability. The Mohr circle represents the state of stress, the effective maximum principal stress is σ'_1, and the minimum principal stress is σ'_3, the diameter of the circle is the differential stress ($\sigma_1 - \sigma_3$) (Streit and Hillis, 2004). Thus, the Mohr circle can be shifted onto the fault failure envelope if the fluid pressure increases, reducing the effective normal stress. The failure envelope of a "strong" rock will be further to the left compared to the failure envelope of a "weak" rock (Thomas and Benson, 2005).

Increases in reservoir pressure also cause an expansion in the target unit, changing the stress field that can spread in the rock layers above and below the target formation. This can alter the effective stress acting on the faults far from the injection zone, inducing

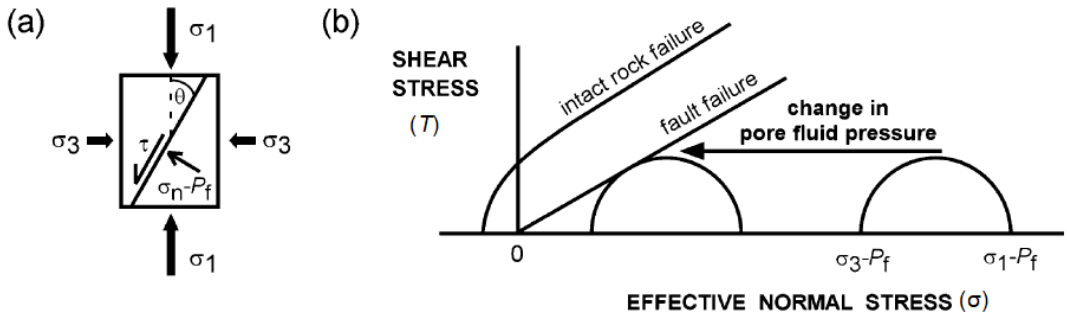

Figure 1.9: (a) Orientation of principal stresses, shear stress, and effective normal stress related to a fault plane. (b) Effects in a Mohr circle because of pore fluid pressure increase on fault stability. Taken from Streit and Hillis (2004).

earthquakes (Nicol et al., 2011). The key factors in this situation are stress in situ, injection pressure, fault properties, and rock characteristics (Mortezaei and Vahedifard, 2015).

It is crucial to estimate the maximum earthquake magnitude that could be induced due to CO_2 injection. McGarr (2014) determined a relationship between the maximum magnitude induced and the volume of fluid injected, implying that large CCS projects could induce events $M_w > 5$, with the condition that the pore pressure affects a fault with a specific orientation and size. According to Zoback and Gorelick (2012), earthquakes with magnitudes as low as M_w 2 - M_w 3 could alter the seal integrity of the CO_2 injection reservoir.

In addition to this, the risk scenarios and probability of occurrence involved in a CCS project should be addressed by a risk assessment that will explain how the seismic events could impact the injection and storage efficiency. According to White and Foxall (2016), a risk assessment involves: a) locate potential seismic sources, which could be individual faults or areas, b) estimate the frequency of occurrence of earthquakes regarding their magnitudes and sources, c) calculate the ground motion, which is the ground velocity and acceleration shaking created by an earthquake, d) obtain the probability of exceeding the ground motions on an annual basis or a specific period, depicted by a curve, e) obtain the probability of vulnerability of an area and f) calculate the annual probability of these risks happening. To develop this kind of assessment for natural seismicity, historical catalogues are helpful. However, for new operations in an area, such as CCS, it can be challenging to establish an expected rate of seismic event occurrence.

Many large CCS projects are operating, such as Sleipner in Norway and Weyburn in Canada; none of them has reported significant seismic activity (Mortezaei and Vahedifard, 2015). However, installing and monitoring seismic networks and creating a seismic hazard model adapted to the conditions of a specific region are necessary methods to mitigate and control the risk related to CO_2 injection (Nicol et al., 2011).

Chapter 4 addresses these issues with the intention of analysing and recommending

mitigation of induced seismicity options in the study area.

1.9 Pipeline Routing

An essential part of a CCS project is linking the CO_2 emission sources to the final sequestration site. This point-to-point connection could be made in several ways (i.e., through pipelines, shipping, rail, and truck) depending on the location, topography, land use, and more factors present in the area (Lacy et al., 2013). This phase of CCS is determined by the regulated frameworks and costs established by the government where the project is carried out. The safety and efficiency of the CO_2 transportation through pipelines does not imply higher risks than the ones the oil and gas industry already faces (Global CCS Institute, 2018).

Most of the CCS projects use pipelines as they can transport CO_2 at a considerable scale, and have been used for over fifty years, with a low rate of failures. For instance, approximately 70 Mtpa of CO_2 are transported in the United States through 8000 km of pipelines, that is 85% of the CO_2 pipelines worldwide (Kearns et al., 2021).

The design and pathway of the pipeline are affected by the geographical and anthropological features between the CO_2 sources and storage points. For this reason, it is necessary to determine the most direct and cost-effective route (Varun Jain et al., 2019). Therefore, the pipeline routing is carried out after determining the CO_2 emission sources and injection sites and before determining the design, length, and diameter of the pipeline. Pipeline routing models might link multiple CO_2 sources to a single injection site, or emissions from a single site to multiple storage locations. Pipeline diameters must be defined according to the anticipated CO_2 flow rate. It is worth mentioning that typically, the CO_2 is best transported when it is a dense-phase liquid, as it allows risk-free changes in the density of the fluid (Serpa et al., 2011).

Many influence factors might affect the outcome of the pipeline routing. According to Serpa et al. (2011), the most relevant are:

- In **populated areas**, constructing a pipeline requires much planning and revision of legal regulations, safety, and technical aspects. It might be more expensive as it requires additional safety measures; hence these areas should be avoided.
- **Existing pipeline infrastructure**, it is recommended to follow pipeline corridors where possible.
- **Terrain**, not all land is suitable for land pipeline construction, as unstable soil will increase the costs and risk of pipeline failure.
- In **sensitive areas**, it is crucial to identify natural protection, biodiversity, and other environmental constraints; in this case, it is necessary to relocate the pipeline route to avoid impacting those areas.

- **Other obstacles**, there are linear features such as roads and rivers that might be present in the path of the pipeline. Even though the prices might increase, there are techniques to cross them. The obstacles, complexity, and location must be assessed, ranked, and identified along the pipeline route.

Another factor to consider is the seismic hazard that could affect the source and injection facilities, especially the pipelines (Verdon, 2014).

1.9.1 Pipeline costs

When planning a pipeline project, the costs involved should be examined, as they can significantly vary from project to project. Since the characteristics of the project area are often unique, it highly depends on the location of the CO_2 sources and injection point, length, terrain and the CO_2 amount transported (Bumb et al., 2009).

Grant et al. (2019) established that the prices in flat terrain are 50,000 USD per inch-diameter per mile, and if the pipeline is offshore, the prices can escalate up to 700,000 USD. The different pipeline elements such as booster, control, metering stations, and valves also add cost.

The various pipeline particularities and costs are broadly discussed in Chapter 5.

1.10 Aims

For years, developed countries have successfully implemented CCS projects. In contrast, developing countries like Mexico have not yet exploited their CCS potential, and its participation to achieve the set global and local goals to fight climate change is imperative. Therefore, some actions, even on a small scale, must be carried out to actively incorporate the country in the efforts to reduce GHG emissions.

The research presented here comprises three different independent assessments that intertwine to produce a site-scale assessment. Some phases and planning of a CCS project could be applied as a prototype study in different fields within the Sureste Basin. The aims of these three assessments are:

- The estimation of the potential CO_2 storage capacity of the Sureste Basin by analysing an oil and gas field, assuming that similar conditions and characteristics can be found in other fields nearby. This field characterisation includes a seismic reflection and well log and structural trapping analysis.
- A fault and critical pore analysis of the faults located in the study area to find the most suitable places for injection also includes a risk assessment where the study of ground motion plays a critical role to prevent seismic hazards.

- The implementation of Geographic Information Systems (GIS) to create cost-effective CO_2 pipeline routes considering the main features and costs involved in the transportation phase in the area.

The effective and matched capacities of the region are implied in these analyses.

It is worth mentioning that there are no official records of matching Mexican industrial CO_2 sources to possible injection points so far. Moreover, the current capacity estimates were done broadly, with no detailed geological analysis to support the storage estimates, making this situation one of the biggest motivations for carrying out this thesis.

1.11 Thesis Outline

I will begin this thesis by introducing the Sureste Basin, in the Southeast of Mexico, currently the most prolific hydrocarbon basin in the country. In Chapter 2, I describe the societal, geographical, and geological characteristics and suitability of CCS by describing some potential storage fields within the Basin.

In Chapter 3, I focus on the Ogarrio field, which is well documented, as it has 510 wells drilled. According to the National Hydrocarbon Commission (CNH, 2012) and to the screening and feasibility studies carried out by Romero and Bashbush (2017) demonstrated that Ogarrio is suitable for fluid injection, including CO_2. From data provided by the SENER and the National Hydrocarbons Commission (CNH), I create a database with the well log information (i.e., porosity, gamma-ray, volume clay) lithology, age, depth, location, and 2D seismic data. This database allows me to evaluate the stratigraphy and structural traps in order to characterise the potential storage volume available for CO_2 within target formations in the field by applying storage capacity assessment methodologies. Furthermore, I compare the storage capacity with the volume of hydrocarbons produced from the field to obtain an acceptable constraint on the fluid volumes that could be removed from or injected into the field and performed analyses to assess the uncertainties in the storage capacity estimates.

However, storing CO_2 implies changes in the subsurface, leading to hazards such as induced seismicity. In Chapter 4, I perform a fault stability analysis to evaluate this issue by using the estimated stress field positions and orientations of the known faults. I complete this with a critical pore pressure analysis that defines the stability of the faults. This chapter also defines acceptable levels of seismic hazard based on historical seismicity in the region, and estimates the maximum seismic release and the largest seismic event based on proposed injection volumes. Finally, I provide recommendations to mitigate induced seismicity hazards through a Traffic Light System.

In Chapter 5, I generate several pipeline routes to connect the CO_2 emission sources around the Sureste Basin to the injection points. These points are chosen by matching the potential storage capacity of the Ogarrio field with the largest emissions sources closest to

the identified injection sites, which are estimated and identified in Chapter 3. To create the routes, I consider the possible obstacles present in the area, such as terrain, vegetation, water bodies, buildings, existing pipelines, roads, and geological faults; therefore, I take into account the results from the fault analysis in Chapter 4. In addition to this, I calculate the potential average capital costs of the routes based on prior CO_2 pipeline transportation and construction in the United States (Grant et al., 2019).

Finally, in Chapter 6, I present the main findings and limitations of this study based on the results, and I remark the contributions and recommendations for future work.

CHAPTER 2

SURESTE BASIN

Mexico has a substantial CO_2 storage potential, SENER (2012) identified 11 basins as suitable for CCS; see Figure 2.1. Excluding the Baja California and Sonora-Sinaloa, all of them have saline aquifers deeper than 800 meters, sectors of sedimentary rock sequences and are located close to CO_2 emitting industrial areas (SENER, 2012). However, the literature has proposed that the Sureste Basin, located in southeast Mexico, is considered one of the most viable carbon capture and storage (CCS) places in the country (SENER, 2012; Jimenez et al., 2011; Romero and Bashbush, 2017; CNH, 2012; Sanchez, 2018; Rodriguez Moreno, 2020). This basin has several mature and depleted oil and gas fields that have been explored by Pemex since 1950 (Guerrero, 2018) and therefore, the geographical, geological, and petrophysical properties of its fields, specifically of its sedimentary sequences and the fact that it has many CO_2 sources within them, makes this basin the focus of this thesis.

The Sureste Basin is one of the most important oil and gas producing basins in Mexico. A range of hydrocarbon types are produced, including dry gas, wet gas, super-light, light, and heavy oil. The production comes from terrigenous and carbonate formations. As reported by Guerrero (2018) during 2018, the Sureste Basin contributed 95% of the oil production and 79% of the gas production in Mexico. Moreover, the terrestrial portion of the Sureste Basin has a high percentage of mature fields, with significant oil reserves still in place, and possibilities for the implementation of CCS.

The Sureste Basin has a long history of oil and gas extraction; the first attempt to exploit a surface deposit called the “San Fernando Oil Mine” took place in 1863. In 1883, a well was drilled 27.4 meters, and in 1886 there was a small production of light oil. In the period from 1957 to 1965, there were important discoveries of fields considered giants at that time: Ogarrio, Magallanes, and Cinco Presidentes (Guerrero, 2018).

This chapter describes the diverse characteristics and factors that compose the Sureste

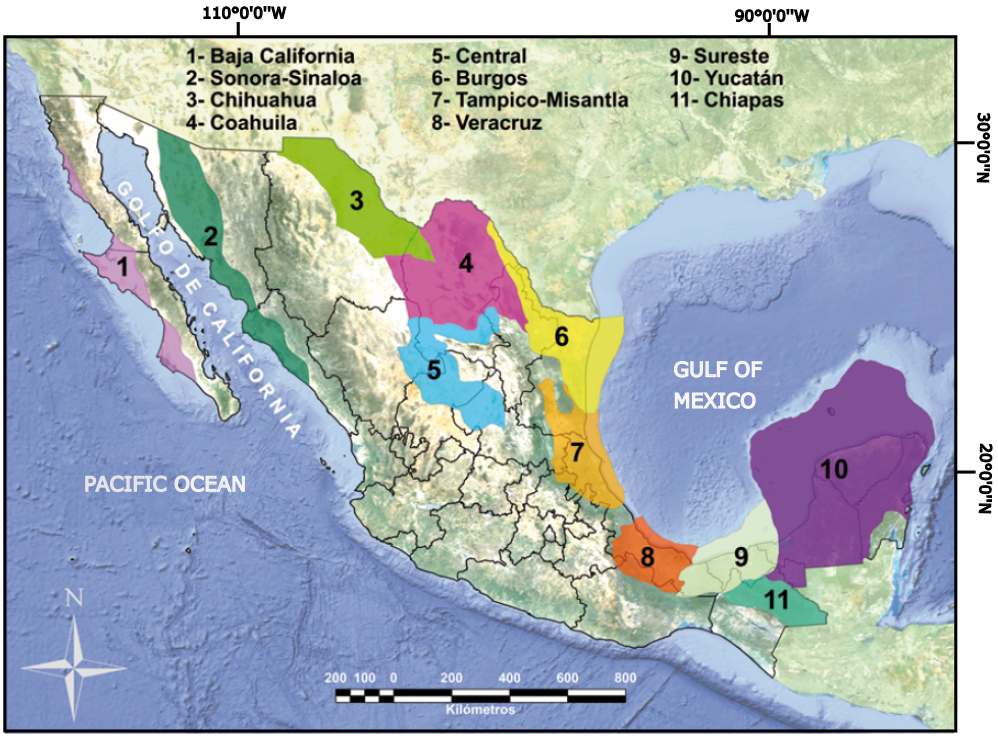

Figure 2.1: Geological basins with possibilities of storing CO_2 in Mexico, modified from SENER (2012).

Basin. It describes the social, geographical, and geological aspects that make this basin an attractive target for CCS. I consider the motivations for CCS in the basin and its theoretical storage capacity from previous literature, which will lead to one of the central questions of this thesis: how much CO_2 can be actually stored in the Sureste Basin?

2.1 General Characteristics

2.1.1 Location

The Sureste Basin is located in the coastal plain of the Gulf of Mexico and the continental platform of the southeast of Mexico (Figure 2.2); it includes a terrestrial and a marine portion. It covers the south of the state of Veracruz, the north of the state of Chiapas, almost the entire state of Tabasco, and the southwestern end of the state of Campeche. It has an area of 59,000 km^2 (CNH, 2014).

It is surrounded by the Cinturon Plegado (Folded Belt) of the Chiapas Basin in the south, the Veracruz Basin in the west, and the Yucatan Platform in the east. It contains the Cantarell field, the most prolific oilfield in Mexico (CNH, 2014).

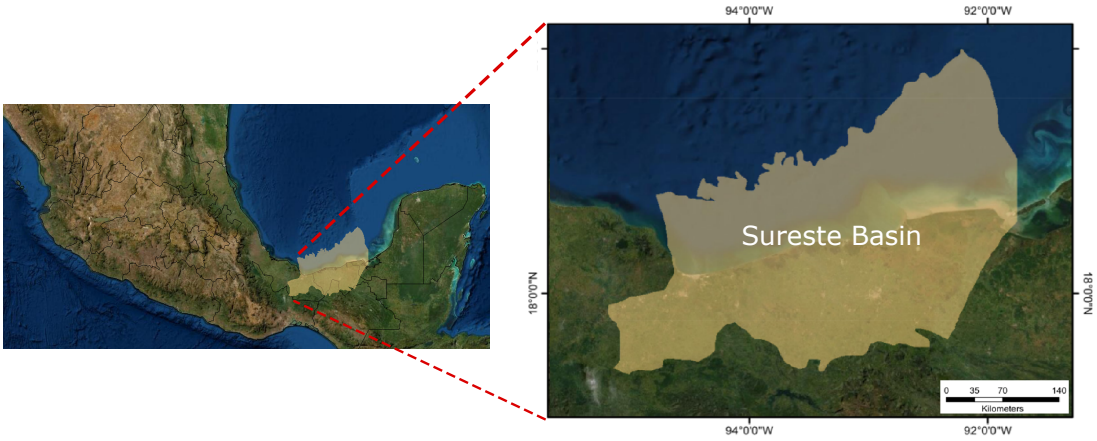

Figure 2.2: Location of Sureste Basin.

When planning a pipeline that will connect CO_2 sources with potential injection sites, factors such as the physiography, hydrography, population, and the location of the primary sources have to be considered. These parameters will determine the path, length, and costs of the pipeline.

To create an optimal route, topography, soils, fluvial systems, urban settings, and other environmental considerations should be analysed to avoid cities, lakes, rivers, mountains, hills, protected natural areas, and roads. Pipelines should not damage existing ecosystems or disturb populated areas (Peletiri et al., 2018). For these reasons, a number of potential pipeline routes were designed to find the optimal routes. This topic will be further developed in Chapter 5.

2.1.2 Physiography

This terrestrial portion of the basin consists of low and humid plains of alluvial origin created by the action of the rivers, which are fed by abundant rainfall. In some areas, there are swampy and flooded depressions (INAFED, 2016).

Most of the territory is relatively flat. There are some elevations to the south that are part of the central plateau of Chiapas. Among the most important hills are El Madrigal, which is approximately 1,000 meters above sea level (masl), the Cerro Jimbal with an elevation of about 600 masl, other elevations are Cerro La Campana, Cerro Pelón, Cerro La Encantada, Cerro de Manatí, Mono Pelado, El Tortuguero. However, their elevation is not greater than 150 m (Alcantara Rojas, 2010) (see Figure 2.3). Most of the territory has elevations no higher than thirty meters above sea level. The areas of low hills that are sometimes found in the basin likely represent areas where positive relief is being created due to the recent tectonic activity of the movement of the saline domes and due to lateral faulting (Enciso de la Vega, 1963).

Figure 2.3: Physiography, main cities and relief distribution in the central part of the Basin. Modified from (Garcia Payro, 2013).

The Basin comprises several biogeographical environments (INAFED, 2016):

- Rainforest Rainforest.
- Tropical savanna.
- Mangrove forest.

2.1.3 Hydrography

The fluvial system in the basin is dominated by the flows of the Usumacinta River, the largest river in Mexico, and the Grijalva River, which is the second largest by flow volume, with numerous tributaries that flow into the Gulf of Mexico. Only the Tonalá River, the Tancochapa, and Pedregal, which serves as the boundary between Tabasco and Veracruz, remain outside this system; the smaller rivers of the Chontalpa River are fed by excess rainwater accumulated in the swamps and the González River (INAFED, 2016). The Coatzacoalcos River has a considerable flow and a low slope; it is fed by the Coachapan and Uzpanapa rivers. Generally, the larger rivers and streams are the tributaries of the rivers mentioned above, and they are of little slope and flow slowly.

The drainage pattern is dendritic; most of its tributaries are permanent and navigable by small boats throughout the year. In the rainy season, their flow increases considerably and overflows, forming swamps and lagoons (Alcantara Rojas, 2010).

In addition to the numerous rivers and streams that cross the area in all directions, many lagoons are scattered throughout its territory. The most important lagoon systems in the area are El Carmen, Pajonal, La Machona, and Mecoacán (INAFED, 2016) (see Figure 2.4).

Figure 2.4: Watersheds, rivers, lakes and lagoons in the central part of the Basin. Modified from (Garcia Payro, 2013).

2.1.4 Population

The distribution of population centres plays a crucial role in the development of CCS projects, both with respect to the locations of large emission points and the routing of pipelines. Therefore, noting the population density and urban development locations is essential.

The Sureste Basin covers almost the whole Tabasco state, which has a population of 2.4 million inhabitants. 59% of the population lives in urban locations and 41% lives rural locations (INEGI, 2020). Table 2.1 shows the most populated cities within the basin, see Figure 2.3 for the location of the main cities in Tabasco.

City	Inhabitants
Villahermosa	683,607
Coatzacoalcos	310,698
Cardenas	243,229
Comalcalco	214,877
Huimanguillo	190,885
Las Choapas	81,080
Agua Dulce	44,104

Table 2.1: Most populated cities in the Sureste Basin, as of 2020 (INEGI, 2020). Coatzacoalcos, Las Choapas, and Agua Dulce are located in the Veracruz state.

2.1.5 CO_2 emission sources

Most of the major CO_2 sources within the Basin are Mexican Petroleum (PEMEX in Spanish) facilities, including petrochemical plants, processing plants, and one refinery, and their emission rate is between 1.5 and 2.1 megatonnes per year (Mtpa) (Lacy et al., 2013).

A significant number of these facilities and oil fields are located in the Cinco Presidentes Region, at the boundaries of the states of Veracruz, Tabasco, and Chiapas. In this region, there are numerous industrial plants with CO_2 emissions above 0.5 Mtpa, within 180 km of oil fields in the region.

Figure 2.5 depicts the CO_2 sources. The Morelos and Cosoleacaque petrochemical plants, and the Lazaro Cardenas refinery are closer to the Cinco Presidentes Region oil fields Rodador, Sitio Grande, Artesa, Carmito, Ogarrio, and Magallanes, within a distance range of approximately 40 – 60 km (Lacy et al., 2013).

Moreover, Lacy et al. (2013) stated that other significant emission sources, see Table 2.2).

Figure 2.5: Industrial CO_2 sources (> 0.5 Mtpa) located near Cinco Presidentes oil fields. Taken from Lacy et al. (2013).

Industry name	Substance	Industrial Sector	Emissions (Mt/year)
Nuevo Pemex Gas Processing Complex	Natural gas	Oil and petrochemical	2.1
Pemex Morelos Petrochemical complex	Natural Gas, including high purity CO_2 stream from ammonia plant.	Oil and petrochemical	1.8
Pemex Cosoleacaque Petrochemical Complex	Natural Gas, including high purity CO_2 stream from ammonia plant.	Oil and Petrochemical	1.7
NGCC Poza Rica	Natural Gas	Electricity generation	0.5

Table 2.2: Industrial CO_2 sources located in the Cinco Presidentes emitting above 0.5 Mtpa. Modified from Lacy et al. (2013).

2.2 Abandoned wells

When thinking about CCS, it is crucial to analyse the conditions under which CO_2 can be captured, transported, and stored. Places such as the Sureste Basin already have detailed records of subsurface conditions relevant to CCS. For example, more than 190 fields have been discovered so far and approximately 9,300 onshore wells have been drilled, including

exploratory wells. Currently, around 1000 wells are operational (Guerrero, 2018), which means that there is plenty of information to analyse the Basin from a CCS point of view.

Also, this implies that around 8,000 onshore wells are abandoned, closed, or inactive (Figure 2.6), and this could indicate a significant risk if CO_2 injection and storage are considered in the area. However, since not every field in the Basin will be suitable for performing CCS operations, the number of wells used will be markedly reduced.

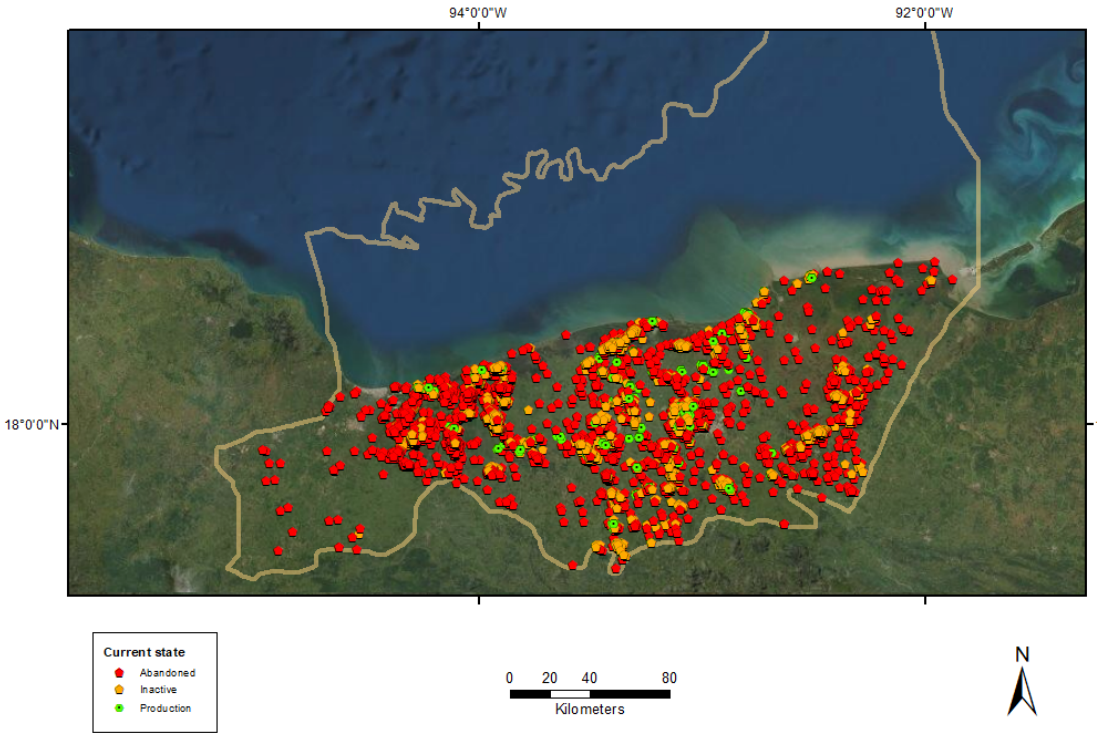

Figure 2.6: Current state of the wells in the terrestrial area of the Sureste Basin.

For instance, previous literature (Romero and Bashbush, 2017; Aulis Garcia, 2015; CNH, 2012) has evaluated fields such as Ogarrio and Blasillo as suitable for CO_2 storage. Ogarrio has 531 wells, 88 of them are abandoned, and 358 are inactive. Whereas Blasillo has 127 wells and 114 are inactive (Figure 2.7). An inactive well is one for which future use or reactivation is planned (SSJV MPEP, 2020). Therefore, for all wells in these fields and before the CO_2 injection starts, it is imperative to assess:

- If they are abandoned.
- How they were abandoned.
- How were they plugged.
- The quality of the plugs.
- What are their depths.
- Do they go down into the storage formation.

- If they are inactive, what are their future plans.
- If they are still producing hydrocarbons, they will need to be sealed.

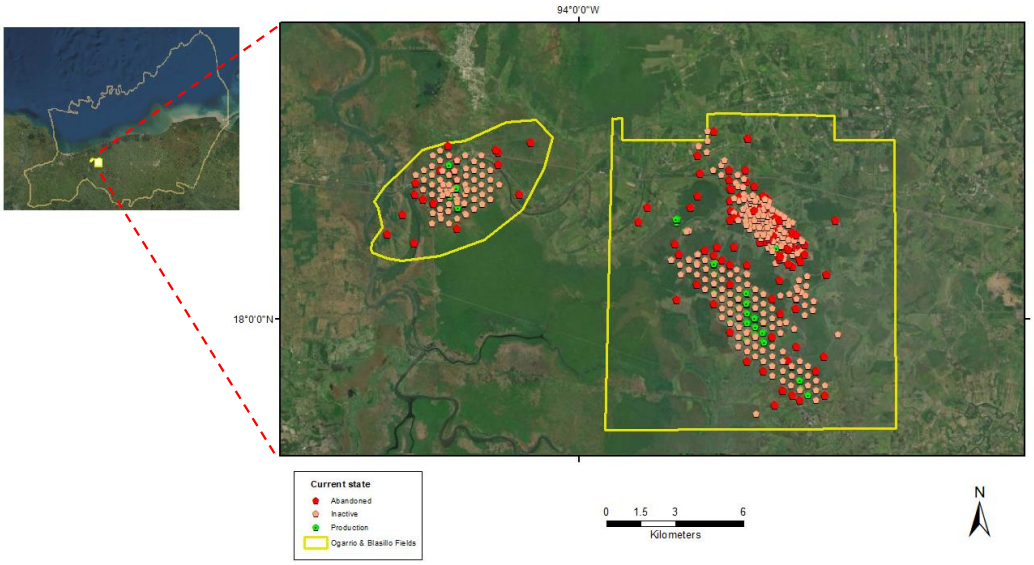

Figure 2.7: Wells within the Ogarrio and Blasillo fields and their current state.

In addition to this, it will be essential to have an updated database with the basic data of the wells, such as location, production and abandonment dates, materials and bore path. Furthermore, after CO_2 injection starts, it will be necessary to monitor them to ensure their integrity is not compromised.

2.3 Regional geology and stratigraphy

The basins of Southeast Mexico developed during the Mesozoic, and their geology is related to the opening of the Gulf of Mexico derived from the fragmentation and dispersal of Pangea.

The sedimentary column ranges from the Middle Jurassic to the Holocene (see Figure 2.8), and is up to 10,000 m thick (Cabrera and Lugo, 1984). Of the overall sedimentary thickness, approximately 6,300 m corresponds to the Cenozoic. Sedimentary facies include shallow marine clastics, evaporites, organic-rich carbonates, oolitic carbonate banks, dolomite breccias, shales, sandstones, and limestones (Talwani, 2011). The environments in which the sediments were deposited vary from neritic to bathyal.

The following subsections describe the key sedimentary formations in the Sureste Basin by age.

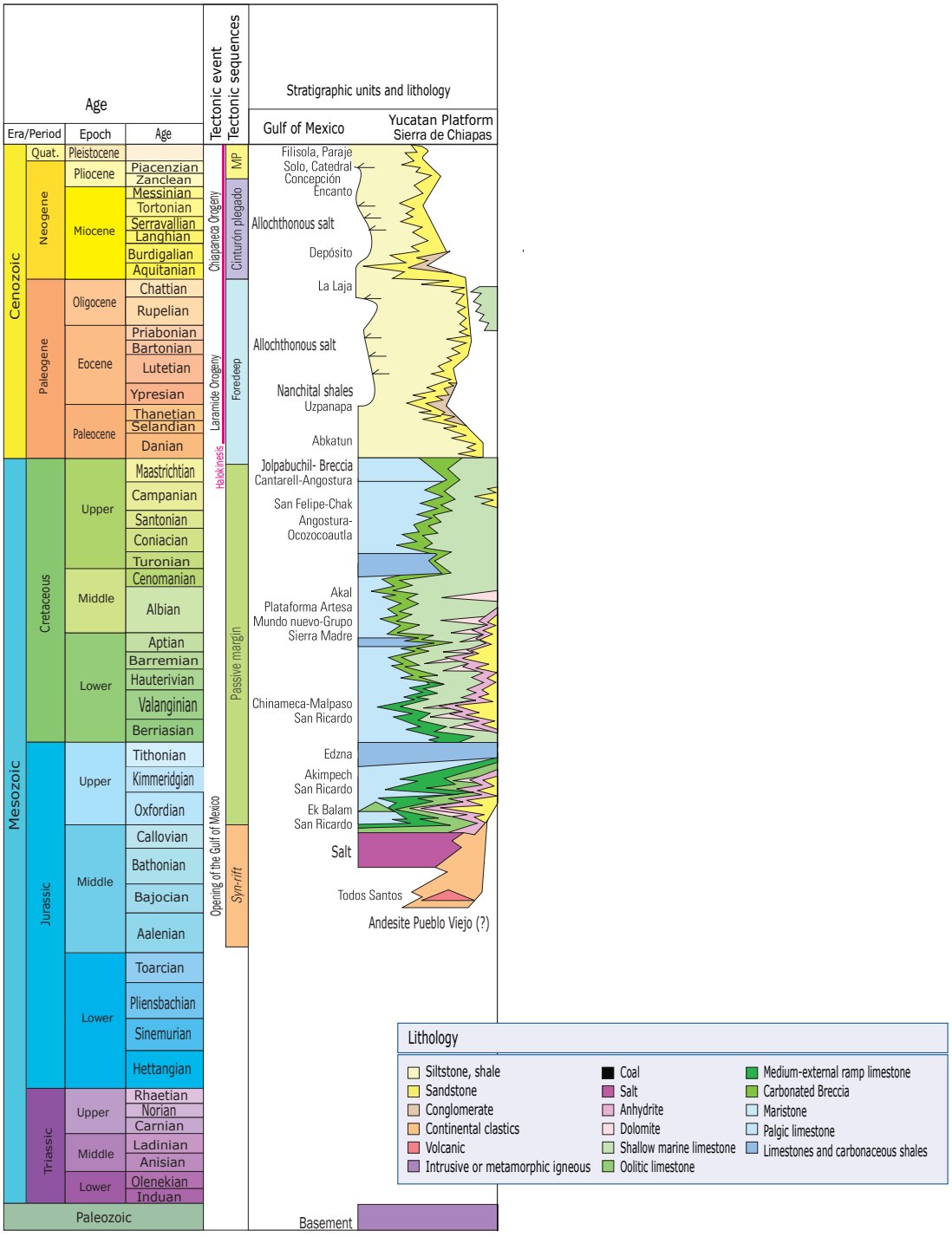

Figure 2.8: Stratigraphic column of the Sureste Basin. Modified from Escalera and Hernández (2010).

2.3.1 Paleozoic

The basement consists of granitoids and Palaeozoic schists as part of a thinned continental crust that formed horsts and grabens associated with extension during the opening of the Gulf of Mexico (Escalera and Hernández, 2010).

2.3.2 Mesozoic

The sedimentation in the Basin started with the deposition of continental red beds corresponding to the *Todos Santos* Formation, derived from the erosion of the basement and volcanic rocks deposited in the grabens during the Late Triassic and Early Jurassic (Escalera and Hernández, 2010). This rock unit covers most of the basement, along with marine evaporites, carbonates, and platform marine facies (Jimenez et al., 2011).

2.3.2.1 Jurassic

Clay and sandy sediments dominate the Lower Jurassic. In the Middle Jurassic during the Callovian, there was an invasion by marine waters from the Pacific that covered an extensive area with poor circulation, shallow waters, and high evaporation. This accumulated thick salt deposits in the central area of the Basin (Mendez, 2007).

On top of the salt, at the end of the Callovian - early Oxfordian, carbonated clayey sediments, clayey limestones, shales of high organic content, and oolitic grainstones were deposited. They transitioned to coastal evaporitic and continental siliciclastic sediments of the *Ek-Balam* Group and the *San Ricardo* Formation (Escalera and Hernández, 2010).

The Upper Jurassic reaches a thickness of up to 1,100 m. The Oxfordian oolitic grainstones developed around diapiric uplifts of the underlying salt. These conditions are maintained in the Kimmeridgian with the deposition of the *Akimpech* Formation. The salt appears as diapirs in rocks from the Jurassic to the Upper Miocene (Mendez, 2007).

During the Tithonian age, the deposits of clay-carbonaceous mudstones and layers of black calcareous shales predominated, and they constitute the primary source rock of the Basin. The Mesozoic source rocks, especially the Tithonian, represent a major part of the oil that has migrated upwards, probably by fault planes, into the Miocene reservoir formations (Mendez, 2007).

The rocks of the Callovian-Kimmeridgian region are typical of shallow water platform deposits with high energy and possess the petrophysical conditions necessary to produce a storage rock (Santiago et al., 1984). In this period, a carbonate sedimentation environment was generated, lasting until the end of the Cretaceous Mendez (2007).

2.3.2.2 Cretaceous

The Lower and Middle Cretaceous present carbonate sediments, dolomites, and a reduction of clay material. In deeper areas, dolomitic limestones were deposited with few sealed

fractures of calcite with light oil impregnation. They cover the upper part of the Upper Jurassic (Tithonian) and remain underlying the different sedimentary facies identified in the Middle Cretaceous. (Mendez, 2007).

In the Lower Cretaceous, anhydrites and dolomites of the *Cobán* Formation are deposited over the continental clastics of *Todos Santos* Formation. In the Albian age, limestone and dolomite are deposited with intercalations of shales and bentonites from the *Akal* and *Sierra Madre* Formations.

In the Middle and Upper Cretaceous, there is a regional unconformity that omits sediments of both ages; these rocks are mainly composed of dolomite (Lopez-Ramos, 1979).

The Upper Cretaceous underlies the Paleocene rocks in a discordant way. The terrigenous material culminates the deposit of a marl sequence with intercalated calcareous breccias of the *Méndez* Formation of the Campanian - Maastrichtian (Lopez-Ramos, 1979).

Due to the physical and faunal characteristics of their sediments, the *Agua Nueva* and *San Felipe* formations have been determined in this period. The *Agua Nueva* consists of calcarenites, biogenic limestones with microfossils. The *San Felipe* comprises alternating layers of bentonitic limestone and microfossiliferous clayey limestone. In addition, the *Jolpabuchil* Formation has been identified in the deep northern parts, and the *Chac* Formation with carbonate breccias, and platform limestones of the *Angostura* Formation to the south and east (Lopez-Ramos, 1979).

A thick pack of carbonate breccias with shallow limestone clasts in the Late Cretaceous was deposited as an apron along the slope. These rocks constitute the main deposits in the Cantarell field and have been called the *Cantarell* Formation (Escalera and Hernández, 2010).

During the Cenozoic, as the sinking of the seabed accelerated and as environmental conditions changed, a thick section of siliciclastic sediments several thousand meters thick was deposited over the salt, evaporites, and carbonates of the middle Cretaceous. The pressure exerted by the column of sediments deposited on the salt, combined with regional tectonic forces, developed the diapirism of the salt and formed domes and other salt structures. Currently, the domes of the western part of the Basin are closer to the surface than those that are in the east and southeast of Tabasco and Chiapas (Benavides Garcia, 1983). The slow subsidence that prevailed during the Cretaceous and even into the Oligocene allowed the source rocks of the Tithonian to remain dormant until the fast subsidence and sedimentation of the Miocene and Plio-Pleistocene pushed them to temperatures suitable for maturing (80-100°C). Hence, the generation of oils occurred mainly during the Miocene to Plio-Pleistocene (Gonzalez and Holguin, 1992).

2.3.3 Cenozoic

The Paleocene, with an average thickness of 250 m, is formed by shale and sand intercalations, typically underlying the Eocene sediments.

Towards the internal parts of the platform, carbonate breccias of the lower part of the *Soyaló* Formation from the Paleocene were also deposited on the limestones of the *Angostura* Formation. Deep-water clay limestones, and shales covered the breccias from the *Abkatún* Formation in the marine part (Escalera and Hernández, 2010).

The Eocene has an approximate thickness of 1,800 m, and its petrology consists of calcareous shales with oil stains in the stratification planes. The Middle and Lower Eocene consists of shales with thin intercalations of limestone and dolomite. The Oligocene contains bentonitic shale and thin clay sandstones. From the Upper Oligocene, hydrocarbons are generated by the maturation of organic matter contained in the Mesozoic carbonate levels up to the present time. The formation of large normal and listric faults favours the flow of hydrocarbons with an important vertical component towards the shallower levels of the Cenozoic (Mendez, 2007).

The Miocene reaches thicknesses from 40 m up to 500 m; it consists of a succession of shales and sandstones. During the Miocene, the Chiapaneca deformation caused uplift and erosion; consequently, the terrigenous influx increased, and the progradation of the southern platform system led to the deposition of sandstones and bentonite shales (Escalera and Hernández, 2010).

The Pliocene, with a maximum thickness of 400 m, consists of grey shales with abundant calcareous concretions. At the beginning of this epoch, a transgressive event occurred and deposited clay rocks that act as regional sealing units (Santiago et al., 1984).

A lithostratigraphic subdivision has been used for the Eocene-Pliocene. It includes the formations: *Uzpanapa* Conglomerate, Shales and Conglomerates: *Nanchital*, *La Laja*, *Depósito*, *Encanto*, *Lower Concepcion* and *Upper Concepcion*, *Filisola*, *Paraje Solo*,*Agueguexquite* and *Cedral*, whose age ranges have been modified as these formations have been further investigated (Escalera and Hernández, 2010).

In terms of CO_2 storage, Jimenez et al. (2011) determined that for various central fields in the basin, the reservoir rocks are the Miocene interbedded rocks: *Encanto*, *Upper* and *Lower Concepcion*. The *Encanto* Formation consists of interbedded sand and shale. The *Lower Concepcion* Formation overlies the *Encanto* Formation and is defined by interbedded thick shale and thin sand bodies. The *Upper Concepcion* is above *Lower Concepcion*, and it consists of shales with a high content of micas, with sandstones occasionally present.

Furthermore, these well-bedded sequences of shale and sandstone can be considered a primary seal, as the shale acts as an impermeable barrier preventing the CO_2 from migrating from the sandstone layers. The caps rocks correspond to the Pliocene rocks *Paraje Solo*, a thick layer of grey shales. It is often overlaid by *Filisola* and *Cedral*, which are also composed of shale and could be considered secondary seals (Jimenez et al., 2011).

It should be noted that a CO_2 storage basin-wide prospective analysis needs to be performed to determine where it can be stored and what formations, depending on the area, could act as reservoir rocks and caprocks.

2.4 Structural geology

2.4.1 Subbasins

The Sureste Basin has four productive subbasins: Saline del Istmo, Comalcalco, Macuspana, and Pilar de Reforma Akal (Figure 2.9).

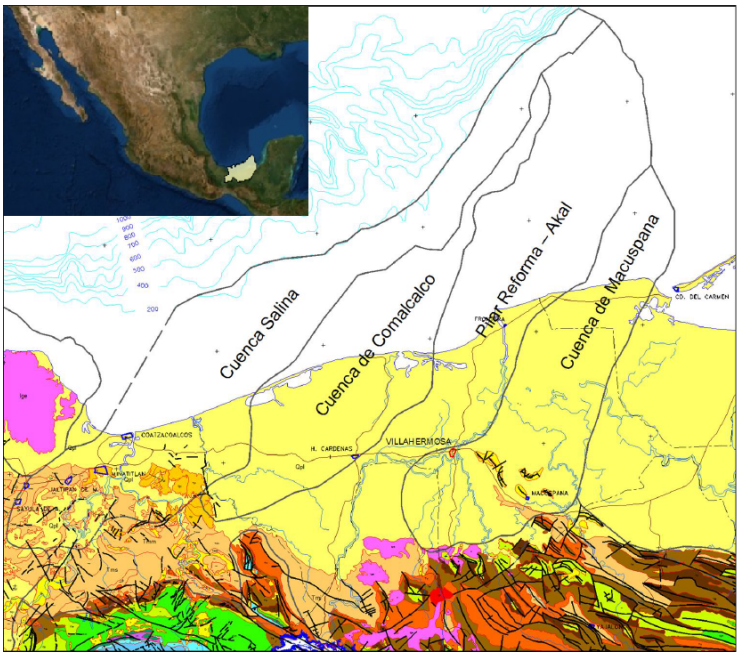

Sedimentary Rocks

Era	Period	Epoch	Key
Cenozoic	Quaternary	Recent	Q
		Pleistocene	Qpl
	Tertiary	Pliocene	Tpl
		Upper Miocene	Tms
		Middle Miocene	Tmm
		Lower Miocene	Tmi
		Oligocene	To
		Eocene	Te
		Plaeocene	Tp
Mesozoic	Cretaceous	Upper	Ks
		Middle	Km
		Lower	Kl
	Jurassic	Upper	Js
		Middle	Tr -Jm

Igneous and Metamorphic Rocks

Metamorphic Basement	Met
Intrusive Rocks	Igi
Extrusive Rocks	Ige

Figure 2.9: Location of the basins within the Sureste basin. Modified from CNH (2014).

2.4.1.1 Saline Basin of the Istmo and Comalcalco

The Saline Basin of the Istmo extends from the front of the Sierra de Chiapas in the south to the Gulf of Mexico in the north, adjoining to the west to the Veracruz Basin and the east by the Pilar Reforma-Akal. This Basin includes the Comalcalco Basin, as both of them are associated with a heavy sediment load and salt deformation (Aulis Garcia, 2015).

Structurally, it is characterized by salt diapirs, walls, and domes that lead to the formation of subbasins such as Comalcalco (Mendez, 2007). In the Saline Basin of the Istmo, the oil production comes from structural traps associated with salt domes in Cenozoic sandstones, mainly of the Encanto Formation of the Lower Miocene. The main fields in the Saline Basin are Tonala-El Burro, El plan, Cinco Presidentes, Ogarrio and Magallanes. The largest salt dome is the Magallanes, about 18 km long by 7 km wide (Acevedo and Dautt, 1980).

2.4.1.2 Pilar Reforma - Akal

The Pilar Reforma-Akal is limited to the west by the system of faults that constitute the edge of the Comalcalco Basin and to the east by the fault system at the edge of the

Macuspana Basin. This subbasin borders the south with the Cinturon Plegado of the Sierra de Chiapas, with a series of anticlinal structures oriented from northwest to southeast (CNH, 2014).

In this area, three overlapping tectonic events can be distinguished that have formed the regional structural framework: a) Initially, an extensional event in the Middle Jurassic, with a series of normal faults as a result of distensive stresses with the consequent formation of pillars in the basement, followed by b) a compressive event characterized by a series of NW-SE oriented folds and ridges. The last event c) identified during the Neogene corresponds to listric faults falling to the NW; they are associated with intrusions of clay and salt (CNH, 2014).

2.4.1.3 Macuspana Basin

The Macuspana Basin is bordered to the E-SE by a system of normal faults that separates it from the Yucatan Platform; to the NW-W by the fault system that delimits the Reforma-Akal Pillar and to the south by the Folded Belt of the Sierra de Chiapas (CNH, 2014).

Miocene-Early Pliocene listric faults characterize this Basin with NE-SW orientation and NW inclination with rollover anticlines associated with the displacement of Oligocene clays. In the marine portion, these faults break and move the Mesozoic rocks to the NW in a raft system, putting the Jurassic salt in contact with Oligocene sediments. Towards its western edge, there are listric faults from the Late Pliocene-Pleistocene with NE-SW orientation and inclination towards the SE and elongated and tight anticlines of the Plio-Pleistocene associated with the inversion of the faults during the Miocene (Escalera and Hernández, 2010; Rodriguez Moreno, 2020).

According to Acevedo and Dautt (1980), the Macuspana Basin hydrocarbon production comes from the Jurassic and Cretaceous dolomitic limestones associated with anticlines and diapiric salt domes.

2.4.2 General structural geology

The Sureste Basin was developed on a passive margin and is related to the plate tectonic interaction in the Pacific region of Mexico and the formation of the nearby overthrust belts (Jimenez et al., 2011).

The main Mesozoic and Cenozoic tectonic elements of the Basin that control the deposition and deformation of the sedimentary sequences and the generation and accumulation of hydrocarbons are the Saline Basin of the Istmo, the Reforma-Akal tectonic pillar, the Macuspana Basin, and the Chiapas Platform. The Macuspana and Saline basins are bounded to the south by the Sierra de Chiapas front. The direction of the faults and structural axes in the Sierra de Chiapas are from NW to SE, and in the Cenozoic basins, the faults have an NW-SW direction, and the northern limit is the Gulf of Mexico (Mendez, 2007).

In the Cenozoic, a distension process led to the reactivation of the Palizada, Frontera, Macuspana, and Comalcalco faults, which caused the subbasins to evolve as horsts or grabens that received the contribution of sediments from the entire Cenozoic. The diastrophism of the Miocene, together with the diapiric effects of the salt, generated the reverse faults that place the rocks of this age (or older) below those of the Middle Cretaceous and the Upper Jurassic (Santiago et al., 1984).

The Reforma - Akal uplift separates the Comalcalco and Macuspana subbasins. There are folded and reverse faulted sedimentary sequences from the Jurassic through Oligocene in the three subbasins. The Macuspana Basin contains Miocene terrigenous sequences altered by steep and dipping normal faults. The Comalcalco Basin lacks these terrigenous sediments, implying synchronous erosion and sedimentation processes. In this basin, the sediments of the Pliocene and Pleistocene can reach around five kilometres in thickness (Jimenez et al., 2011).

In addition to this, Pindell and Kennan (2001) identified the formation of the passive margin of the Basin as the "*circum-Gulf of Mexico*". It consists of three phases: a) Extension faulting (rifting) during the Triassic to Middle Jurassic, creating the basins and establishing their location and orientation, b) extension of the Upper Jurassic (expansion of the ocean floor of the Gulf) favouring the deposit of Tithonian hydrocarbon generating rocks, and c) passive thermal subsidence of the Lower Cretaceous, causing the growth of carbonate platforms, which would be the main reservoir rocks.

2.5 CCS in the Sureste Basin

A major motivation for developing CCS in the Sureste Basin is the decline in gas and oil extraction. The allotments granted to PEMEX for extraction activities comprise mainly mature fields, which have been produced for a long time and are beginning to decline.

However, not every mature field can be selected for CO_2 storage; there is a selection criterion (Table 2.3) that must be considered before starting CCS operations (Raza et al., 2016; Miocic et al., 2016; Chadwick et al., 2008).

Furthermore, it is recommended to implement new technology and improved recovery methods to restore the remaining reserves of oil fields. An alternative is Enhanced Oil Recovery (EOR), as it can store CO_2 and increase crude oil production (Liang et al., 2009). As in the selection of the storage site CO_2, it is also necessary to consider the screening criteria to find the most suitable field to perform CO_2-EOR (Kovscek, 2002; Yáñez Angarita et al., 2022; Gozalpour et al., 2005), see Table 2.4.

Many Mexican reservoirs contain light and some heavy hydrocarbons that fall within the applicability range for injection CO_2, under miscible conditions, as an EOR technique (Sanchez, 2018). Due to this, and since no CCS project has yet been carried out in the country, the Mexican National Hydrocarbons Commission (CNH in Spanish) in 2012

Reservoir parameters	Optimum values
Static storage capacity	Estimated storage capacity much larger than the total amount of CO_2 produced from CO_2 emission sources
Depth	>800 m <2500 m
Thickness	>50 m
Porosity	>20%
Permeability	> 100 mD
Temperature	Minimum temperature of 35°C
Structure	Minimal faulting, trapping structures
Rock type	Sandstones and carbonates
Distance between CO_2 emissions source and target reservoir	<300 km
Lateral continuity of caprock	Uniform, small or no faults
Caprock thickness	> 100 m

Table 2.3: Selection criteria for geological CO_2 storage. Adapted from Raza et al. (2016); Miocic et al. (2016); Chadwick et al. (2008).

Reservoir parameters	Optimum values
Oil gravity	>22 and <48 ° API
Oil saturation and porosity $S_o\phi$	≥ 0.05
Initial oil saturation	>= 26.5%
Oil viscosity	>5 mPa
Remaining oil saturation	60%
Temperature	70°C
Permeability	300 mD
Porosity	20%
	Previous oil production and surface facilities

Table 2.4: Screening criteria for CO_2-EOR, adapted from Kovscek (2002); Yáñez Angarita et al. (2022); Gozalpour et al. (2005).

considered the mature fields Ogarrio, Cunduacán, and Blasillo in the Sureste Basin to implement potential CCS pilot projects.

In addition to the criteria in Table 2.4, these fields have:

- Literature consensus as suitable for CO_2 injection.
- Recovery factor greater than zero.
- Shallowest reservoirs with the lowest possible initial water saturation.
- Reservoirs with the highest remaining volume of oil.

The Ogarrio field

The Ogarrio field belongs to the Cinco Presidentes Production Asset located in Tabasco. This field contains light black oil. It is an onshore field with an original oil volume of 732

million barrels and a cumulative oil production of 98 million barrels by 2012, resulting in an oil recovery factor of 13%. It has an average porosity of 21%, a permeability of 570 miliDarcys (mD), and a temperature of 87°C. The fluid in this reservoir is a light oil with a density of 38° API and a viscosity of 7 cP under the conditions of the initial pressure and temperature of the reservoir. As a result of the characteristics of the type of fluid in this reservoir, the hydrocarbon gas injection process is also very viable. (CNH, 2012).

The Cunduacán field

The Cunduacán field belongs to the Samaria-Luna Production Asset and is located in Tabasco. It is an onshore field with an original oil volume of 1,814 million barrels and a cumulative oil production of 569 million barrels by 2012, resulting in an oil recovery factor of 31%. It is a limestone and dolomite carbonate deposit, has a thickness of 270 m, a 6% porosity, a temperature of 126°C, and its permeability ranges between 95 and 175 mD. The fluid in this reservoir is a super-light oil with a density of 38° API and a viscosity of 0.26 cP under the conditions of the initial pressure and temperature of the reservoir (CNH, 2012).

The Blasillo field

The Blasillo field belongs to the Cinco Presidentes Production Asset. It is also an oil field onshore with an original oil volume of 299 million barrels and a cumulative oil production of 63 million barrels by 2012, resulting in an oil recovery factor of 21%. Its lithology is composed of sandstone and shales; it has a thickness of 50 m, the porosity of the rocks is 23%, its permeability is 215 mD, and its temperature is 92°C. The fluid in this reservoir is a light oil with a density of 35° API and a viscosity of 8 cP under the conditions of initial pressure and reservoir temperature (CNH, 2012).

Based on Sanchez (2018), other fields that can be considered for the implementation of techniques that allow secondary and improved recovery due to their types of oil and gas, the conditions of the reservoirs and the decrease in their production are:

- San Ramon
- Rodador
- Cinco Presidentes
- Magallanes
- Nelash
- Rabasa

Figure 2.10 depicts the location of these and other mature fields in the central area of the Sureste Basin.

In addition to this, in 2017, the development of a pilot project for CO_2 storage started within the Sureste Basin, injecting the CO_2 produced from the Cosoleacaque Petrochemical Center into the Brillante field located in Veracruz state (Arteaga et al., 2015).

The Brillante field is a young field that had a rapid drop in pressure due to production, and its geological and petrophysical characteristics make it a suitable place for CO_2

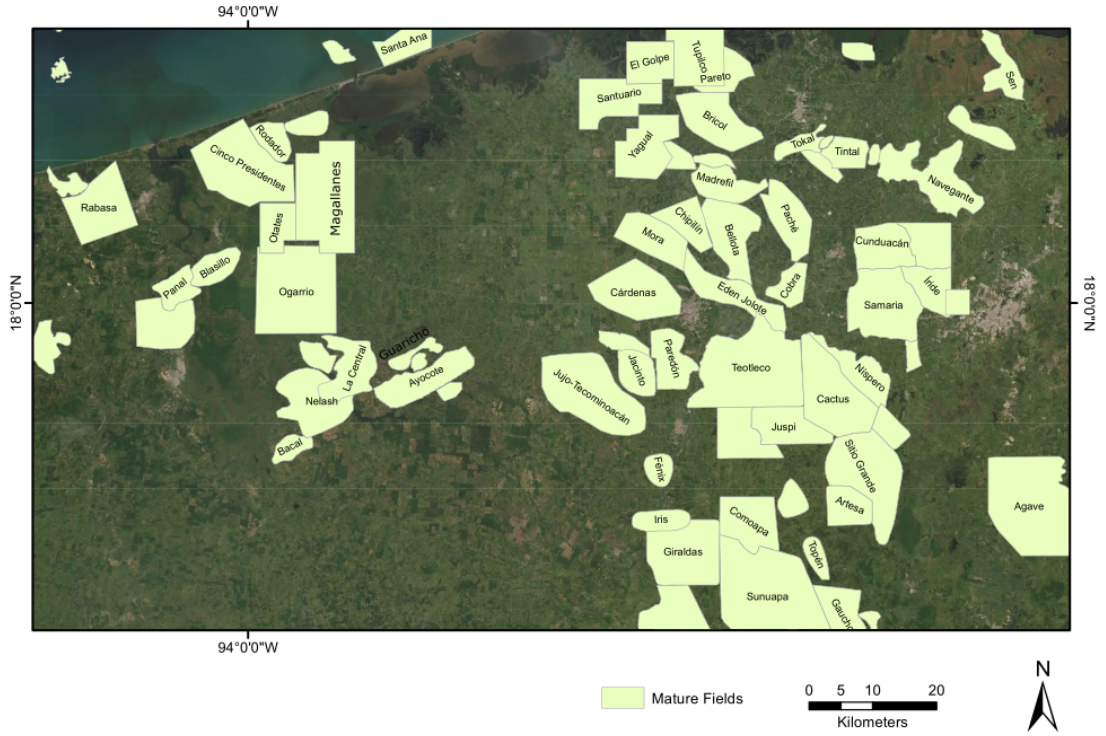

Figure 2.10: Location of some of the matures fields within the Basin.

injection. It is composed mainly of sandstone from the Miocene known as the Encanto Formation, at a depth of 2100 meters (Arteaga et al., 2015). The proximity of the Cosoleacaque Petrochemical Complex to the Brilliante field and the availability of the CO_2 it produces in its ammonia plant makes this a good candidate site for CO_2 capture.

2.6 Theoretical Capacity

The theoretical capacity outlines the maximum physical limit of what a reservoir can store; it considers that the CO_2 can occupy every pore space in the reservoir. It does not take into account physical, geographical, and economic barriers. (Bachu et al., 2007). In recent years standardised methodologies to estimate the storage capacity have been created. There are two main methods: a) static; its parameters are independent of time, and b) dynamic; its parameters vary with time. The selection of any of these methods depends on the data available (Jin et al., 2010).

The dynamic method has different approaches, such as semi-closed, pressure build-up at wells, decline curve analysis and reservoir simulation. These approaches simulate CO_2 flow, estimate the maximum allowable pressure build-up in relation to the time, estimate the injection pressure, and create complex geological models of reservoirs (Pickup, 2013). However, they required a specific and significant amount of data and specialised software usually unavailable to the public or interested parties. Moreover, since it has several

parameters, the uncertainties of the capacity estimates are more significant than the ones in the static models.

For this reason, the static methods are more widely used, as they require fewer parameters and the data can be obtained from open access sources. Also, it is possible to obtain parameter values with the current geological information and public well data through review and computations Jimenez et al. (2011). There are two approaches to this method: a) the volumetric, which calculates the formation pore volume, and b) the compressibility method, which calculates CO_2 volume from the increment of compressibility and pressure.

Due to data availability, the volumetric method is used in this thesis to compute the mass of CO_2 that can be stored in a reservoir. This method was also used to calculate the theoretical storage potential of the Sureste Basin by Jimenez et al. (2011) and the Atlas of Geological Storage of CO_2 in Mexico 2012. According to them, the Basin can potentially store 24 gigatonnes (Gt) due to its geological characteristics.

Jimenez et al. (2011) screened and selected 17 sectors with CO_2 storage potential to estimate the potential CO_2 capacity of the Basin. Eleven of them are onshore, and six are offshore. Several stratigraphic and anticline trap structures were identified. One of the sectors has a Miocene interbedded sequence of sandstone and shale, overlaid by shales of the Pliocene; this interbedded sequence is approximately 240 m thick, located 1550 m deep. It has a low clay content, a porosity of 30%, a permeability of 60 mD, a water saturation lesser than 18% and an expected CO_2 density of 681 kg/m^3. Hence, it has a theoretical storage capacity of around 1.84 Gt of CO_2. This sector can be taken as an average CO_2 storage site within the Basin, and according to Jimenez et al. (2011), it is reasonable to expect to find more sites like this.

These storage sites need to be close or at a reasonable distance from the CO_2 emission sources. For instance, a suitable option for CO_2 storage in the Basin is the Cinco Presidentes Region due to its location close to emission sources and injection sites (González-Díaz et al., 2017).

Additionally, these calculations could be improved with a more thorough and detailed analysis, focused on the sites previously explored by PEMEX, for example, the areas with mature fields, several wells, and borehole data. In this way, some uncertainties could be reduced.

CHAPTER 3

ESTIMATION OF CO_2 STORAGE VOLUMES AT THE OGARRIO FIELD

3.1 Introduction

The purpose of this chapter is to use a combination of different geophysical tools to estimate the potential CO_2 storage volume for a field in the Sureste Basin. This storage capacity estimate is a static calculation based on the available pore space within the target formations. This type of calculation does not involve fluid flow simulations and I do not model injection into target formations.

For a static estimate of capacity, the mass of CO_2 that could be stored can be computed from the available pore volume within the storage formation:

$$MCO_2 = \rho(CO_2) \times A \times T_f \times \phi \times (1 - S_w) \times SER \quad , \tag{3.1}$$

where $\rho(CO_2)$ is the density of CO_2 at reservoir temperature and pressure, A is the lateral extent or area of the target reservoir, T_f is the total thickness of the target reservoir, ϕ is the average porosity, S_w is the water saturation, and SER is the Storage Efficiency Factor, which describes the portion of the available pore space that can be saturated by CO_2 (Bentham et al., 2014).

Structural trapping is the foremost mechanism for CO_2 storage. When injected into a formation, the low density of CO_2 relative to brine means that the CO_2 will be pushed upwards by buoyancy forces (Lie et al., 2014). Hence, the mobile CO_2 will migrate until it reaches the upper bound of the sealing caprock, where it will concentrate, filling the trap. Once this occurs, the CO_2 will move along a spill path connected to a spill point, which the shallowest point in the structural trap. Once the CO_2 reaches the spill point, there will be no further retention, leading to migration of CO_2 beyond the target storage facility

(Møll Nilsen et al., 2014). For this reason, a structural trap analysis is needed to assess the geometry of the storage formation and to determine the area contained within the target trapping structures. This analysis will be performed using seismic reflection data later in this chapter.

The thickness of the storage formations can be estimated from well log analysis. As well as the bulk thickness of the reservoir formation, we must consider the net-to-gross ratio (NTG), which describes the proportion of permeable rock (e.g., sandstone) within the overall reservoir unit, which may also contain lower-permeability layers such as mudstones (Inichinbia et al., 2014). The usable thickness of the formation, T_f, can be estimated from the total reservoir thickness multiplied by the NTG. The average formation porosity can also be calculated from the analysis of well logs.

The formation area, thickness, NTG and porosity define the available pore volume of the reservoir. This data can be used not only to obtain the potential amount of CO_2 that can be injected, but it can also be compared to the hydrocarbon production volume of the field in order to compare potential CO_2 storage volumes from the volumes of fluid already removed from the formations in question.

Furthermore, uncertainties in storage capacity estimates will be assessed, along with the risk of CO_2 leakage from abandoned wells in the area.

We chose the Ogarrio field for this analysis as another study (Romero and Bashbush, 2017) has already identified this site as a potential CCS site, given its favourable geological characteristics. The geophysical data used in this chapter were sourced from the National Hydrocarbons Commission (CNH in Spanish).

3.2 Objectives

The objectives of this chapter are:

- To estimate the CO_2 storage potential of the Ogarrio Field in the Sureste Basin using a combination of geophysical datasets and techniques.
- To use seismic reflection data to map the potential structural traps within the field.
- To use well logs to assess the target formations thicknesses and porosities, in order to compute the pore volumes available for CO_2 storage.
- To compare estimated CO_2 storage capacities with the volume of hydrocarbons produced from the field.
- To analyse the uncertainties in the final storage capacity estimations.

3.3 Ogarrio field

The Ogarrio oil field was discovered in 1957; it is located within the Saline Basin of the Tehuantepec Istmo, in the west of the Tabasco State CNH (2014). The closest cities are

Las Choapas and Agua Dulce in the state of Veracruz, approximate 25 and 30 km away, respectively. The area is located between the 18°00′ and 8°09′N and 93°50′ and 93°58′W, as shown in Figure 3.1. The field is part of the Cinco Presidentes Region and the geological province of the Sureste Basin (Perez Rincón, 1959).

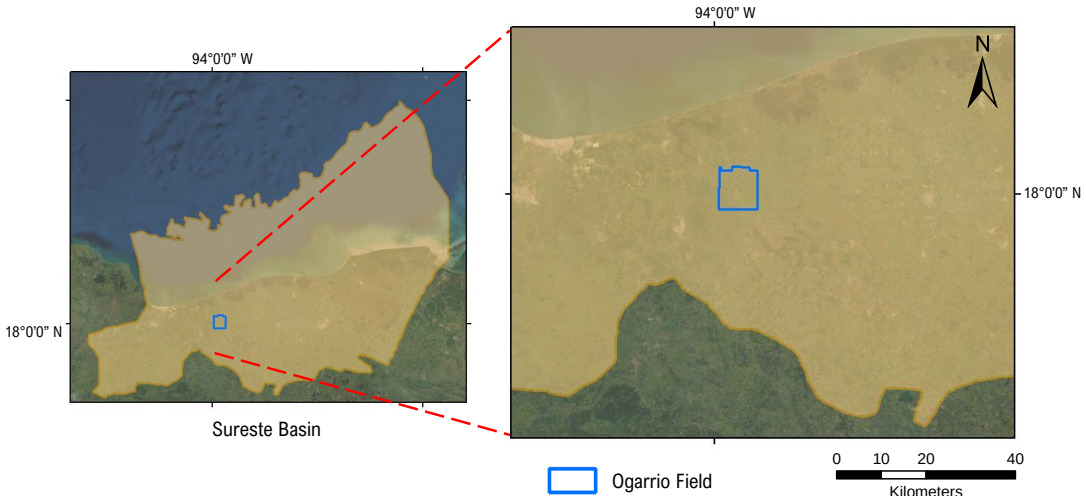

Figure 3.1: Location of the Ogarrio field. It is approximately 13 km by 12 km and it is in the south-central part of the Sureste Basin.

The field area is about 156 km^2, the field began production in October 1960. As of January 1, 2015, 218 million barrels (MMB) of oil and 405 million standard cubic feet per day (MMMcf) of gas have been produced (CNH, 2015). Romero and Bashbush (2017) gives a permeability that ranges from 10 to 200 millidarcys (mD), the average reservoir depths range from 1600 to 3200 m, and an average porosity of 22%. There have been 531 wells drilled in the field, and 80 were still active in 2020 (CNH, 2022).

As mentioned, the CNH and the Ministry of Energy (SENER) provided the information on the Sureste Basin needed to analyse the field. This information includes documentation from more than 1000 wells and 117 2D seismic lines from Ogarrio and surrounding fields. However, most wells have limited, or no data and some 2D seismic lines have a low resolution; for these reasons, only 60 wells and 73 2D seismic lines were considered in the assessments. Figure 3.2 shows the data used in the analyses carried out in the following sections of this chapter.

3.3.1 Ogarrio geology and stratigraphy

In this area, the sedimentary column extends from the Triassic-Jurassic to the Recent (Figure 3.3). The sandstones of the area are from the Neogene, extending from the Lower Miocene in the Deposito Formation to the Upper Pliocene in the Filisola formation (CNH, 2015). I describe the stratigraphy of the Ogarrio Field in chronological order.

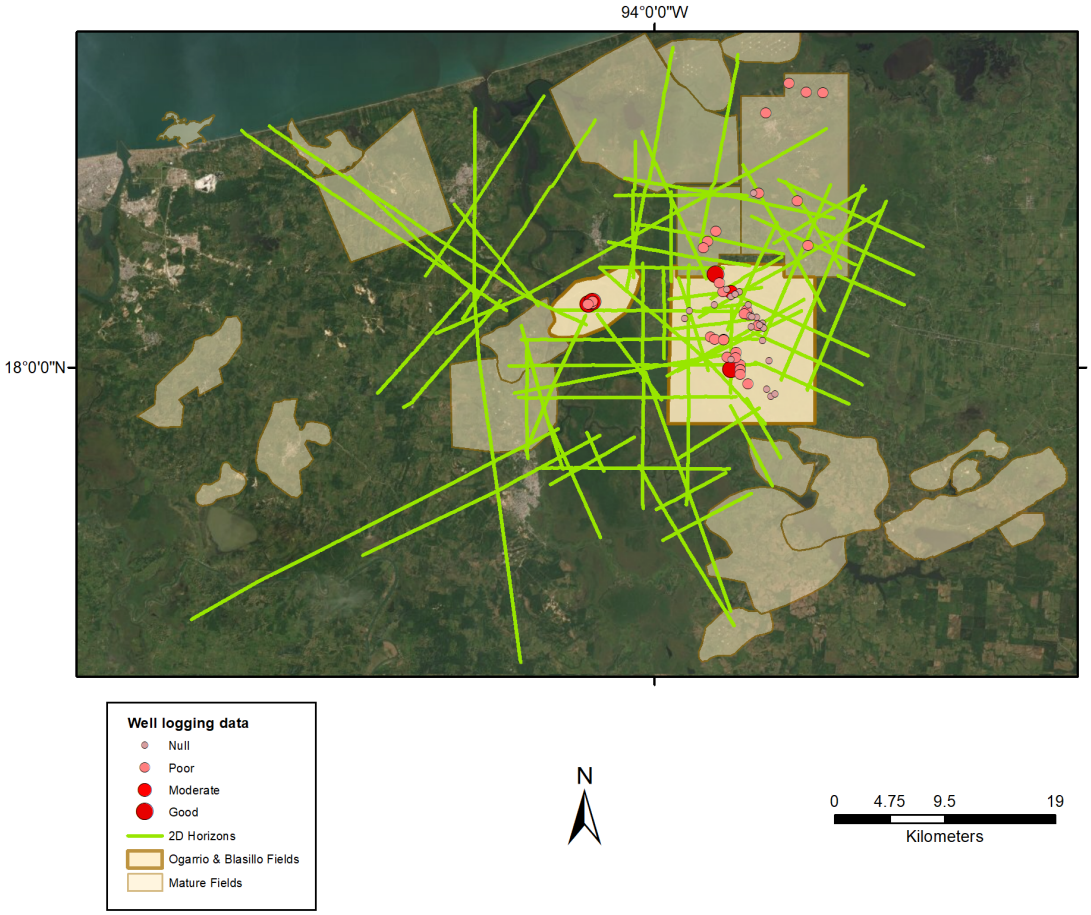

Figure 3.2: Ogarrio and surrounding mature fields, 2D seismic lines, and wells classified according to their logging data quality used to assess and estimate the potential CO_2 storage capacity in the Ogarrio field.

Salt

The salt formations within the Sureste Basin date from the Permian and Triassic. They are formed of halite and anhydrite, with a banded texture, with alternated layers of thicknesses that vary from 2 to 20 cm. They correspond to a marine environment that existed in a closed sea, subject to intense evaporation during the Permian-Triassic, which led to the deposition of large amounts of evaporites (Sanchez Romero, 2019).

These deposits later formed salt domes, diapirs, and other forms of salt-based deformation features. From a hydrocarbon perspective, the resulting structural conditions in the Saline Basin are of great importance since all accumulations of hydrocarbons discovered within it are closely related to these structures. The salt uplift arched the sedimentary strata positively, causing the oil to migrate towards the raised structures following the porous and permeable bodies such as sands sealed by non-permeable bodies (Benavides Garcia, 1983).

At the Ogarrio field, the salt has pushed upwards through later Mesozoic (Jurassic

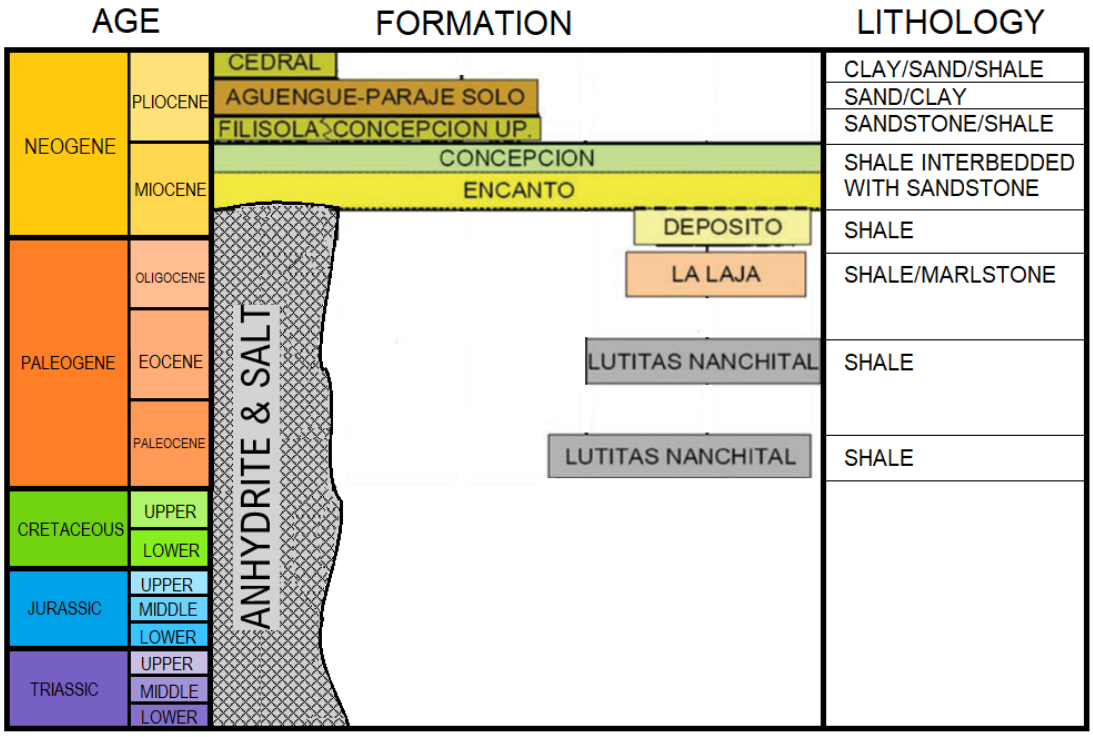

Figure 3.3: Stratigraphy of the study area up to the Jurassic period. Modified from Romero and Bashbush (2017).

and Cretaceous) and Paleogene sediments, such that the Miocene Encanto Formation sits directly on the salt (Sanchez Romero, 2019).

Encanto

This formation sits on the top of the saline intrusion. For this reason, it has suffered significant effects of the ascent of the salt, meaning that its thickness is highly variable from well to well. The maximum thickness that has been found in this field is about 800 meters and the minimum is less than 100 meters. Lithologically, the composition of this formation at Ogarrio consists of various shales, which are plastic at the top and hard and chalky at the base. Interspersed between the shales are fine to very fine-grained sandy bodies of light grey, with angular clasts. This formation has sufficient porosity and permeability to be used as a storage rock, and is the main storage rock of Ogarrio and the surrounding fields (Romero and Bashbush, 2017).

Lower Concepcion

The Lower Concepcion sits above the Encanto Formation and is of late Miocene age. The thickness ranges from 200 to 500 meters. It consists of slightly sandy dark green shales with traces of gypsum. Thin beds of sandstone are also found through the formation(Aulis Garcia, 2015).

Upper Concepcion

The Upper Concepcion, which is of early Pliocene age, overlies the Lower Concepcion,

with an approximate thickness of 500 meters. It was deposited in a medium neritic environment (Cabrera and Lugo, 1984), a marine zone at the edge of the continental shelf, with a depth up to 200 m, with mechanical energy due to the action of waves and currents (Schlumberger, 2016). This formation mainly includes fossiliferous grey shales with abundant intercalations of quartz and calciferous sands deposited in a platform environment.

Filisola

The Filisola overlies the Upper Concepcion and is of early Pliocene age. Its thickness can reach 800 meters. It consists of light grey sand with intercalations of well-cemented calcareous sandstone and soft, slightly sandy grey shales (Aulis Garcia, 2015).

Paraje Solo

The Paraje Solo Formation is of mid-Pliocene age, with a thickness of approximately 500 meters. It comprises a series of light grey sand bodies, with a fine to very coarse grain, some angular and others rounded. There are thin intercalations of carbonaceous shales and plant debris(Aulis Garcia, 2015; Perez Rincón, 1959).

Cedral

The Cedral Formation is of late Pliocene age, with a thickness of around 500 meters. It is composed of continental or brackish water deposits, with with light grey fine to coarse-grained quartz sands. The clasts vary from angular to rounded, and some fragments of pyrite and iron oxide usually appear Perez Rincón (1959).

3.4 Target formations

Reservoirs that are suitable for CO_2 storage must meet a selection of key criteria, described by Meyer et al. (2008) and listed in Table 3.1.

Properties	Application limits
Reservoir depth	1000 to 4000 m
Thickness of reservoir rocks	>20 m
Formation thickness	10 to 20 m
Formation depth	800 to 1000 m
Porosity	$>20\%$
Presence of cap rock formation	

Table 3.1: Application limits in CO_2 site selection.These applications help determine that a reservoir is suitable for CO_2 sequestration.

According to Jimenez et al. (2011), the Miocene Encanto, Upper and Lower Concepcion formations are considered the most important CCS formations in the Sureste Basin due to their geological properties. Overall, they are located in more than 1000 meters depth below sea level, with an average thickness of 300 m (across the entire basin), a porosity of 20-38%, a permeability of 180 mD, a temperature of 60°C, and initial water saturation of

22%, covering an area of 2290 km^2. Hence, they have suitable petrophysical characteristics. Also, their remaining oil volume is considerable, as remaining reserves are about 54 million barrels of crude oil equivalent (MMboe) (CNH, 2020)

The Encanto Formation consists of interbedded sand and shale. The thickness of the sand bodies ranges from 5 m to 60 m, and the thickness of the shale horizons ranges from 3 m to 70 m. The overall thickness ranges from 1200 m to 1300 m. The Lower Concepcion Formation overlies the Encanto Formation and is defined by interbedded thick shale and thin sand layers. The average thickness in this formation is 260 m (Martinez, 2001).

Romero and Bashbush (2017) developed a static model, production forecast, and economic evaluation of the fluid injection feasibility of water, CO_2, and N_2 in the sands of the Ogarrio field, along with a simulation model that determined the influences of the fluid injection through the use of uncertainty analysis. This analysis determined that the sands of this field are good candidates for fluids injection, as they are permeable. Meanwhile, the shales are of low permeability and could act as confining zones to prevent CO_2 migration (USDOE/NETL, 2015).

3.5 Seismic interpretation

The first stage of my analysis is to use seismic reflection data to image the geometry of the target formations (Satinder and Brown R., 2013) in order to compute the area of the target reservoirs. To do so, the seismic data must have sufficient quality and coverage in order to be able to resolve the target layers and to find structures that could trap CO_2.

Around 73 2D seismic sections were identified that cover the Ogarrio field (Figure 3.4). I used these sections to map the geological horizons representing the tops of the Encanto, Lower and Upper Concepcion formations. The Ogarrio 803, 700, 590, 569, and 1255 wells were used as references to identify the relevant horizons within the seismic sections since two-way travel times to the formations were available for these wells. I used OpendTect to display and interpret the seismic sections and mapped horizons. Figures 3.5a, 3.5b and 3.5c show example 2D seismic sections, with the Encanto, Upper, and Lower Concepcion horizons mapped.

The overall reservoir area is about 57 by 64 km. The main structure that can be seen from the interpreted horizons is a broad, open anticline in the northeast of the field area. This is shown in Figure 3.6. This feature runs with a northwest-southeast orientation, with approximate dimensions of 10 km North-South by 12 km East-West. This structure can be observed in all of the three mapped horizons (Figure 3.5).

As reported by the literature and prior seismic studies in the area carried out by Mexican Petroleum (Pemex in Spanish), the anticline shape found in this field corresponds to the saline mass recorded in their reports. A geological cross section of the Ogarrio field taken from Mora-Oropeza (2000) shows the presence of this structure, as seen in Figures 3.7 and 3.8. It is oriented NW-SE with an elliptical shape. Furthermore, since there has

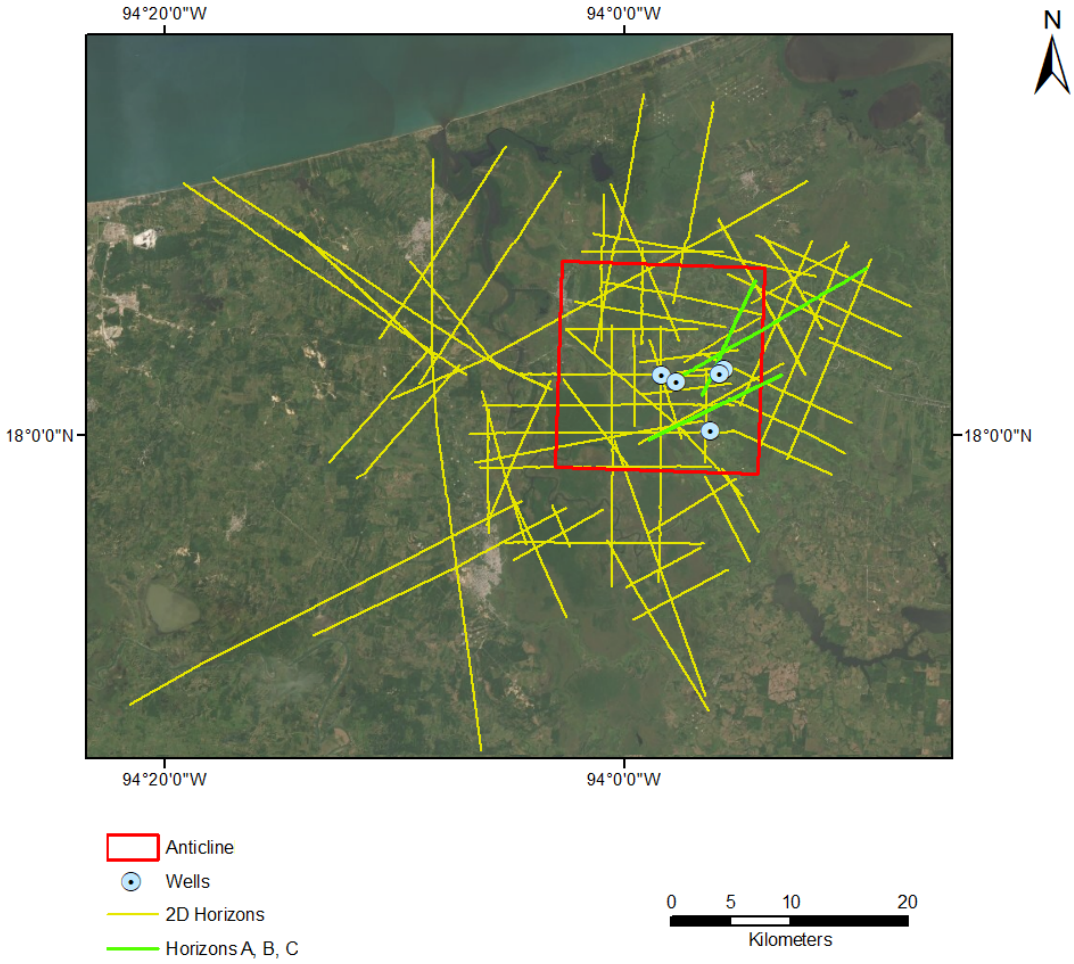

Figure 3.4: Locations of 2D seismic sections used to map the geometry of the Ogarrio field. The horizons highlighted in green correspond to the seismic sections shown in the Figures 3.5a, 3.5b and 3.5c. The wells used to identify horizon depths are marked by blue circles.

not been sediment accumulation since the Pliocene, it is believed that the saline structure is stable (Perez Rincón, 1959).

In addition to this, and based on the available well log data, I created a cross section to show the geology distribution in the eastern zone of the anticline area. Figure 3.9 shows that a structure similar to an anticline is present according to the well logs of the Ogarrio 1527, 655, and 658 wells, where it also seems to be a deep salt structure. This cross section is 4 km away from the one plotted by Mora-Oropeza (2000). The well log data will be extensively analysed in Section 3.6.

Anticlinal structures represent ideal targets for CO_2 storage since they provide trapping structures for the buoyant CO_2. As such, my analysis will focus on the identified anticline structure. In order to compute the potential storage volumes, potential spill points from this structure must be identified.

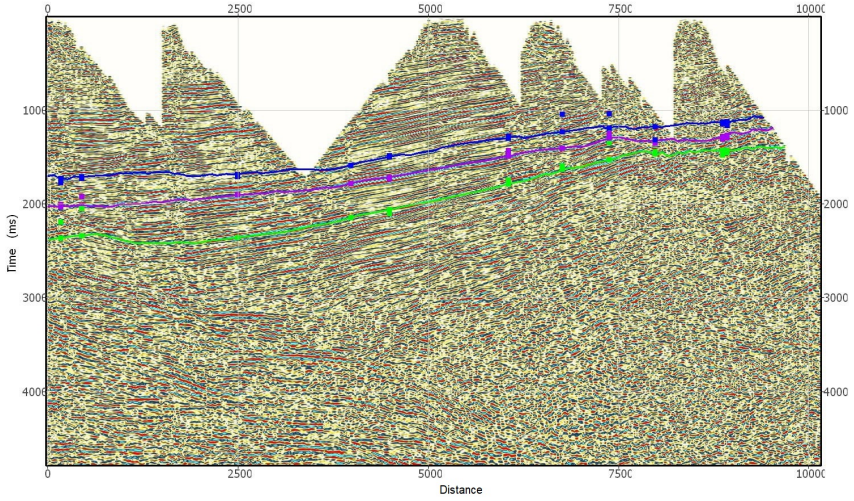

(a)

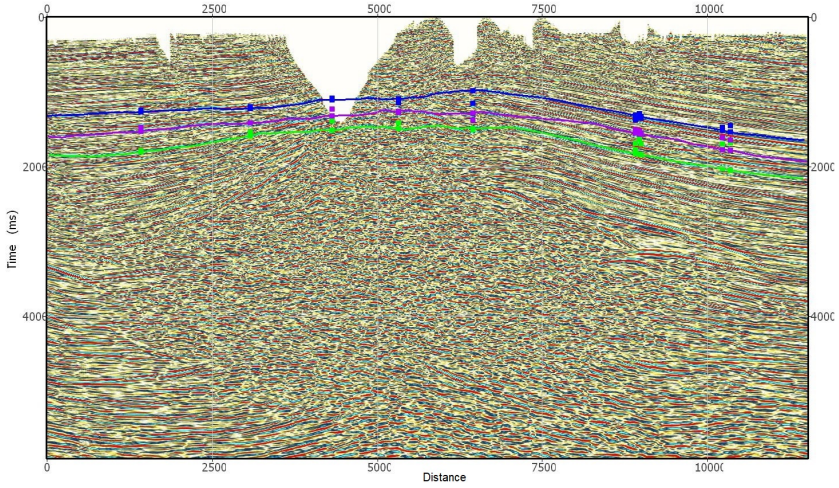

(b)

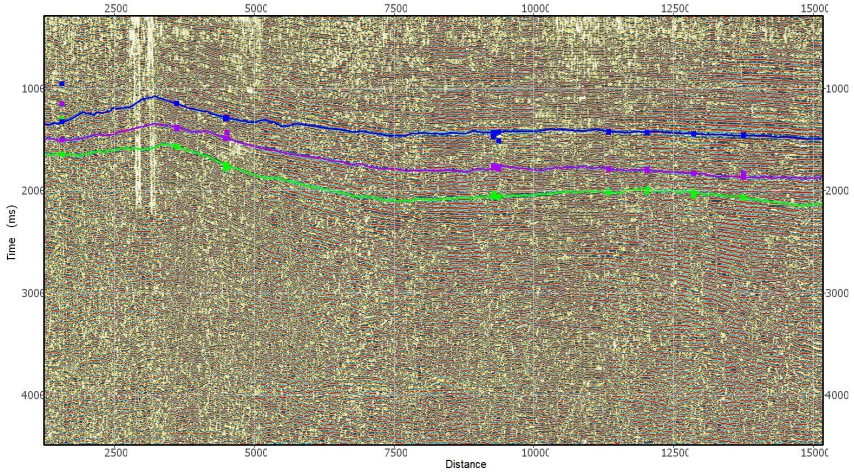

(c)

Figure 3.5: 2D seismic sections showing 2D horizons: the green line is the Encanto formation, the purple is Lower Concepcion, and the blue is Upper Concepcion. Each of these formations sit on different flanks of the anticline. The three sections are NE-SW lines.

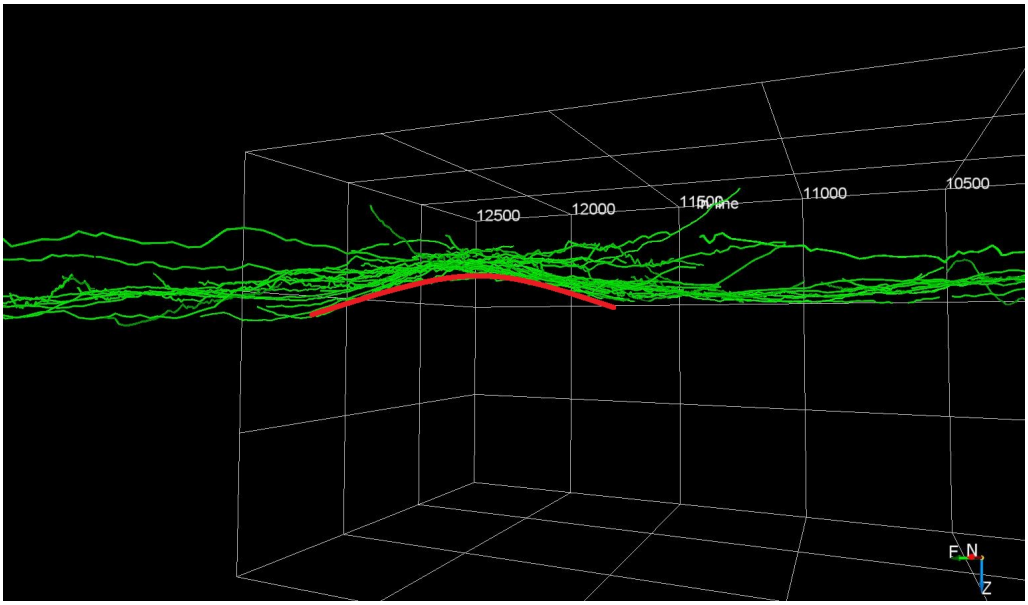

Figure 3.6: Anticline shape highlighted with a red line in the 2D horizons of the Encanto formation.

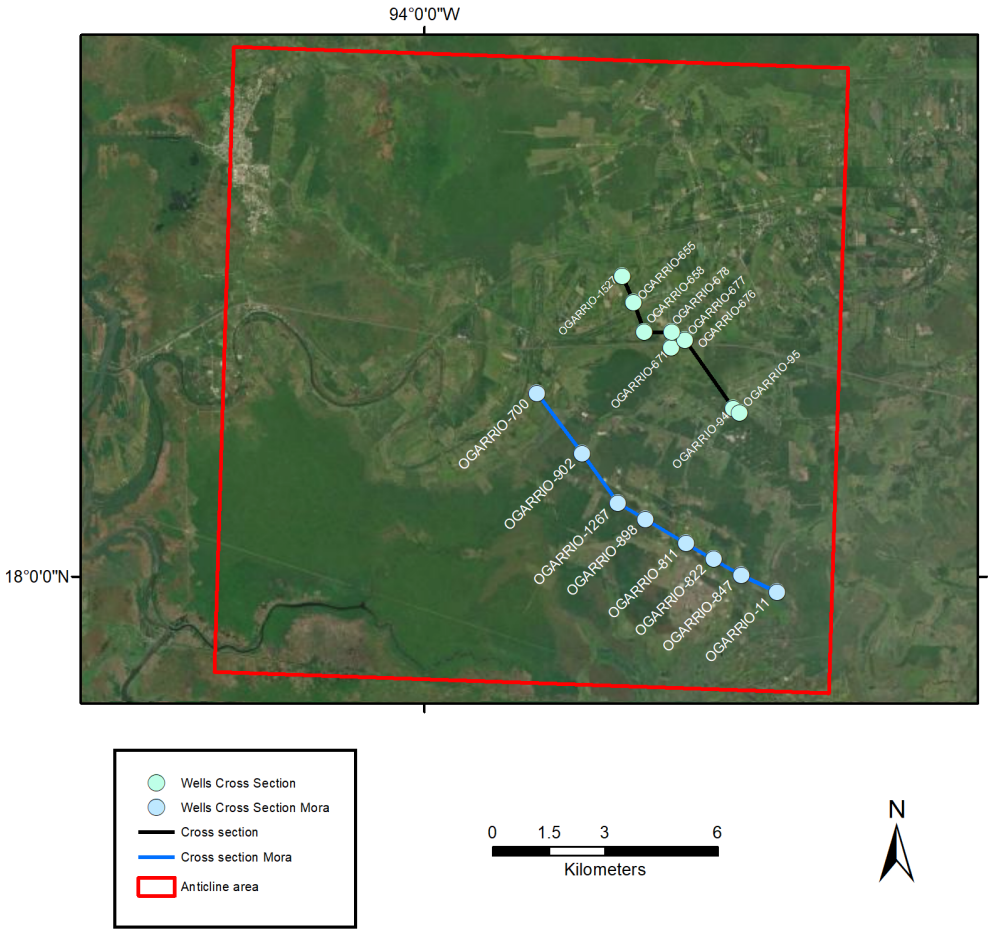

Figure 3.7: Location of the cross sections of the Ogarrio Field created by Mora-Oropeza (2000) in blue and in black the created with the available well log data.

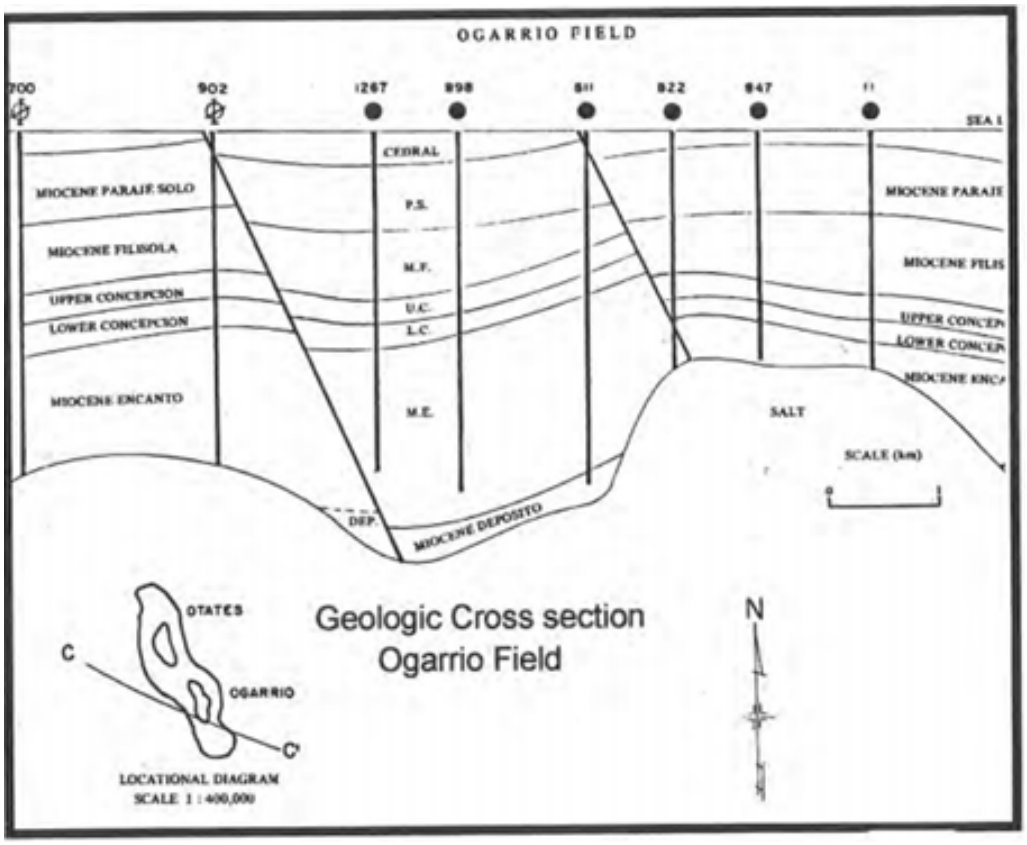

Figure 3.8: Geologic cross section of the Ogarrio field, showing normal faults and salt structure related to Encanto formation. Taken from Mora-Oropeza (2000).

3.5.1 Time vs depth conversion

There are two main types of seismic migration to process seismic data. One is the *time migration*, which generates images in 1-dimensional traveltime; its velocity model sets the data on a 1-dimensional Earth stratified horizontally (Etgen and Kumar, 2012). The other is *depth migration*, which uses a velocity model to locate the data in an accurate physical space (Schlumberger, 2022). Due to insufficient seismic data, this thesis did not apply depth migration, as it requires high-resolution seismic images and accurate knowledge of vertical and horizontal seismic velocity variations.

The horizons derived from the 2D seismic sections are measured in two-way travel time (i.e., seconds), so it is necessary to convert them to meters to compute formation depths.

As the velocity structure is relatively consistent in most available wells, a simple velocity model was used for this conversion. The conversion between two-way travel time (TT) and depth (TVDSS) was taken from a selection of wells for which such information was available (Figure 3.10). All of these relationships followed very similar curves, and so a single cubic polynomial fit was applied in order to compute the average values. The resulting fit (red line in Figure 3.10) is given by the following relationship:

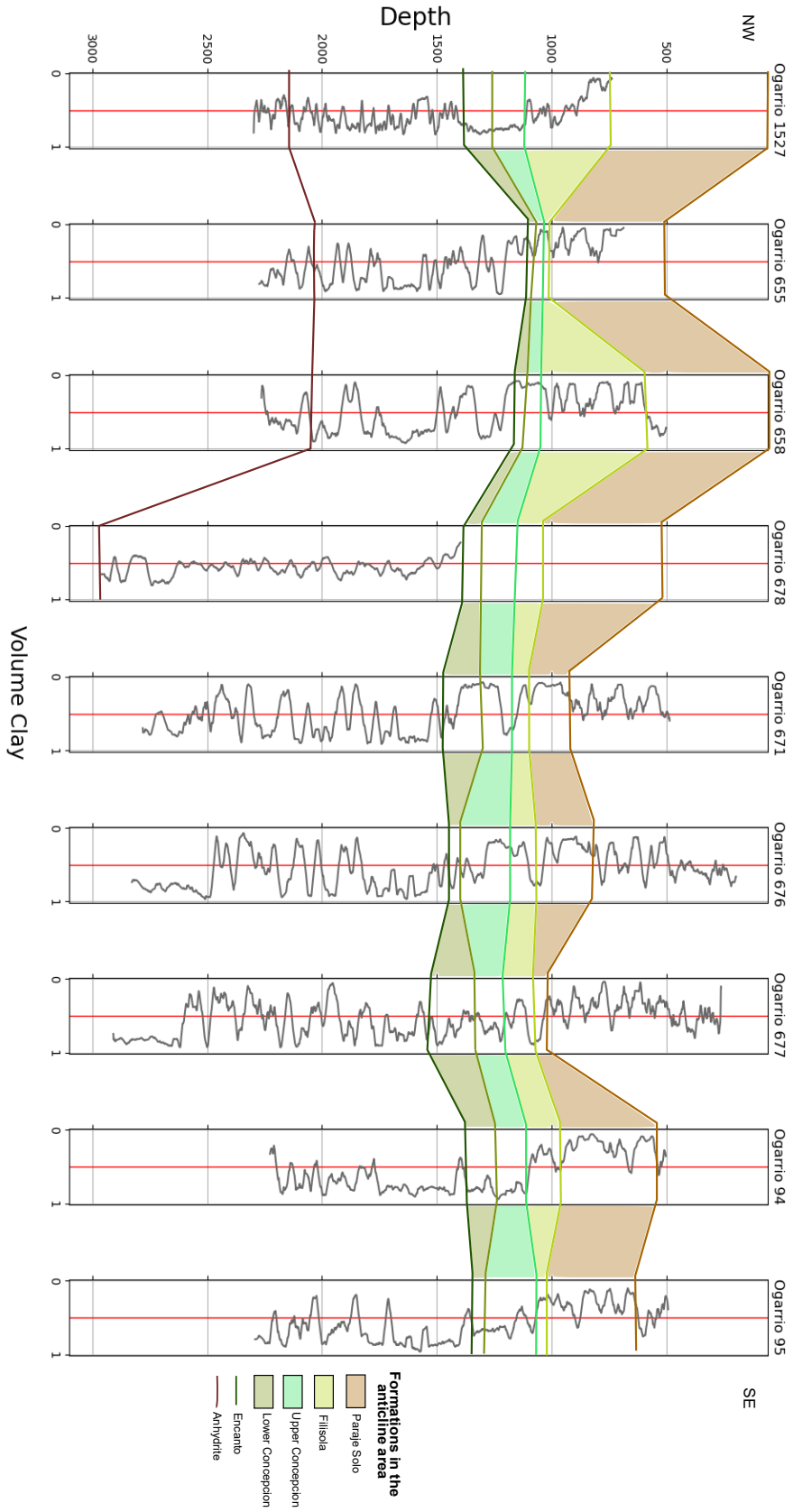

Figure 3.9: Cross section created with the log information from nine wells. The depths of the formations were taken from the CNH data, and the thickness of Encanto is not defined in the Ogarrio 671, 676, 677, 94 and 95 wells due to lack of data.

$$TVDSS = -12.7647 + 786.2373 \times TT + 291.2583 \times TT^2 - 24.3602 \times TT^3 \quad . \tag{3.2}$$

The interpreted TT values from the seismic sections were converted to TVDSS using this equation for subsequent interpolation to map the horizons across the field.

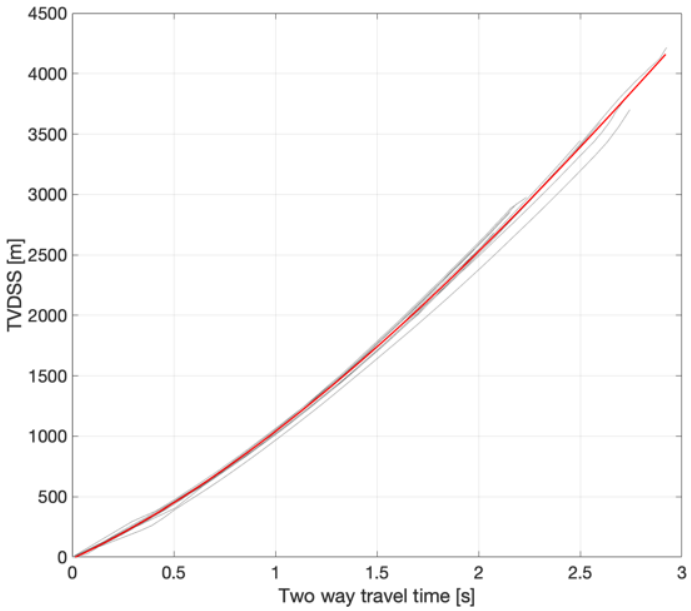

Figure 3.10: Velocity model of the time travel (TT) vs depth (TVDSS) relationship taken from the wells of the area. This relationship is represented by the black lines. The red line represents the average TVDSS as a fuction of TT.

3.5.2 Interpolation

The seismic sections provide two-dimensional profiles of the horizon depths across the field. Interpolation of these observations is required to create three-dimensional structural maps of the identified horizons. We can use these 3D interpolated maps of the subsurface to identify potential spill points, and therefore the areas available for CO_2 storage. Here, I used ArcGIS to interpolate the depths of the 2D horizons, as converted from the travel times to TVDSS, to create 3D surfaces that represent the structure of the anticline (Figure 3.11).

The most commonly used interpolation methods in ArcGIS are Inverse Distance Weighted (IDW), Kriging (K), Natural Neighbour (NN), and Spline with Barriers (SB). Table 3.2 lists these interpolation methods that I used to generate interpolation rasters and 3D surface maps. I then, compared the results (Figures 3.12 and 3.13).

The NN method and the SB method were preferred over the other methods because the distribution and shape of the generated surface are similar in the two methods, and both produced interpolated values that closely matched the depths observed from the wells and the seismic data. On the contrary, IDW and K produced irregular and uneven surfaces

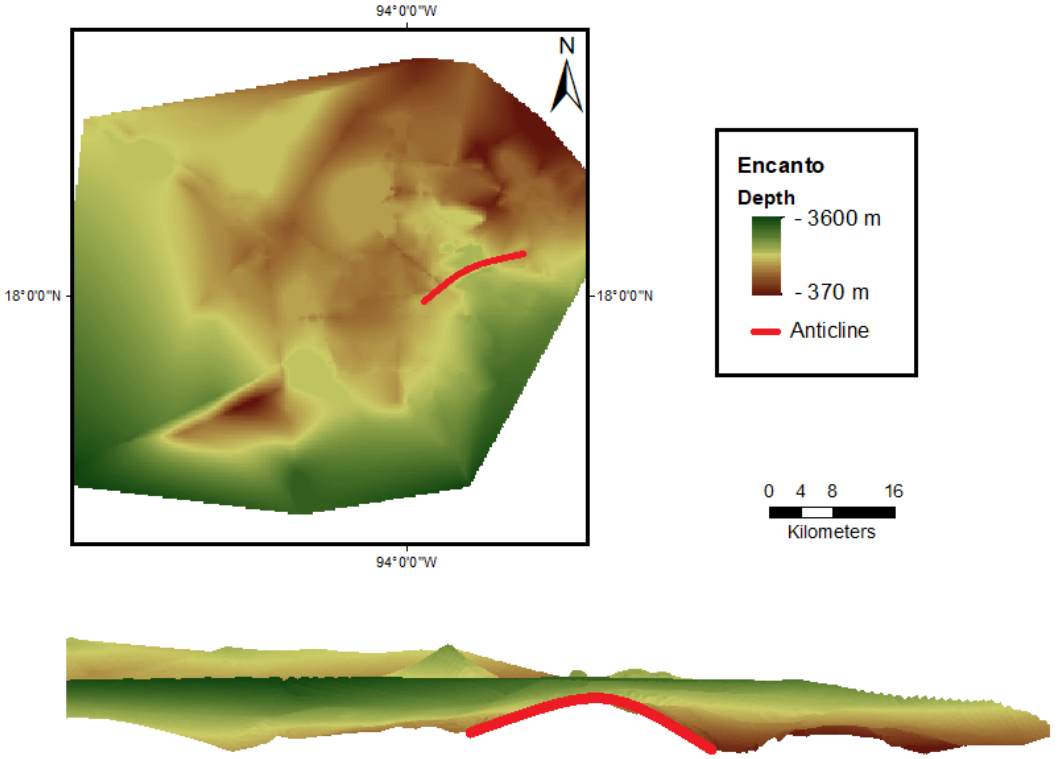

Figure 3.11: 3D model showing the depths of the Encanto formation as interpolated from the 2D seismic horizons. The anticline structure is highlighted by the red curve.

with abrupt and unnatural changes, and the interpolated values are different from the depths of the seismic data, see Figure 3.13. However, since the SB surface is more rounded and smoother, and it is improbable that the actual relief has these characteristics, the NN surface was selected to estimate the potential structure of the anticline.

The 2D horizons show that the highest point of the anticline in the Encanto formation is about 1601 m depth, with the limbs extending to 2600 m depth. In Upper Concepcion, the anticline's highest point is at 1230 m, and the limbs extend to 1800 m. In the Lower Concepcion, the highest point of the anticline is at 1515 m, and the limbs extend to 2200 m. The NN interpolation values correspond to these depths.

There are three main parameters used in the NN interpolation:

1. The input features. In this case, the 2D horizons are represented in points instead of a line.
2. The Z value is the depth of each point of the horizons.
3. The cell size. The smaller the cell size, the higher the resolution and accuracy.

The last parameter is the only value that can differ in each interpolation. Changing the cell size could modify the shape, size, and area of the potential structures of the anticline.

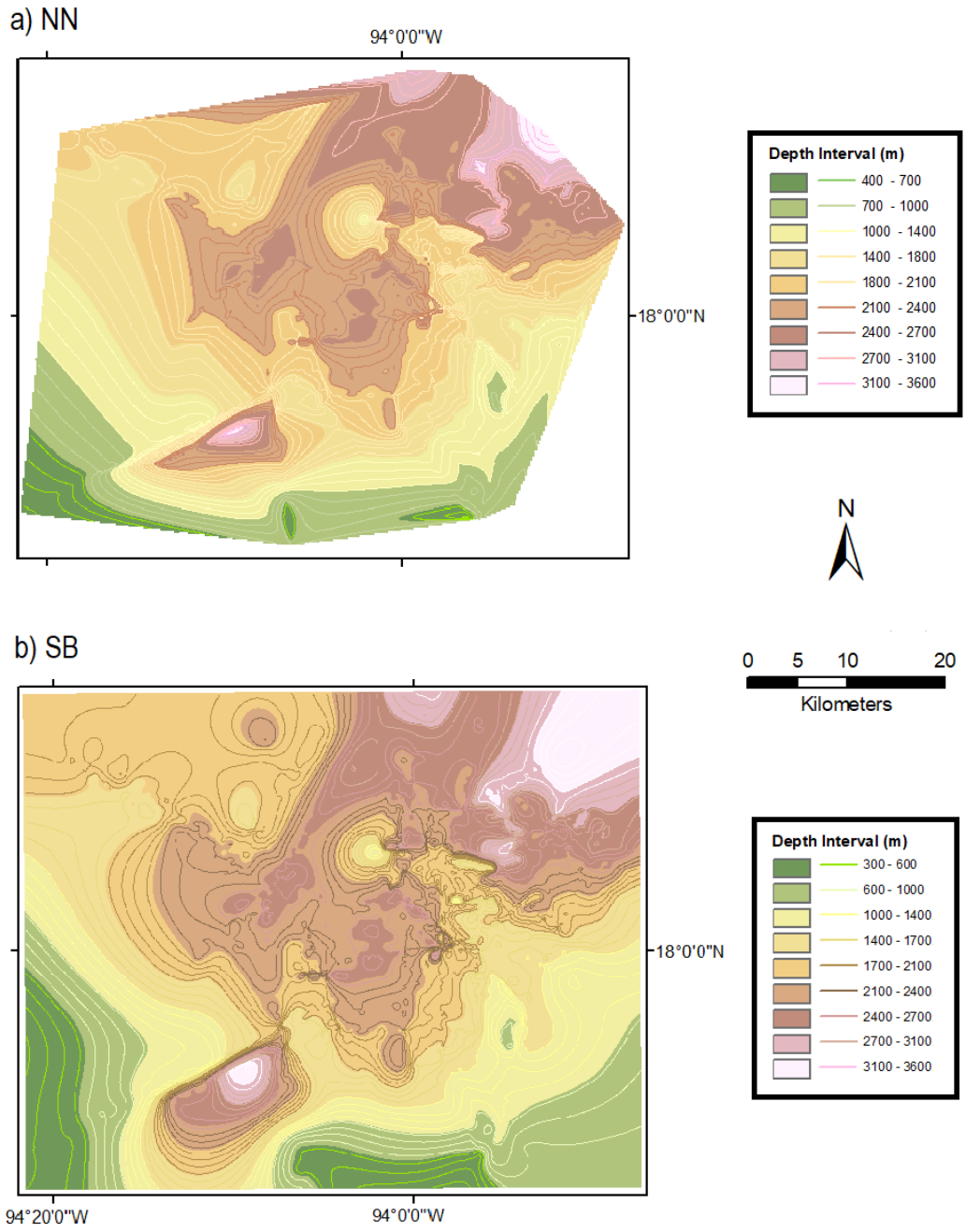

Figure 3.12: Natural Neighbour (NN) and Spline with Barrier (SB) interpolation rasters.

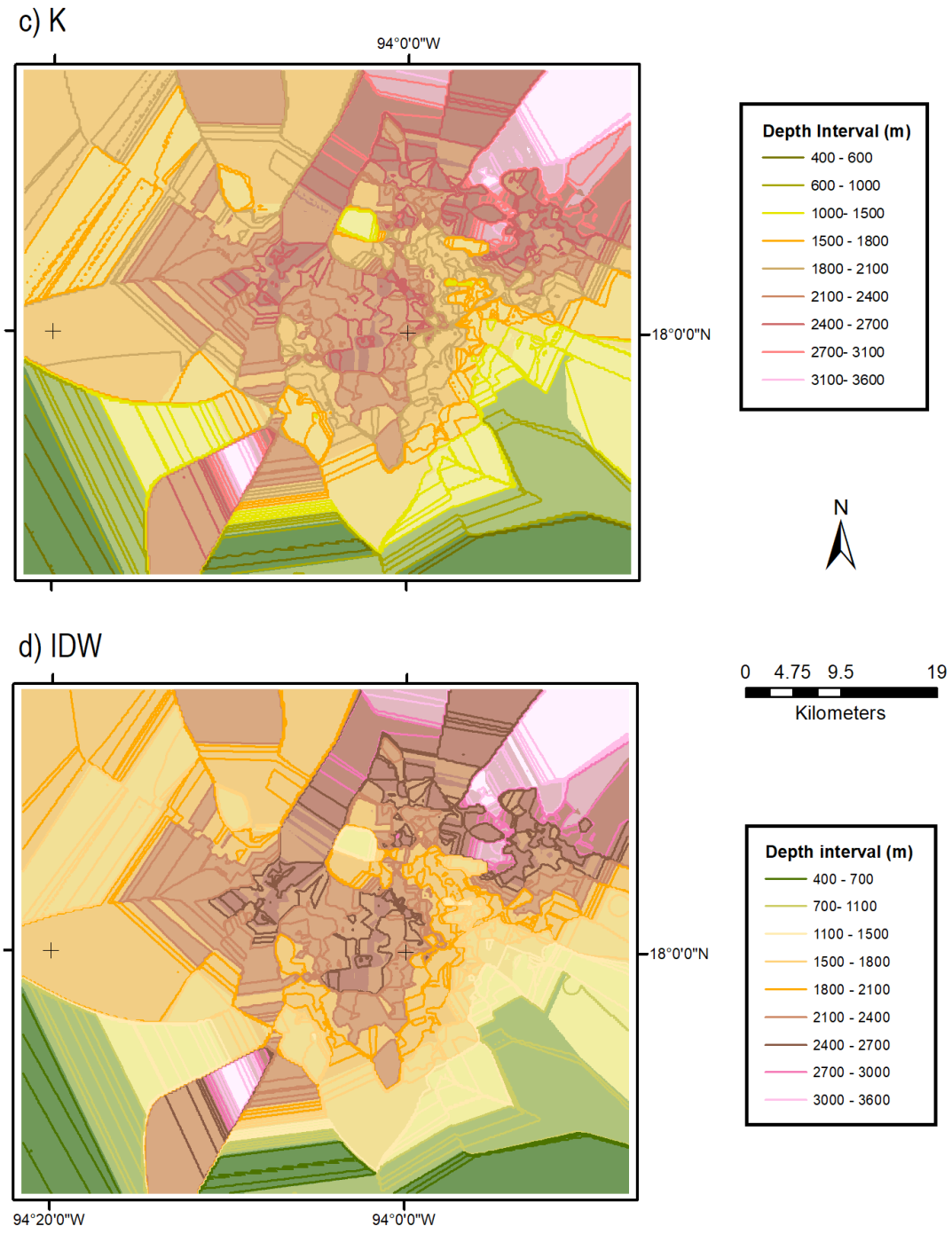

Figure 3.13: Kriging (K) and Inverse Distance Weighted (IDW) interpolation rasters.

Interpolation method	Description	Outcome
Natural Neighbour (NN)	It is local and only uses a subset of samples close to the query point, and the heights are within the samples used (ESRI, 2016).	Smooth interpolation seems to follow a pattern and respect the values of the wells.
Spline with Barrier (SB)	It uses barriers such as polygons to estimate values that minimize the surface curvature using a mathematical function (ESRI, 2016).	Smooth and round interpolation. Some values are not accurate to the wells.
Kriging (K)	Predicts values if the data is normally distributed and stationary, and it considers the distance between known points (Goovaerts, 2019).	Irregular interpolation, abrupt changes in the surface due to this, the values do not correspond to the wells.
Inverse Distance Weighted (IDW)	It uses an average weight of the data to create a surface, and the weights decrease as the distance from the interpolated point increases (GIS Geography, 2020).	Irregular interpolation, steep slopes, the values differ by meters with the wells.

Table 3.2: Comparison of the interpolation methods used to produce 3D surfaces from the 2D seismic horizons.

Therefore the outcome would change the final calculations of the CO_2 storage capacity in the reservoir.

I produced four NN interpolations of Encanto with different cell size values to test how the generated surface changes, see Figure 3.14. From a general point of view, the main difference between them is that the shapes are large, rounder, and continuous in the largest cell size interpolation. In contrast, in the smallest cell size interpolations, many small shapes are slightly separated from each other and are not so round. It is essential to assess how these variations affect the area estimations by analysing the different shapes, as they could act as potential CO_2 trapping structures.

3.5.3 Structural trapping

As described above, the interpolation of the 2D horizons produced a 3D model that extends about 57 by 64 km; see Figure 3.15. With this model, the area of the potential structural traps can be computed.

I extracted contour lines from two interpolation rasters with different cell sizes to determine the spill points and paths. 1) the raster with a cell size of 50 since it has more details in its features, and 2) the raster with a 200 cell size because it is the default size, which means that it was determined by the software based on its properties and has defined features.

The requirement for a closed storage structure is that the contour lines must be connected or represent a closed feature such as a circle to avoid any spill path, which is

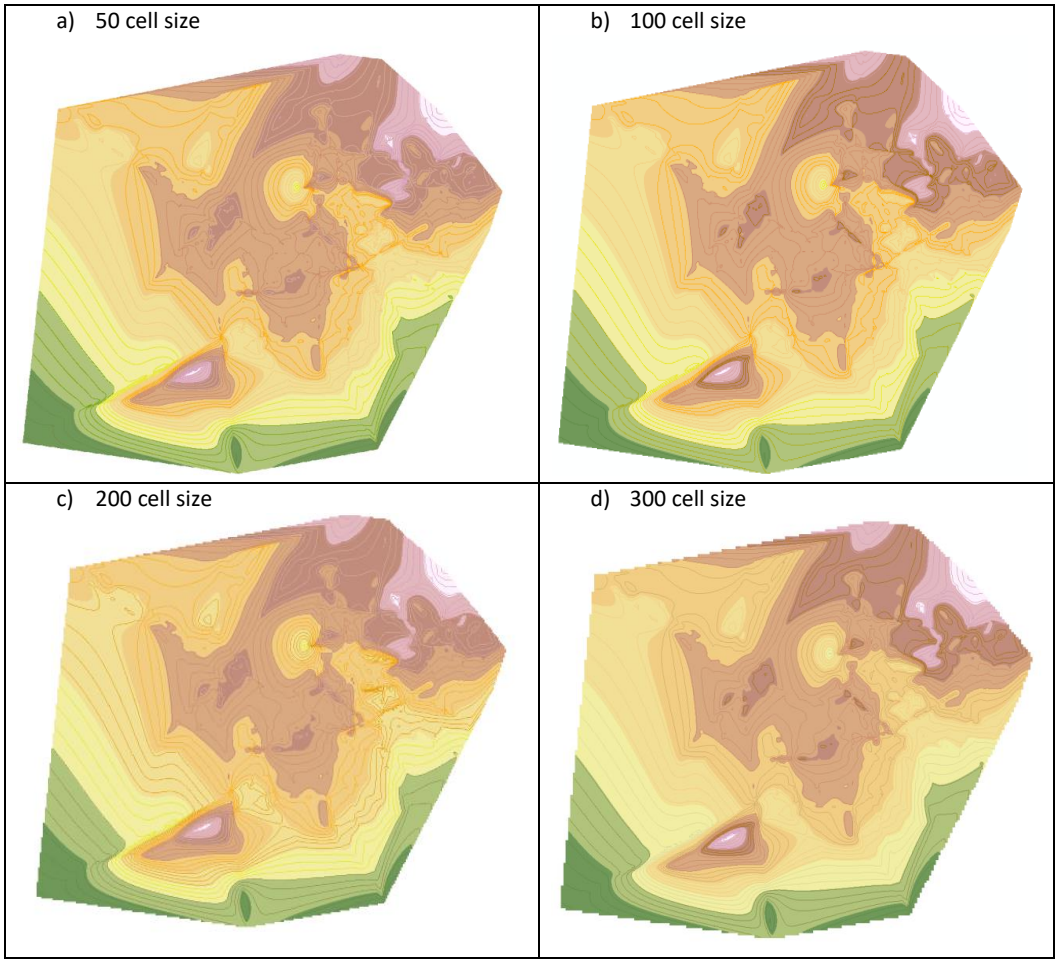

Figure 3.14: NN Interpolations produced setting different cell sizes. a) Corresponds to a cell size of 50, with more and smaller shapes, b) has a cell size of 100, and slightly fewer details in the shapes than a). c) The default cell size, 200, shows shapes with defined endings and average sizes compared with the others, and d) has a cell size of 300; the edges of the features are round and diffuse in some parts.

the path that the CO_2 follows once the trap is filled and could lead to another trap or leak out (Møll Nilsen et al., 2014). Since the interpolation does not give an exact visualisation of the underground relief, I adopted a conservative approach in this assessment. The uninterrupted deepest contour lines determined the maximum trapping areas throughout their perimeter, and the shallowest contour lines determined the minimum trapping areas with an uninterrupted perimeter.

With the spill points, I was able to delineate the potential storage traps. As depicted in Figures 3.16, 3.17, and 3.18, the anticline has three prospective trap structures present in each target formation. However, the extent of the trap and the spill points vary in each formation.

As it can be seen, the structural traps are likely to be the same in the three layers.

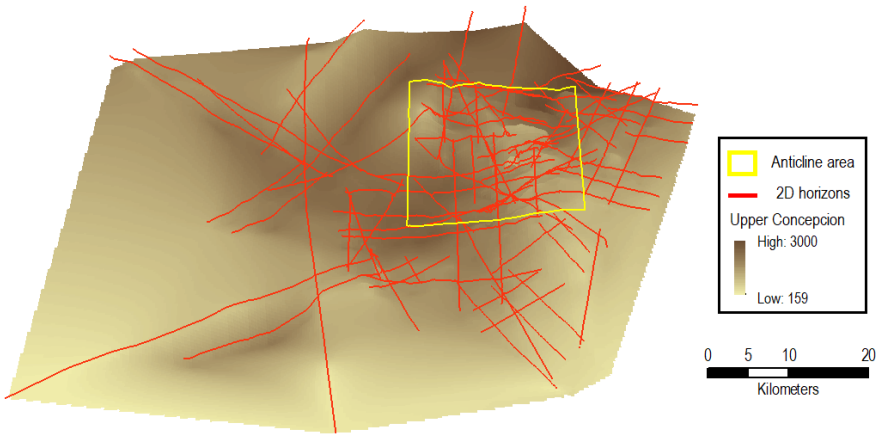

Figure 3.15: 3D model and 2D horizons of Upper Concepcion.

However, Upper Concepcion has the most extensive trapping area, as it is the upper layer and is evenly distributed in the anticline. Lower Concepcion has an intermediate trapping area compared to the other two. Encanto has the smallest trapping areas; this could be mainly because of the stratigraphic configuration. According to the 2D lines, in some places, it appears wider than in others. These structural traps are not connected by a spill path, making them suitable for CO_2 storage.

Table 3.3 lists the maximum and minimum areas of the potential trap structures in the three layers. The raster areas with a cell size of 50 are larger than the raster with a 200 cell size. The most significant difference is 5.6 km^2 between the maximum areas of Upper Concepcion, and the smallest difference is 2.2 km^2 between the minimum areas of Lower Concepcion. These differences are related to the cell size and depth of the features and generate uncertainties. To reduce the uncertainty about the size of the area, I calculated the average areas of the 50 and 200 cell size rasters, see Table 3.4; these area values will be considered in the capacity assessment.

Cell size	Area	Upper Concepcion	Lower Concepcion	Encanto
50	Minimum	22,800,000 m^2	20,800,000 m^2	22,100,000 m^2
200	Minimum	19,500,000 m^2	18,500,000 m^2	19,500,000 m^2
50	Maximum	40,900,000 m^2	39,200,000 m^2	36,800,000 m^2
200	Maximum	35,200,000 m^2	34,600,000 m^2	32,200,000 m^2

Table 3.3: Areas of the potential CO_2 trap structures in the target formations.

Average area	Upper Concepcion	Lower Concepcion	Encanto
Minimum	21,100,000 m^2	19,600,000 m^2	20,800,000 m^2
Maximum	38,100,000 m^2	36,900,000 m^2	34,500,000 m^2
Total	29,600,000 m^2	28,300,000 m^2	27,700,000 m^2

Table 3.4: Average areas of the two different cell size rasters of the trap structures in the target formations.

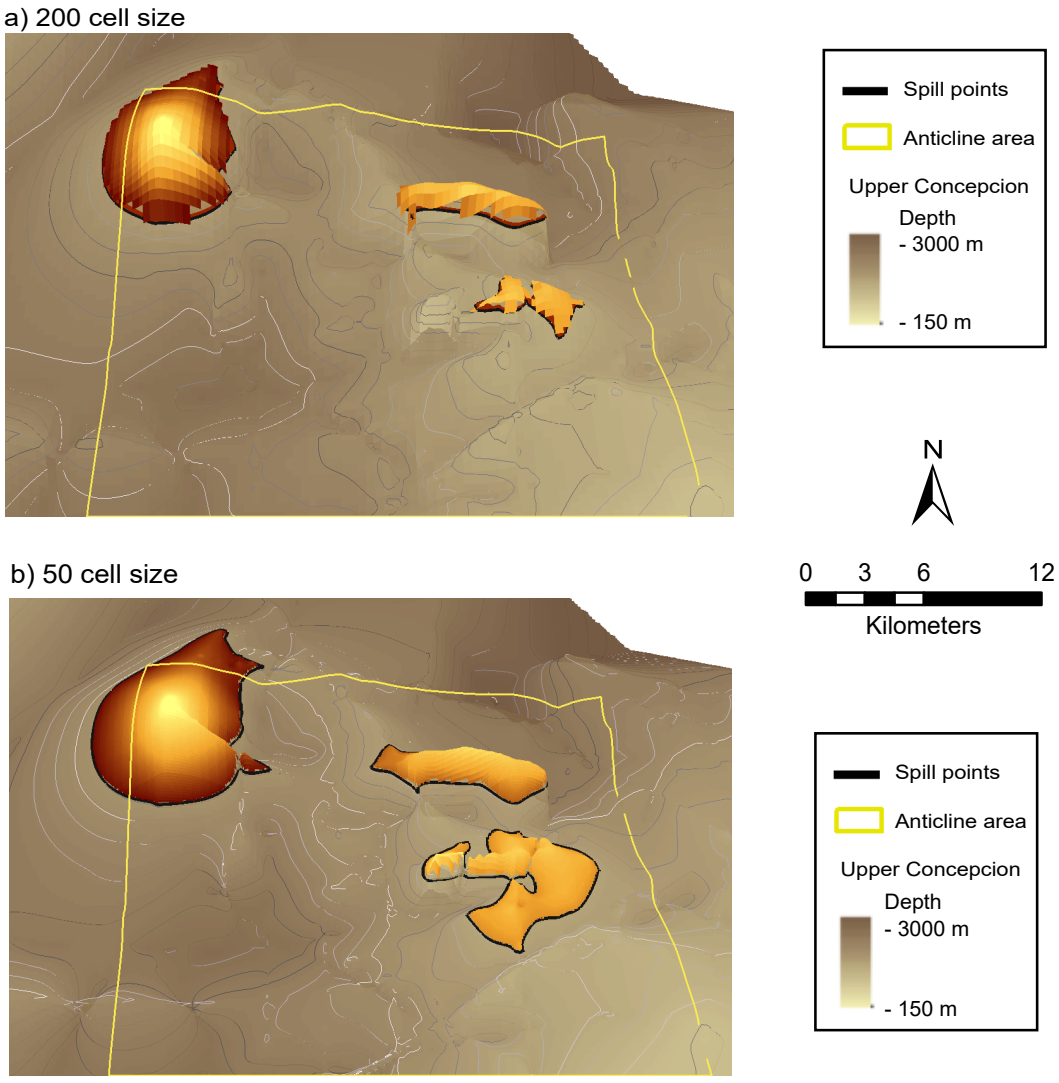

Figure 3.16: Location of the structural traps in Upper Concepcion, shown in bright yellow; the thick black line defines the spill points. a) Is the raster with a cell size of 200 with the minimum area, each trap has a different spill point, one at 1500 m, the other at 1300 m and the other at 1200 m. b) Is the 50 cell size raster with the maximum area; the spill points are at 1300, 1400 and 1600 m depth.

3.6 Well log analysis

Having computed the areas in which CO_2 trapping could take place, I now need to evaluate the Net-to-gross ratio (NTG) and porosities of these formations. I do this using the analysis of well logs from the field. Sixty wells from Ogarrio and nearby fields were identified in the CNH dataset. These logs span a wide range of ages, with varying quality of logs. Some more recent wells have a broad suite of different well log measurements, while others have more limited log information. The depths of the log curves are also variable - some wells start their logs at depths as shallow as 800 m, while others do not start until 2000 m depth.

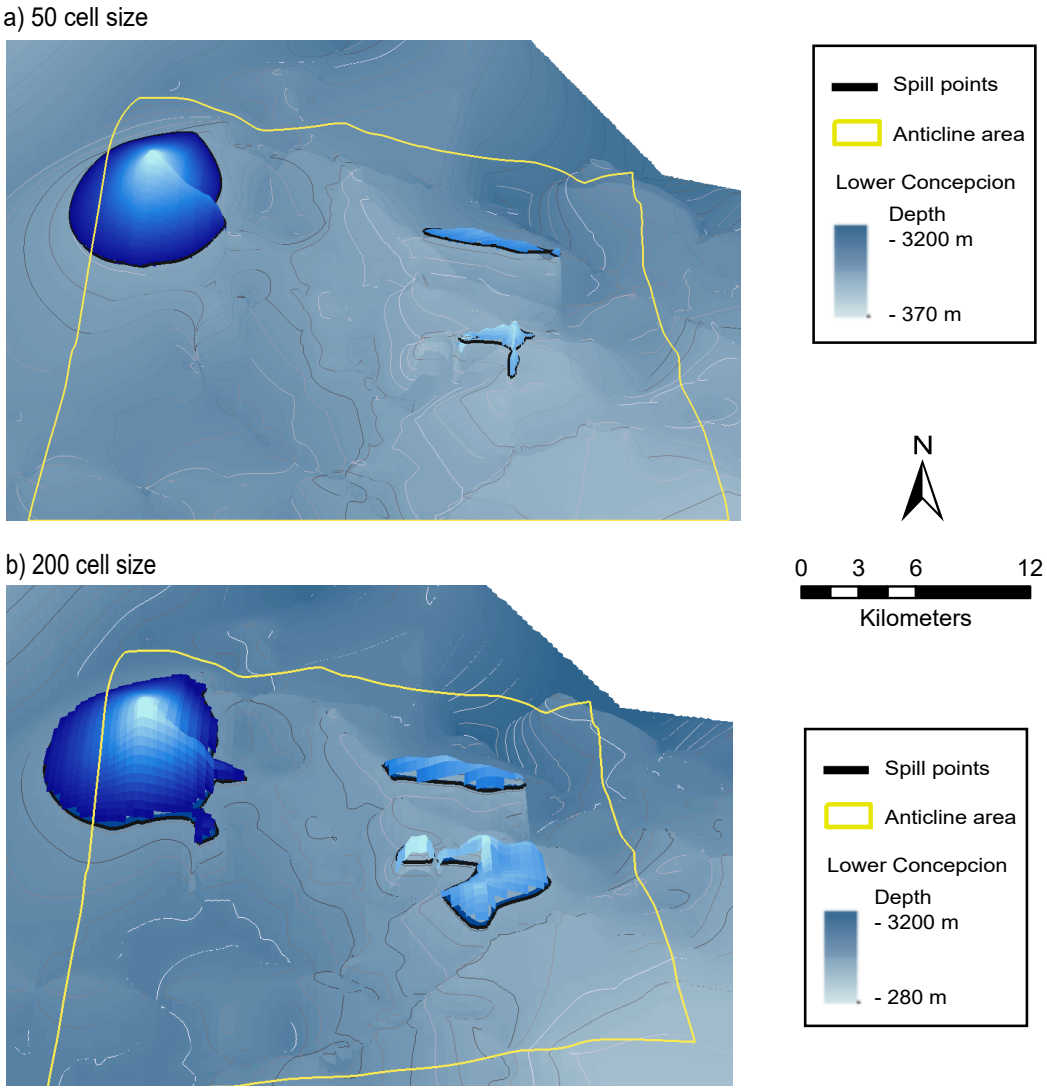

Figure 3.17: Location of the structural trap in Lower Concepcion, shown in bright blue; the thick black line defines the spill points. a) Is the raster with a cell size of 50 with the minimum area, each trap has a different spill point, one at 1800 m, the other at 1500 m and the other at 1400 m. b) Is the 200 cell size raster with the maximum area; the spill points are at 1900, 1600 and 1500 m depth.

In order to compute the storage volumes, data regarding NTG and porosity is required; NTG can be estimated from the proportions of shale and sandstone within the formation. On the other hand, clay volumes are typically calculated from other log measurements, and porosity can be directly estimated from neutron porosity logs. However, different log curves were available; therefore, cross-correlations between different parameters were used to estimate clay volumes and porosities where this information was not directly available.

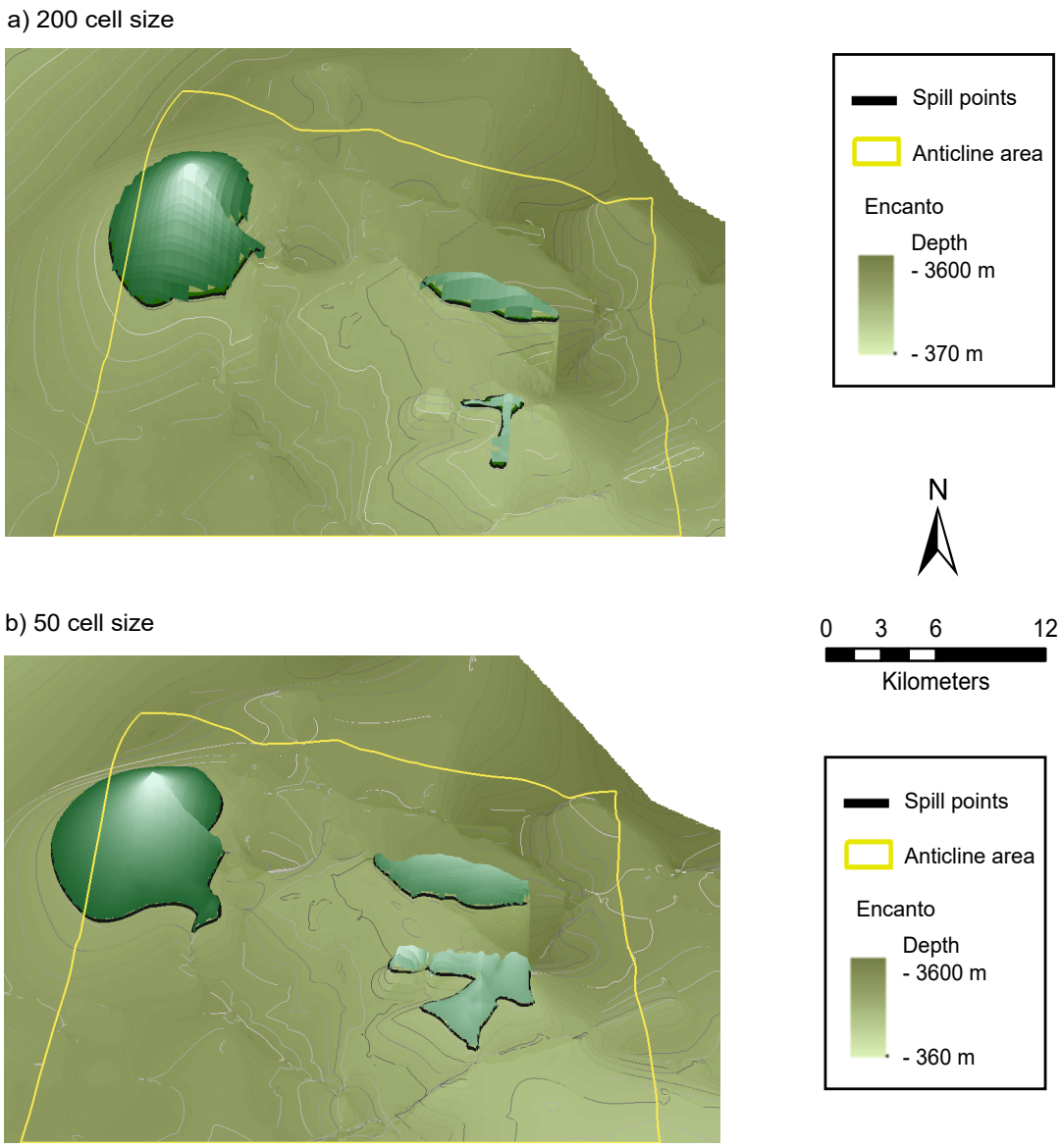

Figure 3.18: Location of the structural trap in Encanto, shown in bright green; the thick black line defines the spill points. a) Is the raster with a cell size of 200 with the minimum area, each trap has a different spill point, one at 2000 m, the other at 1800 m and the other at 1600 m. b) Is the 50 cell size raster with the maximum area; the spill points are at 2100, 1900 and 1700 m depth.

Within the available logs, we identified four parameters that were used in my analysis, listed in (Table 3.5).

I used these curves to obtain:

- The proportion of each formation that is sandstone and shale. VolClay determined my estimates of lithological changes, where I took VolClay < 0.5 to indicate sandstone and VolClay > 0.5 to indicate shale.

Gamma Ray (GR)	Measures the natural radioactivity of the formation. It works as an indicator of the abundance of radioactive minerals such as Uranium, Thorium, and Potassium in rocks; the gamma intensity is the linear combination of each element (Al-obaidi, 2017). As clay minerals contain small amounts of thorium, this measurement is used to estimate the proportion of clay in the formation.
Volume Clay (VolClay)	Calculated from other measurements such as the gamma ray and density logs, it gives the proportion of the rock that is clay or shale.
Porosity (Phi)	Measurement using neutron bombardment, of the rock porosity. (Usman and Haris, 2019).
Bulk density (BD)	Measurement using electron bombardment, of the rock density. Porosity will be inversely proportional to density (Barrass and Zehner, 2000).

Table 3.5: Parameters used in my well log analysis for the Ogarrio field.

- The relative interbedding thicknesses of shale and sandstone in each formation. These thicknesses and the total thickness of each layer were calculated from the VolClay criterion, as described above. These values were used to compute the NTG.
- The average porosity of the sandstone and shale within each formation and the variability of this parameter.

There was only a limited amount of data available for more than fifty wells. I identified four wells, Blasillo 521, 525 and Ogarrio 1483 and 1527 (shown in Figure 3.19), that had log curves for bulk density, porosity, GR, and VolClay. In Figure 3.20, I plot the GR, VolClay and porosity curves for Ogarrio 1483. I used the relationships between these properties to produce regression lines in order to compute VolClay and porosity curves for wells that only had, for example, GR or porosity logs.

Three cross plots showing: porosity versus VolClay, porosity versus GR, and GR versus VolClay, were generated for each of these four wells. The cross-plots corresponding to the well Ogarrio 1483 are shown in the Figures 3.21a, 3.21b and 3.21c.Ogarrio 1483 is used as an example as it has a complete set of data to carry out further analysis. Additionally, I computed the coefficient of determination (r^2) of the three linear regressions; their average value is 0.8, which means that the regressions fit and are relatively high. The cross plots for Ogarrio 1527 and Blasillo 521 have similar regressions and r^2 as Ogarrio 1487; see Appendix A.

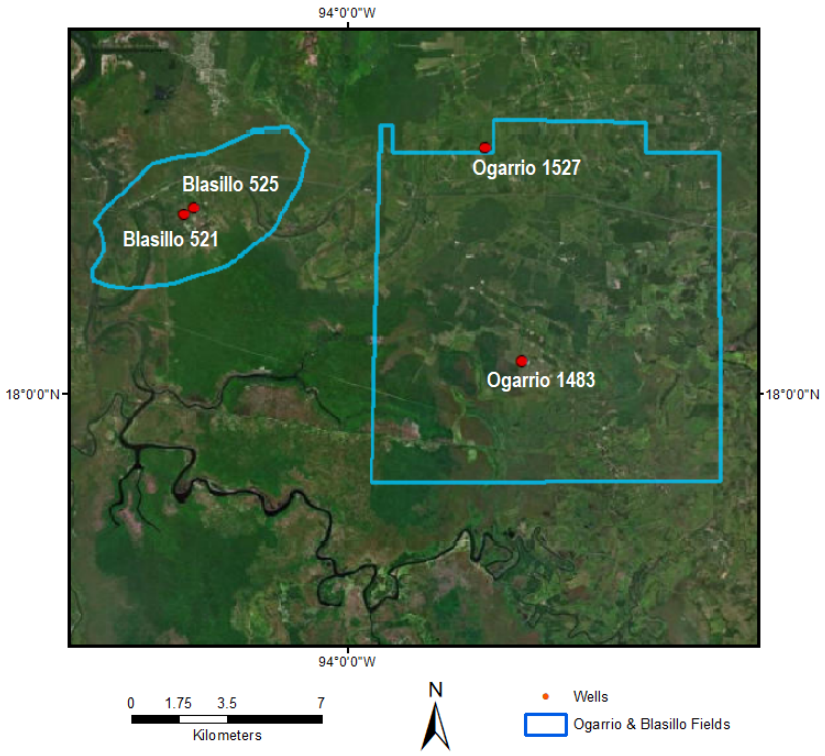

Figure 3.19: Location of the Ogarrio 1483, 1527 and Blasillo 521 and 525 wells.

For fifteen wells, such as Ogarrio 95 (Figure 3.22), the only available log curve was VolClay. For these wells, the VolClay curves were used to compute NTG values.

The only available log curve was the GR log for thirty-five wells, such as Ogarrio 812 (Figure 3.23). The VolClay values used to compute the NTG were generated using the regression as shown in Figure 3.21b.

The log analysis shows that shale is the lithology that predominates, especially in the Lower Concepcion and Encanto formations. However, significant sandstone thicknesses are also present that will provide suitable injection targets.

The log data in the different wells do not follow a pattern. While in some wells, the interbeddings of sandstones and shales are noticeable, in others, there is little interbedding; this indicates that the interbeddings of sands and shales are not laterally continuous.

Table 3.6 shows average values obtained from a compilation of the sixty available well logs, which will be used in my storage capacity assessment.

The well logs, cross plots, and values of the sixty wells used to obtain the results in Table 3.6, along with the code used to compute them, are provided in Appendix A.

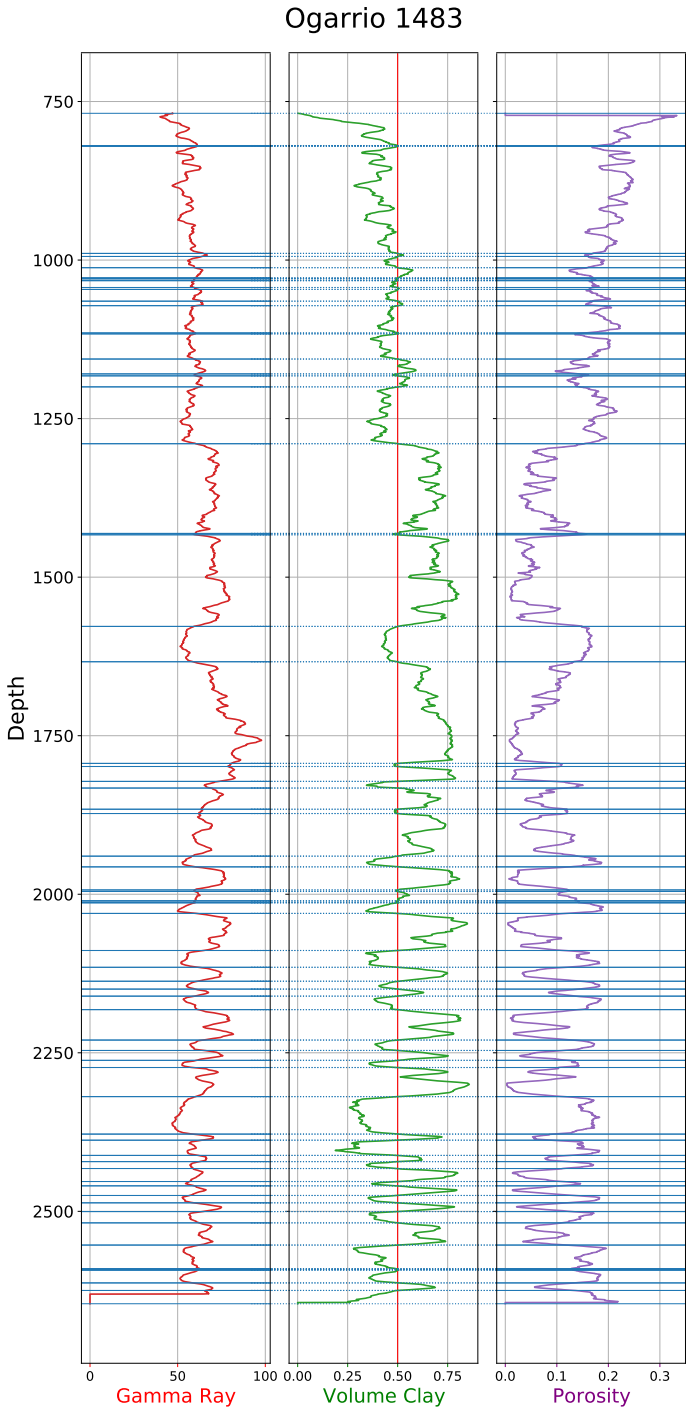

Figure 3.20: Log curves from Ogarrio 1487, showing GR, VolClay, and Porosity as a function of depth. The red vertical line on the VolClay log is used to delimit shale versus sandstone. The blue lines show the interbedding between sandstones and shales.

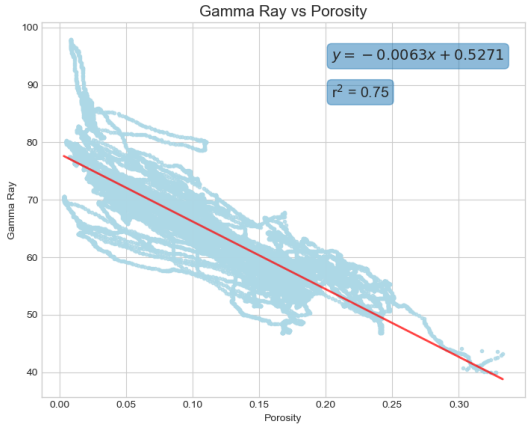

(a) Figure 3.21: Relationship between GR vs Porosity showing the trend line, the linear regression equation, and r^2 of its values from the well Ogarrio 1483. The linear regression of the graph is $y = 0.4231x - 0.3507$, and r^2 is 0.75.

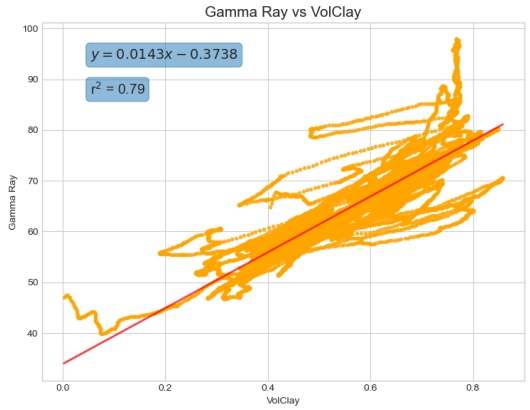

(b) Figure 3.21:Relationship between GR vs VolClay showing the trend line, the linear regression equation, and r^2 of its values from the well Ogarrio 1483. The linear regression of the graph is $y = 0.143x - 0.3738$, and r^2 is 0.79

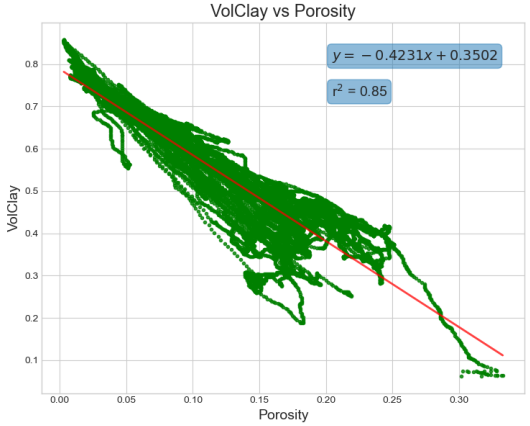

(c) Figure 3.21: Relationship between VolClay vs Porosity showing the trend line, the linear regression equation, and r^2 of its values from the well Ogarrio 1483. The linear regression of the graph is $y = 0.0063x - 0.5271$, and r^2 is 0.85.

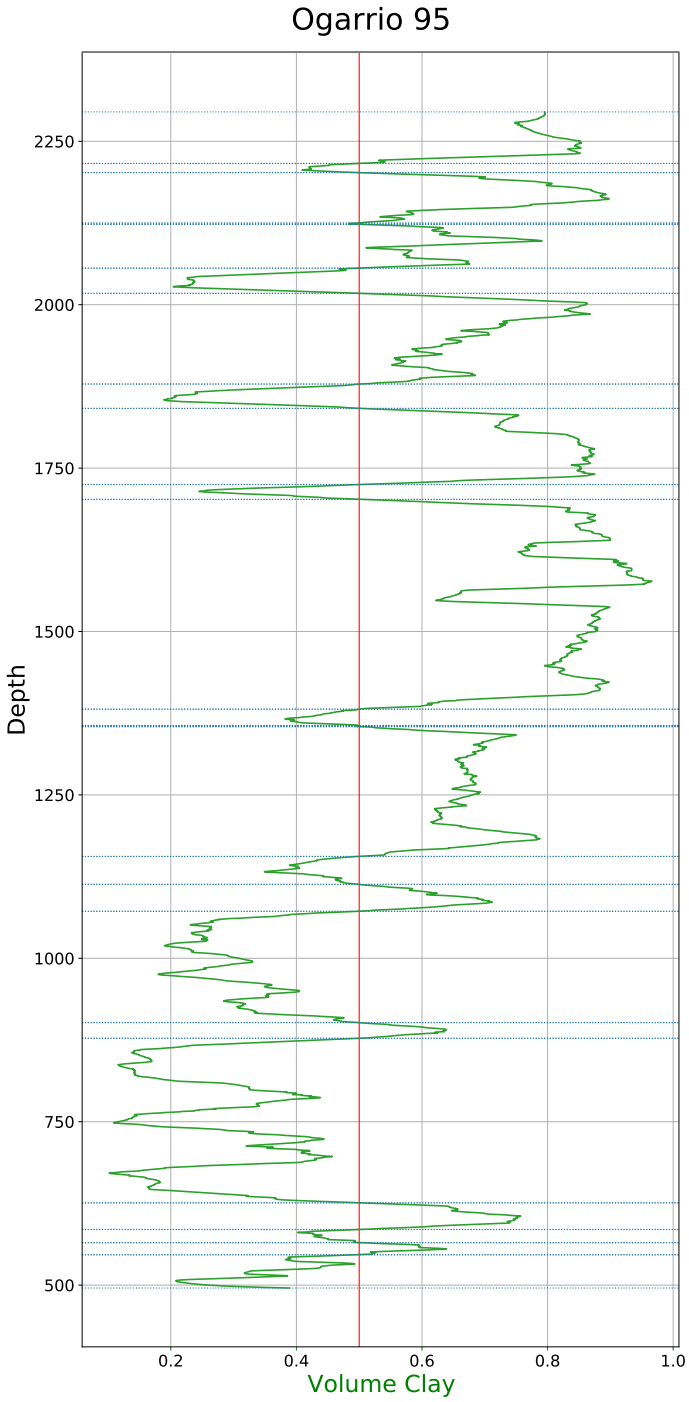

Figure 3.22: Depth versus VolClay from the well Ogarrio 95. Red line represents the change in lithology.

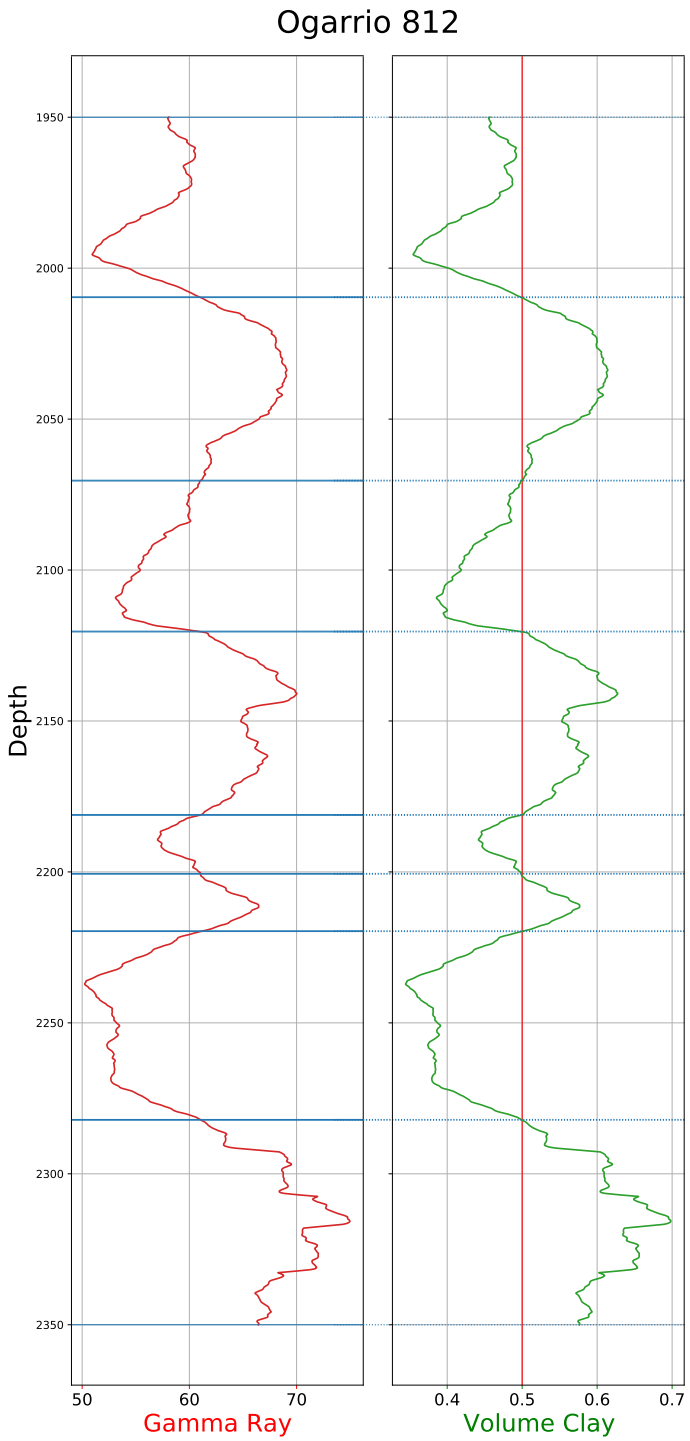

Figure 3.23: Depth versus GR and VolClay from the well Ogarrio 812.

Formation	**Upper Concepcion**		**Lower Concepcion**		**Encanto**	
Lithology	**Shale**	**Sandstone**	**Shale**	**Sandstone**	**Shale**	**Sandstone**
Porosity	0.14	0.14	0.22	0.22	0.14	0.14
Percentage	61.92	40.79	69.99	32.14	65.85	41.9
Volume Clay	0.5	0.49	0.49	0.5	0.49	0.48
NTG		0.4		0.34		0.35
NTG STD		0.28		0.25		0.24

Table 3.6: Average final values of sixty wells analysed. Note that *percentage* refers to the average proportion of shale and sandstone from the wells, and *NTG STD* is the standard deviation of the Net-to-gross ratio in each formation.

It is worth mentioning that these values are only estimates of the actual petrophysics of the rocks in the study area due to most of the available well data from CNH being incomplete and inconsistent because many wells were drilled, analysed and abandoned between the years 1950 and 1980. Linear regressions offer an approximate 80 per cent prediction in GR, VolClay and porosity values, while around 20 % is unknown. Although 20 per cent is a relatively small uncertainty, most wells lack data, increasing possible errors. For instance, only eleven wells were used to calculate the average porosity because even with the regression, many values were not consistent with the porosity range (10% to 25%) of the wells that included porosity in their records. Using them would have affected the final calculations. On the other hand, the GR and VolClay values are within the range of the wells that included these parameters in their records, 35 to 120 API and 0.001 to 0.8, respectively, which gives us confidence in their overall values.

3.7 CO_2 Capacity Assessment

The previous sections provide estimates for three parameters in Equation 3.1: the storage area, thickness, and porosity. The water saturation was taken from the calculations made by Rodriguez Moreno (2020) and Jimenez et al. (2011), where they determined that the average S_w is 20% in the target formations. Next, we can estimate the CO_2 density.

Moreover, at depths greater than 800 m, CO_2 exists as a supercritical fluid with densities of between 300 to 800 kg/m^3 (Chadwick et al., 2008). The density of CO_2 depends on various factors, and it will increase as a function of depth. Iglauer (2018) analysed deep saline aquifers conditions with highly purified CO_2, with a 10 MPa/km hydrostatic gradient and a geothermal gradient of 30 k/km. Figure 3.24 shows the resulting CO_2 density values at specific depths. Kopp et al. (2009) determined that a Median reservoir, which has median parameters for porosity (20%), permeability (123 mD), geothermal gradient (0.03 C/m), depth (1524 m) and salinity (0.048 kg/kg) will be likely to have an average CO_2 density of 660 kg/m^3. The Ogarrio field meets these characteristics, meaning that the CO_2 density at a depth of the target formations will be in the range of 600 to 700 kg/m^3.

With the values described above, the estimation of the mass of CO_2 that can be stored

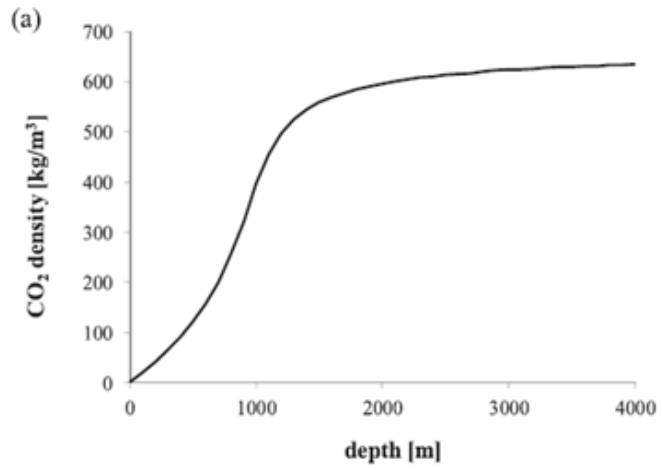

Figure 3.24: CO_2 density against depth according to the analysis carried out by Iglauer (2018).

in the Ogarrio field in each target formation was obtained, as listed in Table 3.7. The Lower Concepcion has the lowest estimated capacity, while Encanto appears to have a considerable storage capacity. This is primarily a factor of the higher thickness of the Encanto Formation and the higher proportion of sandstone (NTG) within this formation. NTG values and thicknesses of the sandstone in each layer are included in Appendix A.

Formation	$\rho(CO_2)$ (kg/m^3)	Area (m^2)	Thickness (m)	Porosity	S_w(%)	MCO_2 (Mt)
Upper Concepcion	600	29,600,000	18.69	0.14	0.20	37
Lower Concepcion	620	28,300,000	17.71	0.22	0.20	55
Encanto	660	27,700,000	306.59	0.14	0.20	628

Table 3.7: Properties and potential storage capacity of the Upper Concepcion, Lower Concepcion and Encanto formations.

The final storage capacity estimate must be modulated by a Storage Efficiency Factor (SER), as shown in Equation 3.1. This factor describes the proportion of the available pore space that is filled with CO_2. This cannot be accurately constrained for a static capacity estimate, but values ranging between 0.1% as the minimum, and 6% as the maximum, are typically assumed (Bentham et al., 2014; Gammer et al., 2011).

3.7.1 Comparison with Hydrocarbon production volume

It is assumed that the volume of oil and gas produced in the reservoirs can be occupied by CO_2 (CSLF, 2008). Agartan et al. (2018) in the Gulf of Mexico proved this. They simulated CO_2 storage volumes based on the capacity of the depleted oil and gas fields in the area and their storage efficiency based on the hydrocarbon recovery factor. Furthermore, Winter and Bergman (1993) estimated the capacity of nonproductive hydrocarbon reservoirs to store CO_2 in the United States, and van der Meer and Yavuz (2009) calculated the storage

efficiency factor in the Netherlands based on the space used by the oil and gas and the total available pore space.

Therefore, the estimated CO_2 capacities can be compared against the hydrocarbon production volumes from the Ogarrio field, as this can provide a reasonable constraint on the volumes of fluid that could be removed from, or injected into, the formations in question.

It is important to convert the produced oil and gas volumes to underground volumes at standard pressure and temperature reservoir conditions (Goodman et al., 2011) due to CO_2 is assumed to be stored in its supercritical phase at the standard reservoir conditions (NETL DOE, 2019).

The cumulative production from the Ogarrio field is around 218 million barrels of oil and 405 billion cubic feet (cf) of gas. I have used these production values to estimate the total volumes of fluids that have been removed from the Ogarrio field. Firstly, for the oil, 218 million barrels are converted to 34,000,000 m^3. The gas volumes are computed at standard conditions, which must be converted to reservoir volumes. 405 billion cf corresponds to 11,000,000,000 m^3 at standard conditions. Assuming a density at standard conditions of 0.7 kg/m^3, this is 7,700,000,000 kg of gas. If we assume a gas density in the reservoir of 200 kg/m^3, the mass of gas will occupy 38,500,000 m^3 within the reservoir.

Combining the total volumes of oil and gas produced from the reservoir is 34,000,000 m^3+ 38,500,000 m^3= 74,500,000 m^3. This value can be compared with the pore volume of each formation, given by:

$$PV = A \times T_f \times \phi \quad . \tag{3.3}$$

We have all of these values from the previous analysis, and the resulting pore volumes are listed in Table 3.8.

Formation	Pore Volume (m^3)
Upper Concepcion (UC)	77,500,000
Lower Concepcion (LC)	110,300,000
Encanto (En)	1,190,000,000
Total pore volume	1,370,000,000
Volume of HC removed	74,500,000

Table 3.8: Total pore volumes of each formation and total volume of hydrocarbons removed.

The SER is obtained as a function of these volumes (Pickup, 2013):

$$SER = \frac{\text{Volume of hydrocarbons removed}}{\text{Total pore volume}} \tag{3.4}$$

Therefore, if we divide the volume of hydrocarbons removed by the total estimated pore volume, we obtain a value of just under 5%. As well as providing a reasonable reality-check in terms of our estimated pore volumes, this production efficiency can be used as a reasonable estimate for the Storage Efficiency Factor. I note that this value of 5 % is within

the range of values used by Bentham et al. (2014); Gammer et al. (2011). The estimated storage volumes with this SER factor applied are listed in Table 3.9.

Formation	Storage Volume (m^3)
Upper Concepcion	3,800,000
Lower Concepcion	5,500,000
Encanto	59,400,000
Total storage volume	69,000,000

Table 3.9: Estimated storage volumes considering a 5% storage efficiency factor using the area of the main formations.

This storage efficiency factor can be implemented in Equation 3.1 to estimate the mass of CO_2 that could be stored at the Ogarrio Field. The resulting values are listed in Table 3.10.

Formation	Storage Volume(m^3)	S_w(%)	$\rho(CO_2)$ kg/m^3	MCO_2 (Mt)
Upper Concepcion	5,100,000	0.20	600	1.9
Lower Concepcion	4,700,000	0.20	620	2.7
Encanto	69,000,000	0.20	660	31.4
Total pore volume	79,000,000	0.20	600	36

Table 3.10: Potential storage capacity of the Upper Concepcion, Lower Concepcion and Encanto formations using a storage efficiency of 5%. Note that the 600 kg/m^3 used in the total pore volume is the CO_2 density at reservoir conditions.

Additionally, not all the pore space occupied by oil and gas could be filled with CO_2, as some residual water can remain confined in the pore space because of gravity or capillarity. Also, the original reservoir pressure can change when the reservoir is depleted, affecting the CO_2 storage capacity (CSLF, 2008). Due to this, it is crucial to analyse the actual reservoir conditions before implementing a project like this in the Ogarrio area to reduce uncertainties. The values presented here are a proposal of the potential amount of CO_2 and SER that the study area can have.

3.8 Uncertainty Analysis

The values listed in Table 3.10 are an approximation based on the best estimates of reservoir properties. It is essential to delimit the lower and upper storage values as affected by the variability of the different parameters that make up Equation 3.1.

The calculation for the upper bound for storage capacity is shown in Equation 3.5:

$$MCO_2 \uparrow = r(CO_2) \times A_{max} \times [T_f \times (NTG + \sigma NTG)] \times (\phi + \sigma\phi) \times (1 - S_w) \times SER_{max} \quad , \quad (3.5)$$

where A_{max} represents the uppermost estimate for the storage structure area from our structural interpolations described above. The maximum area was obtained from the interpolations of Section 3.5.3 by using the lowest possible spill point in the structural

traps. The standard deviations of the net-to-gross ratio and the sandstone porosity obtained from my well log analysis are represented by σ NTG and $\sigma\phi$. SER_{max} is the maximum storage efficiency (6%) used by Bentham et al. (2014).

Similarly, the lower bound is obtained from Equation 3.6:

$$MCO_2 \downarrow = r(CO_2) \times A_{min} \times [T_f \times (NTG - \sigma NTG)] \times (\phi - \sigma\phi) \times (1 - S_w) \times SER_{min} \quad , \quad (3.6)$$

where A_{min} is the minimum reservoir area, and SER_{min} is the smallest storage efficiency factor (1%) used by Bentham et al. (2014).

The resulting upper and lower bounds for storage capacity are shown in Table 3.11.

Formation	Upper Concepcion	Lower Concepcion	Encanto
A_{max} (m^3)	38,100,000	36,900,000	34,500,000
T_R (m)	183.13	225.86	914.47
NTG	0.41	0.35	0.36
σNTG	0.28	0.25	0.24
ϕ	0.14	0.22	0.14
$\sigma\phi$	0.006	0.008	0.036
S_w (%)	0.20	0.20	0.20
ρCO_2 (kg/m^3)	600	620	660
SER_{max} (6%)	0.06	0.06	0.06
A_{min} (m^3)	21,100,000	19,600,000	20,800,000
SER_{min} (1%)	0.01	0.01	0.01
MCO_2 (Mt)↑	25	42	131
MCO_2(Mt)↓	0.4	0.58	1.5

Table 3.11: Summary of parameters and derived values for this chapter, as well as the maximum (red) and minimum (blue) limits of the potential storage capacity in each layer.

These bounds highlight the significant uncertainties that are inherent to a priori estimates of CO_2 storage capacity. The upper and lower bounds represent potentially more than an order of magnitude difference in the storage capacity, a 50-times difference in the computed storage. This highlights the need for improved subsurface characterisation at an early stage of any future project development.

3.8.1 Monte Carlo Analysis

A Monte Carlo analysis is another method of quantifying the general uncertainties in storage capacity. A Monte Carlo simulation predicts the results of the probabilistic approximation of a problem using statistical random sample approaches (Bai, 2014).

First, we define the parameters, ranges, standard deviations, and means of the distributions of the areas, thicknesses, porosities, S_w, and SER of the potential storage sites in the three target formations. We applied a Monte Carlo analysis for each parameter. Since the density of CO_2 is well established, we did not perform a Monte Carlo analysis for this parameter. The area, S_w, and SER ranges were defined by the difference between the

maximum and minimum values. The outcome distributions were determined by the means added by the standard deviation times the normal distribution. Finally, all distributions were multiplied to obtain probability distributions for storage capacity.

The simulation was run for one million iterations; Figures 3.25 and 3.26 show the distributions of the input parameters, and Figure 3.27 depicts the output distributions of the mass of CO_2 (MCO_2) that can be stored.

Figure 3.28 shows the percentage of cases against MCO_2 that could be stored.

As observed in Table 3.12, in 95% of the cases, the amount of CO_2 stored is very low, and in 5% of the cases, the values of MCO_2 increase considerably. Although, due to the characteristics of the formations, these values represent a highly improbable scenario, they cannot be ruled out. The MCO_2 values in 50% of the cases seem to be the most likely scenario; moreover, they are not very different from the values obtained in previous calculations; see Table 3.10.

% of cases	MCO_2 Mt Stored		
	Upper Concepcion	Lower Concepcion	Encanto
5	7.5	16	98
50	2.1	3.2	21.5
95	0.1	0.1	1.2

Table 3.12: Variation of the amount of CO_2 that could be stored in each formation in relation to the percentage of cases.

I calculated the percentiles P05, P50, and P95 of the potential amount of CO_2; these percentiles represent the minimum, median, and maximum values, respectively, that each storage site can store. The maximum values are those that will be exceeded with a confidence of 95%, the median values are the most likely, and the minimum values will be exceeded with a confidence of 5%.

As shown in Table 3.13, the results have significant variations, mainly in thickness and storage capacity. For instance, the difference between P50 and P95 in Encanto is greater than 200 Mt. For Lower Concepcion, the difference is around 27 Mt, and for Upper Concepcion, it is approximately 14 Mt. Ergo, the P50 values, 3.4 Mt in Upper Concepcion, 6.4 Mt in Lower Concepcion, and 32.3 Mt in Encanto, are the most likely storage capacity.

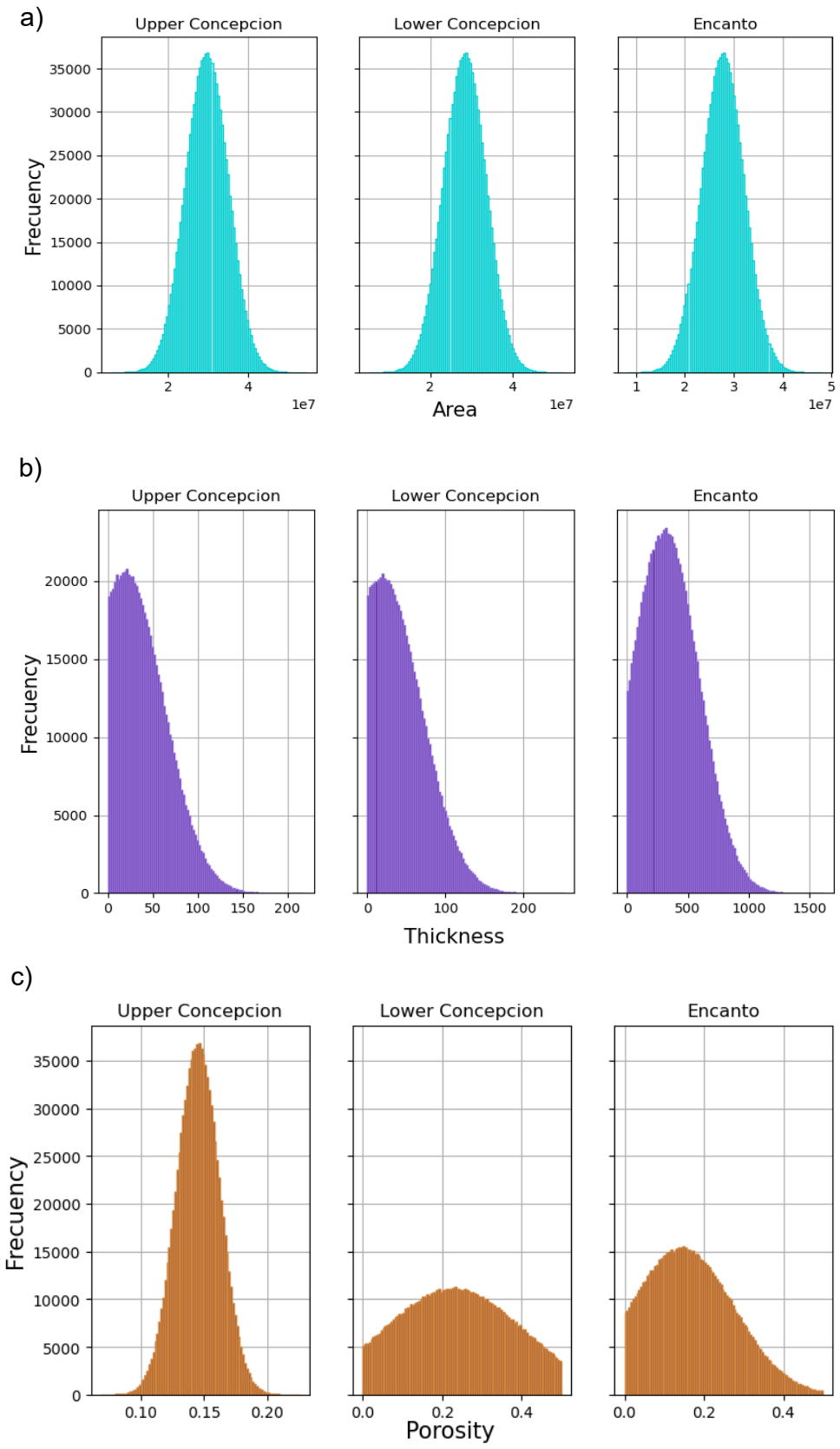

Figure 3.25: Distributions of the a) areas, b) thicknesses, and c) porosities of the potential storage sites.

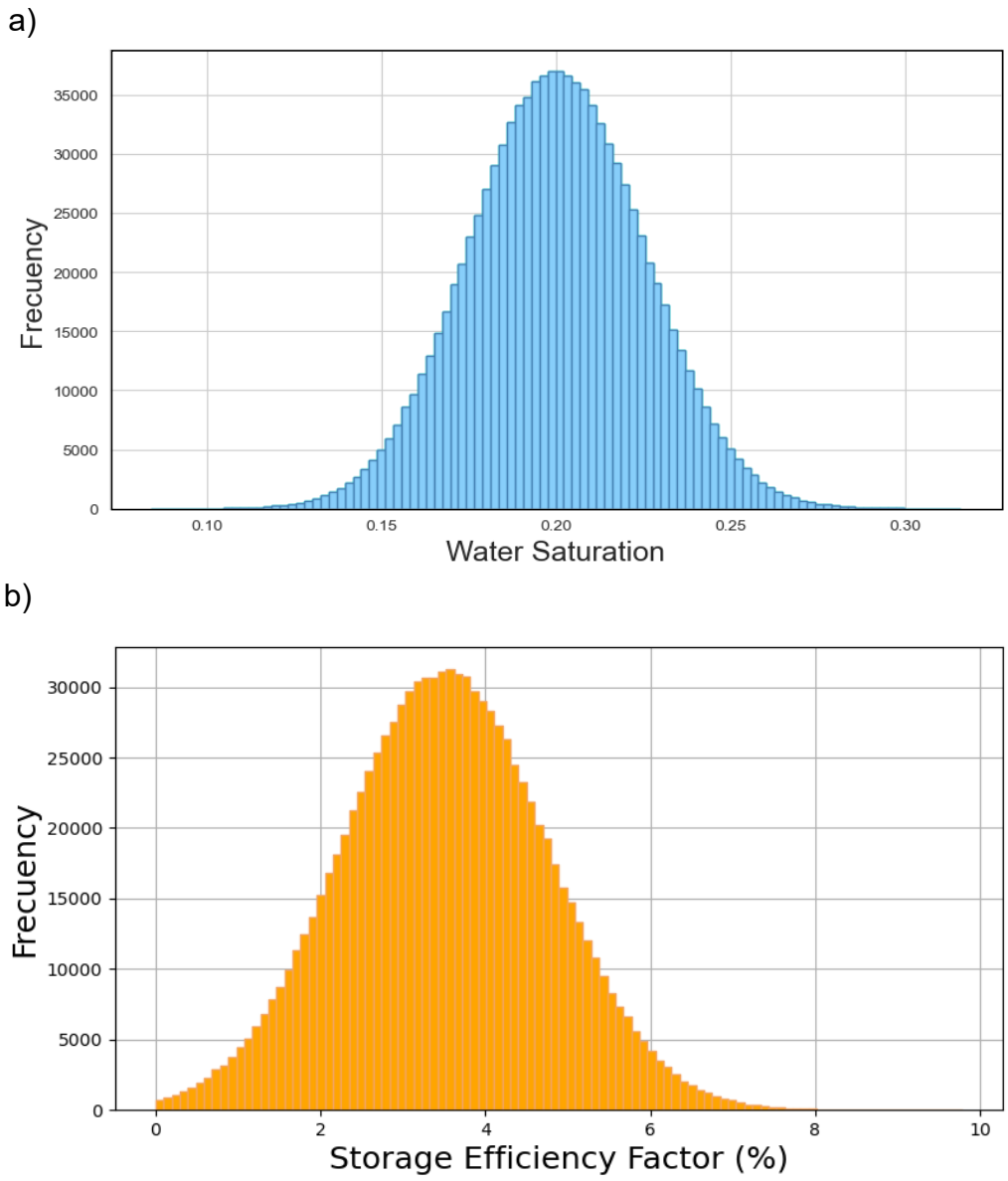

Figure 3.26: Distributions of the a) water saturation (S_w) and b) Storage Efficiency Factor (SER) in the potential storage sites.

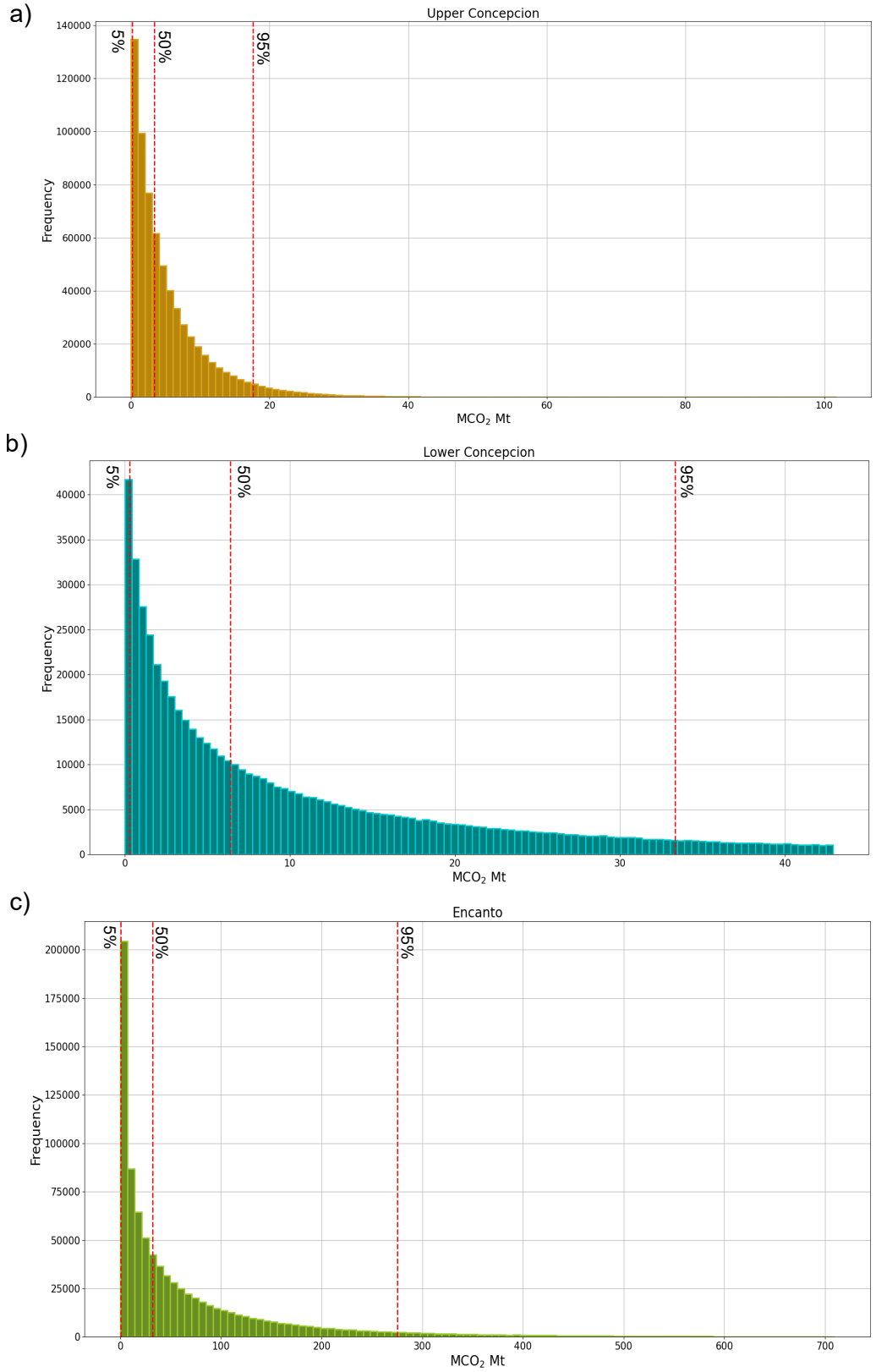

Figure 3.27: Distributions of the MCO_2 Mt that can be store in a) Upper Concepcion, b) Lower Concepcion, and c) Encanto. The red vertical lines show the percentiles P05, P50, and P95.

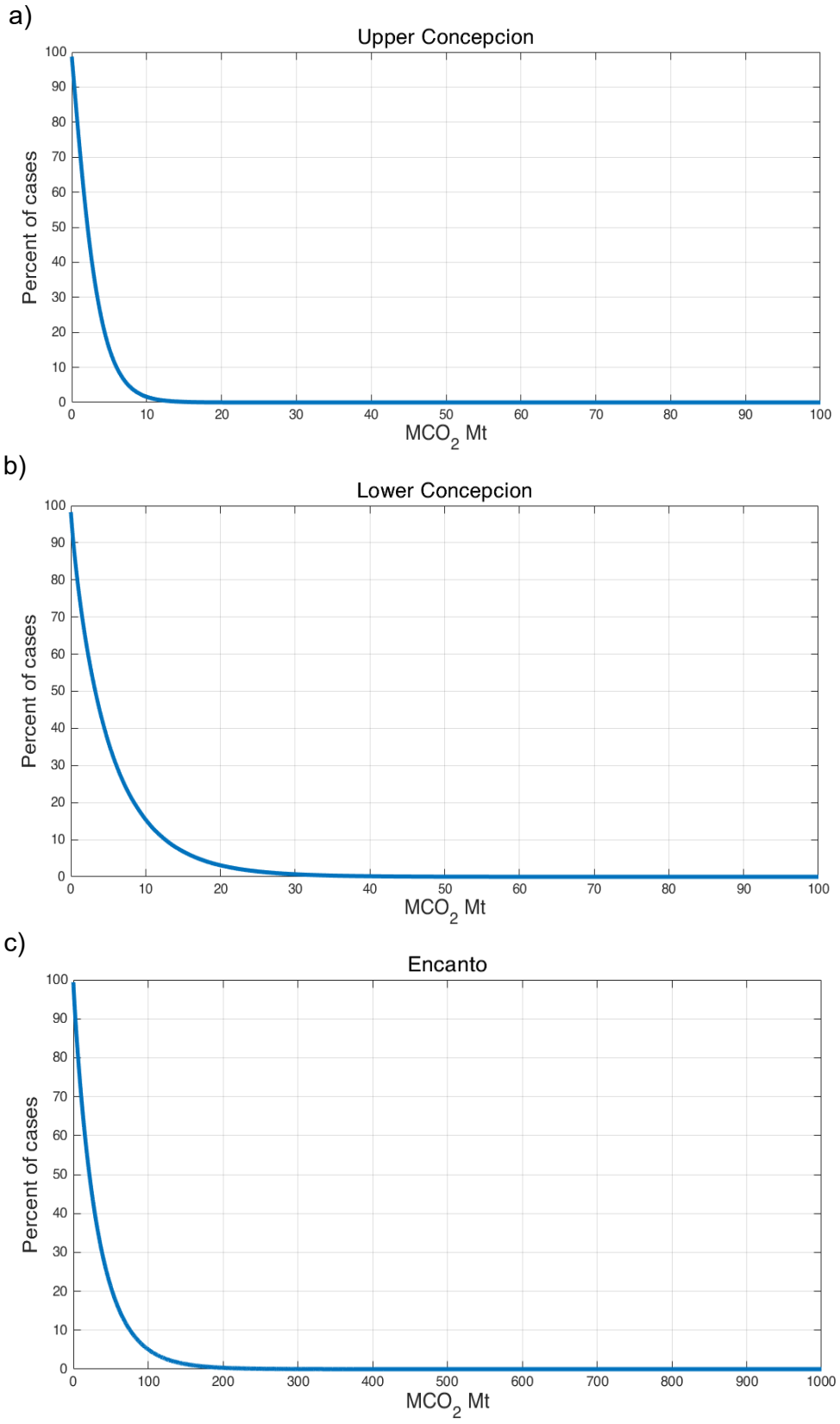

Figure 3.28: Percentage of cases versus the amount of CO_2 that can be stored in the three target formations.

		P05	**P50**	**P95**
	ρCO_2 (kg/m^3)	600	620	660
	SER (%)	1.44	3.5	5.55
	Sw (%)	0.15	0.2	0.24
Upper Concepcion	Area (m^2)	20,800,000	29,600,000	38,400,000
	Thickness (m)	3.83	36.79	94.44
	Porosity (ϕ)	0.11	0.14	0.017
	MCO_2 (Mt)	**0.2**	**3.4**	**17.6**
Lower Concepcion	Area (m^2)	19,700,000	28,300,000	36,800,000
	Thickness (m)	4.17	41.1	109.84
	Porosity (ϕ)	0.03	0.23	0.45
	MCO_2 (Mt)	**0.3**	**6.4**	**33.2**
Encanto	Area (m^2)	20,500,000	27,700,000	34,800,000
	Thickness (m)	50.38	354.04	782.74
	Porosity (ϕ)	0.02	0.16	0.36
	MCO_2 (Mt)	**0.4**	**32.3**	**275**

Table 3.13: Monte Carlo results for potential water saturation, storage efficiency factors, areas, thicknesses, porosities, and amounts of CO_2 that can be stored in each formation. P05 or 5%, P50 or 50%, and P95 or 95% represent the probability of occurrence of the calculated MCO_2 values. Note that only positive values were taken into account.

3.8.2 Risk from abandoned wells

The presence of many wells provides an advantage in terms of data available for geological characterisation. Nonetheless, they also present potential CO_2 leakage pathways.

The anticline area has around 716 wells, and the potential structural traps have approximately 360 wells (CNH, 2022), most of them are abandoned or closed. Therefore in case of leaking, it is crucial to estimate the leakage rates to assess the potential risks.

Alcalde et al. (2018) and Bai (2014) estimated overall leakage rates of the wells according to their integrity and cementation condition. Considering these potential rates and the number of wells in the area, it is possible to calculate prospective leakage rates, see Table 3.14.

	Well cement condition		
	Degraded/fractured	Bad/ high leakage rate	Intact/low leakage rate
Alcalde et al. (2018)	**300 (t year^{-1})**	**230 (t year^{-1})**	**0.0004 (t year^{-1})**
Leakage rate 360 wells	108000	82800	1.44
Leakage rate 716 wells	214800	164680	2.86
Bai (2014)	**1 (kg/day)**	**0.01 (kg/day)**	-
Leakage rate for 360 wells	360	3.6	-
Leakage rate 716 wells	716	7.16	-

Table 3.14: Potential leakage rates of the wells located within the anticline (716 wells) and injection (360 wells) areas.

Moreover, Tables 3.15 and 3.16 show the percentage of the leakage rates in relation to the previously estimated minimum, total, and maximum storage capacities previously estimated.

		CO_2 storage capacity		
	Alcalde et al. (2018)	**0.4 Mt**	**36 Mt**	**131 Mt**
Well condition	**360 wells**	**CO_2 leaked per year (%)**		
Degraded/fractured	108000 t	27	0.3	0.08
Bad/ high leakage rate	82800 t	20.7	0.22	0.06
Intact/low leakage rate	1.44 t	0.0004	0.000004	0.000001
	716 wells	**CO_2 leaked per year (%)**		
Degraded/fractured	214800 t	53.7	0.6	0.16
Bad/ high leakage rate	164680 t	41.17	0.46	0.13
Intact/low leakage rate	2.86 t	0.00072	0.000008	0.000002

Table 3.15: Potential leakage rate percentages of per year of the estimated CO_2 storage capacity in the study area based on Alcalde et al. (2018) leakage rates.

		CO_2 storage capacity		
	Bai (2014)	**0.4 Mt**	**36 Mt**	**131 Mt**
Well condition	**360 wells**	**CO_2 leaked per day(%)**		
Degraded/fractured	360 kg/day	0.008	0.00036	0.0001
Bad/ high leakage rate	3.6 kg/day	0.00008	0.0000037	0.000001
	716 wells	**CO_2 leaked per day(%)**		
Degraded/fractured	716 kg/day	0.016	0.0007	0.0001
Bad/ high leakage rate	7.16 kg/day	0.00016	0.0000073	0.000002

Table 3.16: Potential leakage rate percentages of per day of the estimated CO_2 storage capacity in the study area based on Bai (2014) leakage rates.

Using Alcalde et al. (2018) rates, the highest leak rate per year is 53.7%; this is considered the worst-case scenario where there is a low storage capacity (0.4 Mt) and all wells are in degraded conditions; however, it is improbable to happen. The values of the total storage capacity (36 Mt) under degraded conditions and high leakage rate are greater than 0.1%. In the maximum storage capacity (131 Mt), the rates are lower than or in the range of 0.1%. In intact conditions, the rates are also below 0.1%, which is the acceptable rate caused by the leakage of abandoned wells. Based on Bai (2014) all leakage rates are below 0.01 kg/day, which means that the risk is in acceptable values.

It should be noted that these values are only a potential evaluation of the risk of leakage from abandoned wells in the area. When implementing a CO_2 injection project, it will be essential to conduct a review of the integrity of each of these wells before and during the injection. Also, they will likely need CO_2 monitors close by to check for CO_2 leakage. However, an assessment of well integrity is beyond the scope of this thesis.

3.9 Discussion

In this chapter, we intended to produce an extensive analysis of the seismic and well log data available in one of the main onshore fields of the Sureste Basin that can be applied to more fields with sufficient data.

The methodology developed in this chapter focused only on the Ogarrio field because, given the historical development of oil and gas in the area, a large amount of geophysical data was available compared to the other fields. However, most of the data acquired and used in this project from the CNH were of varying vintage and quality. Furthermore, this field has previously been considered for CCS (Romero and Bashbush, 2017; Jimenez et al., 2011; Rodriguez Moreno, 2020; Sanchez, 2018).

The data displayed demonstrate the characteristics and properties of the subsurface of the Ogarrio field. The data clearly show that the identified formations are suitable for CO_2 injection and that trapping structures are present to prevent CO_2 migration. Nevertheless, our assessment of uncertainties and a Monte Carlo analysis show that despite detailed analysis, order-of-magnitude scale uncertainties exist in potential storage volumes. This highlights a major challenge in the precise estimation of storage capacities prior to developing specific sites. That said, our estimated pore volumes are consistent with the volumes of hydrocarbons produced in the field, suggesting that our best-estimated storage values are a reasonable basis for future plans and developments at the site.

According to Jimenez et al. (2011) and the Geological CO_2 Storage Atlas of Mexico, the Sureste Basin has a theoretical storage potential of 24 gigatonnes (Gt) of CO_2 (SENER, 2012). The study of Jimenez et al. is at a basin-scale and does not identify the storage capacities of specific fields as they selected sectors that do not follow the shape of the fields or subsurface structures. The value of the porosity and thickness are rather generic than well-based observations. It does not cover the Ogarrio and surrounding areas; it instead selects sectors with potential CO_2 capacity.

In that case, given that the total storage capacity we have estimated for the anticline structure present in the three main formations of the Ogarrio field is 36 Mt, this represents only 0.15% of the basin-wide capacity estimated by Jimenez et al. (2011); SENER (2012). In other words, 600 sites of equivalent capacity to the Ogarrio field may be present in the Sureste Basin.

Furthermore, Rodriguez Moreno (2020) estimated that the potential storage capacity of the Ogarrio field is 61 CO_2 Mt. However, this value is based on data from only four wells and does not consider structural traps. This could be the main reason for the 25 CO_2 Mt storage capacity difference. Nonetheless, both values are within an acceptable range as they do not differ significantly.

Additionally, as we have shown here, the produced hydrocarbon volumes may provide a simple means of identifying the potential storage volume, if we were to assume that for any volume of CO_2, there is a ratio to the existing hydrocarbon production that can be

used as a reference to estimate CO_2 storage volumes in nearby fields, assuming that the wells were or will be abandoned according to the appropriate safety standards.

CHAPTER 4

INDUCED SEISMICITY AND SEISMIC FACTORS

4.1 Introduction

The selection of the CO_2 injection site must be made with more than just storage capacity in mind. The injection of millions of tons of CO_2 could lead to hazards such as leakage and induced seismicity (Verdon, 2014). Many projects around the world have shown the importance of addressing the potential hazard caused by induced earthquakes (Cappa and Rutqvist, 2011; Kaven et al., 2015). Induced earthquakes have occurred in areas where industrial activities such as mining (Bischoff et al., 2010), petroleum and gas production (Van Thienen-Visser and Breunese, 2015), natural gas storage (Walsh and Zoback, 2016), wastewater disposal (Vilarrasa et al., 2021) and geothermal energy extraction (Cladouhos et al., 2010) have taken place.

Induced seismicity occurs where human activities alter the subsurface causing earthquakes and releasing tectonic stress. One of the biggest concerns about the induced seismicity is the shaking experienced at the ground surface and the resulting damage to buildings and other infrastructure. In some cases, induced seismicity has even caused fatalities (Foulger et al., 2018). Also, another concern for situations where fluid injection is involved is that small to moderate earthquakes could create a permeable hydraulic pathway that can affect the seal integrity of the storage formation.

A fault will remain quiescent so long as the applied shear stress is less than the strength of the contact, which in turn is controlled by the effective normal stress (Ellsworth, 2013). CO_2 injection can cause earthquakes, as injection creates changes in the effective stress, and in particular, reduces the effective normal stress on geological faults (Mission Innovation, 2017) leading to fault slip. Since both the size of the perturbation and the volume of rock affected will scale with injection volume, this issue will be of greater concern as projects scale up the amount of CO_2 injected into the subsurface.

There are faults whose orientation within the in situ stress field results in a state of incipient failure, such that induced earthquakes are likely to happen with a slight increase in fluid pressure. These faults are known as critically stressed. These conditions will be dependent on the stress conditions at the depth where the earthquake is generated. The shear stress levels in many regions are commonly found to be close to the strength limit of the Earth's crust (Mission Innovation, 2017). The size of the fault and the amount of fault slip is proportional to the magnitude of an earthquake that can occur, see Figure 4.1 (Zoback and Gorelick, 2012).

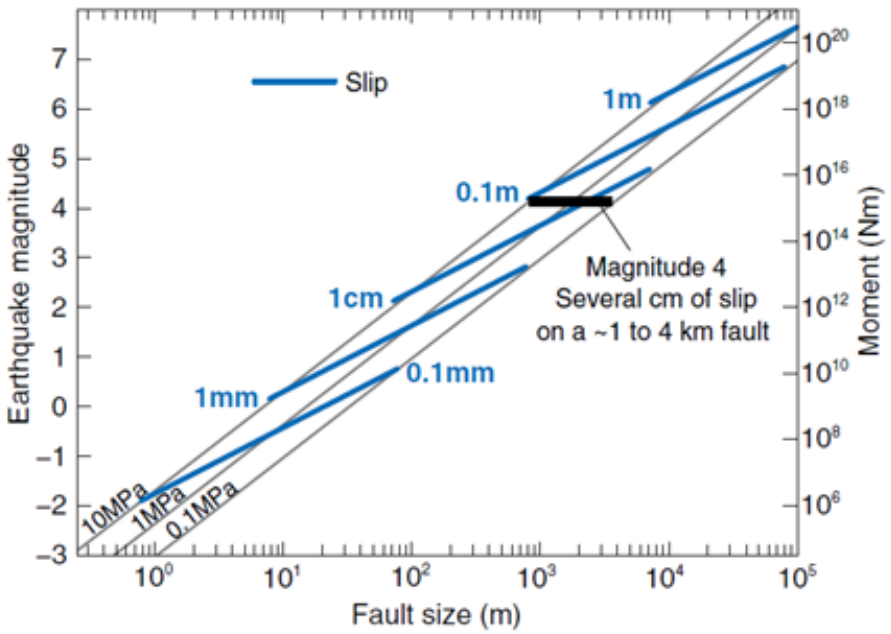

Figure 4.1: Relationship between fault size and earthquake magnitude, the earthquake stress drops range between 0.1 and 10 MPa. From Zoback and Gorelick (2012).

As CCS projects increase in scale, interference among neighbouring CCS projects may occur, producing pressurization and pore pressure changes that extend from 10s to 100s of kilometres from injection wells (Zoback and Gorelick, 2012). If critically stressed faults are found within this area, then induced seismicity may occur. Similar effects have been observed during large-scale wastewater disposal in Oklahoma (Ellsworth, 2013).

This Chapter is divided into two sections. In the first part, I analyse the Sureste Basin to identify tectonic faults and assess whether they are likely to slip or create earthquakes due to CCS operations. In the second half of this chapter, I assess the potential seismic hazard that might be produced by CCS induced seismicity compared to the natural seismic hazard in the region and make recommendations for seismicity monitoring in future CCS projects.

4.2 Objectives

- To analyse the slip tendency and stability of the faults within the Sureste Basin.
- To define acceptable levels of seismic hazard due to CO_2 injection in the area through the peak ground acceleration.
- To obtain the seismic moment release and the largest event based on the pore volumes and different Seismic Efficiency Factors (S_{eff}).
- To establish a Traffic Light System to mitigate the induced seismicity in this proposed project.

4.3 Occurrence of Induced Seismicity associated with large-scale fluid injection

To date, a handful of CCS projects are operational around the world. Some of these have already experienced induced seismicity and are described in the following sections.

4.3.1 CCS and Induced Seismicity

4.3.1.1 Decatur

At the Decatur site, in Illinois, United States, about a million metric tons of supercritical CO_2 was injected into a stable and extensive saline formation at about 2.1 km depth (Kaven et al., 2015). As a result, more than 10,000 seismic events were detected in 2013. The event magnitudes ranged from M_w -1 to M_w 2.

Events were located in three clusters. The first was active since the start of injection, the second was active during a few weeks with minimum activity, and the third one became active a year after the start of the injection (Kaven et al., 2015). These three clusters follow a pattern that may indicate an inhomogeneous permeability structure. A triggering mechanism was identified, showing a hydraulic junction between reservoir and basement, with basement faults cutting into the reservoir, resulting in the activation of pre-existing faults within the crystalline basement (Kaven et al., 2015; Mission Innovation, 2017).

4.3.1.2 In Salah

The In Salah CCS project, Algeria, was an onshore industrial-scale CO_2 storage project. It began operations in 2004, and about 4 Mt of CO_2 were injected over ten years (Stork et al., 2015). The CO_2 was injected into a thin Carboniferous low permeability sandstone at about 1.8 – 1.9 km depth (Rutqvist, 2012).

Stork et al. (2015) detected over 9,000 seismic events over a 1-year monitoring period towards the end of the injection. The maximum magnitude was M_w 1.7. Stork et al. (2015) concluded that a deep fracture zone was activated because of the injection and increased

pore pressure. This fracture zone extended more than 100 meters wide and above the reservoir top. InSAR also detected the deformation associated with this zone.

4.3.1.3 Weyburn

Weyburn is an Enhanced Oil Recovery (EOR) project in Canada. It was a pioneer project in the use of microseismic monitoring using downhole instruments. It has a net storage of 2.7 CO_2 megatonnes per year (Mtpa). Between 2003 - 2010, around 200 microseismic events were detected, ranging between M_w -3.5 to M_w -0.5 over eight years. Verdon et al. (2016) observed that the seismicity was located near the production wells, indicating a complex geomechanical interplay between injectors and producers.

In contrast to these projects, in the Norwegian North Sea, there are two examples of projects that have been operating without any significant seismicity over 20 years.

4.3.1.4 Sleipner and Snøhvit

The offshore gas field Sleipner started in 1996; since then, it has stored more than 17 megatonnes (Mt) of CO_2. The injection formation is the Utsira Sandstone, which is composed of high porosity sand with interbedded shale layers, at a depth of 1000 m Ringrose et al. (2018).

Around 5 Mt of CO_2 have been stored in Snøhvit since its inception in 2008. The selected storage formation is Tubåen; it is located 60 m below the Snøhvit gas producing field, and it is anticipated to store 23 Mt of CO_2 (Maldal and Tappel, 2004).

Both projects use seismic reflection monitoring to monitor saturation and pressure variations related to the CO_2 injection, and this methodology has been widely used as a model in other projects. At Sleipner, time-lapse seismic monitoring was implemented to monitor the spreading of CO_2 in the target formation, and this has proven to be an efficient monitoring tool. At Snøhvit, downhole pressure monitoring has been used to understand the pressure distribution (Mission Innovation, 2017).

No induced seismicity has been detected at either of these sites. However, no local seismic monitoring arrays have been used at either site, so it is possible that smaller-magnitude induced events could have been missed.

4.3.2 Analogous activities and induced seismicity

To date, few large-scale CCS projects have been developed. Hence, our learning about the potential for induced seismicity is limited. Further insight can be gained from examining other sites where large-scale fluid injection, albeit not CO_2, has caused induced seismicity.

4.3.2.1 Oklahoma

In Central Oklahoma, thousands of small to medium-sized earthquakes have been triggered by the injection of produced saltwater from oilfields. The most notable earthquakes were at Prague, with magnitude M_w 5.6 in 2011, the M_w 5.1 Fairview earthquake in 2016, and the M_w 5.8 Pawnee earthquake in the same year (Walsh and Zoback, 2016).

The majority of oil wells in Oklahoma extract more water than oil. The produced water is highly saline. Therefore, it is reintroduced underground as part of water flooding activities (Langenbruch and Zoback, 2017). Towards the beginning of 2012, injection rates increased considerably due to the extensive production in fields where the proportions of water production were remarkably higher than the oil production. According to Langenbruch and Zoback (2017), at its peak in 2015, around 1.3 $\times 10^7$ m^3 of saltwater were injected per month, or 1.5 $\times 10^8$ m^3 per year. The saltwater was injected into the Arbuckle Formation, composed of sandstone and limestone, just above the Precambrian basement rocks. By 2016, the injection rates were decreased by 40%, and consequently, the earthquake rates decreased after some months. It is believed that Oklahoma will return to its normal tectonic levels over approximately five years (Langenbruch and Zoback, 2017).

In Oklahoma, the annual injection rate reached 1.5 $\times 10^8$ m^3 per year. If this volume of CO_2 were to be injected, at an average density of 700 kg/m^3 in the reservoir, this would be equivalent to a 100 Mt rate of CO_2 per year. For some countries, these levels of annual CO_2 storage will be required to make a significant impact on emissions. Hence, the example of Oklahoma wastewater disposal provides an instructive case study that can be compared to the potential impacts of large-scale CO_2 storage.

4.3.2.2 Castor

A series of seismic events were generated by subsurface gas storage operations in the Castor field on the eastern coast of Spain. The Castor field was planned to be the most extensive underground storage facility for natural gas in Spain. After the start of gas injection in 2013, many seismic events occurred around the target reservoir, reaching magnitudes of M_w 4. While the project was thought to be in a low-risk seismicity area, there is a system of faults close to the field, and it appears that the gas injection had reactivated them (Ruiz-Barajas et al., 2017). In response to these earthquakes, the Castor project was abandoned at a high cost to the operator.

These examples show that induced seismicity is a crucial issue for large-scale projects and industries. The effects of induced seismicity can impact the infrastructure and facilities of the project itself and affect the nearby population, leading to the loss of public confidence in the technology and the cancellation of projects. Hence, storage sites must be selected carefully and consider the likelihood of induced seismicity for future CCS projects.

4.4 Assessment of Induced Seismicity Hazard in the Sureste Basin

In this section, I examine the structural geology and stress conditions in the Sureste Basin to assess whether CCS in the basin is likely to cause induced seismicity. I examine the slip tendency and critical pore pressures for faults identified in the geological mapping of the basin. I also examine the available 2D reflection seismic profiles in order to identify faults. Finally, I examine the catalogues of past seismicity.

4.4.1 Slip Tendency Analysis

A slip tendency analysis can be used to assess the stress state and potential for fault reactivation in a storage formation. Therefore, it is a crucial factor for the safety assessment of CCS. The analysis helps to visualize and evaluate the stress conditions that could cause slip on individual faults or fault populations. While the injection pressure should not surpass the fracturing pressure of the caprock, slip can still be generated by smaller pressure changes than this level (Kano et al., 2014).

The maximum shear stress on any surface is determined by the orientation of the surface in a stress field (Morris et al., 1996). Slip will take place on the surface when the shear stress (τ) equals or exceeds the frictional resistance to sliding F, and this is proportional to the normal stress (σ_n) on the surface, and the coefficient of static friction (μ) (Morris et al., 1996).

For slip to occur on a cohesionless fault:

$$F = \mu\sigma_n \leq \tau \quad . \tag{4.1}$$

Therefore, the ratio of the shear stress to the normal stress of a surface is the slip tendency (T_s):

$$T_s = \tau/\sigma_n \quad . \tag{4.2}$$

The slip tendency (T_s) depends on the stress tensor and orientation of the surface. It is possible to obtain the values of the normal stress (σ_n), the shear stress magnitude (τ) and the shear stress direction on the surface if the orientations and magnitude of the principal stress are known (Morris et al., 1996).

4.4.2 Critical pore pressure

An alternative method for examining fault stability is the critical pore pressure. The pore pressure P acts to reduce the effective normal stress. Therefore, by computing the shear and normal stress for each fault, the pore pressure increases at which the fault is likely to slip can be calculated. This is called the critical pore pressure, P_c (Wiprut and Zoback, 2000).

For the critical pore pressure:

$$P_c = \tau - \sigma_n \quad . \tag{4.3}$$

The critical pore pressure is the amount of pore pressure increase needed for faults to slip and therefore defines the fault stability. A low P_c implies that a fault is close to slipping and has the potential to host induced seismicity (Wiprut and Zoback, 2000).

4.4.3 Application to Geologically-Mapped Faults in the Sureste Basin

Fault slip analysis is helpful to understand the state of stress in the injection sites relative to the known faults. Mapping these geological faults, computing their slip tendency and critical pore pressure will improve the understanding of whether the CO_2 injection is likely to cause induced seismicity.

A fault stability analysis requires an estimate of the stress field and the positions and orientation of the known faults. I obtained a fault position, sizes, and orientations database from the National Institute of Statistics and Geography (INEGI). Since the fault dips were not specified, I assumed that they are vertical.

I interpolated the regional maximum horizontal stress azimuths from World Stress Map data (Heidbach et al., 2016), using the SHINE project web tool (Carafa et al., 2015). see Figure 4.2. I obtained stress gradients from measurements at the Cantarell Field made by Celis et al. (2006) and applied these across the basin.

The inputs of the faults needed for this analysis are: strike, dip, friction (μ), stress tensor (derived from stress gradient, maximum horizontal stress azimuth, and an assumed fault depth of 2000 m), and fault length, since the earthquake magnitudes are related to the fault size. With this data, I determined P_c using the following approach.

In order to obtain the shear stress (τ) and normal stress (σ_n) vectors acting on a fault plane, the stress tensor was resolved in a defined failure plane by generating the fault normal vector and the traction vector by multiplying the stress tensor with the fault normal vector.

The fault normal vector n, is given by (Worum et al., 2004)

$$i = \sin(az) \times \sin(inc), \tag{4.4a}$$

$$j = \cos(az) \times \sin(inc), \tag{4.4b}$$

$$k = \cos(inc), \tag{4.4c}$$

$$n = [i, j, k], \tag{4.4d}$$

where az is the fault plane azimuth and inc is the dip.

The traction on the fault is

$$t = -(S \times n), \tag{4.5}$$

where S is the stress tensor.

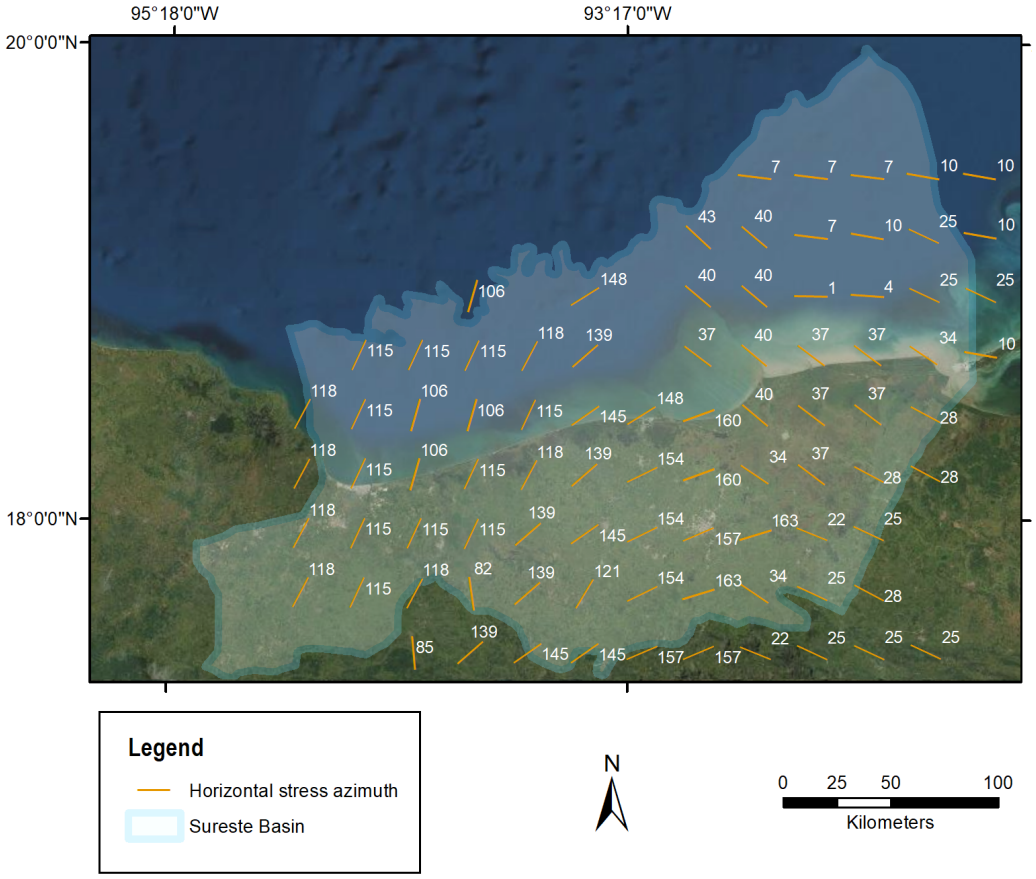

Figure 4.2: Regional maximum horizontal stress azimuths of the Sureste Basin obtained from the World Stress Map (Heidbach et al., 2016).

The normal stress on the fault is

$$\sigma_n = t \cdot n \times n, \tag{4.6}$$

where $t \cdot n$ is the dot product.

The shear stress is given by

$$\tau = -t + t \cdot n \times n \quad . \tag{4.7}$$

Finally, the Critical Pore pressure formula is calculated for each fault

$$P_c = \tau - \sigma_n/\mu \quad . \tag{4.8}$$

I imported the fault positions and their P_c values into an ArcGIS database. The faults, coloured by their P_c values, are shown in Figure 4.3.

Figure 4.4 displays the distribution of the P_c values in the Basin. The histogram shows that most faults are relatively well oriented for failure in the *in situ* stress field. However, the magnitudes of the computed P_c values are very high, with no faults having P_c values

less than 15 MPa. This is a large pressure change, larger than those which have been observed at existing CCS sites such as Sleipner, In Salah and Weyburn (Verdon et al., 2013). This distribution of P_c values is significantly larger than those observed in Oklahoma, where Walsh and Zoback (2016) found typical P_c values of < 5 MPa in regions that had experienced induced seismicity from wastewater disposal.

The P_c values are high because the difference between the maximum stress gradient (SHmax) and the minimum stress gradient (SHmin) is small since SHmax is 25 kPa and SHmin is 20 kPa. In addition, the pore pressure (PP) is relatively low compared to these values, 10 kPa, leading to a high P_c; however, the faults are not close to failure. For instance, Kettlety et al. (2020) analysed the stress acting on the faults in Preston New Road, Lancashire, in the UK, where the area presented induced seismicity due to hydraulic fracturing; the SHmax at this site was 32 kPa, the SHmin was 16 kPa, and the PP was 13 kPa. If we compare the values, on Preston New Road, SHmax was almost twice as much as SHmin, while the stress difference in the basin is 5 kPa, and the PP is higher than the PP in the basin. These high values on Preston New Road resulted in fault failure.

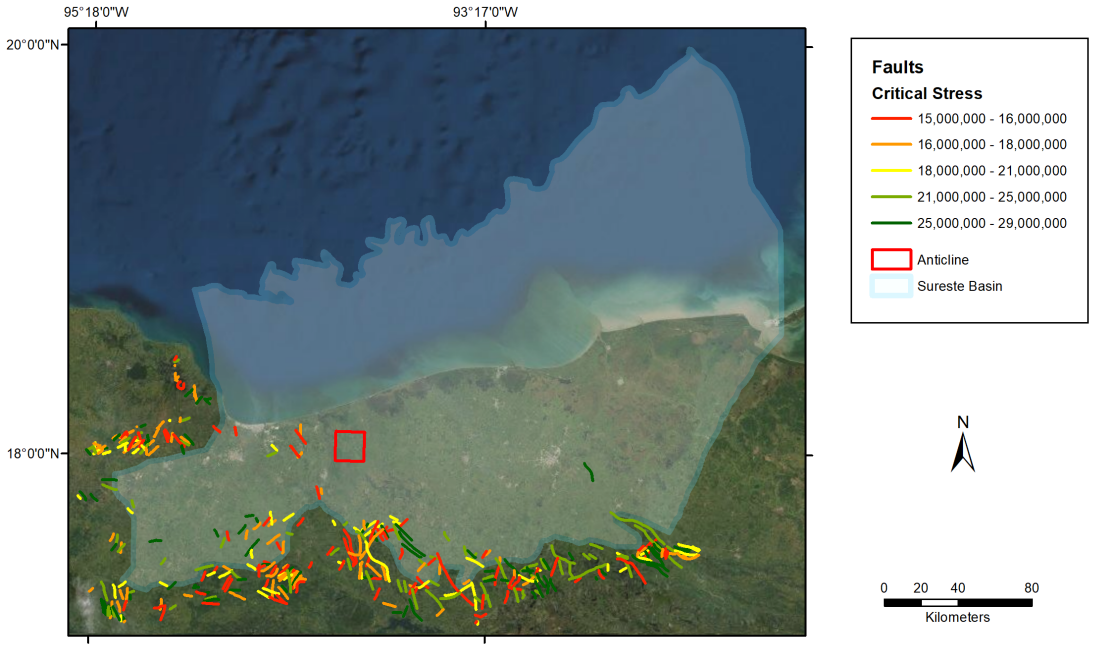

Figure 4.3: Map of faults coloured by their critical pore pressure. The lines are the faults, the red colour represents the low values, which means that these faults are more likely to slip, and the green colour represents the highest values that do not represent a hazard.

Figure 4.5 shows the faults identified around the Ogarrio storage site I studied in Chapter 3. The nearest identified faults are a distance of 20 km from the storage region. Again, the lowest P_c values seen for these faults are > 15 MPa, larger than any expected pressure increase at this distance.

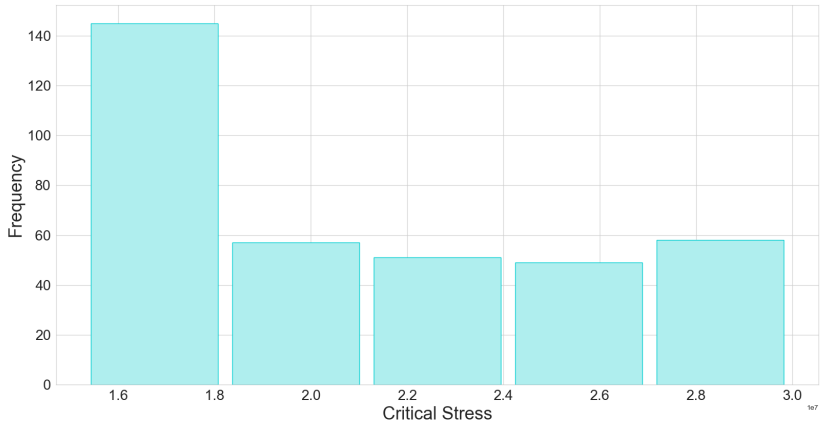

Figure 4.4: Histogram of the P_c values in the Basin.

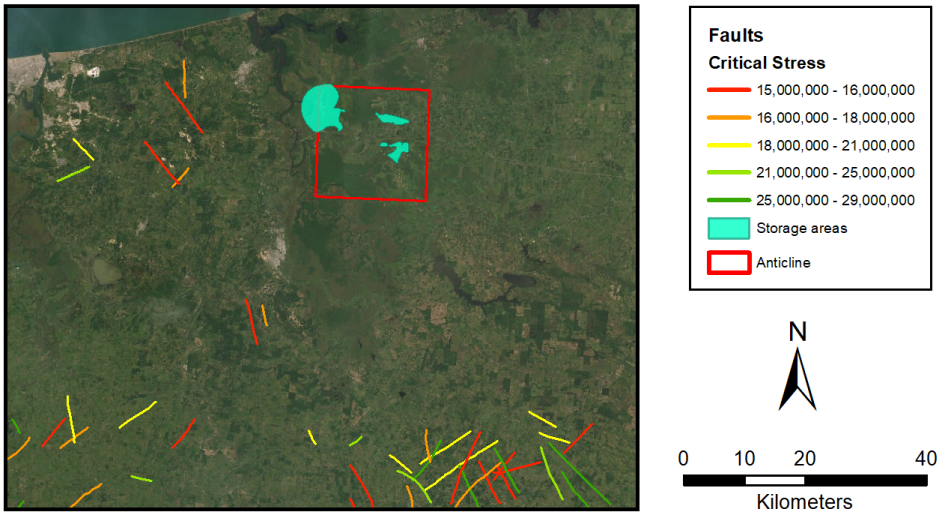

Figure 4.5: Fault analysis in the study area.

4.4.4 The role of basement faults

As described above, Oklahoma is a representative example of the seismicity that high injection volumes can generate. However, there are other cases where the injection volume rates have been high without causing induced seismicity.

Verdon et al. compared Oklahoma with Saskatchewan in Canada, which is another area with high levels of waste disposal activities with no evidence of induced seismicity. The most significant difference between these two projects is that in Saskatchewan, around 1.96×10^9 m^3 of waste disposal was injected in the Mesozoic layer, which has a substantial thickness of rock between it and the basement. In contrast, in Oklahoma, around 1.5×10^8 m^3 of saltwater was injected into the Arbuckle Formation, which extends over the crystalline basement rocks and is hydraulically connected to it.

The proximity of injection to basement rocks has been proposed as a key factor controlling the occurrence of induced seismicity (Schultz and Wang, 2020). The amount of faulting in the basement is usually more significant than in the overlying sediments, and the stresses are usually higher. Hence, if CCS causes pressure changes in the basement rocks, there is a far larger likelihood of causing induced seismicity.

In the Sureste Basin, as can be observed in Figure 4.3, most of the mapped faults are located in the south because these rocks are older than the ones near the coast, and it is where the older basement rocks are exposed. This shows that for the Sureste Basin we observe more faulting in the basement rocks, as is typical. The geological column in Figure 4.6 shows that there are several formations below Encanto and above the basement, mainly composed of shales, such as *Deposito*, *Nanchital*, and *Todos Santos*. There are deposits of anhydrite and salt related to salt migration in the shape of anticlines or domes (Perez Rincón, 1959). Overall, all these layers can have a total thickness of up to 4000 m, while Encanto has an average depth of 1500 m. Thus, there is a considerable thickness of low permeability rocks between the deepest proposed storage formation and the basement. Therefore, based on this analysis and analogous CO_2 injection observations in Saskatchewan, CO_2 injection is unlikely to cause reactivation of basement faults.

4.4.5 Earthquakes in the Sureste Basin

The locations of critically stressed faults can also be inferred from the locations of past earthquakes in the Basin. I obtained the earthquake database for the Sureste Basin from 1959 onwards from the Mexican National Seismology Service (SSN in Spanish) catalogue. I applied a depth cut-off of 30 km to remove seismic events from the underlying subduction slab, which affects the southern part of the country.

The seismicity is relatively low within the Sureste Basin, with around 550 earthquakes above M_w 4 in the last 50 years. The largest event had a magnitude of 6.4 in 1959, and in the last 20 years, the most significant events had a magnitude of 4.5.

Figure 4.7 shows the locations of earthquakes in the Sureste Basin; the largest earthquakes have occurred in the west of the basin; still, some earthquakes above M_w 4.5 have occurred in various locations, especially in the south. The largest and closest earthquake to the field had a magnitude of 4.6 in 1989; see Figure 4.8. All the other seismic activity has been below M_w 4.5. There has not been reported any activity of significance in the last 20 years.

Moreover, there is a relation between earthquakes and faults, as the presence of an earthquake implies the existence of a fault. Figure 4.9 compares the locations of the faults and previous earthquakes in the basin, where this relationship can be observed, especially in the southwest area. However, there have been earthquakes in areas with no mapped faults, and this could be because, as discussed before, some faults may be beneath the sediments close to the basement.

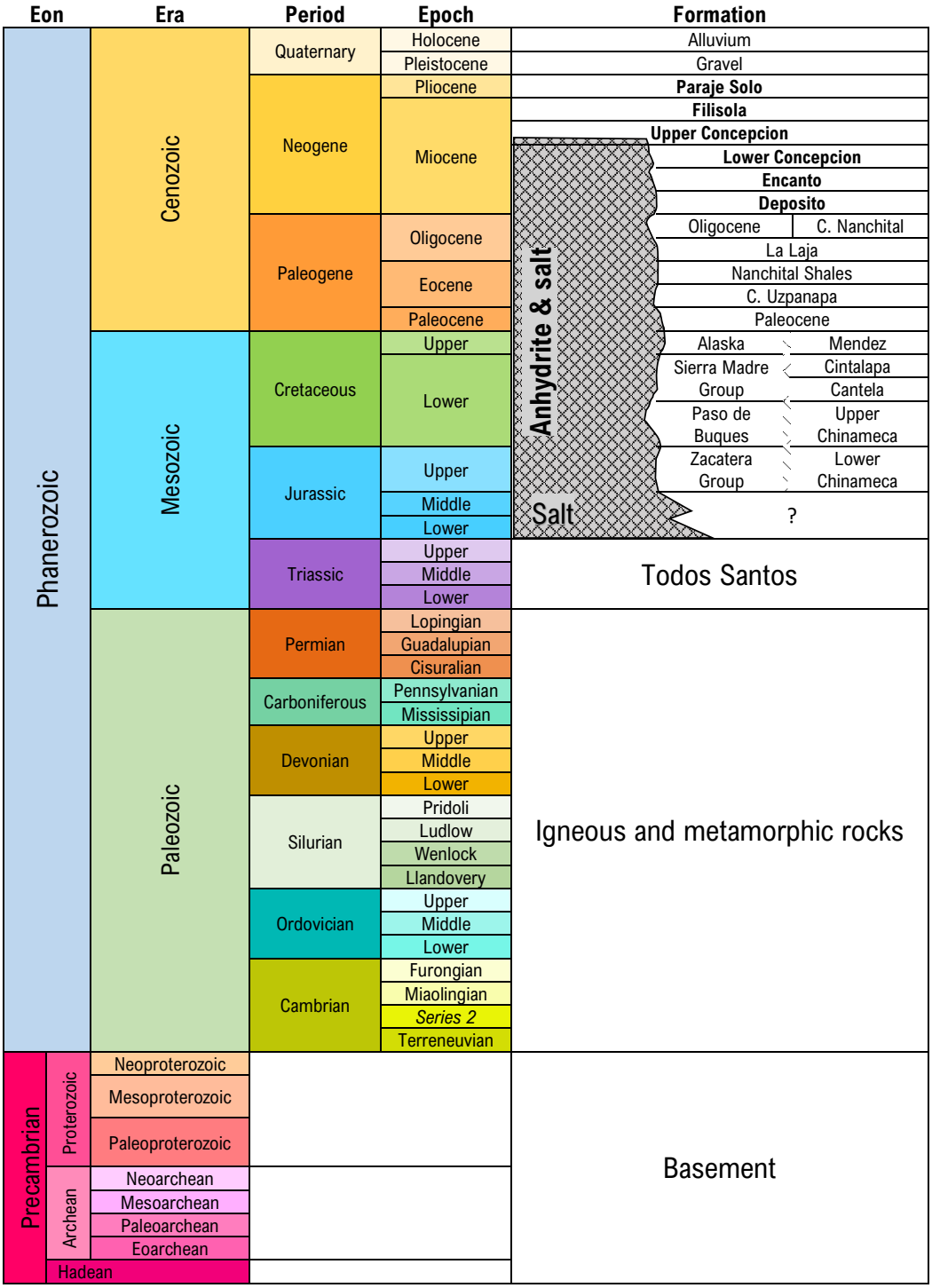

Figure 4.6: Chronostratigraphic chart of the western area of the Sureste Basin, adapted from Sanchez Romero (2019).

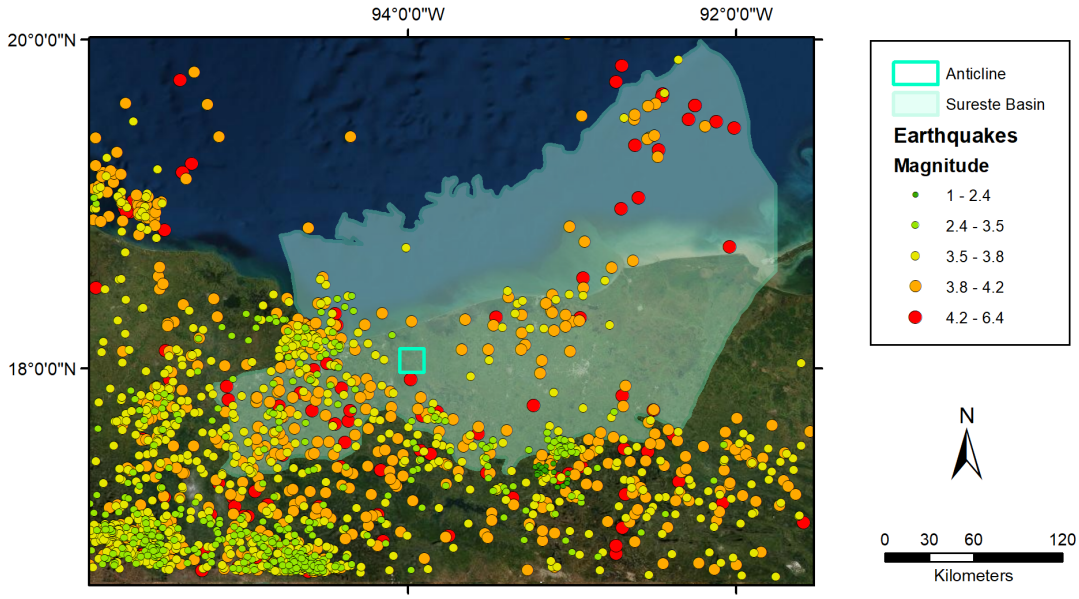

Figure 4.7: Seismicity in the Sureste basin, including the earthquakes from 1959 to 2020. The green points represent the earthquakes below M_w 4.5 and the red ones the earthquakes above this magnitude.

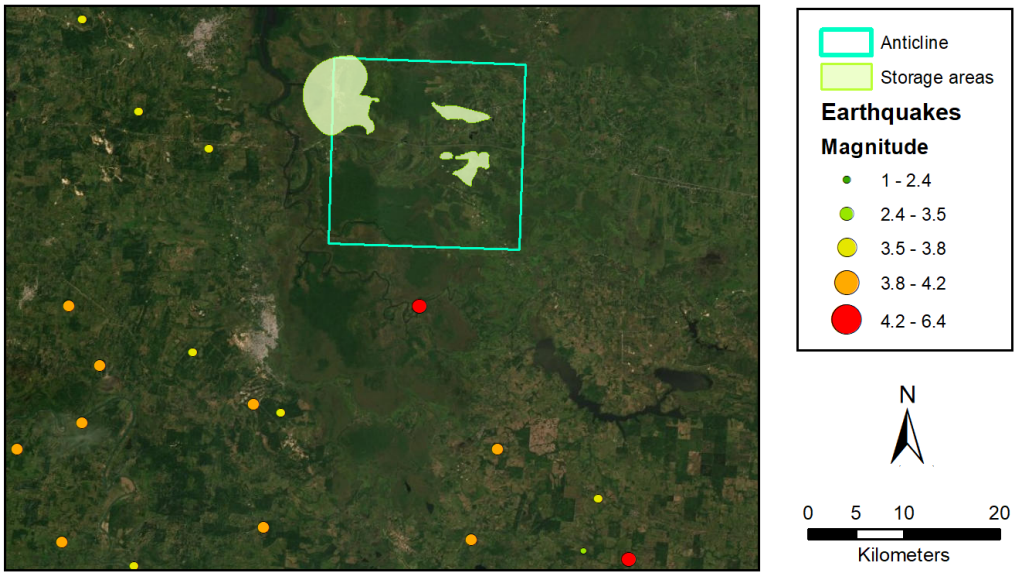

Figure 4.8: Seismicity in the study area. The largest and closest earthquake to the field had a magnitude of 4.6 in 1989.

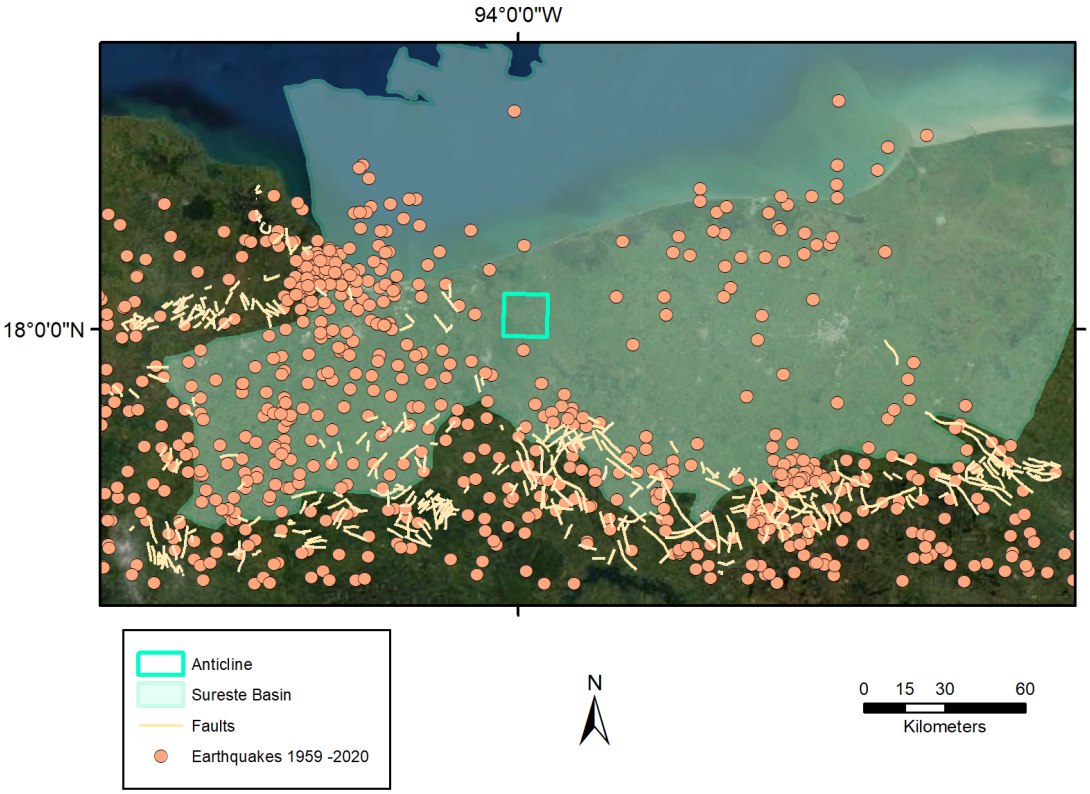

Figure 4.9: Fault distribution and earthquakes from 1959-to 2020 in the Sureste Basin, obtained from INEGI and Mexican National Seismology Service (SSN).

Therefore, since there has been seismic activity at about 15 km away from the storage areas in the past, it could be possible that inactive faults or fractures are present. For that reason, I used the seismic reflection interpretation described in Chapter 3 to identify faults around the proposed storage site. Representative seismic sections are shown in Figures 4.11 and 4.12 (locations of these sections are shown in Figure 4.10). I found no evidence of additional faults within or around the proposed storage anticline.

Furthermore, I selected well logs with sufficient data to generate two cross sections (Figures 4.14 and 4.15) located in the anticline area to identify faults; see Figure 4.13. However, as the seismic reflection cross sections display, there are no visible faults.

Another method to determine faults and fractures is by analysing borehole data. Nevertheless, the data provided by CNH and SENER does not include this kind of information, and therefore this analysis will not be performed in this thesis.

In summary, the proposed injection site at Ogarrio does not have any identified faults nearby. The nearest mapped faults are at a distance of over 20 km, and the stress conditions within the sediments of Sureste Basin are such that significant pore pressure changes would be required to reactivate them. The proposed storage formations are significantly shallower than the underlying basement, reducing the likelihood of pressure transfer into

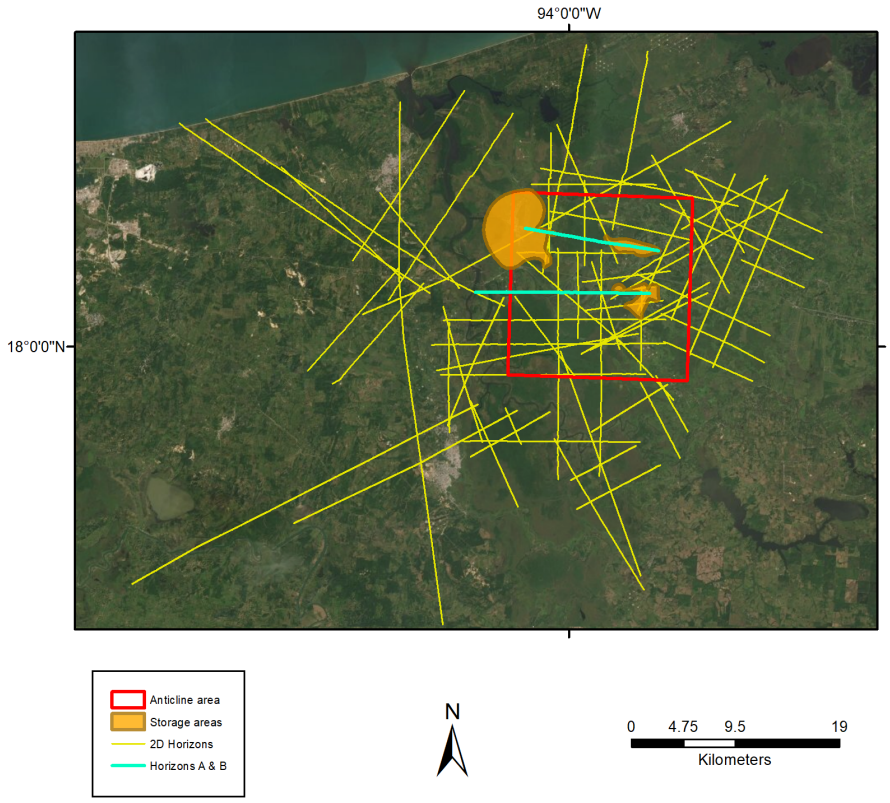

Figure 4.10: Location of the seismic cross sections A and B within the anticline area and potential storage areas.

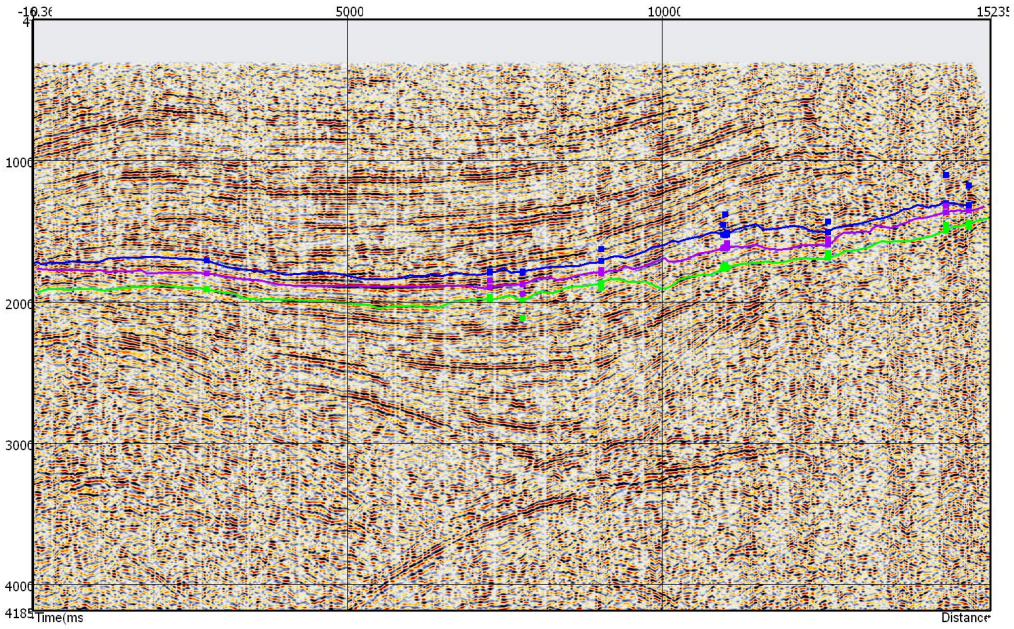

Figure 4.11: W-E seismic cross section A showing that there are no visible faults over the target anticline. The blue line represents Upper Concepcion, the purple line represents Lower Concepcion and Encanto is represent by the green line.

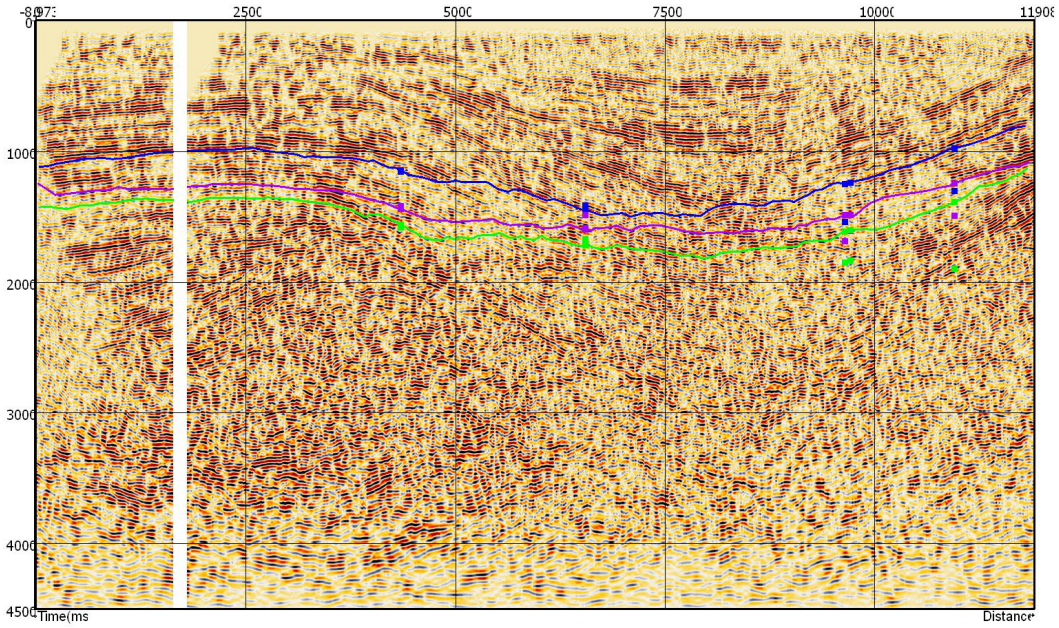

Figure 4.12: Seismic cross section B. Event horizons are the same as in Figure 4.11.

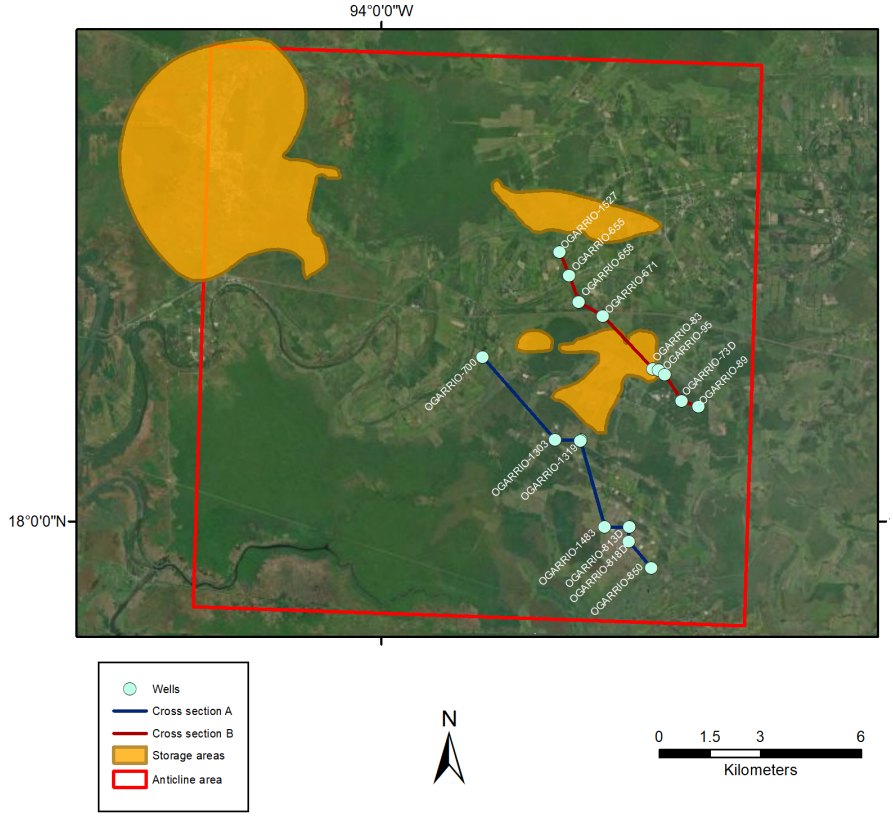

Figure 4.13: Location of the cross sections A in blue and B in dark red the created with the available well log data.

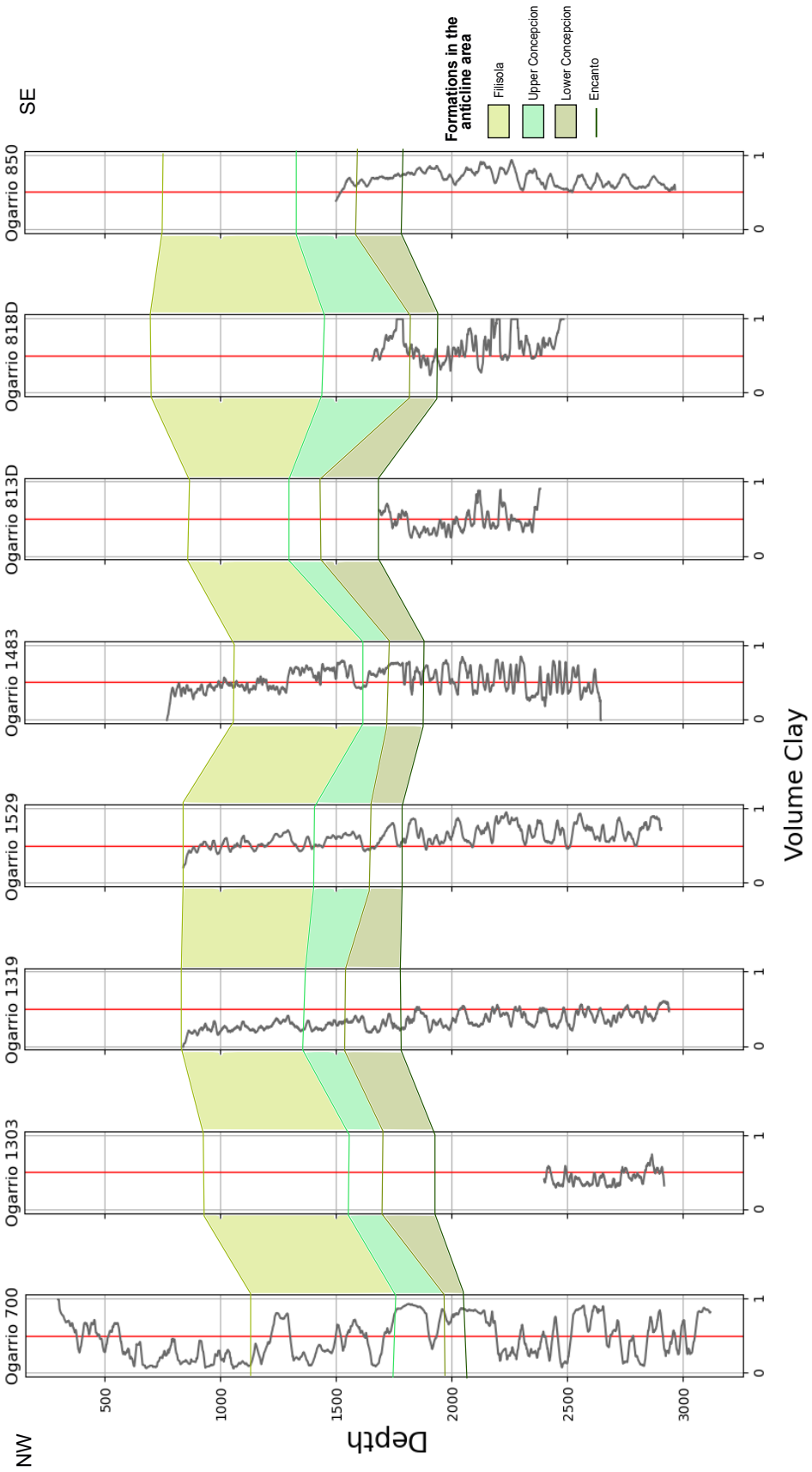

Figure 4.14: Cross section A created with the log information from eight wells, Ogarrio 700, 1303, 1319, 1529, 1483, 813D, 818D, 850. The depths of the formations were taken from the CNH data.

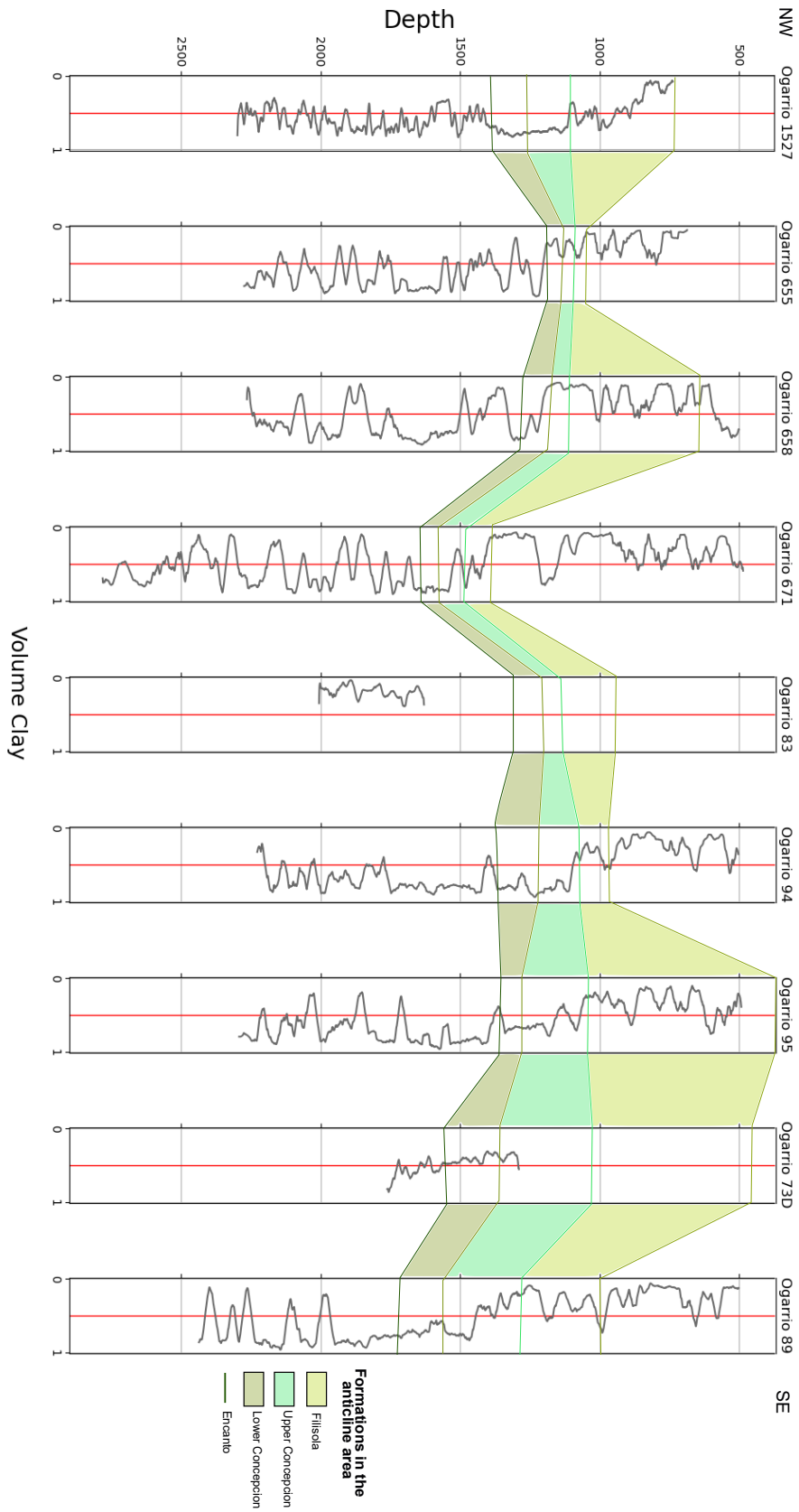

Figure 4.15: Cross section B created with the log information from nine wells, the Ogarrio 1527, 655, 671, 83, 94, 95, 73D, 89. The depths of the formations were taken from the CNH data.

deeper structures that could be more likely to host induced earthquakes. The area has experienced a low rate of past natural seismicity. I, therefore, conclude that the likelihood of generating induced seismicity from CCS at this site is low. However, it is worth noting that there is a non-negligible epicentral uncertainty, as there are no seismic stations nearby; the closest one is at 50 km away.

4.5 Hazards and mitigation

Despite the conclusions above, the geomechanical assessment of potential induced seismicity can be subject to considerable uncertainty. For example, the fault stability analysis at the Castor project suggested a low risk of induced seismicity, yet earthquakes were still generated. It is reasonable to consider what levels of seismic hazard might be acceptable for a CCS project and what monitoring levels might be required to achieve this.

4.5.1 Defining acceptable levels of seismic hazard

Where there is a concern about induced seismicity, a key question is: what level of seismicity is it reasonable to try to avoid? Moreover, what level is it reasonable to accept? There is no correct answer as this is both a question of science and a question of politics and public acceptability. Some people might say that causing earthquakes is not acceptable at all. In these circumstances, it would be difficult to allow any CCS projects anywhere in the world since it is known that some of them have already caused induced seismicity. On the other hand, some people might say that earthquakes that can be felt should be avoided; this would mean that earthquakes of M_w 2 would be the maximum magnitude allowed. However, this level could be challenging to avoid and could mean cancelling projects even though there is no risk of damage to buildings or infrastructure.

It is an acceptable position to suggest that earthquakes big enough to cause damage should not be allowed. This conclusion implies that we should seek to identify what magnitudes might be dangerous and seek to prevent earthquakes at that magnitude. The simplest method to identify this magnitude is by looking at the natural seismic risk.

The levels of ground motion, which is the movement of the surface of the earth due to earthquakes or explosions (USGS, 2020a) and the passage of seismic waves through the basin, are well characterised by natural earthquakes. This is especially true for events that occur in the subduction zone to the south, which tend to have magnitudes above 7. This provides a point of comparison with what could happen if CCS operations trigger an earthquake; what magnitude events within the basin will create equivalent levels of vibration in the basin to the levels of shaking regularly produced by the subduction zone events to the south?

To answer this, I consider the Peak Ground Acceleration (PGA), which is the maximum ground acceleration produced during an earthquake (USGS, 2020b) and is given in units of

gravity (G) or m/s^2. Maps of PGA are based on observations of the distribution of tectonic earthquakes and ground vibrations produced in a region over a certain amount of time, the return period.

Figure 4.16 shows the acceleration map for the 10-year return period for natural earthquakes in the Sureste Basin. This map was produced from the seismic Hazard quantitative information system in Mexico created by the National Autonomous University of Mexico (UNAM) and National Centre for Disaster prevention (CENAPRED in Spanish), developed for the seismic hazard in Mexico in 1996.

As can be seen in Figure 4.16 the levels of ground motion caused by earthquakes in Mexico are dominated by the subduction zone. Further away from the subduction zone, the risk decreases. Knowing only the magnitude of the earthquakes and their intensities gives a simple idea of the spatial distribution of the ground and building effects in a particular region. Nevertheless, it does not indicate what is the probability that this event will happen again. For this reason, the hazard maps help to know the distribution of the intensities in terms of terrain acceleration associated with return periods and to define hazard levels. These maps are key to the design and modification of buildings to reduce vulnerability and as the basis for building codes and regulations.

Hence, it is reasonable to assume that all structures within a region can withstand the shaking levels that occur over a relatively short return period. Thus, if the shaking of 34 cm/s^2 occurs every ten years, it is acceptable to assume that all or most structures in the area can withstand this level of shaking. Ten years is a reasonable time frame for CCS project development, and so it is reasonable to compare the shaking that an induced event could generate to these values.

To obtain the peak ground acceleration that could be generated in the study area by an induced earthquake, I used the Ground Motion Prediction Equation (GMPE) of Akkar, Sandikkaya, and Bommer (Akkar et al., 2014). This ground motion model gives the predictions of PGA, peak ground velocity (PGV), and pseudo-spectral accelerations as a function of distance from an earthquake and magnitude. This model includes a ground surface condition as a function of V_{s30}, spectral periods and the focal mechanism (Akkar et al., 2014). The ground surface condition V_{s30} is set at 700 m/s for the purposes of this analysis.

The Akkar et al. (2014) model also accounts for the epistemic uncertainty in ground motions. The model computes the mean ground motion for a given earthquake magnitude and distance and provides ground motions with standard deviations above and below the mean. Two standard deviations above the mean will give upper 95% confidence intervals, which is the upper limit of the amount of shaking that an earthquake might produce; two standard deviations below the mean will give lower 95% confidence intervals.

According to the acceleration map of the 10-year return period, the area of the study has a PGA of $34cm/s^2$. To compare what magnitude and distance from an induced event will produce the same PGA as the natural hazard, a range of distances (5, 10, and 30 km),

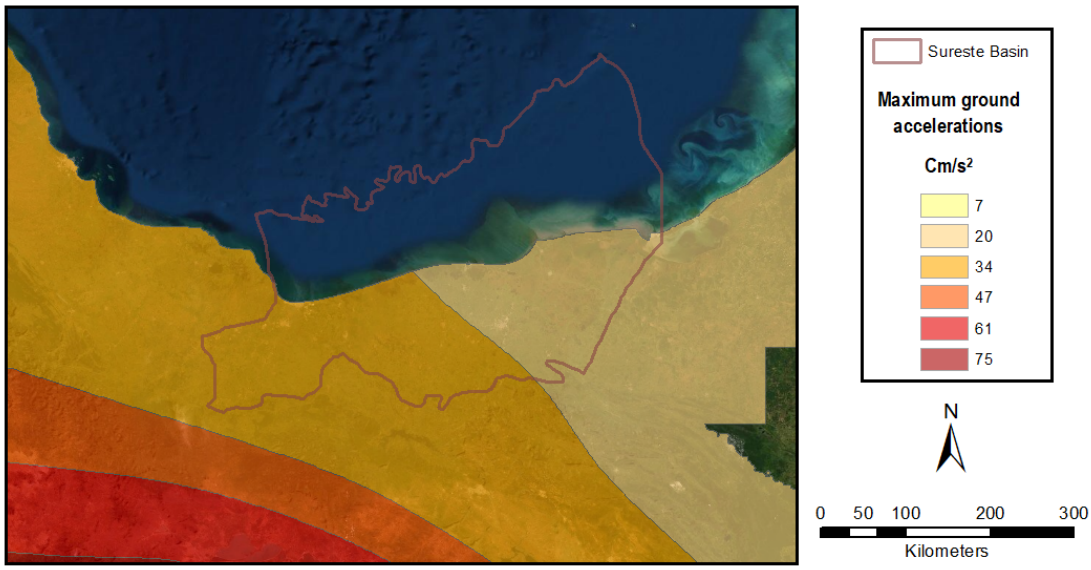

Figure 4.16: Maximum ground accelerations for a 10-year return period map (CENAPRED, 2006), which is the mean time, measured in years, that it takes for an earthquake to repeat itself that exceed a given acceleration.

and a range of magnitudes, M_w 3 to 5, were applied in the model to obtain the mean and 95% values of PGA.

The distance of an earthquake to the hypocenter is one of the factors that will determine the PGA. The Ogarrio field is in a relatively low populated area, since the nearest cities to the field are Las Choapas at 25 km and Agua Dulce at 30 km away from the Ogarrio wells, with a population of approximately 42,000 and 34,000 people, respectively, see Figure 4.17. Small towns and ranches are more common to find in this area of the state, and the closest ones are: La Ceiba, Ejido Blasillo, Tres Bocas at 5 to 6 km away from the wells and then Las Piedras and Blasillo at approximately 8 km away.

Figure 4.18 shows the modelled ground motions as a function of magnitude and distance. As shown in Table 4.1, the 95 % upper bound for PGA of an M_w 4.5 earthquake surpasses the natural hazard PGA of the study area, whereas PGA from magnitude M 4.0 events do not exceed this limit. Thus, it is reasonable to take steps to ensure that events with magnitudes larger than M_w 4.5 should not be allowed to be caused by CCS operations.

4.5.2 Recommendations to mitigate induced seismicity

One approach to mitigating the induced seismicity is based on obtaining the potential magnitude energy release (M_w) based on the pore volumes of the target formations, as modulated by the Seismic Efficiency Factor (S_{eff}).

It is well known that the induced seismicity scales with the volume injected. McGarr (2014) suggested that, in fully saturated formations, the total volume of injected fluid will constrain seismic moments or magnitudes (Figure 4.19). He also proposed that in a

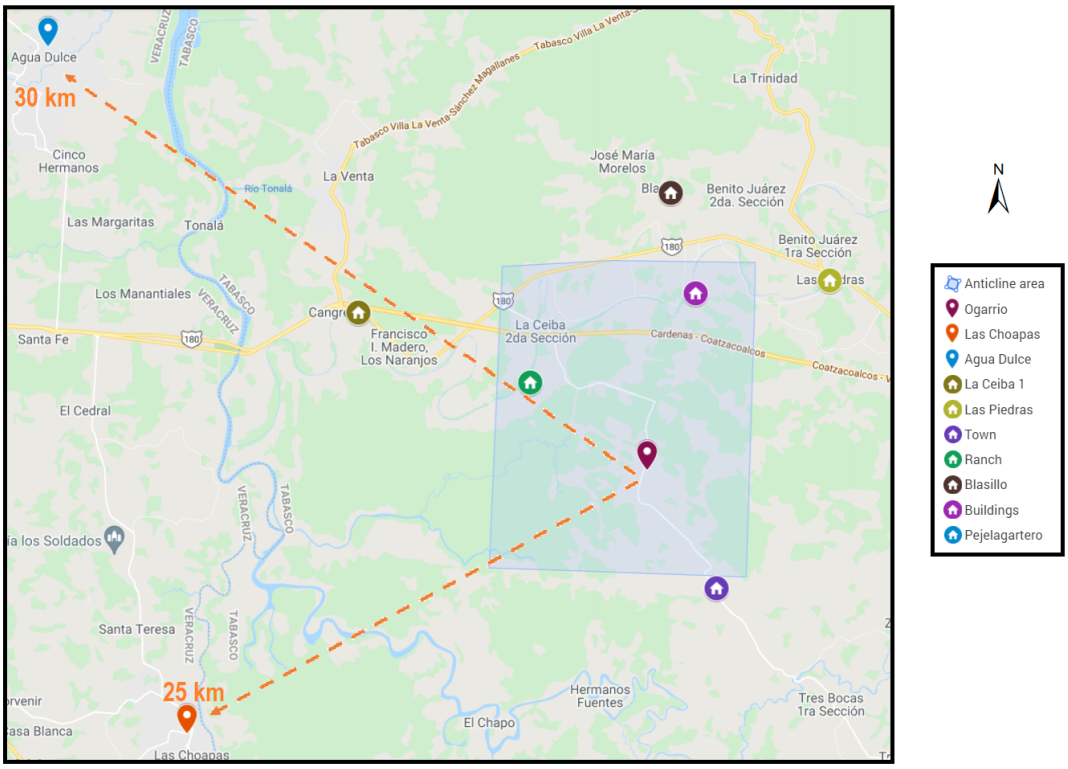

Figure 4.17: Populated areas near the study area. Map created in Google Maps (2021).

controlled injection project, the upper limit seismic moment is defined by the volume of the injected fluid times the modulus of rigidity:

$$M_0(Max) = \mu \Delta V \quad , \tag{4.9}$$

where M_0(Max) is the maximum seismic moment, μ is the modulus of rigidity or shear modulus (often assumed to be 20 GPa in sedimentary rocks), and ΔV is the volume injected.

Figure 4.19 shows how in different real case scenarios, the seismic moments were limited by this equation. Nonetheless, it is assumed that the fault slip response is delimited by a region where the pore pressure increment is present, and even with this limit, there is some uncertainty (McGarr, 2014). Additionally, this approach was designed for single-well injection scenarios, so the validity of this method for multi-well injections is more uncertain.

The equation 4.10 was derived from a model (McGarr, 2014), where the cumulative moment release (ΣMo) has a linear scaling relationship with the injected volume ΔV, as the flow rate is constant during injection, especially during stable slip at a constant rate (Wang, 2020). It is represented by:

$$\Sigma M_0 = K\mu|\Delta V| \quad , \tag{4.10}$$

Magnitude	Distance (km)	Nstd=0	Nstd=2	Nstd= -2
3	5	0.60	3.01	0.12
3	10	0.32	1.61	0.065
3	30	0.056	0.28	0.011
3.5	5	1.81	8.95	0.36
3.5	10	1.00	4.97	0.20
3.5	30	0.19	0.97	0.04
4	5	4.97	24.60	1.004
4	10	2.87	14.25	0.58
4	30	0.63	3.13	0.12
4.5	5	12.64	62.61	2.55
4.5	10	7.63	37.81	1.54
4.5	30	1.88	9.32	0.38
5	5	29.78	147.41	6.016
5	10	18.75	92.84	3.78

Table 4.1: Values of the mean, second, and second negative standard deviations of PGA in the study area, with their different magnitudes and distances from the epicentre of the earthquake. The values that exceed the PGA of the study area (34 cm/s^2) of the natural hazard map of Mexico are in red.

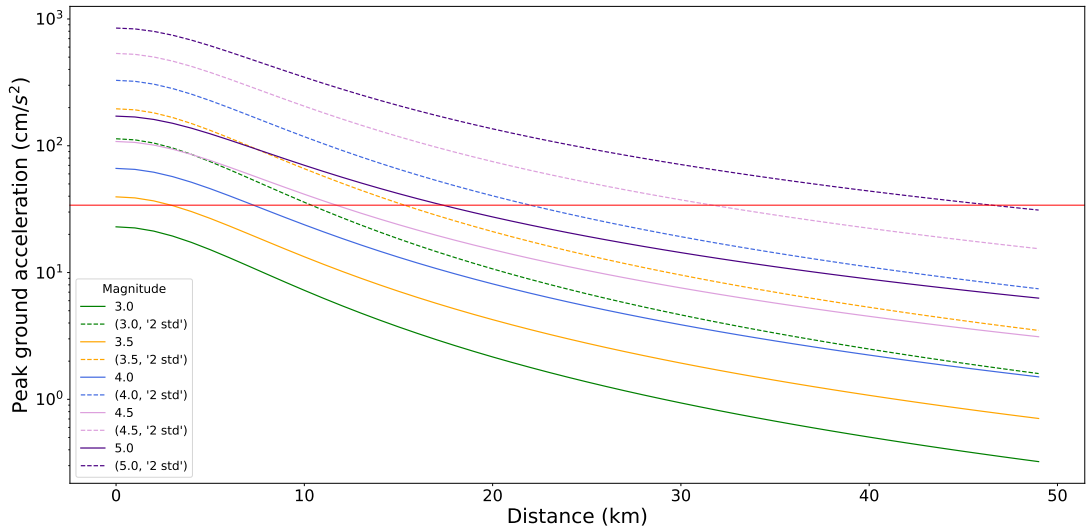

Figure 4.18: Comparisons for normal faulting and a rock site of V_{S30} = 700 m/s. The lines represent magnitude-dependent distance saturation, also the solid lines represent the PGA at a mean standard deviation, while the dashed lines represent the PGA at a second standard deviation.

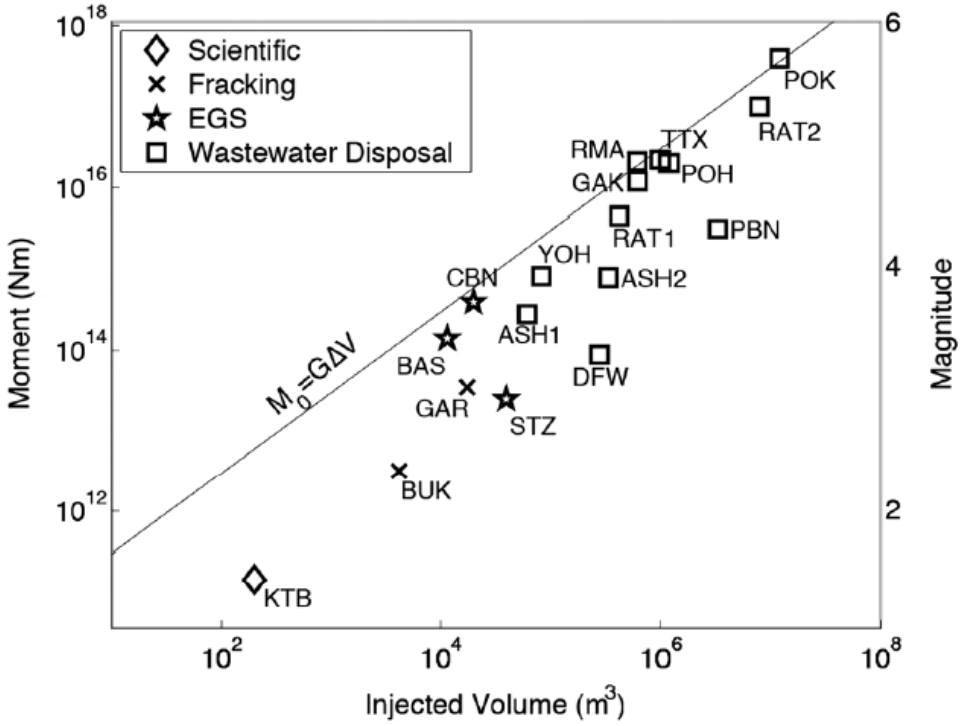

Figure 4.19: Maximum seismic moment and magnitude related to total volume injected since the beginning of injection until the largest induced earthquake in projects dedicated to wastewater disposal, water injection and hydraulic fracturing of oil and gas reservoirs. From McGarr (2014).

where ΔV is the volume change and K is close to 1 (Hallo et al., 2014).

The model proposed by McGarr was modified by Hallo et al. (2012) in order to include aseismic slip and deformation within the medium:

$$\Sigma M_0 = S_{eff} \times K\mu|\Delta V| \quad , \tag{4.11}$$

where S_{eff} is the seismic efficiency ratio which is the ratio of the observed moment to the theoretical cumulative moment. The values of the total seismic moment release in this equation are typically low for fluid injection into soft rock, and these values can be used to estimate the most plausible extent of the released total seismic moment (Hallo et al., 2014). This can be shown by rearranging the equation to obtain S_{eff}:

$$S_{eff} = \Sigma M_0/(\mu \times \Delta V) \quad . \tag{4.12}$$

Since the S_{eff} relates the scaling between volume and magnitude, this value is key to estimating the amount of seismic energy released per m^3 of injected fluid. It is commonly observed to vary from 0.0001% to 100% as the minimum and maximum percentage, respectively (Hallo et al., 2014).

In this way, it is feasible to track the relationship between ΣM_0 and ΔV and measure the seismicity produced as a function of each cubic meter of fluid injected. A low S_{eff} value

indicates a low seismic moment release per volume injected, and the linear relationship between the moment release and the volume change means that the maximum seismic moment is therefore unlikely to be exceeded. This ratio should be measured throughout an injection project to ensure that it is stable over time, since a temporal increase in S_{eff} corresponds to a heightened risk of an induced event capable of damage at the surface.

Once a stable S_{eff} value is obtained, it can be possible to include it in McGarr's equation, giving as a result the expected seismic moment of the largest event:

$$M_0(Max) = \mu \times \Delta V \times S_{eff} \quad . \tag{4.13}$$

Then, knowing the amount of injection volume, the maximum permitted magnitude, and the value of S_{eff}, we can convert the seismic moment, which is in Newton meters (Nm), to a magnitude value (M_w):

$$Mw = \frac{2}{3} \times (\log_{10}(M_0) - 9.1) \quad . \tag{4.14}$$

Since the value of the pore volume was obtained in the previous chapter, and the maximum magnitude limit is 4.5, as described above, it is possible to apply these equations to the study area.

The pore volumes in the main formations are given in Table 4.2. With the aim of estimating the storage volume in the main formations, the pore volume should be multiplied by the Storage Efficiency Factor (SER), in this case, 5%. These estimated storage volumes are also given in Table 4.2.

	UC	LC	En	Total (m^3)
Pore volume	77,500,000 m^3	110,300,000 m^3	1,190,000,000 m^3	1,370,000,000
Storage volume	3,800,000 m^3	5,500,000 m^3	59,400,000 m^3	69,000,000

Table 4.2: Pore volumes and storage volumes for the formations Upper Concepcion (UC), Lower Concepcion (LC) and Encanto (En), considered for storage at the Ogarrio field.

The impacts of different S_{eff} values on the resulting seismic magnitudes are shown in Figure 4.20, and listed in Table 4.3. In the scenario where 100% of the volume change injected in the ground is released as seismic energy, the potential total moment release is the estimated storage volume multiplied by the shear modulus. Table 4.3 shows this moment release and converts these moments to magnitudes, based on the assumption that the largest event releases 50 % of the overall moment release. As can be seen, for the proposed storage volumes at Ogarrio, at a S_{eff} of 100 %, the resulting earthquake magnitudes would produce ground shaking that is significantly larger than that imposed by the natural seismicity.

More typical values for S_{eff} are less than 1% (Frohlich and Wetzel, 2007). In Table 4.3 we recompute the total moment release, and the resulting largest event magnitude, based on S_{eff} = 1% and S_{eff} = 0.1%. From my comparison of the natural earthquake hazard

	UC	LC	En	Total
ΣM_O (S_{eff}=100%) (Nm)	7.75×10^{16}	1.1×10^{17}	1.18×10^{18}	1.37×10^{18}
M_w (Max) (S_{eff}=100%)	4.9	5.09	5.7	5.8
ΣM_O (S_{eff}=1%) (Nm)	7.75×10^{14}	1.1×10^{15}	1.18×10^{16}	1.37×10^{16}
M_w (Max) (S_{eff}=1%)	3.6	3.7	4.4	4.4
ΣM_O (S_{eff}=0.1%) (Nm)	7.75×10^{13}	1.1×10^{14}	1.18×10^{15}	1.37×10^{15}
M_w (Max) (S_{eff}=0.1%)	2.9	3	3.7	3.8

Table 4.3: Potential total seismic moment release and largest event size based on assumed seismic efficiencies, and the proposed storage volumes for the Ogarrio field.

with ground motions given by the Akkar et al. (2014) GMPE equation, I determined that earthquakes of M_w 4.5 should be avoided to ensure that the seismic risk imposed by CCS does not exceed that imposed by natural earthquakes. Given that the modelled potential magnitude of the largest event in Encanto at S_{eff} = 1% is M_w 4.4, lower S_{eff} values may be needed. The computed magnitudes assuming S_{eff} = 0.1% are at an acceptable level, showing that seismic efficiencies of this order of magnitude would indicate a safe level of induced seismicity at which a project should be allowed to continue.

Figure 4.20 shows cumulative seismic moment release as a function of injection volume for seismic efficiencies of S_{eff} of 100%, 10%, 1% and 0.1%. It also shows modelled largest event magnitudes based on the storage volumes for the Ogarrio field at the S_{eff} = 1% level. These calculations show how the continuous measurement of S_{eff} during the early stages of project operation can be used to guide and control the seismicity risk during the life of a project.

4.6 Traffic light system

One of the most common ways to supervise the risk of induced seismicity is a Traffic Light System (TLS), which was introduced by Bommer et al. (2006). A TLS defines different action statuses, described as red, yellow, and green, which indicate the actions that should be followed to mitigate the risks. The green light implies no alteration in the planned operations, the yellow light requires de-escalating operations, and a “red light” entails ceasing all operations.

TLSs assume that if all activities are suspended, future induced seismicity will be avoided. However, in reality, some cases of induced seismicity have continued to increase after the injection has stopped (Igonin et al., 2021). These “trailing” events, as well as large jumps in magnitude during injection, pose a challenge for TLSs (Verdon and Bommer, 2020). It is crucial to set the red light level at a suitable magnitude such that trailing events and magnitude jumps do not exceed the level that is to be avoided from a risk assessment perspective, based on ground motion characteristics computed using the expected magnitudes, depths, distances, and ground environment.

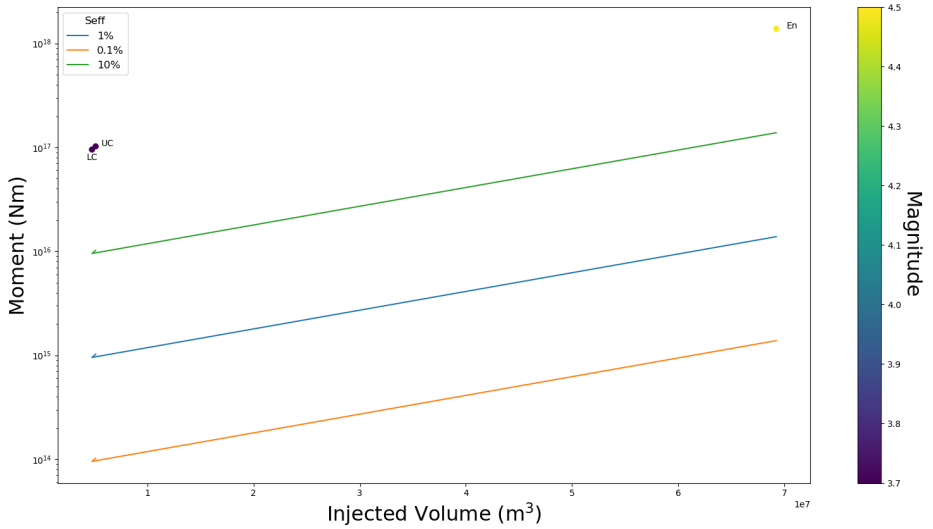

Figure 4.20: Derived from Figure 4.19, the colour of the three dots represent the modelled largest magnitude event based on the storage volume of each formation (UC, LC, En) at S_{eff} = 1%. The lines represent the equation M_o(Max)=$\mu\Delta\times$ S_{eff}, which is the modulus of rigidity times the injected volume of CO_2 times the seismic efficiency moment.

Verdon and Bommer (2020) explained how induced seismicity sequences tend to evolve with magnitude jumps, such that 90% of the studied cases had trailing events or jumps of less than two magnitude units. This means that it is necessary to set a red light threshold at least two magnitude units before the limit to be avoided.

If an earthquake of N magnitude creates the same amount of vibration as an earthquake of X magnitude in the subduction zone, then an earthquake with less magnitude than N is the desirable limit. Since there is a range of two order of magnitude, the TLS will be set at a magnitude of N-2. Thus, if an earthquake of magnitude N-2 occurs, the project will have to stop operations because there will be a risk that the next earthquake will be magnitude N, which is the maximum tolerable level of shaking.

As discussed in Section 4.5.1, the largest magnitude induced event that should be permitted is M_w 4.5. Consequently, the upper bound of the TLS will be two magnitudes less than this magnitude; thus, my recommendation is that the Red Light should be set at M_w 2.5 for CCS operations at Ogarrio.

The primary way to avoid seismic events of this magnitude is by monitoring the area continuously. The Mexican National Seismic Network provides some degree of monitoring. However, prior to any CCS operations taking place, a performance assessment of this monitoring should be performed to determine the smallest magnitude that can be detected around the Ogarrio site. Is the Mexican National Seismic Network capable of detecting below M_w 2.5 earthquakes so the TLS can run with the existing technology, or is additional monitoring for a CCS project needed?

One way to calculate the monitoring detection threshold is through the Gutenberg-Richter Law, which states that the N number of earthquakes in a given region, greater than any magnitude M, is proportional to the magnitude (Crampin and Gao, 2015):

$$\log_{10}[N(>M)] = a - bM \quad , \tag{4.15}$$

where a is a positive parameter that denotes the level of seismicity and b is typically close to 1 for tectonic earthquakes. Then, reformulating this equation by taking the logarithms of both sides, we have:

$$\log_{10}(N) = a - bM \quad . \tag{4.16}$$

Therefore, the G-R relationship is represented by a straight line with slope b when $log_{10}(N)$ is plotted against M. At low magnitudes, N will fall below this line. This is not because the b-value is low, but because these small events have been missed because the monitoring array did not detect them. This effect is known as the "roll-off" of the b-value (Bhattacharya et al., 2009).

In Figure 4.21, I plot the event magnitudes for earthquakes detected by the National Seismologic Service (SSN in Spanish) for the Sureste Basin. In this case, the roll-off occurs at relatively high magnitudes, at M_w 3.8. Considering that the detection threshold of 3.8 is well above my proposed TLS threshold, it is clear that additional dedicated seismic monitoring will be needed at future CCS sites in the basin.

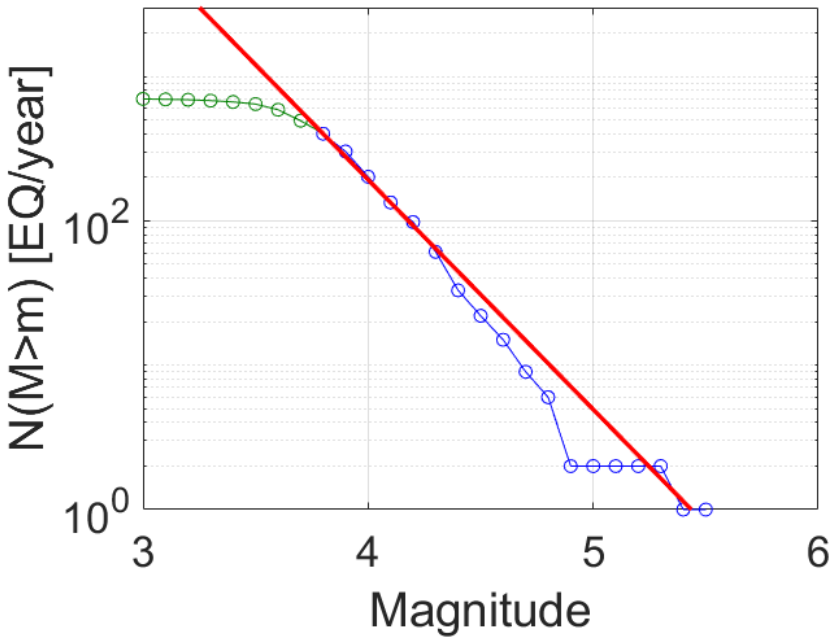

Figure 4.21: Gutenberg-Richter plot for earthquakes detected by the SSN in the Sureste Basin. The curved line a dots shows observed events, while the red line shows the theoretical G-R relationship. The b-value roll-off for the earthquake catalog is observed at relatively high magnitudes.

4.7 Caprock integrity

When addressing hazards related to CO_2 injection and sequestration, not only should the induced seismicity be considered but also the integrity of the caprock, as it plays an essential role in storage security.

Ideally, the caprock should be homogeneous, impermeable, and without faulting; however, this is unlikely in an extensive area, as it could present discontinuities, have low-porosity, and faults. Furthermore, the caprock must be above the storage formations to confine the injected CO_2. In its supercritical condition, CO_2 will remain at the top of the storage formations in contact with the caprock (Rutqvist and Tsang, 2002). The thickness of the caprock should be at least 150 m, and the presence of multiple layers of caprock is even more suitable to ensure storage security (Miocic et al., 2016).

The most critical factors determining CO_2 retention for thousands of years and preventing leakage, along with abandoned wells, are faults and fractures in the caprock (McCraw et al., 2016). When CO_2 is injected into a reservoir, the pore pressure increases and the effective stresses decrease, leading to deformation of the reservoir rocks that, in turn, causes vertical displacement of the caprock, failure, fault reactivation and leakage. Fractures caused by stress changes may damage the sealing characteristics of the caprock (Karimnezhad et al., 2014). Injection of CO_2 can also induce shear failure of the caprock and reactivate faults in the caprock. The pressure close to a fault during injection decreases the effective normal stress, reducing the shear strength of the fault (Shukla et al., 2010).

According to Rutqvist and Tsang (2002) the caprock is more likely to have a fault failure in its lowest part, as this is where the effective mean stress is reduced more, causing hydromechanical changes. Additionally, leakage could occur if the caprock is fractured under pore fluid pressure of the accumulated CO_2 upward pressure in the lower part of the caprock; this tends to occur when supercritical CO_2 transitions to its liquid or gaseous phase (Shukla et al., 2010).

In some cases, CO_2 injection can also cause hydraulic fracturing along pre-existing faults and fractures in the caprock; this could occur if the reservoir pore pressure is greater than the pore pressure and tensile strength of the caprock (Miocic et al., 2016). For this reason, the compression and tension of the caprock should be strong enough to stand the change in stress fields during and after injection (Shukla et al., 2010). Therefore, the caprock pressure should be higher than the reservoir pressure to avoid fluid migration from the layers below the caprock, as this behaves as a hydraulic barrier (Miocic et al., 2016).

The magnitude of the seal capacity of the caprock is defined by the breakthrough pressure, which, in turn, is determined by the capillary pressure within the large pores. The breakthrough pressure in the caprock is reduced when CO_2 is injected, and this pressure must be determined before CO_2 storage begins. In the event that it is greater than the original reservoir pressure, it can help determine the overpressure that can be

implemented to store CO_2, and it is crucial when designing and applying in a CO_2 injection project (Li et al., 2006).

Another factor that could affect the caprock integrity is the temperature. Khurshid and Fujii (2021) stated that the temperature of the injected CO_2 and the reservoir temperature should be compatible because as soon as the supercritical CO_2 is injected, its temperature drops. A low-temperature CO_2will decrease the temperature of the reservoir, leading to its contraction and shrinkage, inducing tension, and creating fractures in the reservoir and the caprock close to the injection wells. Therefore, CO_2 injection reduces reservoir temperature and thermal stresses and induces tensile stresses, causing a decrease in the reservoir breakdown pressure, which is the pressure at which a rock formation fractures and admits fluid injection (Khurshid and Fujii, 2021).

Furthermore, when there is an organic content in the caprock and if supercritical CO_2 is in contact with it, it could cause a slight alteration in the permeability and porosity of the caprock, creating micro cracks that could lead to macro fractures in the caprock (Shukla et al., 2010).

Additionally, the integrity of the caprock can be damaged by the depletion of oil and gas reservoirs as the initial pressure of the reservoir changes and, therefore, the storage capacity could be reduced. On the contrary, if the pressure is raised above the initial reservoir pressure and if it remains below the capillary entry pressure and the fracture pressure of the caprock, the storage capacity can increase because the CO_2 is compressed under these circumstances (CSLF, 2008). Also, since oil and gas extraction could cause subsidence on the ground surface, CO_2 injection could cause elevation of the ground, as it reduces the effective stress of the reservoir (Rutqvist and Tsang, 2002).

In summary, to keep storage under safe conditions, the injected CO_2 pressure must be lower than the original reservoir pressure, assuming that the sealing capacity of the caprock used to trap oil and gas is adequate to retain CO_2. In addition, the sealing pressure of the caprock must be determined before implementing a CO_2 storage project and should not be exceeded at any injection time. To ensure this, the injection pressure and rate must always be controlled and monitored (Li et al., 2006). Also, it is necessary to understand the rock stresses that confine fractures, fluid pressures, and flow properties within fractures in a CO_2 storage context, as the injection rate of CO_2 and the initial stress state significantly impact the caprock failure tendency (McCraw et al., 2016).

To minimise damage, it is crucial to predict the likelihood of fracturing under various reservoir conditions and injection scenarios and to know the size, direction and orientation of the fractures (Lavrov, 2016). The deformation of the caprock and the migration of CO_2 in the short and long term could be predicted by creating numerical models, applying different values in the parameters, such as pressure and confining pressure, present in the natural CO_2 storage conditions (McCraw et al., 2016). These models are an effective way to determine the caprock integrity. However, these models are outside the scope of this thesis.

4.8 Discussion

The World Bank established a regulatory framework for CCS in Mexico, where guidelines were taken from existing regulations worldwide and in the USA. Furthermore, some legal, economic, technical, and infrastructure guidelines were adapted from the ones that already existed in Mexico, especially from the oil and gas industry. This document covers all stages of the CCS process and essential issues that a project like this may need to manage, such as environmental, social, safety requirements, different liabilities, and legal implications.

However, this report did not consider some hazards, such as earthquakes and caprock integrity. This is likely because induced seismicity is less of an issue for petroleum production, which withdraws fluids from the ground, than for CCS, which injects fluids creating pore pressure increases.

In this chapter, I address the induced seismicity issues pertaining to CCS in the Sureste Basin, including recommendations for how this should be monitored, managed, and mitigated in future projects. In addition, I introduced the importance of the caprock integrity in the reservoirs when injecting and storing CO_2 from a general point of view, and I strongly suggest performing the pertinent analyses to assess the properties and integrity of the caprock if a project of this type was to be considered in the Ogarrio area.

The fault and stress analysis presented here indicates that overall, the Ogarrio anticline area is expected to be a safe place to carry out CCS operations. However, it was noticeable that some faults in the area are well oriented for slip in the in situ stress field. My estimates of stress magnitudes were based on observations from the Cantarell field, but if the magnitudes differ across the basin, these faults could be at greater risk of slip than modelled here.

Equally, the available fault data does not cover the whole Sureste Basin since it is based on the interpretation of proprietary seismic surveys. While I have searched for faults around the Ogarrio field using the available 2D seismic lines, it is possible that additional faults could be present that have not been identified. Experience at other sites has shown induced seismicity occurring on faults that could not be mapped even in 3D seismic datasets (Clarke et al., 2019; Eaton et al., 2018). This is especially problematic for strike-slip faults, which do not cause vertical displacement visible in 3D seismic.

The expected ground motions from induced seismicity are a pivotal issue. Mexico is classified in seismic zones, which serve as the basis of the construction regulations that establish the minimum requirements for buildings and other civil works to make them sufficiently safe against the effects produced by an earthquake (CENAPRED, 2006). The Basin is an intermediate intensity zone with infrequent earthquakes, but the Basin also experiences ground shaking generated by larger earthquakes in the subduction zone to the south. The ground motion return periods define the levels of vibration that buildings and infrastructures are expected to withstand.

In addition, there is a social acceptability factor that should be considered. People

living in the zone are used to a certain level of ground shaking, which is low, with a 3.7 average magnitude. Near the Ogarrio site, there have not been any significant seismic events. Therefore, the inhabitants do not expect to feel an anthropogenic earthquake. It is crucial to provide public information and education to improve public acceptance of moderate levels of induced seismicity.

Based on the levels of natural seismic hazard in the region, my recommendation is that induced events of magnitude M_w 4.5 or larger must be prevented. To do so, I propose the implementation of a traffic light system, with M_w 2.5 as the maximum magnitude that should be permitted during the operation of a CCS project. All parties involved in the project, including residents of nearby areas, must be aware of this information. It should be included in future guidelines, along with publicly available earthquake monitoring data. Dedicated local seismic monitoring will be required to operate such a traffic light scheme.

From the start of the project, it is crucial to know how much seismic energy is being released as a result of the injection. During the early stage of any fluid injection project, the cumulative moment release as a function of injection can be defined as:

$$\Sigma M_0 = \alpha V^n \quad , \tag{4.17}$$

where V is the volume stored, n is close to 1, α is the scaling coefficient, which is the scaling between the amount of volume injected and the amount of seismicity released, which tends to remain constant.

Therefore, the volume injected and the amount of seismicity released should be measured. The scaling coefficient can then be determined to ensure that it remains below an acceptable value. If it is below the threshold, this reassures the project to continue forward without generating induced seismicity at a level that could be damaging. This monitoring should be done right from the initiation of the project, as it is currently unknown if large-scale fluid injection in this area may cause earthquakes or not since such operations have not been done before.

CHAPTER 5

PIPELINE ROUTING

5.1 Introduction

The CCS process has many stages that complement each other. Storage capacity is not helpful unless we can connect it to a CO_2 source. There are many ways to achieve this, including pipelines, ships, or terrestrial transport. This chapter will focus on the pipelines as the primary method of CO_2 transportation. Also, it is essential to identify cost-effective routes from CO_2 sources to the storage location. One way to identify them is with a pipeline routing model. Yousefi-sahzabi et al. (2011) described Geographic Information Systems (GIS) as a powerful tool that can be implemented in CCS, allowing the transportation to be carried out most efficiently. I generated various routes from different emission points, such as oil and gas industries, to different injection points within the Ogarrio field. These routes were computed considering different weightings of various obstacles or features present in the area. For instance, an unmovable obstacle such as a building or a protected natural area will significantly influence the path of the pipeline.

In this chapter, I will also review the matched capacities in the area to evaluate if the storage capacity of the reservoir is enough to inject the CO_2 emitted by the nearby industries and for how long can these emissions be stored in the reservoir?. Additionally, it will question whether it could get the same volume in nearby areas if the emissions surpass the storage capacity. This appraisal is based on the preliminary analysis undertaken in Chapter 3. Where I calculated the probable storage capacity in the Ogarrio field through a series of assessments that include seismic interpretation, well log analysis, and interpolation. It was determined that 36 Mt of CO_2 could potentially be stored in an anticline structure present in the three main formations whose characteristics meet the criteria for such activity. It is worth mentioning that it is likely that there are other anticline structures in the nearby area, and they could increase the storage capacity.

To complement this, in Chapter 4, I evaluated the likelihood of fault slipping according to their critical pore pressure and generation of induced seismicity in the area by considering parameters such as fault location, peak ground motion, and pore volume obtained in Chapter 3. I concluded that the site is low risk for fault slip, and the maximum magnitude earthquake allowed is M_w 4.5, to not exceed the natural levels of seismicity that could cause any damage in the region.

The fault information will be considered in the creation of the routes. The pipelines will follow a variable path depending on the geographical and anthropogenic features (i.e., towns, water bodies, buildings, swamps) that could represent an obstacle to the routing. As mentioned before, each feature will have a weight that will determine the direction that the pipeline might take, depending on its impact on the area.

5.2 Objectives

- The main objective of this chapter is to find the best cost-effective pipeline route from the emission points to the injection points.
- To analyse the behaviour of the routes when different weights are assigned to the features that might be present in the route.
- To match capacities in the field by correlating the amount of CO_2 emitted by the industry within a specific distance with the potential storage capacity that the target formations are expected to have.

5.3 Pipelines

One essential step in the CCS process is the transportation of CO_2; this is done by linking emission sources and storage sites. The transportation stage is assessed by costs and regulating frameworks established by the government that prioritize the safety of the people. The method of transport depends on the geographical and economic situation of the project. While in some places, shipping is the best option, the optimal option is a pipeline in most projects, and they are widely used to safely transport significant amounts of oil (Parfomak et al., 2013), gas (Lin, 2015), water (Kracman et al., 2001), and other substances (Melaina et al., 2013), for long distances worldwide. Nonetheless, it is essential to understand how they work and to consider any hazard that has already happened to pipelines that transport other substances to avoid damage.

Moreover, it is proven that pipelines are an appropriate choice for CCS projects, as they have been used for over fifty years, with a low rate of failures (Duncan and Wang, 2014).

5.3.1 History of CO_2 pipeline projects

In 1972, the first commercial-scale CCS project using a pipeline started activities in Texas at the Val Verde gas processing plant. The emissions from this plant were transported to an oil field, its storage scale is 4 Mtpa, it is still operational, and its pipeline is 130 km long. Nine other active pipeline CCS projects, also in the USA, initiated operations between 1970 to 2010. They are merely focused on Enhanced Oil Recovery (EOR). In China, the Sinopec EOR project, and in Brazil, the Santos Basin Pre-Salt offshore project have been operating since that period (Loria and Bright, 2021).

In 2014, in Canada, the Boundary Dam project in Saskatchewan became operative; it captures CO_2 from a coal-fired plant to an EOR facility, and it has a 66 km-long pipeline. Another project in Canada, Quest, was the first project to capture CO_2 emissions from oil sands extraction and transport it through pipelines. Two years later, in Illinois, the Archer-Daniels-Midland (ADM) ethanol facility was the first non-EOR project in the USA to start CO_2 sequestration (Loria and Bright, 2021).

By 2020, there were two more projects in Alberta, Canada, part of the Alberta Carbon Trunk Line (ACTL), which is the largest CO_2 capacity pipeline of the world, with a length of 240 km (Cole and Itani, 2013).

At present, there are 29 functional CCS projects and 106 new projects in development; most of them will use pipelines as their primary transport method (Global CCS Institute, 2021).

5.3.2 CO_2 requirements and composition

The CO_2 transport chain consists of 1) the capture of the CO_2, where is it conditioned or purified to its ideal transportation composition, 2) compression at adequate pressure for the pipeline, where it can be recompressed, and 3) injection in the selected storage site finally.

The CO_2 pipelines must be designed and constructed to reflect the different chemical and physical characteristics of CO_2, including changes in its flow and its composition (Serpa et al., 2011).CO_2 is best transported at its supercritical state, which means that it has the density of a liquid and the viscosity of the gas. Its pressure and temperature must be above 73.8 bar and 31.1°C respectively, and must be dehydrated (Svensson et al., 2004). Moreover, the composition of CO_2 is affected by the emission source and the capture method and equipment; it usually has particles of water vapour, H_2S, N_2, Hg. According to Serpa et al. (2011), these particles can cause pressure increment and temperature descend and have a corrosive effect that could damage the integrity of the pipeline materials, causing cracking. The water is hazardous as it could hydrate the CO_2 and create corrosion.

5.3.3 Pipeline elements

The projects worldwide are different, and they all have specifications related to their purpose; for that reason, some characteristics cannot be standardised. Table 5.1 shows the variations present in CO_2 pipelines.

Feature	Range
Length (km)	1.9 -808
External diameter (mm)	152 -921
Capacity designed (Mtpa)	0.06-28
Pressure min (bar)	3-151
Pressure max (bar)	21-200
Compressor capacity (MW)	0.2 -68
Material	Carbon Steel, Stainless steel

Table 5.1: Features of CO_2 pipelines and its measurement range worldwide, modified from International Energy Agency (2014).

The majority of CO_2 pipelines are made of carbon-manganese steel; a corrosion-resistant alloy steel, however it has a poor resistant to corrosion. A practical solution to corrosion is the use of coatings in the pipelines (Serpa et al., 2011). Other materials such as stainless steel are more resistant to corrosion but more expensive, this and carbon-steel-lined stainless steel are recommended to be used in the transportation of the liquid phase of CO_2 (Adi Jatmoko and Kusrini, 2018).

Then, the pipeline system is composed of the following elements (Table 5.2):

Element	Description
Booster stations	These compressor or recompression stations are located in the inlet and along the pipeline to balance the pressure loss as a result of friction and changes in the terrain inclination; the number of stations depends on the length and inclination of the pipeline.
Metering stations	They read the flow rate of CO_2 and are distributed randomly.
Valves	These devices are evenly distributed that block the flow of CO_2 in a specific section or are ultimately used mainly for maintenance purposes, usually located at 10 to 20 km from each other.
Control stations	Used to remotely control the pipeline status, they constantly gather data (i.e., pressure, temperature, flow rate).
Pigs	Advanced equipment that regularly examines the interior of the pipelines to find any anomalies.

Table 5.2: Elements of a pipeline, according to Serpa et al. (2011).

5.3.4 Pipeline diameter

A pivotal factor in the pipeline design is the diameter, and it varies in function of the pressure and flow rate, which is affected by the volume that will be captured and stored. The pressure is also affected by the velocity and material used; it tends to decrease with

the diameter and pipeline length. Other factors that influence the diameter are length, temperature, viscosity, density, elevation, and friction factor. Moreover, a larger diameter could mean higher costs, while a smaller diameter could mean changes in the pressure and transport speed (Peletiri et al., 2018).

5.3.5 Pipeline construction

This project is only focused on onshore pipelines.

The steps before the construction are the design, routing, and land and right-of-way acquisition. The guidelines and processes to construct a CO_2 pipeline are similar to the oil and gas pipelines. The procedure is quite meticulous and must follow specific standards.

Usually, the pipelines are buried, and in this case, the land is dug in a trench shape with an approximate two to four meters depth. Some pipeline sections (approximately 10 m each) are assembled and welded before putting them in the trench; then, the other sections are assembled. To avoid corrosion, the pipeline is coated and then covered (Serpa et al., 2011).

When there are obstacles such as highways, rivers, swamps, and buildings, usually to avoid issues, the pipelines are constructed below or dug deeper. There is not a specific burial depth. However, the minimum recommended is 1.2 m, and the maximum varies according to the type of soil, the features in the area, and location (International Energy Agency, 2014). Following this, the pipeline is linked to the emission source and the storage site. The boost stations, valves, and metering stations are also installed. Some pressure and hydrostatic tests must be carried out before the operations start (Fractracker Alliance, 2021).

5.3.6 Comparison with gas pipelines

CO_2 pipelines have always been compared with natural gas pipelines. Whereas they have some similarities, such as their framework and construction, their chemical and physical characteristics are not alike.

The design specifications vary in the CO_2 pipeline because of its properties; they should also have thicker walls due to the CO_2 being in its supercritical state; the material should resist freezing temperatures and high pressures. On the other hand, it is possible to re-use natural gas pipelines if they are suitable to handle the requirements for CO_2 transportation (i.e., pressure, volume, temperature). The re-utilization also minimizes costs (Noothout et al., 2014).

Depending on the country and given that pipeline CCS projects are the first of their kind in some places, the CO_2 pipelines are subject to the same regulations and frameworks as natural gas pipelines. Nevertheless, there are countries such as Canada that have already created guidelines for CO_2 pipelines (Noothout et al., 2014).

5.3.7 Pipeline failure

There are two main types of pipeline failures: 1) puncture caused by an external factor, corrosion or material deficiency, and 2) a rupture that ground displacements or mechanic faults can cause. The risk of rupture is more common than a puncture (Koornneef et al., 2009).

Many studies tried to compare the failure risk of gas pipelines with the CO_2 pipelines since some of them are constructed under the same guidelines. Nevertheless, the substances behave differently, and their reaction when vented or leaked is not similar. While natural gas is ignitable, CO_2 is not a flammable substance. Moreover, CO_2 gas is heavier than air and spreads in the atmosphere. Also, it is colourless and odourless; for this reason, it can stay unnoticeable. It can produce headaches, dizziness, increased heartbeat when inhaled and, when exposed for a long time, be lethal (Duncan and Wang, 2014).

When there is a puncture leak, and the CO_2 is in a liquid state will gush out in a powdery white cloud and at freezing temperature. Its dispersion time is affected mainly by wind direction and speed; nonetheless, no air currents increase the chances of CO_2 releasing from pipelines. One way to mitigate this leak is by reducing the valves distances and replacing the pipeline walls with thicker walls (Duncan and Wang, 2014).

Buried pipelines have a different seismic response than the structures located on the ground. Their construction is based on the approximation of ground strain, and their inertial forces are limited and reduced, representing a risk regarding seismic safety (Papadopoulos et al., 2017).

Additionally, there are cases where the ground suffers displacement because of the soil response to the seismic waves, which directly affects the pipelines.

5.3.7.1 Southern California

O'Rourke and Palmer (1996) recorded the damage caused by the pipelines operated by Southern California Gas Company between 1933 to 1995, where at least 11 earthquakes above magnitude M_w 5.8 had their epicentre within the pipeline system. In most cases, there were no damage or displacements even though the epicentre was approximately 5 km from some of the pipelines. However, four earthquakes generated surface ruptures in pipelines constructed before 1930, as they were more susceptible to travelling ground waves; also, the material they were made of oxyacetylene was corroded and currently is discontinued. Moreover, only a small area within the company infrastructure suffered ground deformation related to surface faulting, liquefaction, and landslides.

In other situations, the damage to the pipelines could be due to ground motion changes and the heterogeneity of the ground along with the structural attributes.

5.3.7.2 Mexico City

In 1985 a M_w 8.1 earthquake, damaged the pipelines of the central water system in Mexico City. Although the epicentre was 380 km from the city, the seismic wave propagation was enough to cause lateral spreads, faulting, and landslides that affected permanently the ground where the pipelines were constructed (O'Rourke and Ayala, 1990). These displacements were attributable to the ground motion in the soil, which in the city is a lake zone, increasing the transmission of seismic waves. The pipelines were made of reinforced concrete, and it was found out that this material is not ductile enough to absorb relative displacements between them (Milian, 1980).

Then, it can be assumed that not only do the seismic factors influence the buried pipeline disruptions, but also the material they are made of can be a determinant factor in the amount of damage. Moreover, sometimes the CO_2 is processed and transported with other substances, making the CO_2 more susceptible to corrosion.

5.3.7.3 Sartaria, Mississippi

In February 2020, a CO_2 pipeline exploded in Sartaria, Mississippi. This pipeline was part of the CO_2 capture for EOR project carried out by Denbury Inc, it was necessary to evacuate around 300 people, and 49 were hospitalized. It was found out that the CO_2 was pressurized with hydrogen sulfide (H_2S), and the H_2S increments the corrosiveness of CO_2 and causes considerable health reactions (Zegart, 2021).

Despite this and reported by Koornneef et al. (2009) the failure risk is small compared to natural gas pipelines. It could be reduced by physically securing the pipelines by burying them deeper or adding a concrete membrane.

5.3.8 Impact on the public

The opinion of the society is a determinant factor in the development of CCS projects; for that reason, it is crucial to have an unambiguous communication with the public that might be directly affected by this kind of project.

There is a misconception about this topic. Some people associate unrelated CO_2 industry incidents, fracking and geological storage potential hazards with CO_2 pipelines. On top of that, these pipelines do not represent an observable service or utility in their everyday lives.

In 2010 in the Netherlands, the Barendrecht CCS project was cancelled because the project managers did not explain to the community the project objectives and people were misinformed of the consequences that its development implied (International Energy Agency, 2014).

As previously mentioned, the pipeline risks are relatively low; however, the public must know what risk this kind of project entails. For this reason, basic information about these projects should be available in diverse and accessible formats.

5.4 Features of the area

Features affect and play an essential role in designing a route, their presence might or might not affect its length, and therefore the cost of the route; these features could be natural or man-made.

Several features can be found between the emission sources and the injection sites in the study area. They are part of the physiography, hydrology, and human development in the region.

Each feature is depicted in a vector data file or raster layer that contains its characteristics such as name, type, size, location, and other specifications. These layers form a database that can be modified, merged, or displayed in GIS software (ArcGIS).

5.4.1 Physiography

The study area is part of the coastal plain of the Gulf of Mexico. Therefore, the surface is mainly flat and predominantly has swampy lowlands, generally flooded with herbaceous vegetation (see Figure 5.1). The areas of low hills that are sometimes found in the zone possibly represent areas where positive relief is being created due to the recent tectonic activity of the movement of saline domes and lateral faulting (Perez Rincón, 1959).

5.4.2 Hydrology

The main fluvial network is constituted by the Coatzacoalcos River with its tributaries Coachapa and Uxpanapa, and the Tonala River with its tributaries which are the Zanapa, Tancochapa and Blasillo rivers (Perez Rincón, 1959). The Blasillo River forms the main drainage channel in the Ogarrio area.

These rivers have a slight slope and slow flow; in the rainy season, their flows increase considerably and overflow, forming swamps and lagoons, as well as numerous meanders. The closest lakes and lagoons to the site are La Palma Lagoon, El Rosario Lake, and Yucateco Lake.

The Gulf of Mexico is 24 km north of the Ogarrio field. See Figure 5.1.

5.4.3 Vegetation

Due to the characteristics of the humid tropical climate that predominates in the area, the vegetation is very exuberant; it is higher in the lower swampy areas and hills, and it is low in shrubs. We can find precious woods in wooded areas, such as cedar and mahogany (Alcantara Rojas, 2010). The areas with dense vegetation are in the north, see Figure 5.2.

5.4.4 Crops

The most important cyclical crops in the area are: corn, orange, lime, pineapple , cacao , sugar cane, and rice (INEGI, 1996). Even though the study area is mainly dedicated to

other economical activities, small crop fields are present, as shown in Figure 5.2.

5.4.5 Towns

The Ogarrio field is located in Huimanguillo, Tabasco. This county has approximately 160,000 inhabitants. The most important towns are La Venta with around 9000 people, the village Estación Chontalpa with 5,500 inhabitants, and Francisco Villa with about 3000 residents. All other towns have less than 3000 people living there, and there are many farms and villages 5 km away from the field (Ayuntamiendo Huimanguillo Tabasco, 2019).

Figure 5.3 shows the biggest cities closest to the study area are Las Choapas at 25 km with about 42,000 inhabitants and Agua Dulce at 30 km away with around 34,000 residents; both are located in the Veracruz state (Muros et al., 2021).

5.4.6 Buildings

The most common types of buildings, such as schools, houses, recreation facilities, and industrial facilities, can be found within 40 km of the Ogarrio field.

Mexican Petroleum (Pemex) owns several oil and gas installations throughout the area; these include collection, measurement, compression stations, pumping and distribution stations, separation tanks, drilling platforms, valves, and administrative buildings, see Figure 5.3.

5.4.7 Roads and railways

There are different ways to access the region from any point of the country.

The Transeismic railway connects Coatzacoalcos, a major city at 55 km from the study area on the Pacific coast. Moreover, the Transeismic highway connects Coatzacoalcos with different localities in Tabasco. The main highway that crosses the area is 180D. Some minor roads and paths communicate the small towns within the study area (Alcantara Rojas, 2010). Figure 5.3 displays the roads and buildings present in the area.

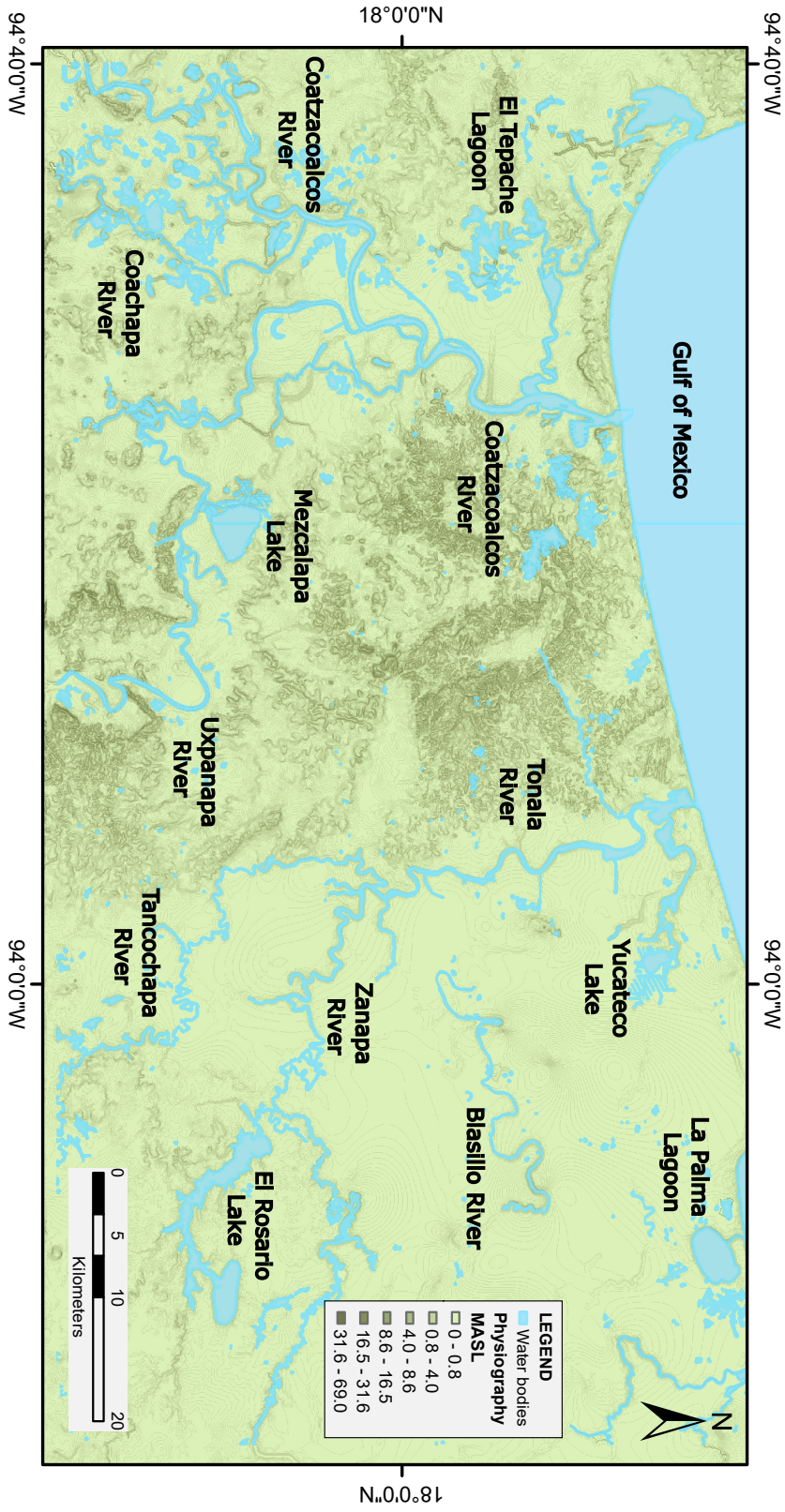

Figure 5.1: Relief and hydrology of the study area.

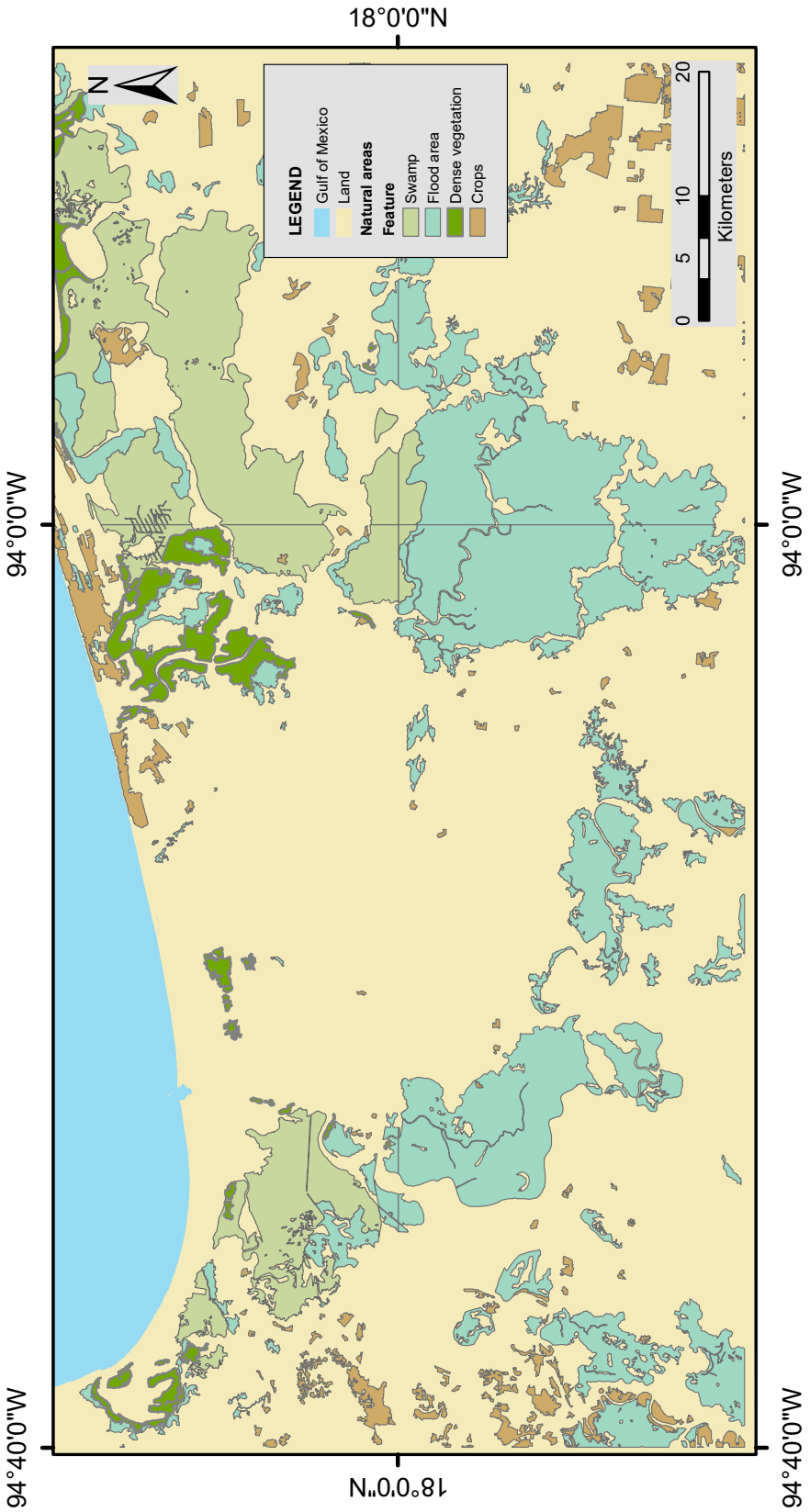

Figure 5.2: Natural features including swamps, flood areas, dense vegetation and crops in the study area.

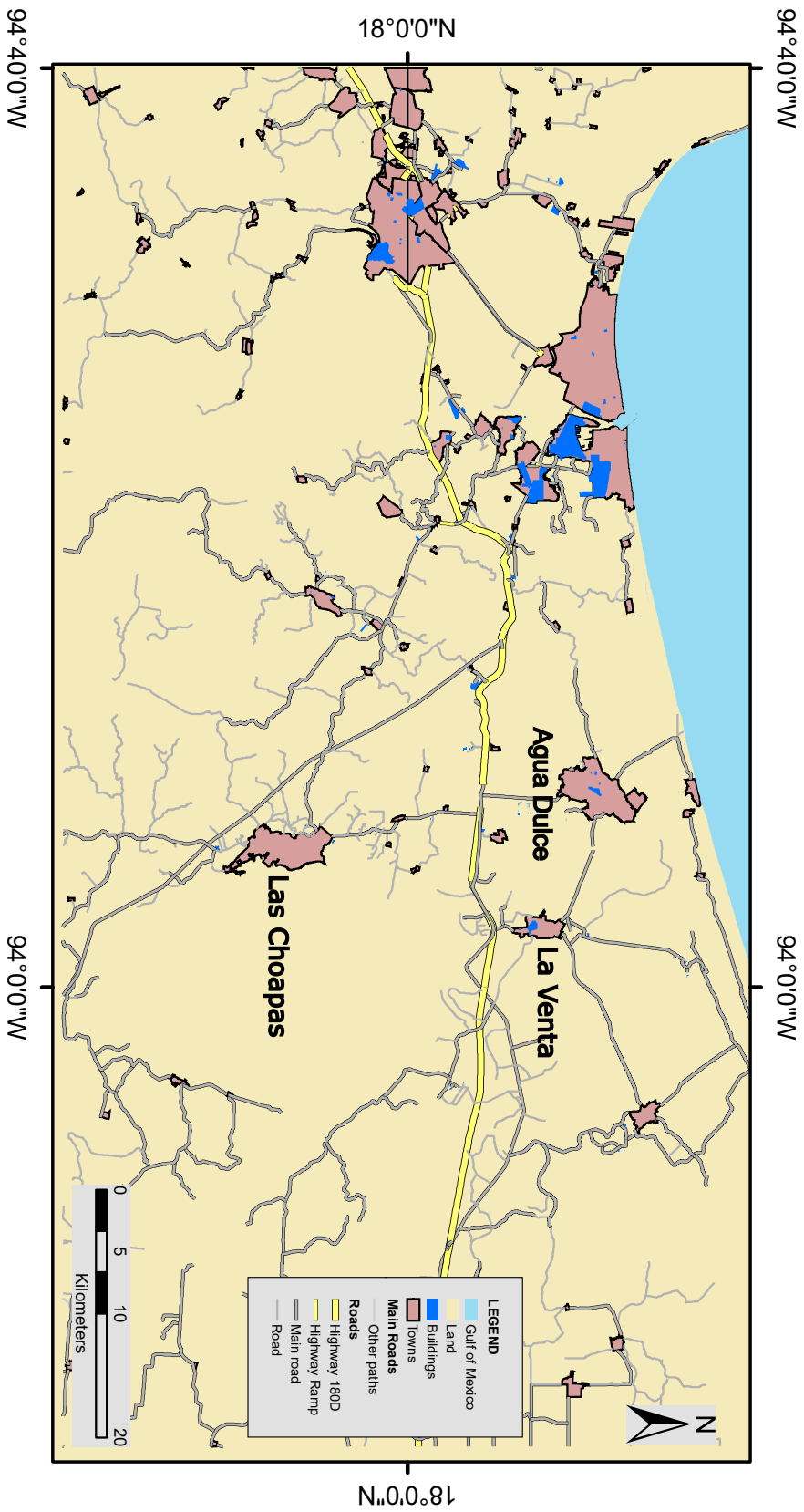

Figure 5.3: Buildings, towns, and roads in the study area.

5.5 Methodology

A practical route selection process is the key to reducing pipeline construction and operational costs. There are traditional techniques to create routes using maps, aerial photographs, and other materials with information about the features within the starting and ending points. However, if there is an unforeseen obstacle or an error, the whole process has to start again, consuming resources and time; also, this type of technique does not consider environmental or social aspects in the routing (Mahini and Abedian, 2014).

On the other hand, GIS technology is a widely used tool to create routes. It generates usable pipeline routing maps by incorporating criteria such as position, geological characteristics, population data, and environmental conditions in a single digital geographical environment (Yildirim et al., 2007).

Since the problem solving includes a diverse set of attainable alternatives, subject to a decision-maker and a vast number of assessment criteria, the creation of routes will be based on the multicriteria decision-making (MCDM) approach. Along with the GIS, the MCDM evaluates and integrates the digital geographical environment with the choices of the decision-maker to gather data to make a final decision (Malczewski, 2006).

An MCDM approach that has been applied in different scenarios, such as to generate gas and oil pipelines (Yildirim et al., 2017; Macharia and Mundia, 2014), establish power lines (Bagli et al., 2011), and create highway routes (Sarı and Sen, 2017), is the "Least Cost Path Analysis" (LCPA). Its purpose is to connect a start point to a destination point through the cheapest path on a surface. This surface or slope map, generated with a Digital Elevation Model (DEM), is a grid, and each grid cell has an assigned cost; this is also known as a *Cost Surface map*. Moreover, the slope map depends on the topography. Therefore, the more slopes on the route, the more expensive the pipeline will be. The cost values or units could be different according to the type of layer (e.g., dollars, metre, time). If there are different layers with different values, the algorithm will assign them a common ratio scale (Bolstad, 2016).

The LCPA is executed using raster data and its algorithm works as follows:

- The starting point has a cumulative cost of zero, and the ending point has a defined value of cumulative cost. The calculation begins by computing the cost of crossing the adjacent cells, the eight neighbouring cells, creating a 3x3 cell window that moves through the surface, and adding the cost to the starting cell; see Figure 5.4.

- The algorithm then searches for the first cell that does not have an assigned value and searches again for its eight neighbours to find those that already have accumulated costs.

- For each cell in the window, the cost of crossing is added and the smallest costs are registered as the new accumulated costs of each cell.

- The cell with the lowest cost is now assigned as the starting cell, and then the process is repeated. If the new starting cell already has a value, the cumulative cost is compared with it; if it is lower, it replaces the current value; if it is higher, the algorithm moves to the next starting cell.

- The process is repeated until every cell is assigned a cumulative cost, generating an *Accumulated Cost Surface map* (ACSM).

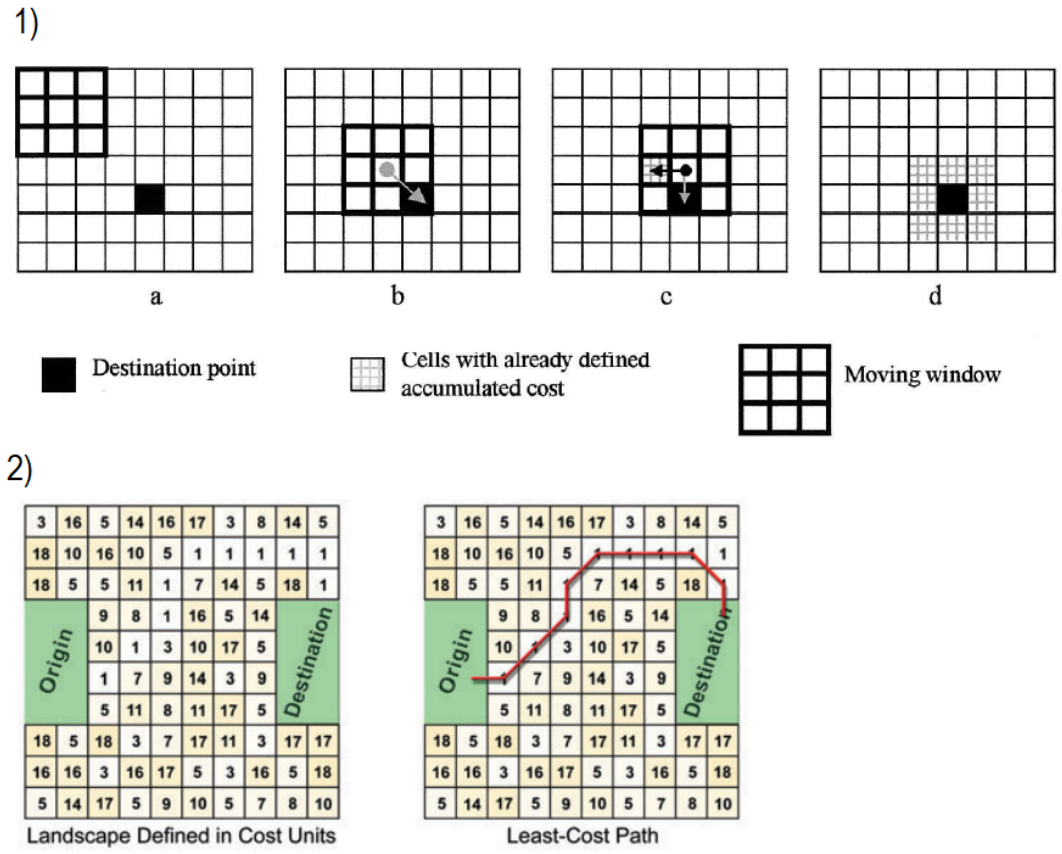

Figure 5.4: 1.a) Shows the 3x3 cell window, where the central cell is the starting point, b) the window moved, finding a new starting point and eventually the ending point, c) shows next possible directions, d) all cells around the ending point have accumulated costs. Taken from Collischonn and Pilar (2000). 2) Surface defined in cost units showing the least-cost path. Taken from (Rudnick et al., 2012).

However, a direction raster is needed to create the least-cost path, which determines the route to follow from any cell. In this raster called *Cost Back Link*, each cell has a code from 0 to 8, 0 is the source location, and the other numbers show the location point out the direction to follow (Sarı and Sen, 2017), see Figure 5.5. After this, the path can be generated. It is worth adding that a single source may be routed to multiple endpoints.

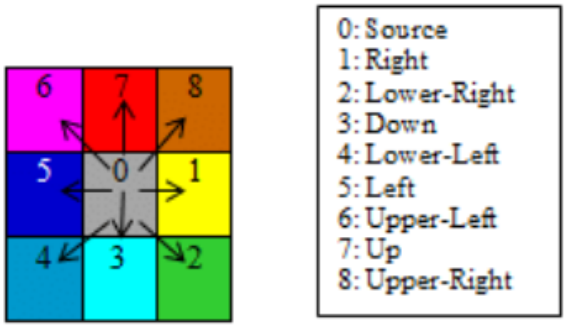

Figure 5.5: Cost back link raster calculation. Taken from (Sarı and Sen, 2017).

Nevertheless, the resulting maps can be affected by obstacles. In order to create the least-cost path, it is crucial to consider the possible obstacles or features in the pipeline route, such as terrain, vegetation, water bodies, buildings, existing pipelines, roads, and geological faults. Therefore, before LCPA was performed, the first step was gathering raster layers with different features to create a database. It includes specific features such as the ones associated with buildings (e.g., schools, industrial facilities, electrical substations, and houses). For this project, all Sureste Basin GIS data were obtained from the National Institute of Statistics and Geography (INEGI in Spanish). Additionally, each obstacle must have a specific influence value or weight (Section 5.5.1).

This thesis defines the start point of the route as the emission point or the place where the CO_2 will be extracted and encapsulated to be transported, which in the Sureste basin is usually located in the oil and gas facilities where refining activities are or were executed. Furthermore, the route endpoint is defined as the injection point, which is the anticline in Ogarrio, where some exhausted wells could be used for injection.

I produced sixteen routes to produce a wide range of routing options, as there are four different emission points and two injection points. The goal of this analysis is to explore and analyse how different weights of each parameter and start and end points affect the resulting routes. The farthest emission point is 70 km away from the possible injection points; this distance is crucial because it will reduce the distance-cost routing.

5.5.1 Assigned weights

The purpose of defining the weights is to lessen negative impacts on the natural and sociological surroundings and to produce the most cost-efficient route from the emission source to the storage point (Yildirim et al., 2017). These weights reflect the importance that the features present in the area can have.

Since most of the features are close to or inside communities, it is worth mentioning that these weights are heavily affected by social, environmental, economical, geographical, and geophysical factors (Balogun et al., 2012). Thus, the pipelines must decrease the probability of damaging and disrupting effects on people and the environment as much as

possible.

To that end, it is crucial to consider the legal frameworks in the area and to consult the opinions of policymakers, environmentalists, pipeline experts, and people who live near the potential location of the pipelines, as their input will help assign the weights of each feature (Balogun et al., 2012). However, according to several authors, this means that the weights can change according to the requirements, priorities, and interests of people and stakeholders (Sarı and Sen, 2017; Balogun et al., 2012; Zwick, 2009; Macharia and Mundia, 2014; Bagli et al., 2011; Durmaz et al., 2019).

Then, in the LCPA, the accumulated cost surface map is created as a function of the weight of the features. Hence, the more heavily weighted the features are, the more the LCPA algorithm will avoid them. Each feature layer has a weight on a scale of 1 to 5. Where 1 is the preferable parameter to follow the route and 5 is not a suitable choice. Table 5.4 details the weight implications.

Weight	**Explanation**
1	Preferable area where to trace the route.
2	Route can cross the area.
3	Route can cross the area but avoid if possible.
4	Route should avoid area.
5	Avoid area.

Table 5.3: Explanation of assigned weights.

Since interviewing people interested in the topic was outside the scope of this project, I performed the LCPA with different weights to portray the main interests that society and stakeholders can have, which are environmental, social, and economic. For example, from an environmental perspective, natural features, such as lakes or protected areas, will be the heaviest features, while from a social perspective, populated areas will be the heaviest.

The generated database contains more than 20 features present in the area. Since weighting, all these features could drastically change the results of this analysis, and due to computational cost, I grouped them into categories according to their characteristics; for instance, a lake and a lagoon can be merged into one feature (water bodies). In this way, the number of features was reduced and represented as geographical data displayed in raster layers that are part of different categories according to their type (i.e., buildings, natural features).

Each feature of the raster layer has a relative weight ranging from 1 to 5 (Zwick, 2009), and each raster should be assigned a percentage influence, indicating its importance in relation to other categories. The influence will vary depending on their features, approximated cost, relevance, and location on the route, as described in Section 5.4. The sum of the influences of the categories must be 100 (ESRI, 2018); see Table 5.4. Then, the weights of each raster cell are multiplied by the percentage of influence to add the outcomes to create a weighting map and the ACSM, see Figure 5.6.

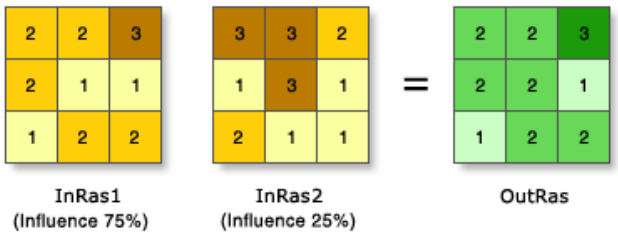

Figure 5.6: Weighted overlay with range values from 1 to 3, where the centre cells are 1*0.75=0.75 and 3*0.25 = 0.75, their sum is 1.5, and because the raster must be in integers, the resulting cell value is rounded to 2. Taken from ESRI (2018).

Category	**% Influence**	**Feature**	**Weight**
Natural features	15	Vegetation	2
		Crops	2
		Protected areas	5
		Flooding areas	4
Buildings	15	Schools	5
		Pemex facilities	5
		Houses	5
		Service facilities	5
Towns	15	Cities	4
		Villages	3
Water bodies	15	Lakes	5
		Lagoons	4
		Rivers	3
Roads	15	Highways	4
		Main roads	3
		Minor roads	2
Slopes	10	Slopes	3
Faults	15	High risk	5
		Low risk	4
Total influence = 100			

Table 5.4: Categories, their features, and an example of their relative weighting hierarchy used for the LCPA.

It is worth mentioning that the building features weight 5 because they are immovable, while the towns feature weight 4 and 3, as they are sparsely populated in the area, and the houses are usually far from each other.

According to chapters 3 and 4, there are no significant faults close by, and the seismic activity is relativity low. However, at least two faults within the study area could cross the possible routing paths; in this case, to avoid any induced seismicity, a radius area of 2 km away from the faults will be taken as the “faults” category.

Note that the existing pipelines will be used as a reference in creating the routes, but they will not be considered in the weight factors as they do not directly affect the routing.

Figure 5.7 shows the three outcome rasters of Route 3 (R3) produced during the LCPA to understand the methodology better. The weighted overlay map shows the heaviest features in green, which means that the route can only go through the red cells. The ASCM displays the accumulated cost related to the start point, and the Cost Back Link map shows the direction the route should follow; the least-cost path is represented in this map with a black line.

5.5.1.1 Influence values

As mentioned above, the influence values of all categories must add up to 100%. They were assigned to show the relative importance of each of the features contained in the categories to represent their relevance over the features of other categories in the creation of the least-cost path (Zwick, 2009).

Different values of influence were given for each generated route; see Table 5.5. As mentioned before, I designated the values considering the contrasting preferences that decision-makers and the population could have and whether the categories are present or not.

Category	R1	R2	R3	R4	R5	R6	R7	R8	R9	R10	R11	R12	R13	R14	R15	R16
Natural features	35	35	25	25	25	25	20	20	25	20	25	25	25	20	15	15
Buildings	25	20	20	20	15	15	10	10	15	10	10	10	10	15	20	15
Water bodies	15	10	20	15	15	15	10	15	5	10	10	15	10	15	25	15
Towns	15	10	10	10	10	10	20	20	10	20	20	20	25	25	20	15
Slope	0	10	5	0	5	5	10	5	5	10	5	10	10	10	5	10
Roads	0	5	10	5	5	5	10	5	15	10	5	10	15	10	10	10
Faults	10	10	10	25	25	25	20	25	25	20	25	10	5	5	5	20

Table 5.5: Different values used in the routes.

As it is noticeable, the natural features have a more considerable influence overall since it is crucial to preserve these areas, and they are present throughout the area.

In the majority of the routes, the buildings have high values, as most of them are in populated areas, and some are within a short distance of an oil and gas pipeline. For these reasons, it was feasible to assign them a weight below natural features but above other features such as water bodies. The routes where the value is 10% is because there are few to no buildings in the surroundings.

Almost all towns in this area are small communities or farms with few houses and basic infrastructure; this is why in some cases, their selected weight is lower than the water bodies. However, these towns are located between emission and injection points in other routes (i.e., R13, R14), making it necessary to assign a high influence value.

The water bodies are a common feature since this is a low-lying flat area, and it is expensive to build upon them. Nonetheless, they are not always in the area where the route could be built. Hence, the value is low in routes such as R9.

Since there are not many slopes, the influence value assigned to this category tends to be small.

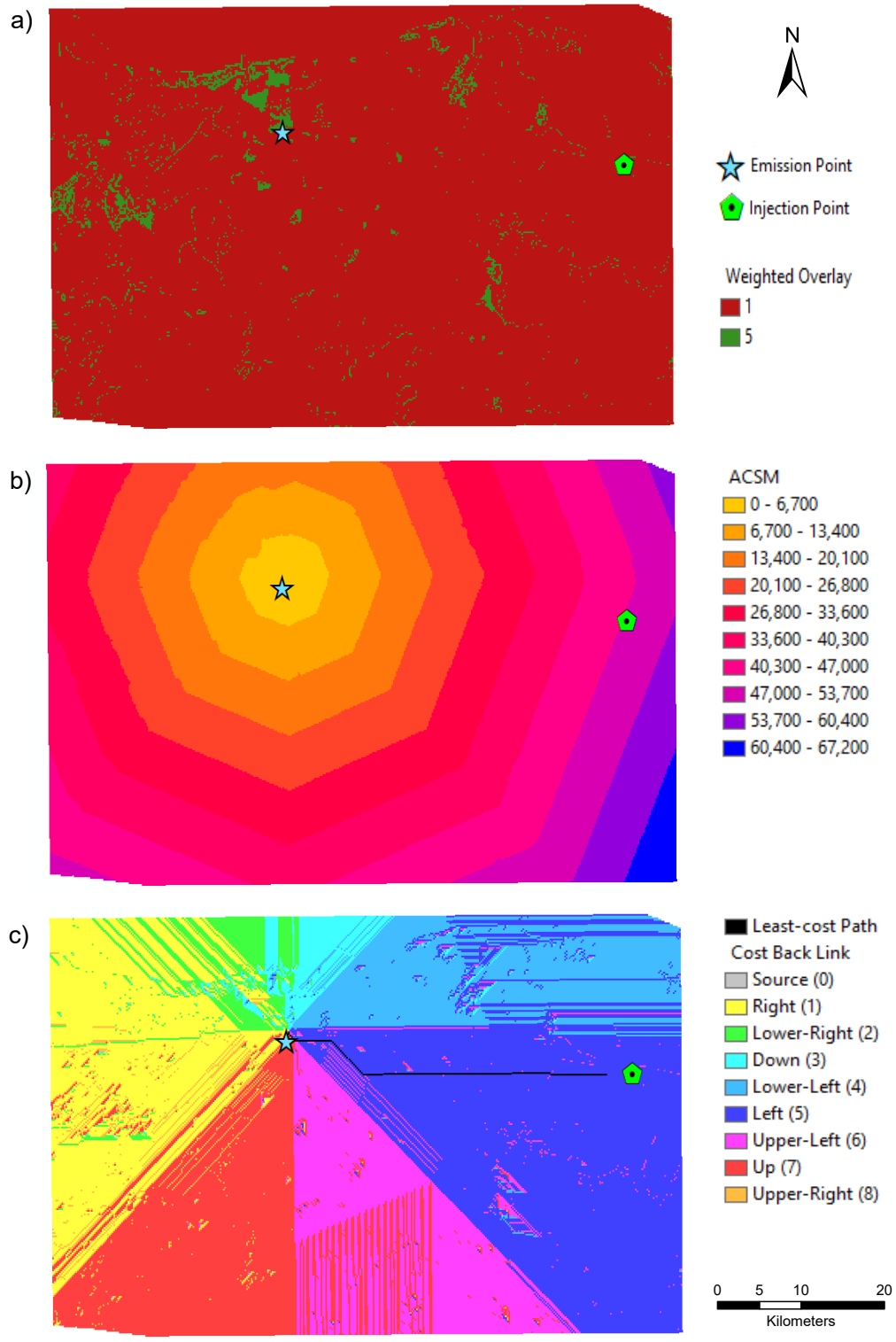

Figure 5.7: Three rasters are generated during the LCPA, a) is the weighted overlay map, b) is the ASCM, and c) is the Cost Back link map with the least-cost path of Route 3.

There is one main road and a highway crossing area; according to Pemex data, some oil pipelines are located near the roads, which means that it is proved that it is viable to have pipelines there. Therefore, they have a minor influence. The R5 is the only route with a high value for the roads, as it was one of the main features present between the linking points.

The fault category is one of the most relevant because any infrastructure nearby could represent a potential risk. It is worth mentioning that there are two faults in the middle of the area where the actual oil and gas pipelines are supposed to go through.

Additionally, I separated the routes by the three main interests and perspectives mentioned previously; see Table 5.6. This table also demonstrates that there could be various options to meet the interests involved in pipeline planning and routing.

Interests	**Routes**													
Environmental	R1	R2	R3	R4	R5	R6	R7		R9			R12	R13	R14
Social	R1	R2	R3	R4	R5	R6		R8	R9				R13	R14
Economic				R4	R5		R7	R8	R9	R10	R11		R13	R14

Table 5.6: Routes created according to the main interests of the stakeholders. R15 and R16 are not considered here because they are the shortest and only connect emission points.

Figure 5.8 displays how the influences of the main interests affect the possible paths that the routes can take. Figure 5.8a shows the environmental perspective, where the natural features and water bodies influence more than the other categories. Figure 5.8b reflects the social perspective in which buildings and towns have more influence than the others. Figure 5.8c indicates the economic perspective in which slopes and buildings have the most significant influence. Note that the faults category has a great influence on the three scenarios.

5.5.2 Routes comparison

5.5.2.1 Emission Sources and Injection Points

Only four emission points were considered for this project due to their emission amount and distance. Two of them are oil and petrochemical complexes owned by Pemex, and two are electric power generation installations working for Pemex (see Table 5.7). All of them are less than 70 km away from the potential injection sites; this distance is because the other biggest emission points are closer (less than 10 km) to other mature fields that could be CCS sites.

The total emissions of these plants are 2 CO_2 Mtpa. This information was obtained from the Pollutant Release and Transfer Registry (RETC in Spanish) website (SEMARNAT, 2019). Figure 5.9 shows the location of the emission and injection points.

- The Complejo petroquímico Pemex Morelos (Pemex Morelos Petrochemical complex) is emission point 1 (EP1), 44.8 km away from the two injection points.

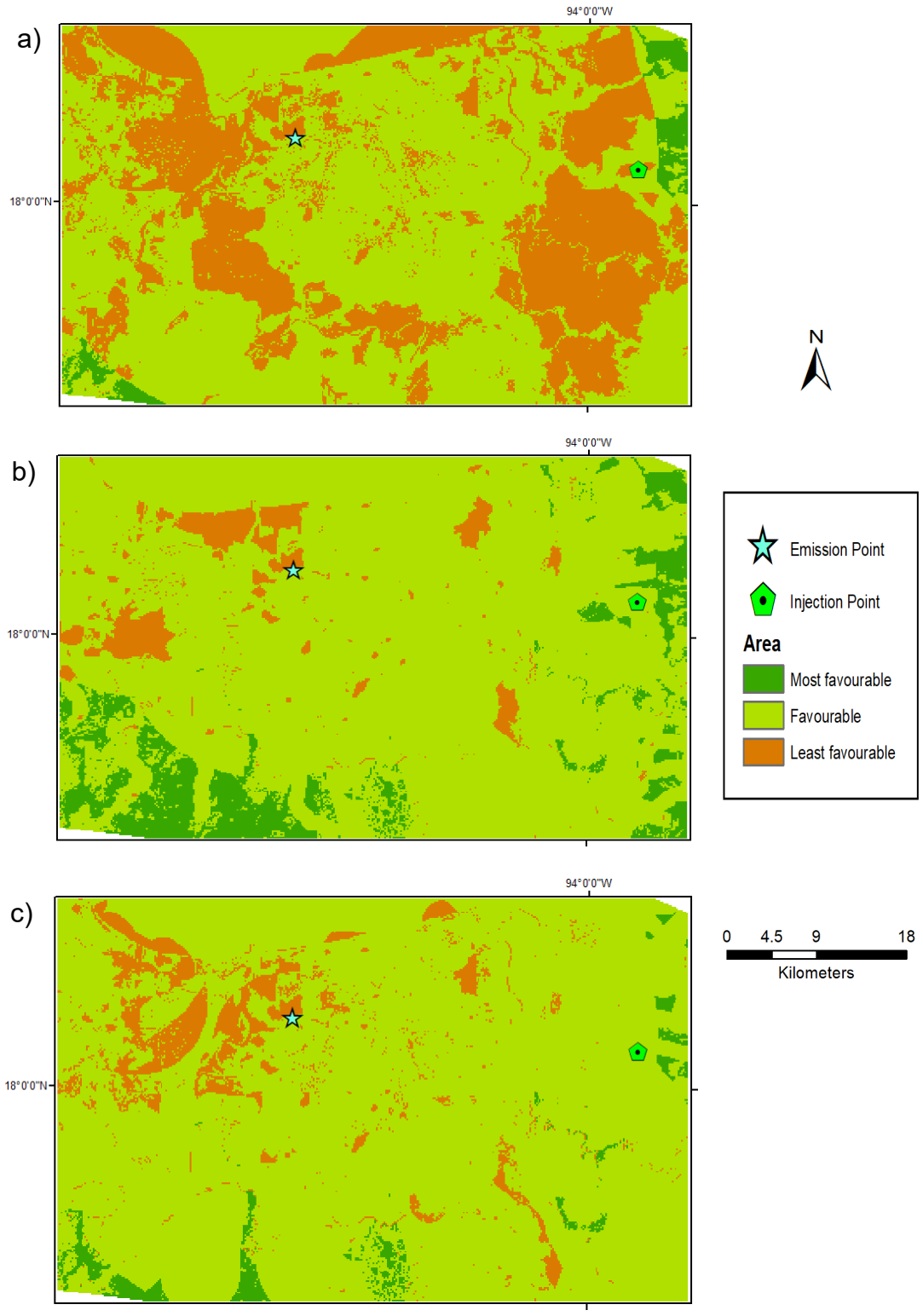

Figure 5.8: Representative weighting maps of the influence of the categories from an a) environmental, b) social, and c) economic perspective. The orange colour represents the least favourable area to follow a path, the light green is a favourable area, and the dark green is the most favourable area.

Company name	Description	CO_2(Mtpa)
Pemex Morelos Petrochemical complex	It operates with nine processing plants where products derived from ethylene and propylene such as ethylene oxide, glycols, High Density Polyethylene, Acrylonitrile are generated (Morelos, 2008).	1.35
Energia Infra	Generation and commercialization of electrical energy using compressed and liquefied gases.	0.51
Clean Energy Cogeneration Cosoleacaque	Energy cogeneration plant using gas turbines and steam turbines.	0.36
Rabasa separation station	Gas-liquid separation battery for the transport of hydrocarbon.	0.25

Table 5.7: Emission sources close to the injection site, considered in the pipeline routing. All the sources are located in the Veracruz state.

- Energia Infra is emission point 2 (EP2), located at 44.7 km from the injection sites.
- The emission point 3 (EP3) is the Cogeneración de energía limpia de Cosoleacaque (Clean Energy Cogeneration Cosoleacaque) at 70 km from the injection points.
- Located at 28 km from the injection points is the Estación de separación Rabasa (Rabasa separation station) (EP4).

The injection points are depleted oil wells from the Ogarrio field, and they are located within the structural traps in the anticline area.

- The well *Ogarrio 598* is the injection point 1 (IP1).
- The well *Ogarrio 669* Injection point 2 (IP2).

5.5.2.2 Routes

Route 1

This route starts at EP1 and ends at IP1. The most heavily weighted category is the natural features which are very close to the IP1. The buildings are the second most heavily weighted, followed by the water bodies and towns; even though these features are sparsely present between the linking points, the influence was set high to demonstrate how it affects the outcome. On the other hand, the route goes through a fault because the fault influence is low. Additionally, neither the slope nor roads categories were included. The route crosses the highway twice, which is not optimal, and it proves that the road category should have an adequate weight in this project. Despite the area being mainly flat, assessing what happens when the slopes have an assigned weight in the following routes will be necessary. It has a length of 50.8 km.

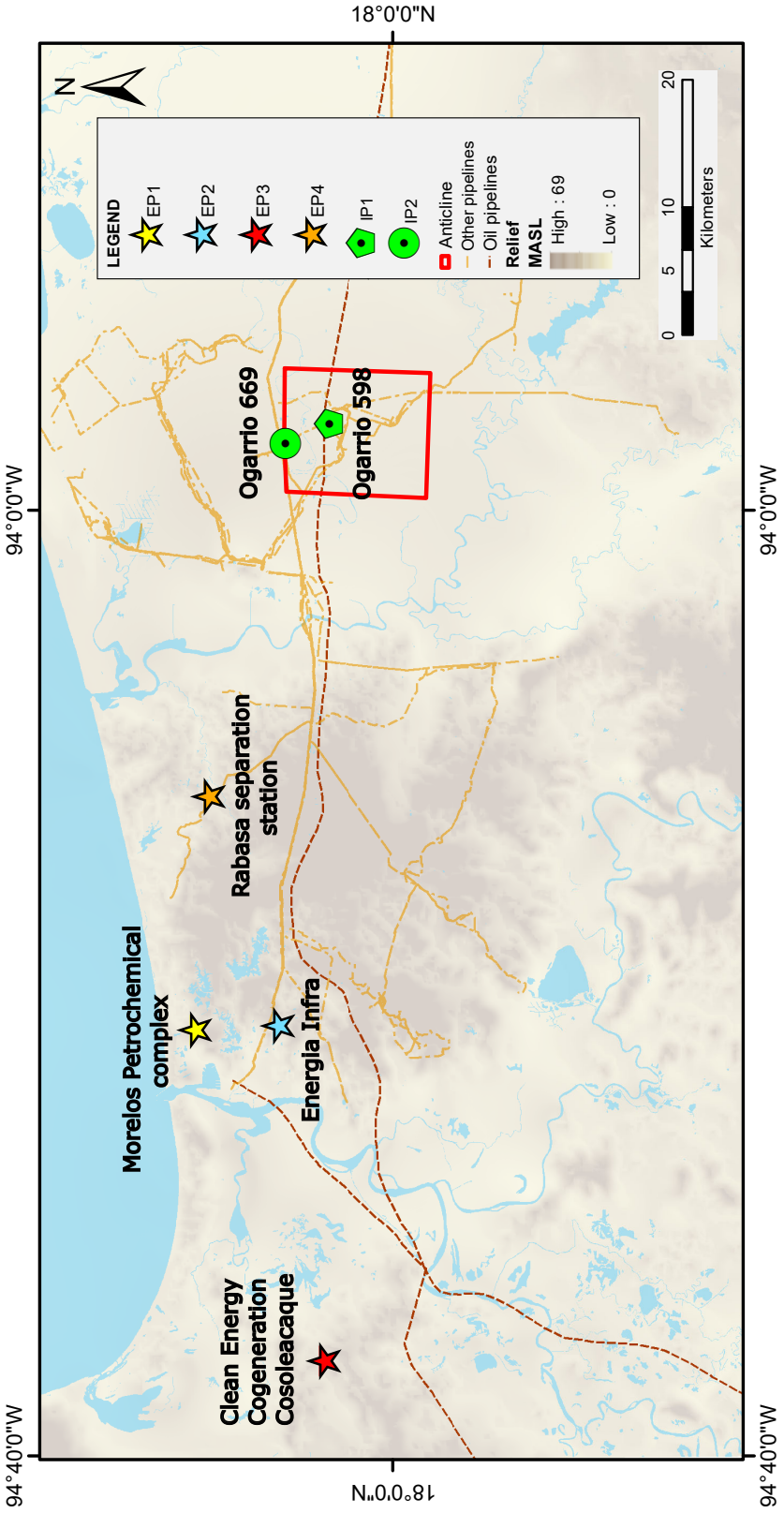

Figure 5.9: Map of the emission sources and injection points, showing the anticline and the existing pipelines in the surroundings.

Route 2

This route also starts at EP1 and ends at IP1; however, the slopes and roads are included with low values, and only the natural features and faults have the same values as R1. Regardless of the assigned weight, this route crosses natural areas and water bodies; it avoids faults. This could be due to an indirect influence from the other categories, as most of them have the same influence as the faults, and they get similarly avoided. It has a length of 49.5 km.

Both routes 1 and 2 are depicted in Figure 5.10.

Route 3

Figure 5.11 shows that this starts at EP1 and ends at IP1. It has a length of 50.6 km. The most heavily weighted is the natural features, followed by the buildings and water bodies. This route passes through a fault, meaning that the fault category should have a higher influence value.

Route 4

This route has the same input and outputs as the previous routes. The categories with more weight are the natural features and faults. For this route, no weight was assigned to the slopes as the zone does not show changes in elevation. The result is a route that only crosses a highway and avoids all other features (Figure 5.11). Its length is 51 km.

Note that routes 3 and 4 have the same path closer to the injection site.

Route 5

This route avoids most features and almost follows the path of the highway and the path of the existing oil and gas pipelines, as shown in Figure 5.12. It could be a suitable option for a pipeline starting from the EP2 to the IP2. It has a length of 47.8 km.

Route 6

The starting point is EP3, and the ending point is IP2. This route is partially comparable to Route 5, as observed in Figure 5.13. Nevertheless, it crosses a town and a river. In this context, it would be necessary to examine the actual site to assess if a pipeline could safely cross these features. It has a length of 76.9 km.

Route 7

Figure 5.14 depicts this route, it starts at EP1, and its destination point is at IP2. In this one, the buildings, faults, and towns have more weight. The outcome shows a route length of 47.4 km that does not avoid one fault and crosses the natural areas.

Route 8

The start point of this route is at EP1 and ends at IP2, with a length of 48.3 km, see Figure 5.14. The faults are the most heavily weighted category, and despite the natural features being the second most heavily weighted, the route crosses them. The routes may go through the natural features because they are the most extensive feature, making it difficult to avoid them without making a significant turn, extending the length of the route quite significantly. The slopes and roads have the same low weight.

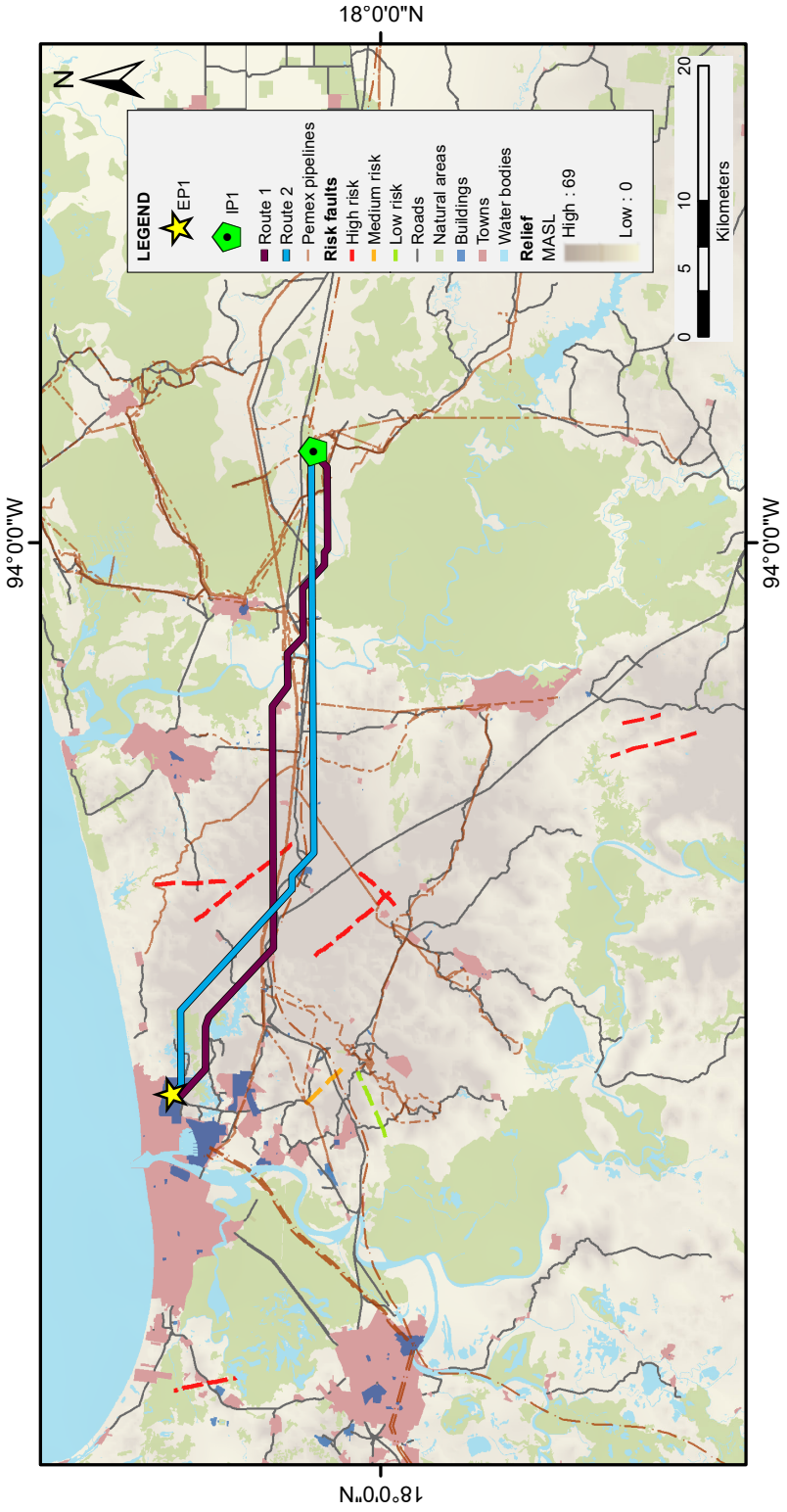

Figure 5.10: Routes 1 and 2.

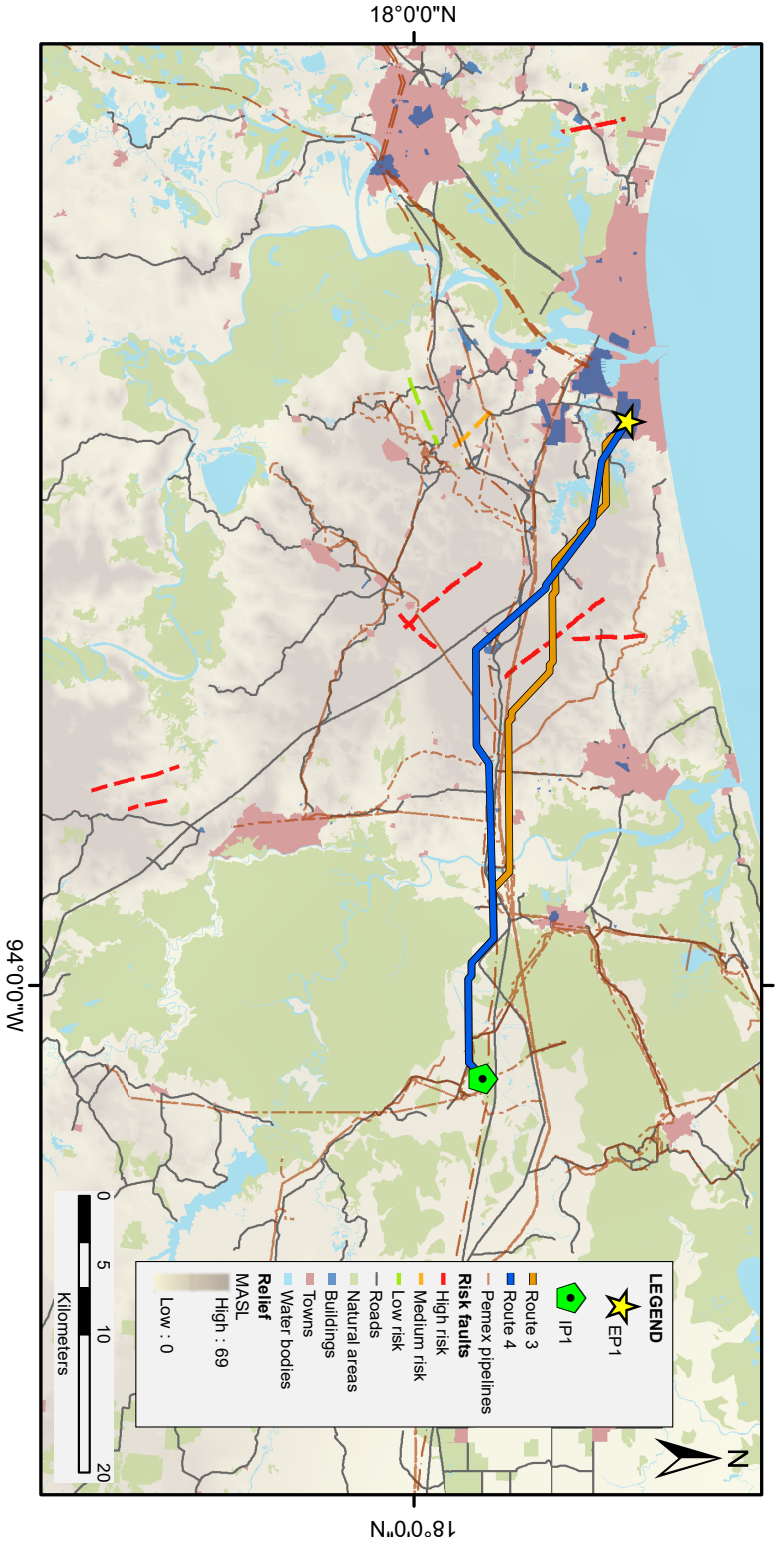

Figure 5.11: Routes 3 and 4.

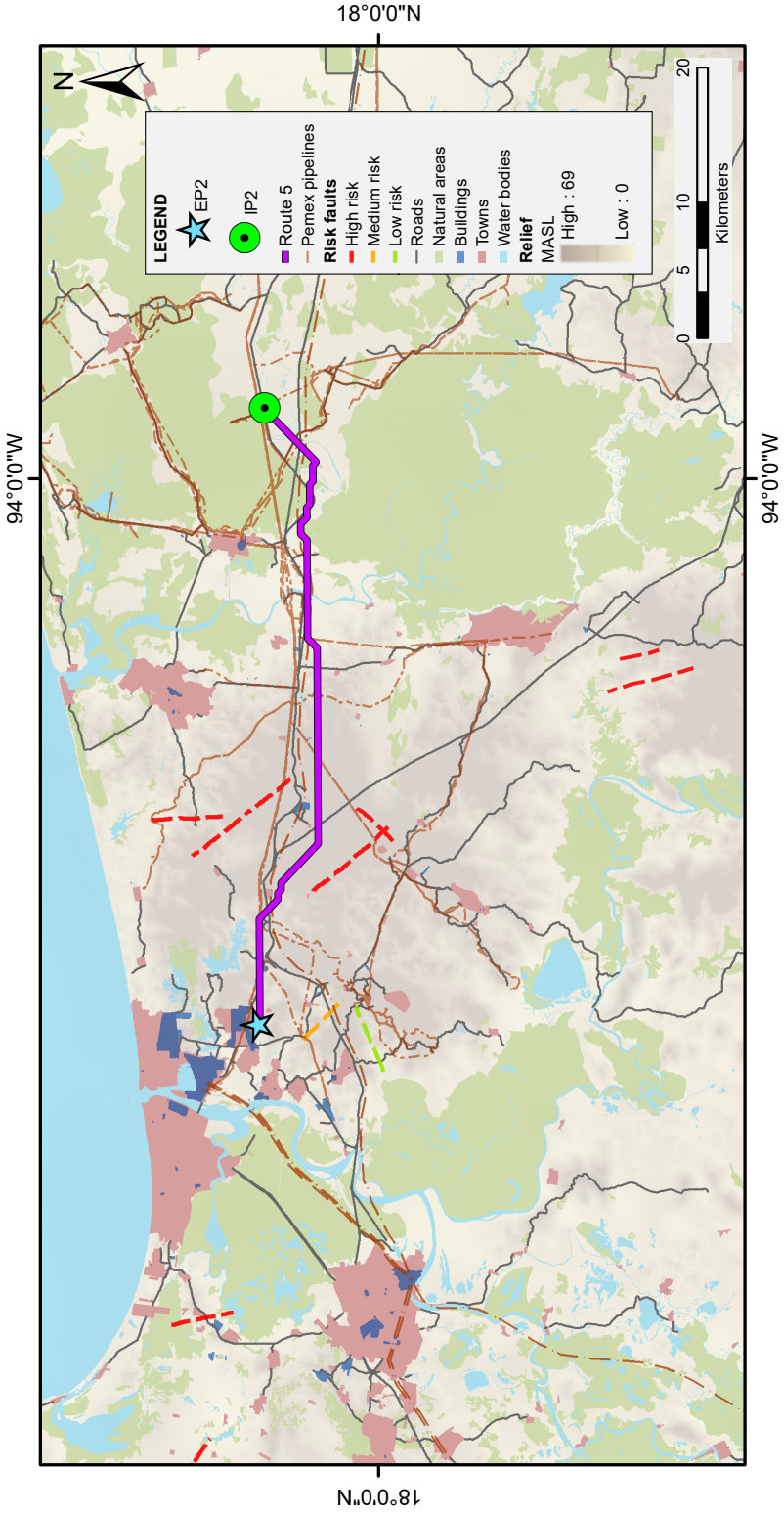

Figure 5.12: Route 5.

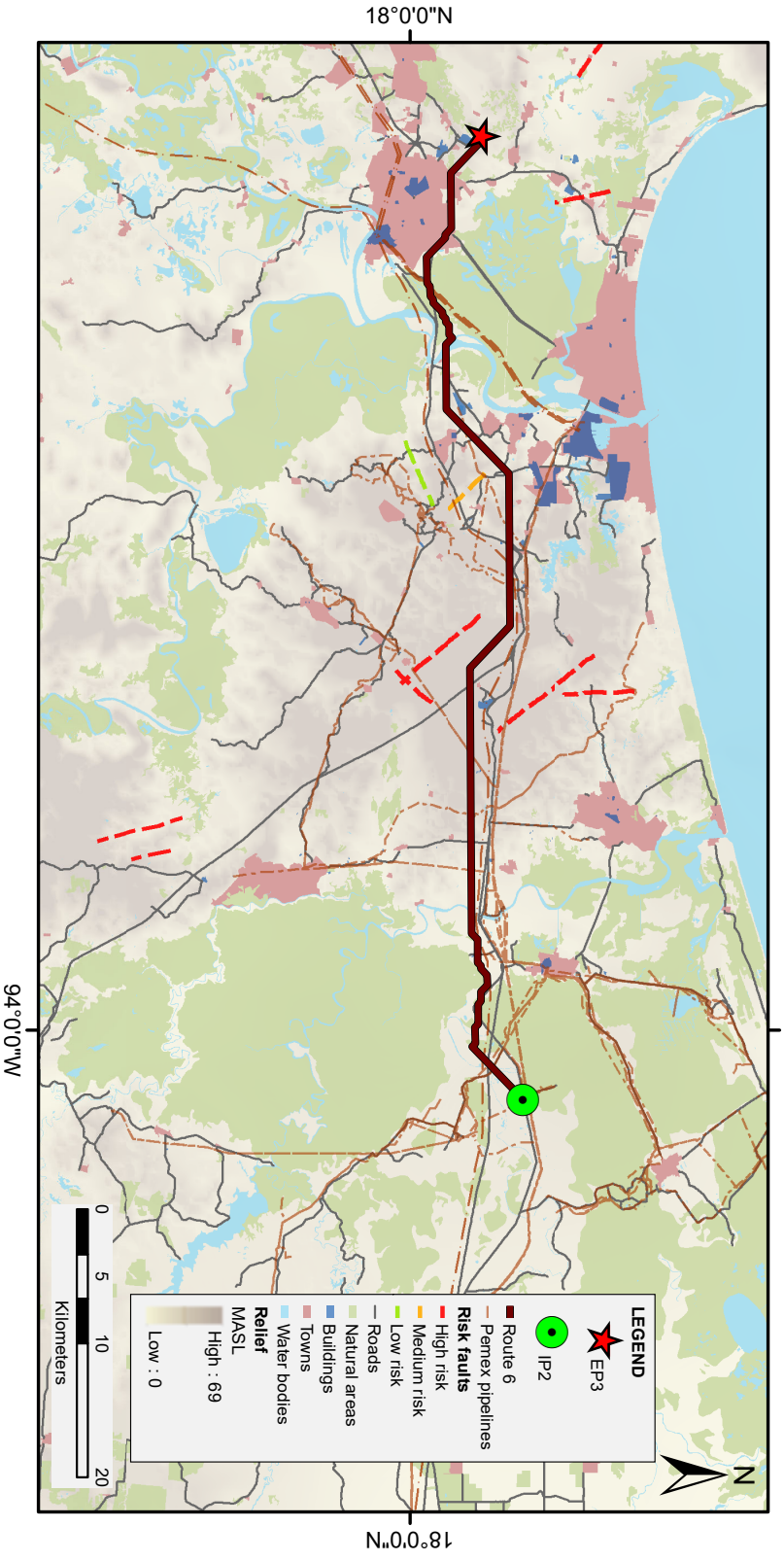

Figure 5.13: Route 6.

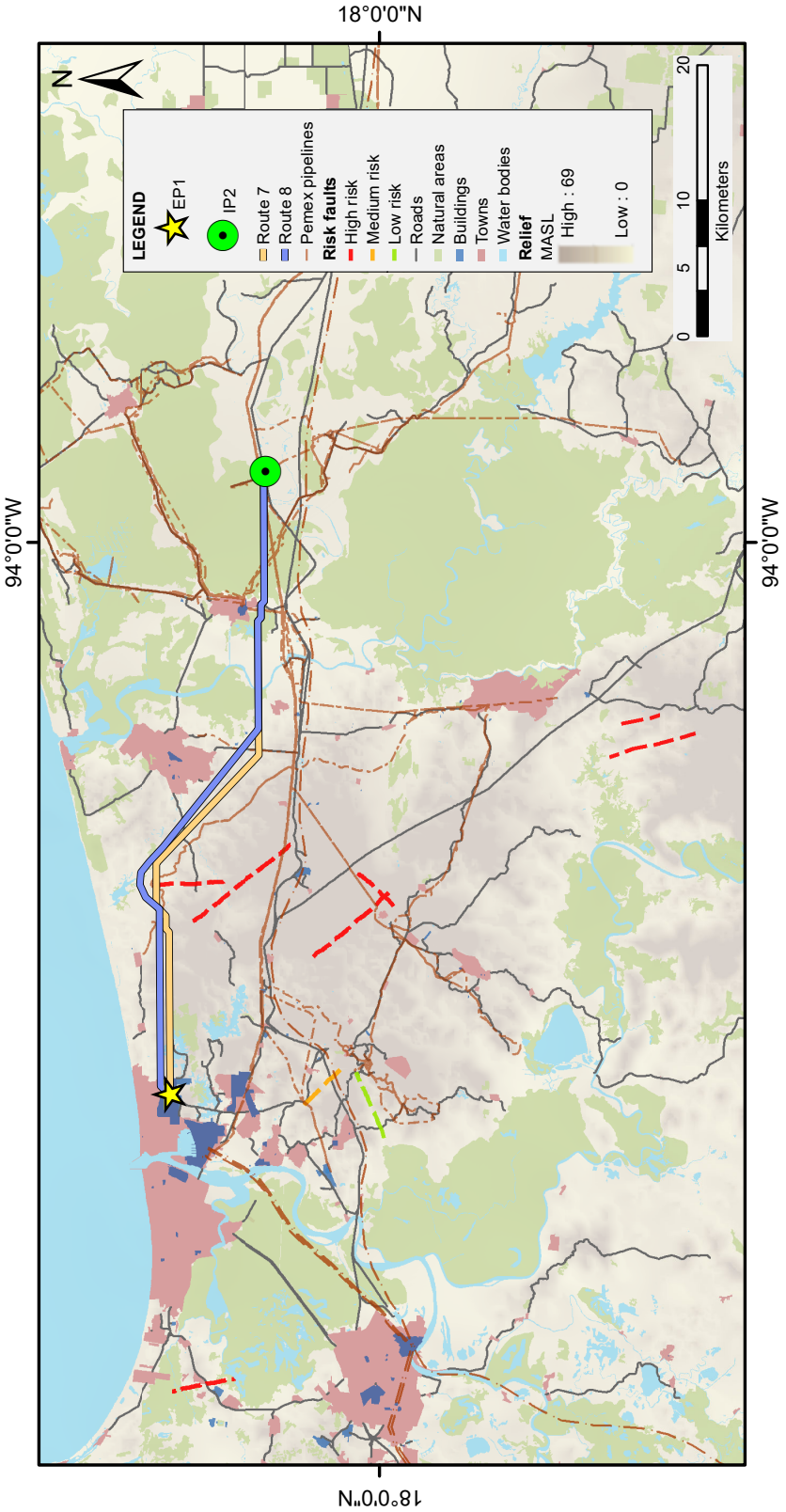

Figure 5.14: Routes 7 and 8.

Route 9

Faults and natural areas are the most heavily weighted categories, while the rest of the categories have low values. The outcome of this route seems viable, as displayed in Figure 5.15. The start and endpoint are EP2 and IP1, respectively, and it has a length of 48.5 km.

Route 10

Despite the towns and faults and natural features being the most heavily weighted, it crosses the natural features; this could be due to the value of the influence of the other categories, which are the same. The length is 72 km. The start point is at EP3, and the ending point is at IP1, see Figure 5.16.

Route 11

This route has the same start and destination point as route 10. However, the weights on this route are different from that route, as shown in Figure 5.16. Again, the most heavily weighted are the faults and natural areas, whereas the slope and roads have lesser weight than other categories. This route is similar in some points to route 10, but it does not avoid completely natural features and is less straight than route 10. The length is 75.6 km.

Route 12

It starts at EP4, ends at IP1. Its length is 32.7 km, refer to Figure 5.17. Despite the most heavily weighted values are the natural features and towns, it crosses some extension of them. The values of the other categories are rather homogeneous.

Route 13

Figure 5.17 show that this route starts at EP4 and its destination is at IP1, with a length of 32.7 km, and in contrast to route 12, the towns and roads have more influence than route 12, and the faults have meagre influence. This route avoids most of the obstacles.

Route 14

The weights in this route are different. The natural features and towns are the most heavily weighted, followed by water bodies and buildings. The faults have a low weight due to the absence of faults present between the points. The result is a route that avoids everything except for the roads, albeit they are small roads, as displayed in Figure 5.18. Its start point is at EP4 and ends at IP2. With a length of 32.3 km.

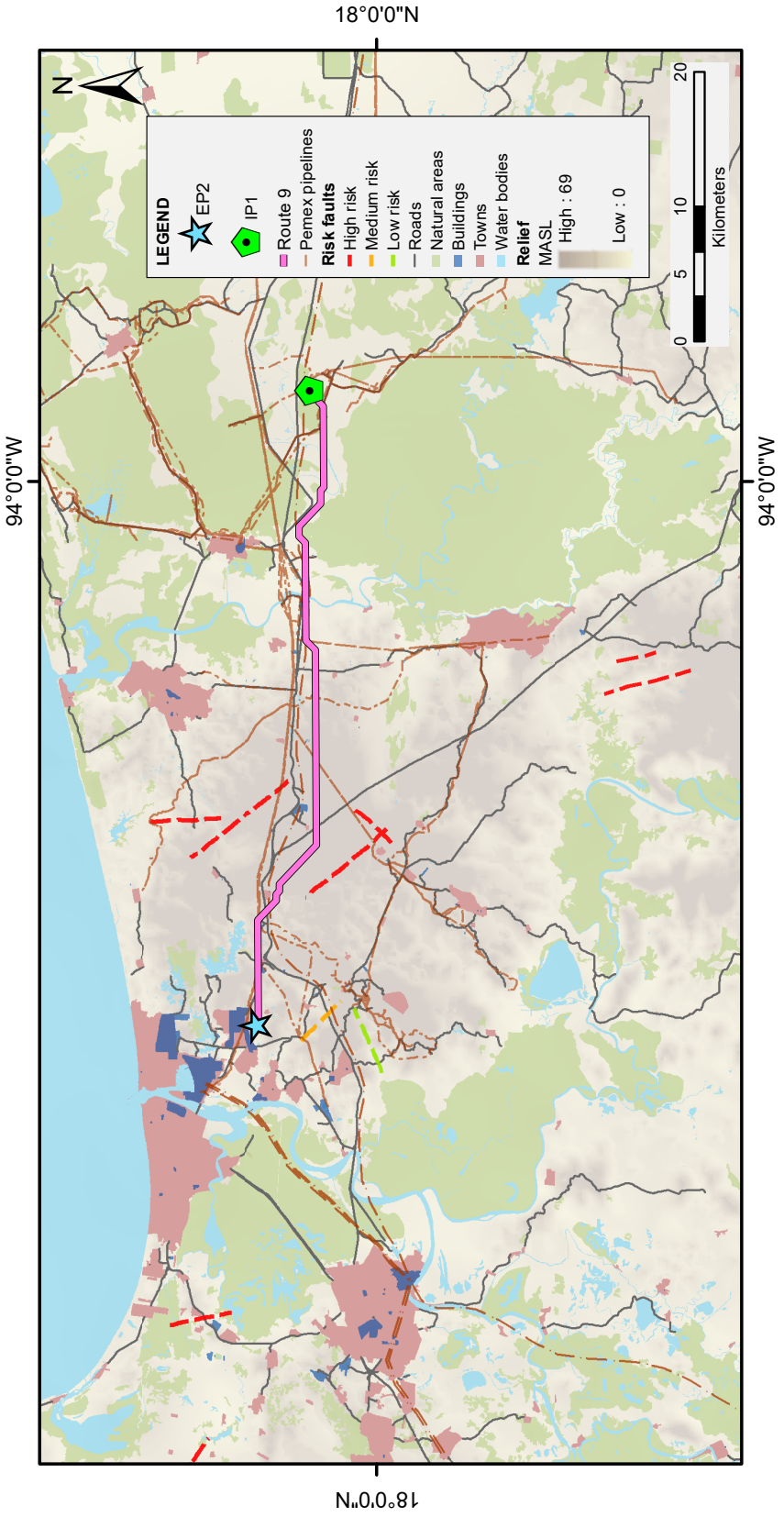

Figure 5.15: Route 9.

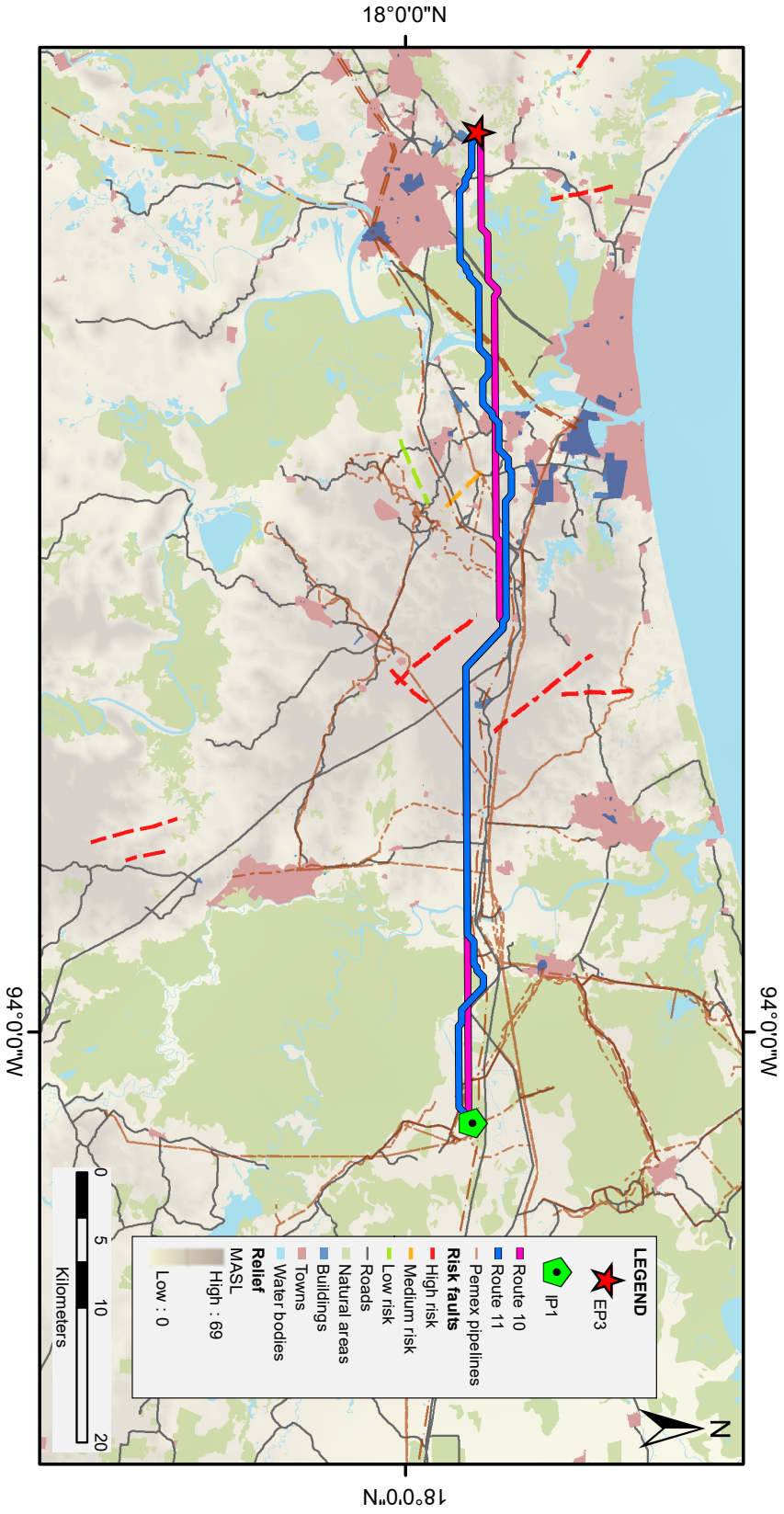

Figure 5.16: Routes 10 and 11.

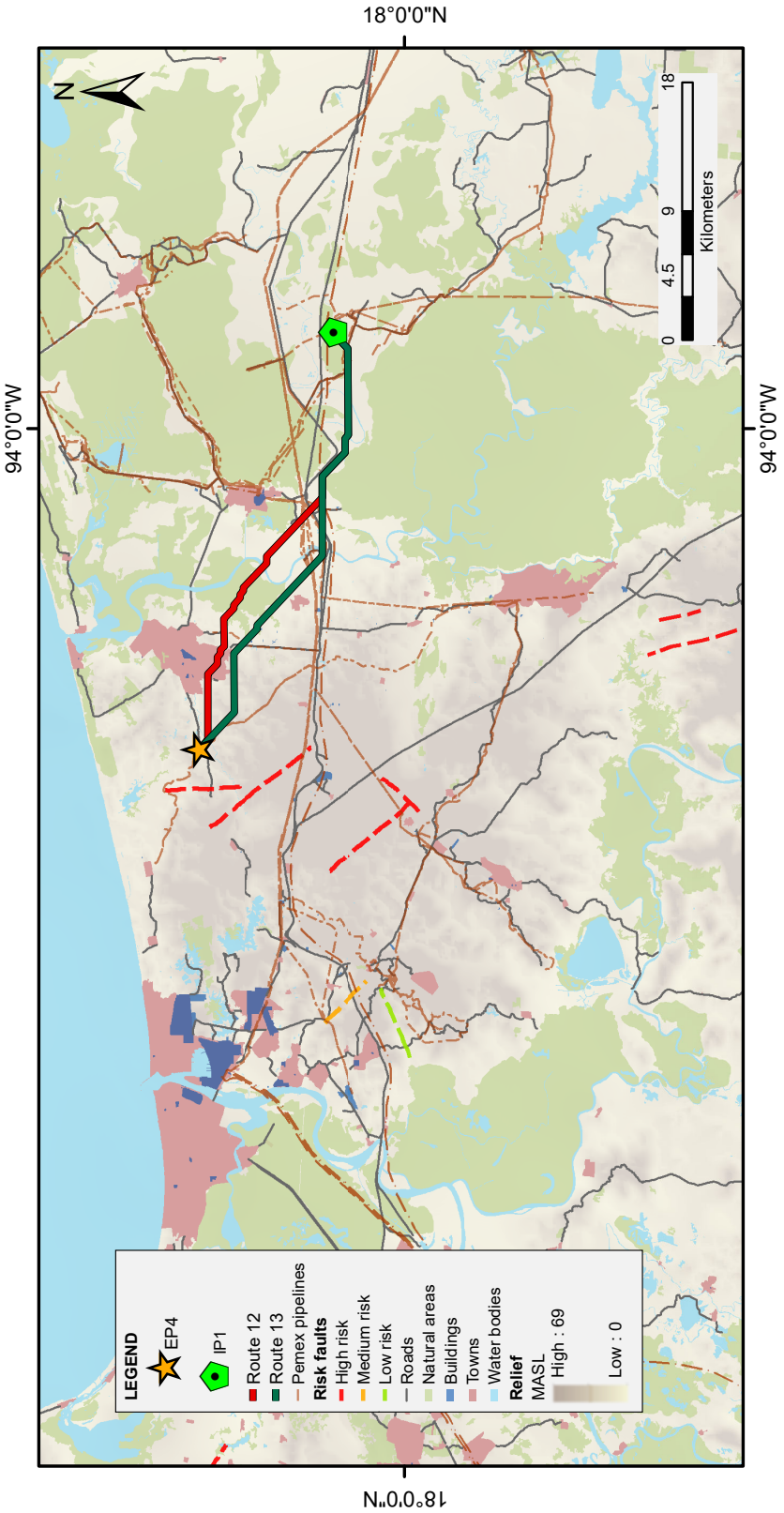

Figure 5.17: Routes 12 and 13.

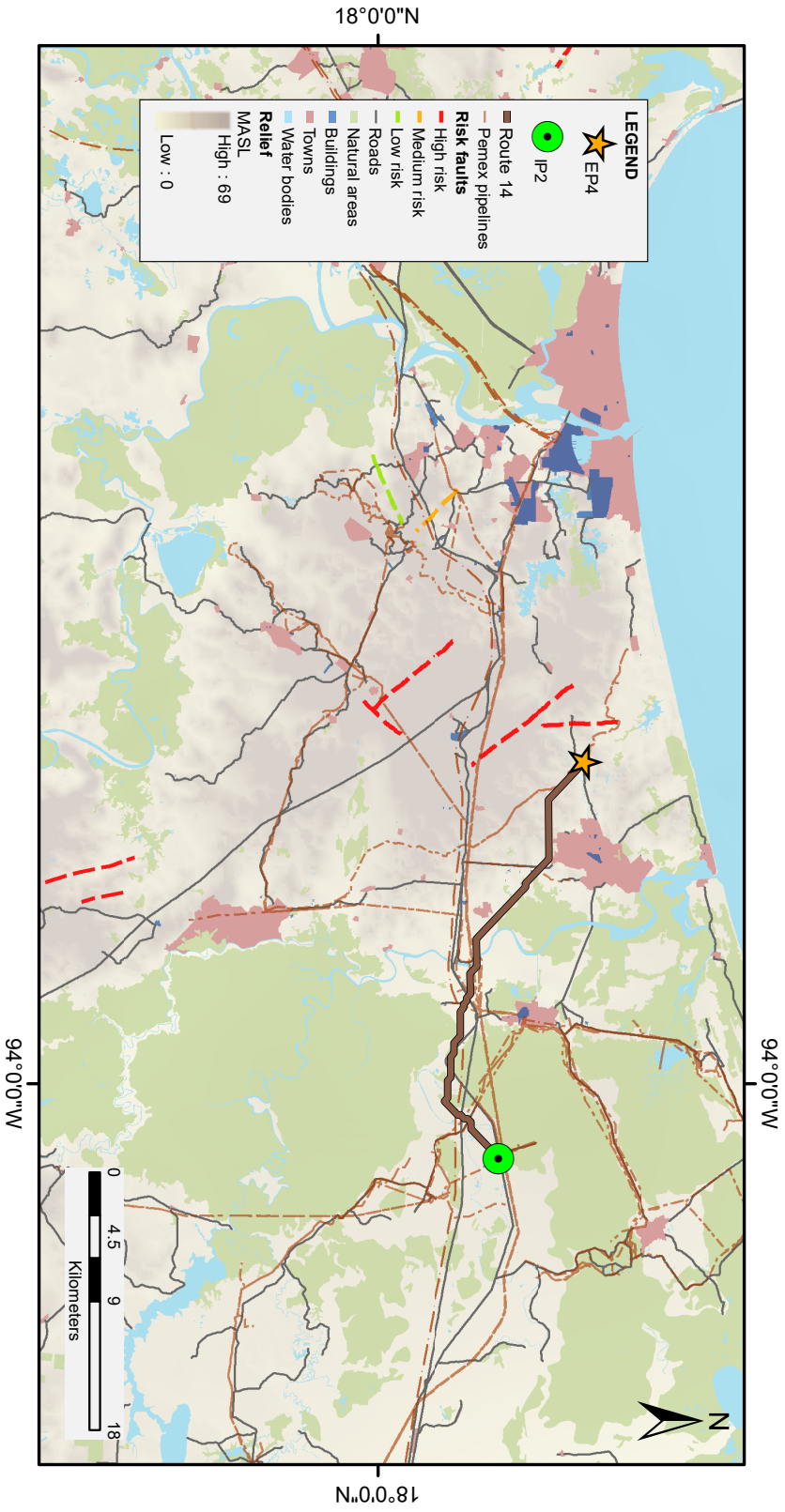

Figure 5.18: Route 14.

Route 15

As depicted in Figure 5.19, this route links EP1 to EP2, since they are approximately 6 km away from each other and according to Fritze (2009) the pipeline costs could be reduced by connecting emission sources into a single pipeline and then connecting them to the store site. This route is 7.5 km in length. The most heavily weighted category is the water bodies, followed by the buildings and towns. The rest of the obstacles have low weights because they do not influence this route.

Route 16

This route also connects two emission points, EP1 and EP4; they are 17 km from each other. The only notable feature between these points is a fault; for this reason, it has the most heavily weighted value while the other features have a similar weight. The result is a route with a length of 19.4 km that correctly avoids the obstacles, refer to Figure 5.19.

The route between EP3 and the other emission points was not computed because it is further away from the others, around 26.5 km, and there are numerous features to avoid. Therefore, it is better to connect directly to the injection points.

An extra option is to follow the existing pipelines without considering the parameters. Nonetheless, since that information is not entirely available to the public and there are only some vector data files with an estimated location, and as mentioned in Section 5.5.1, these pipelines will be used only as a reference for this project.

Note that more routes were generated; however, they were not considered for the final analysis, as they failed some basic criteria or did not iterate the weights properly.

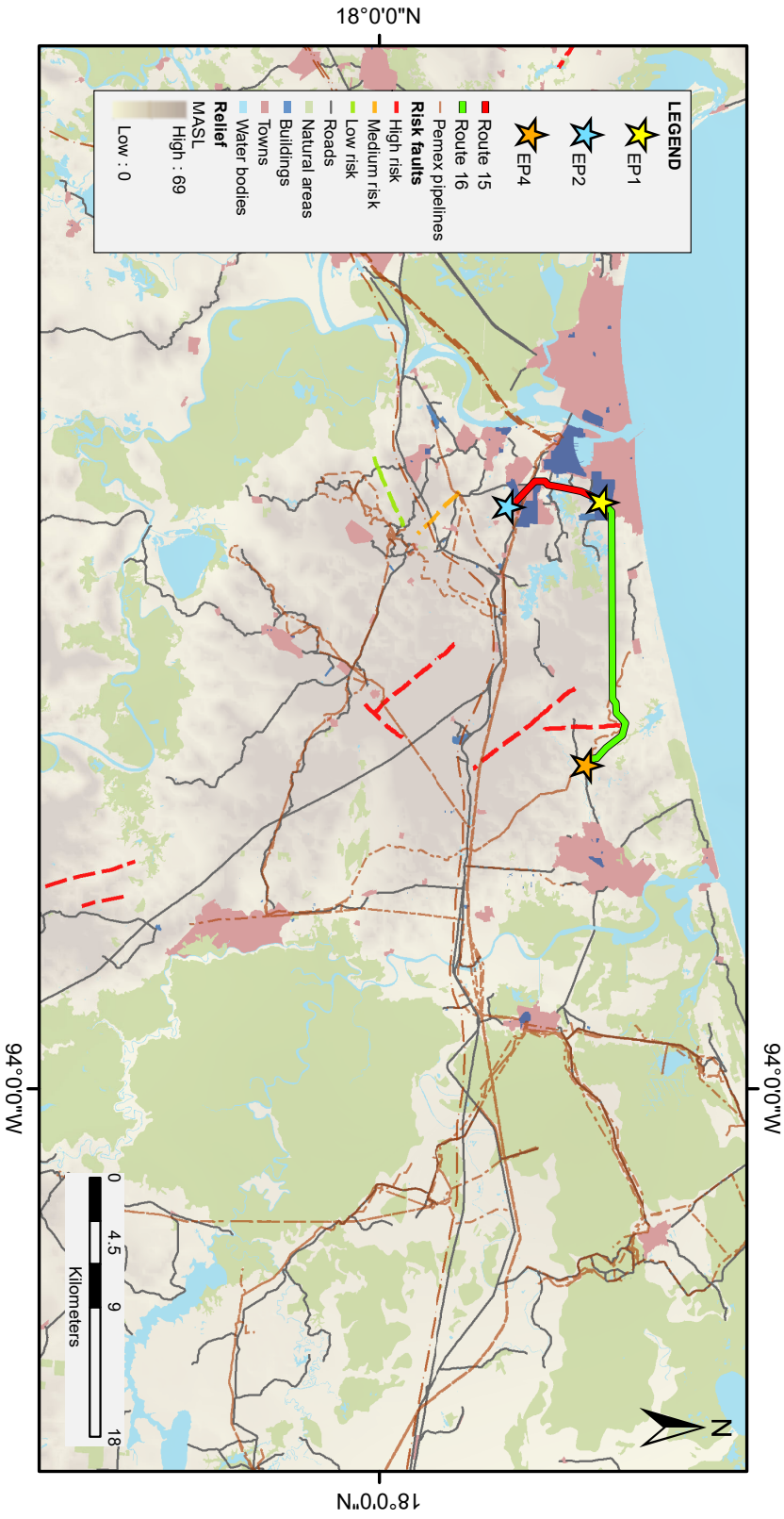

Figure 5.19: Routes 15 and 16.

5.6 Discussion

5.6.1 Results of routing algorithm

The four routes that link the EP1 and IP1 have different outcomes; while R2 (Figure 5.10) and R4 (Figure 5.11) avoid the present fault in the middle, the path followed by R2 seems to be straighter, and it crosses most of the other features, whereas R4 looks smoother than R2. Moreover, R1 and R3 cross the fault, but their overall path is quite different. All these variations are a function of the influence values chosen, see Table 5.5. For instance, the influence values of R1, R2, and R3 are the same for the faults category (% 10), and for the rest of the categories, the influences only vary a 5%. However, the influence of the slope and roads varies from 0 to 10% in the three routes, which is also the main difference between the four routes. It seems to indirectly affect the behaviour of the routes closer to the fault area.

The pathways are similar for the two routes from EP1 to EP2; however, the fault in between the linking points is not entirely avoided by R7, while R8 completely avoids it, see Figure 5.14. Only two categories vary a 5% between these two routes, water bodies, and faults. In this case, it seems to be a direct influence due to the change of the weights in the faults category, which demonstrates that the less variation (5%) in the weights, the more considerable variation in the outcomes.

R5 and R6 have the same weights in all categories and the same injection point (IP2), see Figures 5.12 and 5.13. Nonetheless, the emission points are different (EP2 and EP3, respectively), and the route from the start point is different, but it is almost identical from the middle to the destination point. Another similar comparison can be made for R9 and R11, as the EPs are different, and both connect to EP1, see Figures 5.15 and 5.16. However, the weights differ around 5% in most of the categories. On the other hand, R10 has the same linking points and almost the same weights as R11. The faults and natural features have less influence (5%) in R10; for this reason, this route behaves differently as it is straighter than R11, meaning it does not avoid these categories, see Figure 5.16.

R12 and R13 connect EP4 with IP1 (Figure 5.17); the weights vary in the water bodies, towns, and roads and faults categories by a 5% resulting in two different paths where R12 does not avoid the towns and natural features. Since the weight in both routes is the same in the natural features category, it is possible to conclude that the changes in the other categories indirectly influence the outcome of the route.

Despite having different IPs, R13 and R14 (Figure 5.18) have a similar pathway. Only the towns and slopes categories have identical weights, which means that the variations in the rest of the categories do not affect the resulting routes. It is likely that the presence or absence of features between the EPs and IPs determine its direct or indirect influence over the other features and where a slight change in weights could mean a significant difference in the algorithm outcome; in other places, it barely affects the result.

5.6.2 Cost-effective transporting

There are various alternatives to transport CO_2 from the emission source to the injection site, such as trucks, shipping, rail, and pipelines. However, pipelines so far have been suggested to be the most suitable option for transport CO_2 (Metz et al., 2005), since they can be constructed in almost all kinds of environments, including mountains, cities, deserts, and the sea. Moreover, the pipelines can transport CO_2, gas and oil for longer distances than any other available transporting option, and the leakage risk in pipelines is minimal.

The pipeline technology costs are affected mainly by the distance, terrain, amount transported, and its location (Bumb et al., 2009), and offshore pipelines are more expensive than onshore pipelines. The price can escalate if the pipeline is built in rocky terrain, a natural reserve area, or an area with features such as water bodies or significant populations, see Table 5.8.

Terrain	**Capital Cost (USD/inch-Diameter/mile)**
Flat, Dry	USD 50,000
Mountainous	USD 85,000
Swamp, Wetland	USD 100,000
River	USD 300,000
Populated areas	USD 100,000
Offshore	USD 700,000

Table 5.8: Pipeline cost criteria according to Kinder Morgan company, modified from (Grant et al., 2019).

In 2005, Metz et al. divided the costs into three main categories: 1) construction costs that include the materials and equipment needed for its installation and human resources; 2) operations and maintenance (O & M) costs, which involves monitoring and energy costs, and 3) legal, project management, and regulatory costs. There is an established O & M annual cost in the United States of 8,454 USD per mile, and the pig (see Table 5.2) needed to scan anomalies in the pipeline costs 1.4 million USD, plus capital costs per year and installation (International Energy Agency, 2014).

When transported in its supercritical state, the CO_2 must stay higher than the critical pressure in the pipeline. To maintain this level of pressure, recompression stations are needed. Nonetheless, these stations are expensive, Mohammadi et al. (2019) determined that they could cost up to 70 million USD per year (M$/year), and an increment in the pipeline diameter is an effective way to reduce the cost compared with the use of a recompression station. Moreover, the design of a cost-effective pipeline should consider the diameter, distance, wall thickness, materials, and inclination.

Several studies concluded that the transportation and sequestration costs in average settings and terrain vary from \$7 to \$10/tCO_2 (Mohammadi et al., 2019). However, Smith et al. (2021) estimated that the overall cost of a project where some factors such as length, magnitude, monitoring settings, geological features and transport changeability range

from \$4 to \$45/tCO_2.

In the same study (Smith et al., 2021) calculated some standard CO_2 storage and transport costs in different parts of the world, Mexico included. That study used a Base Case in which 3.2 Mtpa of CO_2 were transported in 160 km (100 miles) with a cost of \$11.2/tCO_2 in Mexico, where the transport cost is \$3.22/tCO_2, and the storage cost is \$8/tCO_2. At larger scale (15 Mtpa) and over the same distance, the transport cost will be \$1.19/tCO_2, and the storage cost will be \$6.24/tCO_2, giving a total cost of \$7.44/tCO_2.

The country with the most extensive pipeline infrastructure globally is the United States; to this day, it has over 8000 km of pipelines. The first and foremost projects are Cortez, Sheep Mountain, Val Verde, Bravo, Canyon Reef Carriers, and Weyburn. This one is located on the USA-Canada border, it is 330 km long, transports around 5000 tonnes per day, and its approximate pipeline construct cost in 1997 was \$110 million (Metz et al., 2005). Furthermore, there are CO_2 pipeline projects developed worldwide, some estimated pipeline costs of these projects are shown in the following Table 5.9.

Project	Pipeline Cost	Country	Year	Capacity (Mtpa)	Length (km)	Diameter (mm)
Canyon Reef Carriers	46 million USD	USA	1972	4.4	354	324-420
Cortez	700 million USD	USA	1982	24	808	762
Weyburn	110 million USD	Canada	2008	2	330	305 -356
Quest	140 million USD	Canada	2012	1.2	84	324
Quinshui	39.35 million USD	China	2006	0.5	116	152
Longannet	210 million USD	UK	2011	2	100 On/270 Off	500 to 900
ROAD	100 million USD	Netherlands	2010	5	5 On/20 Off	450
Gorgon	6.4 million USD	Australia	2011	4	8.4	269 -319

Table 5.9: Estimated costs for CO_2 pipelines around the world. Modified from International Energy Agency (2014).

5.6.2.1 Transportation via trucking

The CO_2 transport is not limited to pipelines; in some specific cases where the distances are shorter (maximum 160 km), and the volumes are lower (less than 500 ktCO_2/y), trucking transport is a cost-reduced option. The cost will depend on the trucking acquisition, fuel prices, labour costs, taxes, insurance, and O & M costs. (Psarras et al., 2020).

In 2020, Psarras et al. analysed trucking as a mode of transport and using standard parameters (i.e., fuel price, human resources, transport maintenance, CO_2 tanker container price). For this kind of transport, the CO_2 must be liquefied and loaded in cryogenic tanks and compressed to 1.7 MPa and −30°C. It was determined that the maximum transport payload per shipment is 30 tCO_2 and that the maximum cost is between \$50 to \$60/tCO_2, see Figure 5.20. Therefore, at lesser volumes, the costs are subject to truck purchase and rental prices (Psarras et al., 2017).

A truck hauling study implemented by Psarras et al. (2017) calculated the costs of CO_2 capturing and transporting by considering industries such as glass, pulp and paper manufacturing, and iron and steel processing located at a distance shorter than 140 km

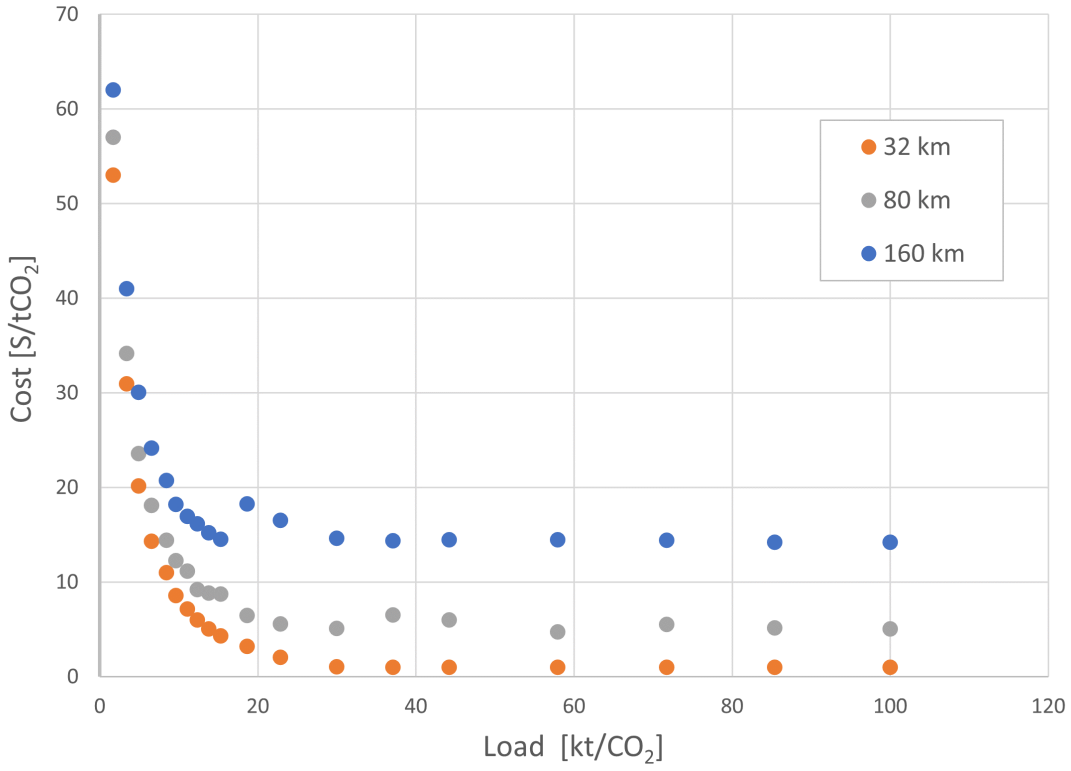

Figure 5.20: Cost of transportation via trucking as a function of load at a distances of 32,80 and 160 km, respectively. Modified from Psarras et al. (2020).

from the storage site. The amount of CO_2 emissions, distance, and the actual CO_2 delivered were the only factors that affected the outcome of this study, where the lowest cost was \$36.96/tCO_2, with a 64 km distance and 33.7 kt/CO_2 emitted per year. The highest cost was \$67.33/tCO_2 with a 140 km distance and 20.8 kt/CO_2. It is worth mentioning that these values only considered the technical operations and should be updated, which means that the costs might increase with the factors mentioned at the beginning of this section.

Summarising, Smith et al. (2021) determined that the cost for transporting through a pipeline and storing CO_2 in Mexico ranges between \$7 to \$11/tCO_2, and this cost depends on the distance and volume of CO_2 transported. On the other hand, the use of trucks could be a convenient option for this project due to the short distance from the capture source to the storage sites (less than 70 km) and the amount of CO_2 that could be transported (nearly 600 kt per source per year). The costs would be less than \$36/tCO_2 according to Psarras et al. (2017). However, there are factors to consider in the transport method selection, such as the existing pipeline infrastructure and the availability of the special tanks and trucks needed for this task.

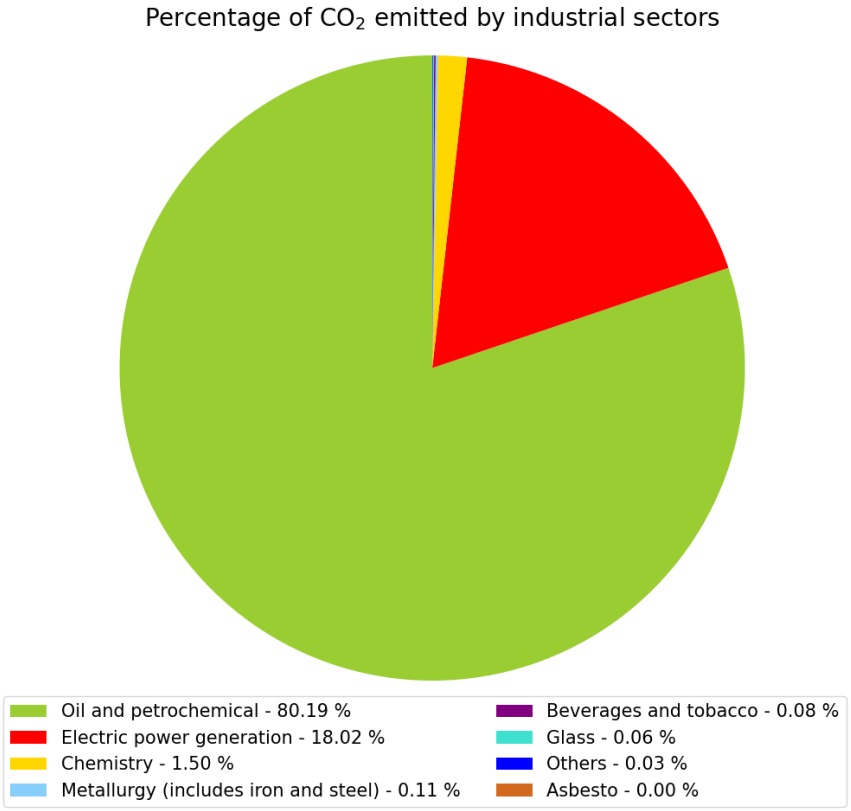

Figure 5.21: Percentage of CO_2 emission by industry sector in the area.

5.6.3 Matched Capacities

There are 75 emission points within a radius of 100 km around the injection points, including industry sectors such as chemistry, electric power generation, beverages and tobacco, asbestos, metallurgy, glass, and mainly oil and petrochemical industries, see Figure 5.21.

Altogether, they emit around 8 Mt of CO_2 per year. If the potential storage capacity for one anticline is 36 Mt CO_2, it would be possible to capture and inject CO_2 from these emission points for four and a half years. Since this is a shorter period than the average duration of a CCS project, it is crucial to select the primary emission sources, which would be the ones with the most significant emission amounts.

The Table 5.10 shows the six most significant emission points that could be the principal targets as they emit around 5 Mt per year; this means that there could be a constant injection of CO_2 for seven and a half years.

Nevertheless, the Gas Processor Centre of Nuevo Pemex and Abent 3T are located within the Níspero and Cactus oil fields. In this case, it would be necessary to study these and other nearby fields to analyse their geological characteristics to find if they are suitable injection points where the CO_2 could be constantly stored underground for a more extended period.

Company name	Industrial sector	CO_2(Mtpa)
Gas Processor Centre of Nuevo Pemex	Oil and petrochemical	2.13
Pemex Morelos Petrochemical complex	Oil and petrochemical	1.35
Abent 3T	Electric power generation	0.63
Energia Infra	Electric power generation	0.51
Clean Energy Cogeneration Cosoleacaque	Electric power generation	0.36
Rabasa separation station	Oil and petrochemical	0.25
Total CO_2 (Mtpa)		5.25

Table 5.10: Largest emission sources near the injection site.

All this implies that the source distance could be reduced from 100 to 70 km, as it was considered in the routing, then other minor emission points could be included in the project. Nevertheless, the emission points used in the routing emit around 2 CO_2 Mtpa, which could be an acceptable amount, increasing the average life of the project to 20 years.

5.7 Conclusions

A crucial thing to consider in the development of pipeline routing is public opinion. In many cases, most people are not well informed about the hazards of hosting buried pipelines or on-ground pipelines.

CO_2 pipelines could imply a higher risk than oil and gas pipelines; for this reason, the community must be aware of their presence and the consequences of disrupting their operations. For instance, the people affected in Sartaria, Mississippi incident were unaware of the pipelines next to their town, as some of them did not know what CCS was. This situation and the Barendrecht CCS project, which was cancelled because people were misinformed about it, could be avoided by informing the general public about this kind of project to obtain their acceptance.

Due to the economic activities of the study area, the population is aware of the oil and gas infrastructure, including existing pipelines and trucks that carry these hydrocarbons. Furthermore, some organized crime groups in Mexico illegally extract oil and diesel from pipelines and vehicles to sell them in the black market. Unfortunately, there have been pipeline incidents like the one that killed 137 people in an oil pipeline explosion in the Hidalgo state in the centre of Mexico in 2019 (Bloomberg, 2019). For this reason, it is imperative to educate and inform the public about the dangers of damaging pipelines and vehicles.

Due to the characteristics (i.e, inland and short distance) of this project, the selection of the transport type is reduced to pipelines and trucks. Both have pros and cons; although the pipelines could be more expensive, they could also be a good option as there is some previous experience in the area. Some pipelines could be reused for CCS purposes, and materials and equipment could also be available at a reasonable price. There is a regulatory framework

and groundwork that could be used as a guide in their implementation. Whereas some existing trucks could be adapted to the necessary conditions to transport CO_2, reducing costs. However, the emissions from these vehicles should be assessed. Therefore, they should be in good condition and have very low emissions. Additionally, the existing oil and gas transportation guidelines should be used as a basis for this kind of transportation.

Despite many factors that directly affect the costs of capture, transport, and storage CO_2, in this chapter, I focused only on the transportation cost, specifically the pipeline costs. To calculate the capital costs of the pipelines, first it was necessary to estimate the diameter of the pipelines; this was done based on the relation of the diameter as a function of the CO_2 flow rate computed by Heddle et al. (2003); see Figure 5.22. I then obtained the diameters according to the potential flow rate of each emission point. In addition, I calculated the cost per ton of CO_2 stored per day based on storage costs in Mexico ($8/t$CO_2$) according to Smith et al. (2021); see Table 5.11.

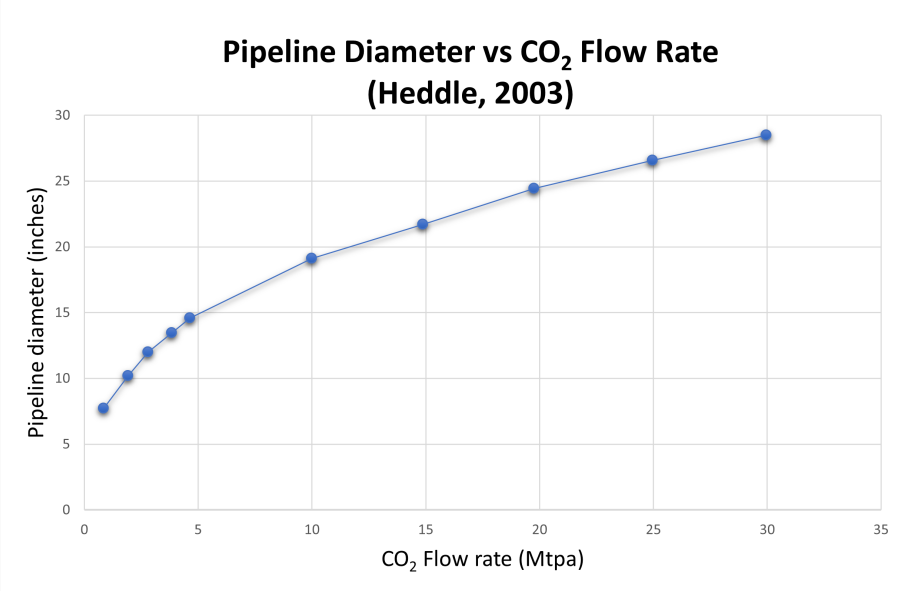

Figure 5.22: Diameter (inches) as a function of CO_2 mass flow rate, modified from Heddle et al. (2003).

Emission Points	CO_2 Mtpa	CO_2 (tpd)	Diameter (in)	CO_2 storage cost (USD)
EP1	1.35	4000	10	32,000
EP2	0.51	1400	8	11,200
EP3	0.36	1000	6	8,000
EP4	0.25	700	6	5,600
R15 (EP1+EP2)	1.86	5000	15	40,000
R16 (EP1+EP4)	1.57	4400	15	35,200

Table 5.11: Emission points, their CO_2 emission per year, their approximate diameter, based on the relation established by Heddle et al. (2003), and the cost per day to store their CO_2 emitted.

Using Table 5.8 as a reference and considering that the terrain in the study area is swampy, despite being flat, the capital cost of the pipeline diameter (inch) per mile will be 100,000 USD. The approximate costs for each pipeline are shown in Table 5.12.

Route	Length (km)	Length (mi)	Diameter (in)	Cost (USD)
1	50.8	31.6	10	31,600,000
2	49.5	30.8	10	30,800,000
3	50.6	31.4	10	31,400,000
4	51	31.7	10	31,700,000
5	47.8	29.7	8	23,700,000
6	76.9	47.8	6	28,680,000
7	47.4	29.5	10	29,500,000
8	48.3	30	10	30,000,000
9	48.5	30.1	8	30,100,000
10	72	44.7	6	26,820,000
11	75.6	47	6	28,200,000
12	32.7	20.3	6	12,100,000
13	32.7	20.3	6	12,100,00
14	32.3	20.1	6	12,000,000
15	7.5	4.7	15	7,000,000
16	19.4	12.1	15	18,100,000

Table 5.12: Average capital costs of the sixteen pipeline routes according to Grant et al. (2019).

Excluding routes 15 and 16 that connect two emission points and could be linked to the other routes, the average length of the routes is 46.5 km or 28.9 miles, and the average cost is USD 30,000,000. It is worth mentioning that the O & M costs and other additional costs are not included in this calculation, and they could significantly increase them.

The weight and influences were mainly based on the features between the emission and injection points when creating the routes. The priorities were towns, buildings, and natural features as they must not be affected by the pipeline project; other features could be adapted or modified if needed. This point of view depends on the motivation of the stakeholders involved.

Thus, the assigned weights and influences play a determining role since minor differences in them can significantly change the routing outcome. For instance, an influence of 20% will typically avoid the features; in contrast, an influence of 25% will avoid them, as it is shown in the fault weighting of routes 7 and 8 (Figure 5.14), where this difference defined if the pipeline crosses the fault or not, and the routes are alike.

In other cases, the pathways differ from one to another despite having the same weights due to the indirect influence of the other categories. In routes 1 and 2 (Figure 5.10), the natural features and faults have the same weight, but considerable changes in the slope and road categories modified their pathways.

In contrast, some routes show a direct influence, where some categories are upweighted from one to the other, and the route changes markedly, such as routes 3 and 4 (Figure 5.11),

where the change in the fault category influence implies avoiding it or not. Other routes show similarities associated with different emission points because the weights are the same; ergo, the start point of route 6 (EP3) (Figure 5.13) is further away from the start point of route 5 (EP2) (Figure 5.12). However, from this point, both routes follow almost the same path.

In summary, it is possible to avoid a specific category or feature by a) assigning a high influence value or b) by manipulating the other categories. The first option is likely to work everywhere, and the second depends on a given site's specifications. It should be noted that subtle changes in weightings other than objects to be avoided can have unpredictable indirect effects.

Additionally, to select the best route options, it is essential to consider the interests of groups of stakeholders, which usually are three. The first one is the environmental interest, which in most cases defines the costs and actual route of the pipelines. The second interest is social; for some, this is the most important one since this type of project aims to benefit humanity, and their safety and tranquillity must be assured. The third is the economic interest that can impede their realisation in some places due to the high costs. In account of this, Table 5.13 shows the most suitable route choice for each interest based on how the environmental and social features (i.e., water bodies, natural features, towns, and buildings) are avoided by the route and their costs, according to Table 5.12.

Best routes	**Linking point**	**Interests**
R4	EP1 to IP1	Environmental, Social and Economic
R5	EP2 to IP2	Environmental, Social and Economic
R6	EP3 to IP1	Environmental and Social
R8	EP1 to IP2	Social and Economic
R9	EP2 to IP1	Environmental, Social and Economic
R11	EP3 to IP1	Social
R13	EP4 to IP1	Environmental, Social and Economic
R14	EP4 to IP2	Environmental, Social and Economic

Table 5.13: Best route options and linking points according to the main interests of the stakeholders.

The routes mentioned in Table 5.13 are also the preferable route options between each emission and injection point.

In summary, I created 16 routes to demonstrate that several options could be modified according to the priorities of stakeholders and society. These options can also help to consider and include unexpected obstacles in route planning.

It is worth mentioning that the real world will have significant differences with the data used. Hence, the pipelines could have other suitable routing options. Regardless of this, the routes obtained in this chapter can be used as a model in future pipeline planning as they can be easily modified and some of them could be adapted to real pipeline routes to reduce costs.

CHAPTER 6

CONCLUSIONS

This thesis has assessed the CO_2 storage capacity in a mature field within the Sureste Basin, considered the likelihood of induced seismicity in the area due to CO_2 injection, and developed pipeline models to link CO_2 emissions sources to the mature field. In this chapter, I will emphasise the key findings and discuss the scope for further work in order to develop the potential for CCS in the Sureste Basin.

6.1 Summary of results

In Chapter 2, I examined the Sureste Basin from a geographical and geological point of view and its potential for CCS. Previous literature has determined that this basin is suitable for capturing CO_2 from industrial facilities and storing CO_2 in different mature oil and gas fields. There are many fields within reasonable distances from each other (less than 20 km); one of the main assets is the Cinco Presidentes Region, where CCS has already been considered.

In Chapter 3, I calculated the potential storage capacity of one of the fields of the Cinco Presidentes Region, the Ogarrio field, based on seismic interpretation and well log analysis. Three target geological formations were chosen based on their suitable properties: Upper Concepcion, Lower Concepcion, and Encanto. According to the seismic interpretation of the 2D lines, they contain structural traps appropriate for CO_2 sequestration. However, Encanto is the most suitable choice due to its petrophysical characteristics. Based on a static equation for potential storage volumes, I estimate that it is possible to store 31.4 CO_2 Mt in Encanto, 1.9 Mt in Upper Concepcion, and 2.7 Mt in Lower Concepcion. The total storage capacity of the anticline structure is 36 Mt. I note that this value is smaller than some other estimates for this field. This is likely because other estimates are based on much broader-scale and regional analysis rather than a detailed examination of lithological

properties and structural geology. Also, they do not include a detailed assessment of probable spill points from the anticline structure. This reduction in potential storage volumes with a more detailed analysis is expected given the typical CO_2 capacity pyramid shown in Chapter 1. Additionally, in Chapter 3, I then include an uncertainty and Monte Carlo analyses that I will discuss further in the following section.

In Chapter 4, I presented an assessment of the induced seismicity potential for future CCS operations. I computed the slip likelihood of the faults in the basin based on the critical pore pressure and concluded that the risk of generating significant levels of induced seismicity is low, as the Miocene storage targets have low levels of faulting and are not in hydraulic communication with the basement.

Based on the existing levels of ground motion produced by natural earthquakes in the basin and within the subduction zone to the southwest, I define the maximum magnitude that should be permitted for an induced event due to CO_2 injection in the region as M_w 4.5. Magnitudes lower than this may be acceptable as they would produce ground motions in the closest populated areas that are no larger than those experienced from natural earthquakes on a regular basis.

Additionally, I computed the largest seismic event in each target formation that might be expected based on seismic efficiencies from similar injection projects observed elsewhere. The resulting modelled magnitudes ranged from M_w 2.9 to 5.8.

In order to prevent larger magnitudes, I recommend the establishment of a Traffic Light System with a red light (which means that operations should be halted) set at M_w2.5. Since a 2-unit difference in magnitude is needed as a safety gap to avoid the impacts of magnitude jumps and post-injection magnitude increases.

In Chapter 5, I describe the pipeline requirements for CO_2 transport, storage, and the features of the study area that could denote an obstacle, and I created sixteen cost-effective pipeline routes that connect the selected CO_2 sources to the structural trap points in the Ogarrio field. I created these routes based on a Least Cost Path Analysis; its decision making relied on the cost or weight of the different obstacles. The weights assigned depended on the location of the linking points and if the obstacles were present between them or not. These weights are subjective and could change according to the interests of the stakeholders of a CCS project. In addition, I matched the capacities between the industrial emission points within the Cinco Presidentes region and the Ogarrio field, which resulted in the selection of five emission points. Since the routes are cost-effective, it was crucial to investigate the potential costs in USD of the sixteen routes, and they range between 7,000,000 USD to 31,700,000. These prices consider the terrain type and the length of the pipeline. The lengths range between 7.5 to 76.9 km. These routes vary their length because they have different emission and injection points.

6.2 Overall findings

The three principal analyses of this thesis, carried out in the anticline area within the Ogarrio field, led to 1) the estimation of CO_2 that can be potentially stored, 2) the likelihood of induced seismicity due to CO_2 injection, and 3) the creation of pipeline routing models to connect the CO_2 sources to that area. Even though the results obtained could be used as a base for future assessments in this field and other similar sites, there are uncertainties. For instance, at the beginning of this study, some information and data from older wells and seismic surveys were discarded as outdated, illegible, or unclear. Despite the efforts to use the best data available, there are and will be uncertainties in the calculations. In particular, the Storage Efficiency Factor (SER) cannot be defined in advance and is typically allowed to vary over an order of magnitude from 0.1% to 6% (Bentham et al., 2014).

To further address the uncertainties in storage capacity, I calculated a range of capacity values with an uncertainty analysis and a Monte Carlo analysis to cover what is possible and what is likely at 5% to 95% confidence levels. The results in the uncertainty analysis vary over two orders of magnitude from 0.4 Mt (5% uncertainty) to 131 Mt (95% uncertainty) and from 3.4 Mt (5% confidence) to 275 Mt (95% confidence) in the Monte Carlo analysis, which is a considerable difference. Using the CO_2 sources selected in the analysis of the matched capacities in Chapter 5, these numbers could mean that if the storage capacity is 0.4 o 3.4 Mt, then the Ogarrio site is not suitable for CCS purposes. On the other hand, if the capacity is 131 o 275 Mt, then CO_2 from a range of emission points could be injected for up to 26 or 55 years at the site. These numbers affect the duration of the project and the design of the pipelines, as the flow rate CO_2 would change, and the risks of leakage and seismicity could increase or decrease. Notably, these levels of uncertainty were found for a site with extensive subsurface data - even larger uncertainties may be found for places where subsurface data is lacking.

Nonetheless, uncertainties of this scale are not uncommon with subsurface projects, especially in oil and gas projects. Typically, these kinds of projects look at a range of uncertainties that can be faced while trying to extract hydrocarbons. The methodology to calculate the oil volume is similar to the CO_2 storage capacity. Usually, the industry deals with the resulting uncertainties by developing a project portfolio that includes various prospective oil and gas producing fields, such that the risks are offset. Under this premise, the Sureste Basin is a good example because it has several mature fields. Thus, in a scenario where a CCS project is planned in a real scenario in Ogarrio, only for the actual storage capacity to fall at the lower end of the uncertainty range, then the field would not be suitable. However, there would be other fields where the capacity values could be more substantial. Therefore, a CCS project should develop a portfolio of sites, providing flexibility, incrementing the injection sites and CO_2 sources.

As mentioned before, the amount of seismic activity is expected to scale with the CO_2 injection volume; while Ogarrio is likely to be a low-risk site, other fields could have more

storage capacity. Nonetheless, they could present earthquakes and even the risk of leakage; for that reason, the portfolio must include hazard assessments for each field considered.

Furthermore, the portfolio should include more potential pipeline routing models like the ones created in this thesis that interconnect different sites to others to create a CO_2 pipeline network in the Basin or even be adapted to the existing oil pipeline infrastructure.

One of the main conclusions of this thesis is that even with the best quality data, the fact that there will be a substantial uncertainty in storage volumes is inevitable. Nevertheless, how do we deal with that level of uncertainty? This question could be answered on the one hand by developing an actual CCS project at the site. Then the amount of CO_2 that can be injected, the behaviour, and the risk of leakage will be known, reducing the uncertainties. On the other hand, since implementing a full-scale CCS project takes years and is very expensive, another solution is to create different storage scenarios by using previous and active CCS projects as a base and thoroughly analysing quality data from the specific site. These scenarios and their analyses could be managed in the portfolio, giving more chances to address issues and reduce uncertainties at future sites.

6.3 Recommendations

6.3.1 CO_2 storage

It is crucial to investigate and analyse possible structural traps in the basin as they define the CO_2 storage capacity. Using 3D seismic data and borehole image logs would be beneficial in understanding and gaining insight into the subsurface configuration in the area.

Furthermore, prior experience in the storage of natural gas, petroleum and other fluids in salt caverns (Li et al., 2021; Zhang et al., 2022) suggests that they could provide a medium CO_2 storage option. They could be natural or artificial, usually constructed in thick deep salt domes (Shi and Durucan, 2005).

Storing CO_2 in salt caverns is an option that has not been widely considered due to its high costs; however, it could be an alternative option where conventional options are not available or limited. For instance, they could be a temporary storage site for large volumes of CO_2 until oil and gas reservoirs become available, as they need to be depleted beforehand (Bachu and Dusseault, 2005).

The storage security of salt caverns is high because the salt could have low permeability or be impermeable. The overlying formations have their pores plugged by crystalline salt for a sizeable thickness, reducing their porosity and permeability. Also, the salt is insoluble in CO_2; therefore, the cavern acts as a natural seal (Bachu and Dusseault, 2005). Furthermore, salt has a creep and plasticity behaviour that makes it self-sealing and self-healing. Therefore, any fissures and fractures created due to drilling or dissolution processes will be healed, and the seal will be regenerated (Zhang et al., 2022). In case of

a fracture, the amount of CO_2 released will cause the pressure inside the cavern to drop, closing the fracture. In addition, salt caverns can withstand pressure up to 80% fracturing threshold when storing fluids and have a considerable volumetric capacity (thousands to millions of cubic metres) (Bachu and Dusseault, 2005).

The possibility of CO_2 leakage into overlaying or underlying formations and fractures is very low in a salt cavern, as the recrystallised salt has occluded porosity. However, the highest risk of leakage is because of abandoned wells if their integrity is damaged as they become a conduit for CO_2 to flow upward to the surface (Bachu and Dusseault, 2005).

For this reason, proper well sealing is mandatory in this type of project. Moreover, monitoring the cavern closure behaviour is highly recommended to ensure the innate creep behaviour of salt (Bachu and Dusseault, 2005). Together with a geomechanical model of the cavern and the overlaying formation response over time (Shi and Durucan, 2005).

In the Sureste Basin, several saline bodies can be used for CO_2 storage. Therefore, they could be a good target along with the depleted oil and gas reservoirs if the geological configuration above these bodies is suitable for CO_2 injection. However, the literature estimates in the Sureste Basin are based on large areas that do not consider details in the fields, such as structural traps where storage can take place; only the general geological structures are taken into account. Hence, detailed analyses at regional and local scales are needed.

6.3.2 Fault analysis, caprock integrity, and monitoring

Estimating the stress state of the faults at prospective storage sites is crucial. The selection of the site should not have shown active faulting and tectonic activity and historically should have a low occurrence of natural seismicity (Verdon, 2014).

Installing a seismic monitoring network prior to injection in the study area can considerably reduce the risks associated with induced seismicity due to CO_2 injection and storage. Seismic monitoring enables operators to set the injection rate to diminish the risks of induced seismicity (Verdon, 2014). Nevertheless, storage sites should be as far as possible from urban settlements and seismically-sensitive infrastructure (Nicol et al., 2011),

Regarding caprock integrity, the CO_2 injection projects should include some expected range of acceptable pressure variations to achieve adequate injectivity and avoid damage to the integrity of the reservoir. An accurate determination of reservoir fracture pressures should be made to control the maximum allowable injection pressure during CO_2 injection (Bohloli et al., 2017).

Karimnezhad et al. (2014) studied that close to the injection well, induced pore pressure and geomechanical changes are more concentrated at early injection times. Therefore, the area of the caprock close to them is the one with the highest probability of rock failure. For this reason, injection wells should be as far from faults and fractures as possible to avoid

induced seismicity and fault reactivation (Shukla et al., 2010).

Furthermore, to improve prediction, numerical models to investigate the geomechanical effects and responses of CO_2 injection ensure that pressure increases do not affect the mechanical stability of the caprock. This can be complemented with a model that also includes the chemical processes in the reservoir and the caprock (Karimnezhad et al., 2014).

Monitoring should not only be used to prevent induced seismicity and leakage. It is also imperative to monitor the CO_2 once injected underground to predict and estimate its future behaviour and avoid damage to the caprock integrity. It is also essential to monitor the durability, structural integrity, and safety of any wells that penetrate the storage formation to avoid leakages (Bachu, 2003).

6.3.3 Pipelines

The pipeline routes generated in this project could be used as a model or base for future pipeline network creation; here, I showed that their paths could be modified easily, or different pipelines could be joined to the same path to save costs. Monitoring the ground motions during pipeline construction and installation should be mandatory. Therefore, the Traffic Light System should also be considered in this phase of the CCS.

There are many sites similar to Ogarrio that are suitable for CO_2 storage due to the geological characteristics of the sedimentary basins that have multiple fields and reservoirs (Aulis Garcia, 2015), most of them are located on the east side of Mexico. For that reason, it is essential to connect the emission sources distributed throughout the country through pipelines, as it is the most cost-effective option in the territory.

In order to reduce the CO_2 emissions from the primary emitting sources (e.g., carbon, electric, thermoelectric, and steel plants), it will be necessary to create a plan for the construction of a national CO_2 pipeline network, as in Mexico, there are many sources with large emissions volumes. Many of these sources are far from the hydrocarbon exploitation areas.

A CO_2 pipeline network would make it cost-effective to transport CO_2 from a distant emission point to an injection point. A techno-economic analysis should be carried out to develop the said networks that make their construction as efficient and profitable as possible (Sanchez, 2018). Moreover, it will be necessary to consider CO_2 natural sources and CO_2 from natural gas separation mechanisms (Lacy et al., 2013).

6.4 Future work

It is important to emphasise that the results shown here are only estimates due to the limitations and lack the data. For example, the 2D seismic data had to be interpolated to cover the entire subsurface of the study area. In addition, potential structural traps have

around 360 wells; however, only 60 wells were used for well log analysis, and information such as fault stress gradients had to be inferred from previous literature. Therefore, well log, borehole, and 3D seismic data are highly needed to reassess the well log analysis in Chapter 3 and the fault analysis carried out in Chapter 4. Another thing to consider is that there has been seismic activity in zones where I did not find faults with the data I have, which entails the possibility that there are more faults than the ones I analysed. Furthermore, it is essential to update the level of hydrocarbon production in Ogarrio since the information I used was from 2018, as well as the CO_2 emissions from the sources used in Chapter 5. To generate precise pipeline routes, the features of the area should be studied and mapped using a real-world approach, as the data used in that process are not the latest version.

For all these reasons, the next step to address the data limitation will be to obtain an agreement with the CNH, SENER, SSN, and PEMEX to acquire and gather complete, accurate, and up-to-date well log, seismic, and fault information. Thus, with an updated database, all analyses could be performed again in the Ogarrio area to obtain results with reduced uncertainties.

In this sense, a local-scale study like this has not yet been carried out in Mexico. This could mean the beginning of similar projects and a deeper seismicity analysis in several mature fields within the Sureste Basin and other basins in the country.

Therefore, further action would involve investigating other surrounding fields to estimate their potential storage capacity to build an overall portfolio, requiring a team of experts on the topic. This portfolio will likely include geology, petrophysics, caprock, well integrity, seismic and hazard assessments, and pipeline routing models adaptable to different sites.

It is necessary to promote the development of this type of project in Mexico. However, to do so, it is imperative to educate the public on what a CCS project entails, the probability of induced seismicity, and the potential impact it can have in the localities where CO_2 storage is carried out. It could be done by disseminating information in accessible formats for the public to understand and accept this type of project.

Finally, it is essential to communicate with industry stakeholders and consider other approaches to CCS. Since the CCS technology could imply high costs from capturing to storing, EOR could be more feasible than sequestrating CO_2. This option and other similar approaches should be contemplated and evaluated to get Mexico to take an active part in CCS and efforts to reduce global warming.

BIBLIOGRAPHY

Acevedo, J. S. and Dautt, O. M. (1980).
Giant Fields in the Southeast of Mexico.
Gulf Coast Association of Geological Societies Transactions, 30(June):1–31.

Adi Jatmoko, F. and Kusrini, E. (2018).
Analysis of CO2 transmission pipelines for CO2 enhanced oil recovery networks: Gas field X to oil field Y.
E3S Web of Conferences, 67:1–8.

Agartan, E., Gaddipati, M., Yip, Y., Savage, B., and Ozgen, C. (2018).
CO2 storage in depleted oil and gas fields in the Gulf of Mexico.
International Journal of Greenhouse Gas Control, 72(September 2017):38–48.

Akkar, S., Sandıkkaya, M. A., and Bommer, J. J. (2014).
Empirical ground-motion models for point- and extended-source crustal earthquake scenarios in Europe and the Middle East.
Bulletin of Earthquake Engineering, 12(1):359–387.

Al-obaidi, S. H. (2017).
Oil & Gas Research Calculation Improvement of the Clay Content in the Hydrocarbon Formation Rocks.
Oil & Gas Research, 3(1):1–2.

Alcalde, J., Flude, S., Wilkinson, M., Johnson, G., Edlmann, K., Bond, C. E., Scott, V., Gilfillan, S. M., Ogaya, X., and Stuart Haszeldine, R. (2018).
Estimating geological CO2 storage security to deliver on climate mitigation.
Nature Communications, 9(1).

Alcantara Rojas, C. (2010).
Origen, evolución e importancia económica de la Cuenca Salina del Istmo.
PhD thesis, UNAM.

Arteaga, M., Rodriguez, F., and Baez, I. (2015).
Inyección de bióxido de carbono en el campo Brillante.
Ingenieria Petrolera, 55(10):608–623.

Aulis Garcia, R. (2015).
Evaluación Geológica y Petrolera del Campo Cinco Presidentes en la Cuenca Salina del Istmo.
PhD thesis, UNAM.

Ayuntamiendo Huimanguillo Tabasco (2019).
Población - H. Ayuntamiento Constitucional de Huimanguillo. Tabasco. 2018 - 2021.

Bachu, S. (2003).
Screening and ranking of sedimentary basins for sequestration of CO2 in geological media in response to climate change.
Environmental Geology, 44(3):277–289.

Bachu, S. (2015).
Review of CO2 storage efficiency in deep saline aquifers.
International Journal of Greenhouse Gas Control, 40:188–202.

Bachu, S., Bonijoly, D., Bradshaw, J., Burruss, R., Holloway, S., Christensen, N. P., and Mathiassen, O. M. (2007).
CO2 storage capacity estimation: Methodology and gaps.
International Journal of Greenhouse Gas Control, 1(4):430–443.

Bachu, S. and Dusseault, M. B. (2005).
Underground Injection of Carbon Dioxide in Salt Beds.
Developments in Water Science, 52(C):637–648.

Bagli, S., Geneletti, D., and Orsi, F. (2011).
Routeing of power lines through least-cost path analysis and multicriteria evaluation to minimise environmental impacts.
Environmental Impact Assessment Review, 31(3):234–239.

Bai, M. (2014).
Risk assessment for CO2 leakage along abandoned wells using a monte carlo simulation in a CO2 sequestration site.
Petroleum Science and Technology, 32(10):1191–1200.

Balogun, A.-l., Matori, A.-n., Lawal, D. U., and Chandio, I. (2012).
Optimal Oil Pipeline Route Selection using GIS : Community Participation in Weight derivation and Disaster Mitigation.
International Conference on Future Environment and Energy, 28:100–104.

Barrass, S. and Zehner, B. (2000).
Responsive sonification of well-logs.
Proceedings of the 6th International Conference on Auditory Display (ICAD 2000), 0(October):72–80.

BEIS (2020).
International CCUS Programme: Annual review 2020.
Technical report, Department for Business, Energy & Industrial Strategy, Goverment of UK.

Benavides Garcia, L. (1983).
Domos Salinos del Sureste de Mexico, Origen : Exploración : Importancia Económica.
Boletin de la Asociacion Mexicana Geologico-Petrolera, XXXV(1).

Bentham, M., Mallows, T., Lowndes, J., and Green, A. (2014).
CO2 STORage evaluation database (CO2 Stored). The UK's online storage atlas.
Energy Procedia, 63(0):5103–5113.

Bhattacharya, P., Chakrabarti, B. K., and Samanta, D. (2009).
Fractal models of earthquake dynamics.
Reviews of Nonlinear Dynamics and Complexity, 2(m):107–150.

Bischoff, M., Cete, A., Fritschen, R., and Meier, T. (2010).
Coal mining induced seismicity in the Ruhr area, Germany.
Pure and Applied Geophysics, 167(1-2):63–75.

Blackford, J., Bull, J. M., Cevatoglu, M., Connelly, D., Hauton, C., James, R. H., Lichtschlag, A., Stahl, H., Widdicombe, S., and Wright, I. C. (2015).
Marine baseline and monitoring strategies for carbon dioxide capture and storage (CCS).
International Journal of Greenhouse Gas Control, 38:221–229.

Bloomberg (2019).
A Gas Heist Gone Wrong, an Explosion, and 137 Deaths in Mexico - Bloomberg.

Bohloli, B., Ringrose, P., Grande, L., and Nazarian, B. (2017).
Determination of the fracture pressure from CO2 injection time-series datasets.
International Journal of Greenhouse Gas Control, 61:85–93.

Bolstad, P. (2016).
GIS fundamentals : a first text on geographic information system.
Eider (PressMinnesota), 5th edition.

Bommer, J. J., Oates, S., Cepeda, J. M., Lindholm, C., Bird, J., Torres, R., Marroquín, G., and Rivas, J. (2006).
Control of hazard due to seismicity induced by a hot fractured rock geothermal project.
Engineering Geology, 83(4):287–306.

Bumb, P., Desideri, U., Quattrocchi, F., and Arcioni, L. (2009).
Cost optimized CO 2 pipeline transportation grid: A case study from Italian industries.
World Academy of Science, Engineering and Technology, 58:138–145.

Burnside, N. M. and Naylor, M. (2014).
Review and implications of relative permeability of CO2/brine systems and residual trapping of CO2.
International Journal of Greenhouse Gas Control, 23:1–11.

Cabrera, R. and Lugo, J. (1984).
Estratigrafía y Sedimentología de las Cuencas Terciarias de México.
Bol.Asoc.Mex.Geol.Petr., XXXVI(2).

Cao, C., Liu, H., Hou, Z., Mehmood, F., Liao, J., and Feng, W. (2020).
A Review of CO2 Storage in View of Safety and Cost-Effectiveness.
Energies, 13(3):600.

Cappa, F. and Rutqvist, J. (2011).
Modeling of coupled deformation and permeability evolution during fault reactivation induced by deep underground injection of CO 2.
International Journal of Greenhouse Gas Control, 5:336–346.

Carafa, M. M., Tarabusi, G., and Kastelic, V. (2015).
SHINE: Web application for determining the horizontal stress orientation.
Computers and Geosciences, 74:39–49.

Celis, E., Garcia-Hernandez, J., Morales-Ramirez, J. M., Cabrera-Toledo, C., Sheridan, J., Ward, C. D., and Wiprut, D. J. (2006).
Fault Leakage Potential Analysis in the Cantarell Field, Mexico, using Geomechanics.
In *SPE Annual Technical Conference and Exhibition*.

CENAPRED (2006).
Guía básica para la elaboración de atlas estatales y municipales de Peligros y riesgos.
Technical report, CENAPRED, Mexico.

Chadwick, A., Arts, R., Bernstone, C., May, F., Thibeau, S., and Zweigel, P. (2008).
Best practice for the storage of CO2 in saline aquifers.
British Geological Survey Occasional Publication No. 14, Keyworth, Nottingham, 14 edition.

Cladouhos, T., Petty, S., Foulger, G., Julian, B., and Fehler, M. (2010).
Injection induced seismicity and geothermal energy.
Transactions - Geothermal Resources Council, 34 2(June 2014):1106–1113.

Clarke, H., Verdon, J. P., Kettlety, T., Baird, A. F., and Kendall, J. M. (2019).
Real-time imaging, forecasting, and management of human-induced seismicity at Preston new road, Lancashire, England.
Seismological Research Letters, 90(5):1902–1915.

CNH (2012).
El Futuro de la Producción de Aceite en México: Recuperación Avanzada y Mejorada IOR-EOR.
Technical report, Comisión Nacional de Hidrocarburos.

CNH (2014).
Atlas Geológico Cuencas Del Sureste - Cuencas Del Sureste - Cinturón Plegado De La Sierra De Chiapas .
Technical report, CNH.

CNH (2015).
Opinión técnica Solicitud de Migración de la Asignación A-0244-M-Campo Ogarrio a un contrato para la Exploración y Extracción.
Technical report, Comision Nacional de Hidrocarburos.

CNH (2020).
0498 CNH: Asociación de PEMEX: Área 4 Ogarrio – Proyectos México.

CNH (2022).
IICNIH.

Cole, S. and Itani, S. (2013).
The alberta carbon trunk line and the benefits of CO2.
Energy Procedia, 37:6133–6139.

Collischonn, W. and Pilar, J. V. (2000).
A direction dependent least-cost-path algorithm for roads and canals.
International Journal of Geographical Information Science, 14(4):397–406.

Crampin, S. and Gao, Y. (2015).
The Physics Underlying Gutenberg-Richter in the Earth and in the Moon.
Journal of Earth Science, 26(1):134–139.

Crippa; M., Oreggioni, G., Guizzardi, D., Muntean, E., Schaaf, Solazzo, L. V., Monforti-Ferrario, Olivier, F., and Vignati, J. (2021).
GHG emissions of all world countries.
Technical report, Joint Research Centre.

CSLF (2008).
Comparison between Methodologies Recommended for Estimation of CO2 Storage Capacity in Geological Media.
Technical Report April, Carbon Sequestration Leadership Forum.

Damen, K., Faaij, A., and Turkenburg, W. (2006).

Health, safety and environmental risks of underground CO2 storage - Overview of mechanisms and current knowledge.
Climatic Change, 74(1-3):289–318.

Danaci, D., Bui, M., Petit, C., and MacDowell, N. (2021).
En Route to Zero Emissions for Power and Industry with Amine-Based Post-combustion Capture.
Environmental Science and Technology, 55(15).

Dávila, M., Jiménez, O., Castro, R., Arévalo, V., Stanley, J., and Cabrera, L. M. (2010).
A preliminary selection of regions in Mexico with potential for geological carbon storage.
International Journal of Physical Sciences, 5(5):408–414.

del Potro, R. and Diez, M. (2015).
Induced Seismicity in Underground Gas Storage - The Case of Castor, Offshore NE Spain.
77th EAGE Conference and Exhibition - Workshops, (June):4–6.

Duncan, I. J. and Wang, H. (2014).
Estimating the likelihood of pipeline failure in CO2 transmission pipelines: New insights on risks of carbon capture and storage.
International Journal of Greenhouse Gas Control, 21:49–60.

Durmaz, A. , Ünal, E. , and Aydın, C. C. (2019).
Automatic pipeline route design with multi-criteria evaluation based on least-cost path analysis and line-based cartographic simplification: A case study of the MUS project in Turkey.
ISPRS International Journal of Geo-Information, 8(4):1–18.

Eaton, D. W., Igonin, N., Poulin, A., Weir, R., Zhang, H., Pellegrino, S., and Rodriguez, G. (2018).
Induced Seismicity Characterization during Hydraulic-Fracture Monitoring with a Shallow-Wellbore Geophone Array and Broadband Sensors.
Seismological Research Letters, 89(5):1641–1651.

Ellsworth, W. L. (2013).
Injection-Induced Earthquakes.
Science, 341(6142):1–8.

Enciso de la Vega, S. (1963).
Estudio mineralógico y petrográfico de algunos domos salinos del Istmo de Tehuantepec.
Boletín del Instituto de Geología, 65.

Escalera, J. and Hernández, U. (2010).

Provincias petroleras de México.
Technical report, WEC.

ESRI (2016).
Comparing interpolation methods—Help | ArcGIS for Desktop.

ESRI (2018).
Weighted Overaly (Spatial Analyst)—ArcGIS Pro | Documentation.

Etgen, J. T. and Kumar, C. (2012).
What Really is the Difference Between Time and Depth Migration? A Tutorial.

Farokhpoor, R., Bjørkvik, B. J., Lindeberg, E., and Torsæter, O. (2013).
CO2 wettability behavior during CO2 sequestration in saline aquifer -An Experimental study on minerals representing sandstone and carbonate.
Energy Procedia, 37(1876):5339–5351.

Foulger, G. R., Wilson, M. P., Gluyas, J. G., Julian, B. R., and Davies, R. J. (2018).
Global review of human-induced earthquakes.
Earth-Science Reviews, 178(July 2017):438–514.

Fractracker Alliance (2021).
Oil and Gas Pipeline Construction: Step-By-Step Visual Guide.

Fritze, K. (2009).
Modeling CO2 Storage Pipeline Routes in the United States by.
PhD thesis, Duke University.

Frohlich, C. and Wetzel, L. R. (2007).
Comparison of seismic moment release rates along different types of plate boundaries.
Geophysical Journal International, 171(2):909–920.

Gammer, D., Green, A., Holloway, S., and Smith, G. (2011).
The energy technologies institute's UK CO2 Storage Appraisal Project (UKSAP).
Society of Petroleum Engineers - Offshore Europe Oil and Gas Conference and Exhibition 2011, OE 2011, 2(148426):1045–1058.

Garcia Payro, O. (2013).
Bloque II. Regiones naturales de Tabasco y su biodiversidad.
In *Formación y dinámica del relieve del territorio de Tabasco. Distribución del relieve en el territorio de la entidad*.

Gierzynski, A. O. (2016).
Implications of Permeability Uncertainty During Three-phase CO2 Flow in a Basalt Fracture Network.
PhD thesis, Virginia Polytechnic Institute.

GIS Geography (2020).
Inverse Distance Weighting (IDW) Interpolation.

Global CCS Institute (2018).
Fact Sheet: Transporting CO2.

Global CCS Institute (2019).
The Global Status of CCS 2019.
Technical report, Global CCS Institute.

Global CCS Institute (2020).
Facilities - Global CCS Institute.

Global CCS Institute (2021).
The Global Status of CCS 2021.
Technical report, Global CCS Institute.

Gonzalez, R. and Holguin, N. (1992).
Las Rocas Generadoras de Mexico.
AMPG, XLII(1):9–23.

González-Díaz, A., González-Díaz, M. O., Alcaráz-Calderón, A. M., Gibbins, J., and Lucquiaud, M. (2017).
Priority projects for the implementation of CCS power generation with enhanced oil recovery in Mexico.
International Journal of Greenhouse Gas Control, 64(October 2016):119–125.

Goodman, A., Hakala, A., Bromhal, G., Deel, D., Rodosta, T., Frailey, S., Small, M., Allen, D., Romanov, V., Fazio, J., Huerta, N., McIntyre, D., Kutchko, B., and Guthrie, G. (2011).
U.S. DOE methodology for the development of geologic storage potential for carbon dioxide at the national and regional scale.
International Journal of Greenhouse Gas Control, 5(4):952–965.

Google Maps (2021).
Ogarrio.

Goovaerts, P. (2019).
Kriging Interpolation.
Geographic Information Science & Technology Body of Knowledge, 2019(Q4).

Gozalpour, F., Ren, S. R., and Tohidi, B. (2005).
CO2 EOR and storage in oil reservoirs.
Oil and Gas Science and Technology, 60(3):537–546.

Grant, T., Morgan, D., and Gerdes, K. (2019).
Quality Guidelines for Energy System Studies: Carbon Dioxide Transport and Storage Costs in NETL Studies.
Technical Report August.

Guerrero, G. (2018).
Potencial Petrolero en las Cuencas del Sureste Gildardo Guerrero.
In *Ryder Scott Petroleum Consultants*.

Hallo, M., Eisner, L., and Ali, M. Y. (2012).
Expected level of seismic activity caused by volumetric changes.
First Break, 30(7):97–100.

Hallo, M., Oprsal, I., Eisner, L., and Ali, M. Y. (2014).
Prediction of magnitude of the largest potentially induced seismic event.
Journal of Seismology, 18(3):421–431.

Han, W. S. (2008).
Evaluation of CO2 trapping mechanisms at the SACROC northern platform: site of 35 years of CO2 injection.
PhD thesis, The New Mexico Institute of Mining and Technology.

Heddle, G., Herzog, H., and Klett, M. (2003).
The Economics of Carbon Dioxide Storage.
page 115.

Heidbach, O., Rajabi, M., Reiter, K., and Ziegler, M. (2016).
WSM Team: World Stress Map Database Release 2016. V. 1.1.

Hepple, R. P. and Benson, S. M. (2003).
Implications of surface leakage on the effectiveness of geologic storage of carbon dioxide as a climate change mitigation strategy.
Sixth International Conference on Greenhouse Gas Control Technologies, I(4):261–266.

Hill, B., Hovorka, S., and Melzer, S. (2013).
Geologic carbon storage through enhanced oil recovery.
Energy Procedia, 37:6808–6830.

Hosseininoosheri, P., Hosseini, S. A., Nuñez-López, V., and Lake, L. W. (2018).
Impact of field development strategies on CO2 trapping mechanisms in a CO2–EOR field: A case study in the permian basin (SACROC unit).
International Journal of Greenhouse Gas Control, 72(April):92–104.

Ide, S. T., Friedmann, S. J., and Herzog, H. J. (2006).
CO2 leakage through existing wells: current technology and regulations.

8th International Conference on Greenhouse Gas Control Technologies, pages 1–6.

IEA (2012).
World Energy Outlook 2012.
Technical report, International Energy Agency, Paris.

IEA (2021).
About CCUS – Analysis.
Technical report, International Energy Agency.

Iglauer, S. (2018).
Optimum storage depths for structural CO2 trapping.
International Journal of Greenhouse Gas Control, 77(August):82–87.

Igonin, N., Verdon, J. P., and Eaton, D. W. (2021).
Change in microseismic anisotropy lag time reveals stress changes around a fault.
SEG Technical Program Expanded Abstracts, 2021-Septe:1206–1210.

INAFED (2016).
Medio Físico - Tabasco.

INEGI (1996).
La agricultura en Tabasco.
Technical report.

INEGI (2020).
División municipal de Tabasco .

Inichinbia, S., Sule, P. O., Hamza, H., and Ahmed, A. L. (2014).
Estimation of net-to-gross of among hydrocarbon field using well log and 3D seismic data.
IOSR Journal of Applied Geology and Geophysics, 2(2):18–26.

International Energy Agency, I. (2014).
CO 2 Pipeline Infrastructure.
Technical report.

IPCC, Masson-Delmotte, V., Zhai, P., Pörtner, H.-O., Roberts, D., Skea, J., Shukla, P., Pirani, A., Moufouma-Okia, W., Péan, C., Pidcock, R., Connors, S., Matthews, J., Chen, Y., Zhou, X., Gomis, M., Lonnoy, E., Maycock, T., Tignor, M., and Waterfield, T. (2018).
Global warming of 1.5°C, An IPCC Special Report on the impacts of global warming of 1.5°C above pre-industrial levels and related global greenhouse gas emission pathways, in the context of strengthening the global response to the threat of climate change,.
Technical report, IPCC.

ITJ (2019).
CO2 transport by rail reduces greenhouse gas emissions.

Jimenez, O., Davila, M., Arevalo, V., Medina, E., and Castro, R. (2011).
Geological Carbon Dioxide Storage in Mexico: A First Approximation.
Earth and Environmental Sciences, (June 2015).

Jin, M., Pickup, G., Mackay, E., Todd, A., Sohrabi, M., Monaghan, A., and Naylor, M. (2010).
Static and dynamic estimates of CO2-storage capacity in two saline formations in the UK.
SPE Journal, 17(4):1108–1118.

Kano, Y., Funatsu, T., Nakao, S., and Kusunose, K. (2014).
Analysis of changes in stress state and fault stability related to planned CO2 injection at the Tomakomai offshore site.
Energy Procedia, 63:2870–2878.

Karimnezhad, M., Jalalifar, H., and Kamari, M. (2014).
Journal of Natural Gas Science and Engineering Investigation of caprock integrity for CO 2 sequestration in an oil reservoir using a numerical method.
Journal of Natural Gas Science and Engineering, 21:1127–1137.

Kaven, J. O., Hickman, S. H., Mcgarr, A. F., and Ellsworth, W. L. (2015).
Surface Monitoring of Microseismicity at the Decatur , Illinois , CO 2 Sequestration Demonstration Site.
Seismological Research Letters Volume, 86(4):1–6.

Kearns, D., Liu, H., and Consoli, C. (2021).
Technology Readiness and Costs of CCS.
Technical Report March, Global CCS Institute.

Kettlety, T., Verdon, J. P., Butcher, A., Hampson, M., and Craddock, L. (2020).
High-resolution imaging of the ML 2.9 august 2019 earthquake in lancashire, United Kingdom, induced by hydraulic fracturing during preston new road PNR-2 operations.
Seismological Research Letters, 92(1):151–169.

Khurshid, I. and Fujii, Y. (2021).
Geomechanical analysis of formation deformation and permeability enhancement due to low-temperature CO2 injection in subsurface oil reservoirs.
Journal of Petroleum Exploration and Production, 11(4):1915–1923.

Koornneef, J., Spruijt, M., Molag, M., Ramirez, A., Faaij, A., and Turkenburg, W. (2009).
Uncertainties in risk assessment of CO2 pipelines.
Energy Procedia, 1(1):1587–1594.

Kopp, A., Class, H., and Helmig, R. (2009).
Investigations on CO2 storage capacity in saline aquifers — Part 2 : Estimation of storage capacity coefficients.
International Journal of Greenhouse Gas Control, 3:277–287.

Kovscek, A. R. (2002).
Screening criteria for CO2 storage in oil reservoirs.
Petroleum Science and Technology, 20(7-8):841–866.

Kracman, B., Martin, R., and Sztajnbok, P. (2001).
The Virginia Pipeline: Australia's largest water recycling project.
Water Science and Technology, 43(10):35–42.

Lacy, R., Serralde, C., Climent, M., and Vaca, M. (2013).
Initial assessment of the potential for future CCUS with EOR projects in mexico using CO2 captured from fossil fuel industrial plants.
International Journal of Greenhouse Gas Control, 19(6):212–219.

Langenbruch, C. and Zoback, M. D. (2017).
Response to Comment on "How will induced seismicity in Oklahoma respond to decreased saltwater injection rates?".
Science Advances, 3(8):1–10.

Lavrov, A. (2016).
Dynamics of stresses and fractures in reservoir and cap rock under production and injection.
Energy Procedia, 86(1876):381–390.

Lee, J. Y., Weingarten, M., and Ge, S. (2016).
Induced seismicity: the potential hazard from shale gas development and CO2 geologic storage.
Geosciences Journal, 20(1):137–148.

Li, P., Li, Y., Shi, X., Zhao, A., Hao, S., Gong, X., Jiang, S., and Liu, Y. (2021).
Stability analysis of U-shaped horizontal salt cavern for underground natural gas storage.
Journal of Energy Storage, 38:102541.

Li, Z., Dong, M., Li, S., and Huang, S. (2006).
CO2 sequestration in depleted oil and gas reservoirs-caprock characterization and storage capacity.
Energy Conversion and Management, 47(11-12):1372–1382.

Liang, Z., Shu, W., Li, Z., Shaoran, R., and Qing, G. (2009).

Assessment of CO2 EOR and its geo-storage potential in mature oil reservoirs, Shengli Oilfield, China.
Petroleum Exploration and Development, 36(6):737–742.

Lie, K. A., Nilsen, H. M., Andersen, O., and Møyner, O. (2014).
A simulation workflow for large-scale CO2 storage in the Norwegian North Sea.
Computational Geosciences, 20(3):607–622.

Lin, C. (2015).
Syrian Buffer Zone-Turkey-Qatar Pipeline.
ISPSW Strategy Series: Focus on Defense and International Security, (367).

Lindeberg, E. and Bergmo, P. (2003).
The long-term fate of CO2 injected into an aquifer.
In *Sixth International Conference on Greenhouse Gas Control Technologies*, number 7465, page 489–494, Amsterdam.

Lopez-Ramos, E. (1979).
Geologia de Mexico, Tomo III.
Trillas, Mexico City, 2nd edition.

Loria, P. and Bright, M. B. (2021).
Lessons captured from 50 years of CCS projects.
Electricity Journal, 34(7):106998.

Macharia, P. M. and Mundia, C. N. (2014).
GIS Analysis and Spatial Modelling for Optimal Oil Pipeline Route Location. A Case Study of Proposed Isiolo Nakuru Pipeline Route.
Proceedings of 2014 International Conference on Sustainable Research and Innovation, 5(May):91–94.

Mahini, A. and Abedian, S. (2014).
Routing of Road Network through Least Cost Pathway Algorithm to Minimize Impacts on Environment.
Journal of the Indian Society of Remote Sensing, 42(3):517–527.

Malczewski, J. (2006).
GIS-based multicriteria decision analysis: A survey of the literature.
International Journal of Geographical Information Science, 20(7):703–726.

Maldal, T. and Tappel, I. M. (2004).
CO2 underground storage for Snøhvit gas field development.
Energy, 29(9-10):1403–1411.

Martinez, F. (2001).
Geologic Study of the Miocene Rodador Field and its Exploitation Possibilities, Tabasco State, Southeastern Mexico.
The western Gulf of Mexico Basin: Tectonics, sedimentary basins, and petroleum systems: AAPG Memoir, 75:433–441.

McCraw, C., Edlmann, K., Miocic, J., Gilfillan, S., Haszeldine, R. S., and McDermott, C. I. (2016).
Experimental investigation and hybrid numerical analytical hydraulic mechanical simulation of supercritical CO2 flowing through a natural fracture in caprock.
International Journal of Greenhouse Gas Control, 48:120–133.

McGarr, A. (2014).
Maximum magnitude earthquakes induced by fluid injection.
Journal of Geophysical Research: Solid Earth, 119:1008–1019.

Melaina, M. W., Antonia, O., and Penev, M. (2013).
Blending Hydrogen into Natural Gas Pipeline Networks: A Review of Key Issues.
Technical report.

Mendez, B. (2007).
Geoquímica e isotopía de aguas de formación (salmueras petroleras) de campos mesozoicos de la Cuenca del Sureste de México: implicación en su origen, evolución e interacción agua-roca en yacimientos petroleros.
PhD thesis, UNAM.

Metz, B., Davidson, O., de Coninck, H., Loos, M., and Meyer, L. I. (2005).
Carbon Dioxide Capture and Storage.
Technical report.

Meyer, R., May, F., Muller, C., Geel, K., and Bernstone, C. (2008).
Regional search , selection and geological characterization of a large anticlinal structure , as a candidate site for CO 2 -storage in northern Germany.
Environmental Geology, 54:1607–1618.

Milian, G. A. (1980).
Diseño sísmico de tuberías enterradas.

Miocic, J. M., Gilfillan, S. M., Roberts, J. J., Edlmann, K., McDermott, C. I., and Haszeldine, R. S. (2016).
Controls on CO2 storage security in natural reservoirs and implications for CO2 storage site selection.
International Journal of Greenhouse Gas Control, 51:118–125.

Mission Innovation (2017).
Mission Innovation Carbon Capture, Utilization, and Storage Workshop.
Technical report, US DoE, Houston, Texas.

Mohammadi, M., Hourfar, F., Elkamel, A., and Leonenko, Y. (2019).
Economic Optimization Design of CO2 Pipeline Transportation with Booster Stations.
Industrial and Engineering Chemistry Research, 58(36):16730–16742.

Møll Nilsen, H., Lie, K. A., Møyner, O., and Andersen, O. (2014).
Spill-point analysis and structural trapping capacity in saline aquifers using MRST-co2lab.
Computers and Geosciences, 75:33–43.

Mora-Oropeza, G. (2000).
3-D geologic model of the deep-water Deposito and Encanto formations (Miocene-Pliocene) in the Saline basin of southeast Mexico.
PhD thesis, Colorado School of Mines.

Morelos (2008).
Complejo Petroquimico Morelos - Coatzacoalcos.

Morris, A., Ferrill, D. A., and Henderson, D. B. (1996).
Slip-tendency analysis and fault reactivation.
Geology, 24(3):275–278.

Mortezaei, K. and Vahedifard, F. (2015).
Numerical Simulation of Induced Seismicity in Carbon Capture and Storage Projects.
Geotechnical and Geological Engineering, 33(2):411–424.

Mota, J. and Heras, B. (2018).
CCUS Implementation in Mexico : towards a sustainable energy sector.
14th International Conference on Greenhouse Gas Control Technologies, (October).

Muros, S., Pañetados, P. Y., Metalica, P., Baldosa, P. E. N., En, M., La, L. A., En, V., and Metálica, C. (2021).
Febrero de 2021.
(2):80–82.

NETL DOE (2019).
Carbon Storage FAQs.

Nicol, A., Carne, R., Gerstenberger, M., and Christophersen, A. (2011).
Induced seismicity and its implications for CO2 storage risk.
Energy Procedia, 4:3699–3706.

Noothout, P., Wiersma, F., Hurtado, O., and Macdonald, D. (2014).
CO 2 Pipeline Infrastructure.
(January).

Nordbotten, J. M., Celia, M. A., Bachu, S., and Dahle, H. K. (2005).
Semianalytical solution for CO2 leakage through an abandoned well.
Environmental Science and Technology, 39(2):602–611.

O'Rourke, M. J. and Ayala, G. (1990).
Seismic Damage to Pipeline: Case Study.
Journal of Transportation Engineering, 116(2):123–134.

O'Rourke, T. and Palmer, M. (1996).
Earthquake Performance of Gas Transmission Pipelines.
Earthq. spectra, 12(3):493–527.

Papadopoulos, S., Sextos, A., Kwon, O.-S., Gerasimidis, S., and Deodatis, G. (2017).
Impact of spatial variability of earthquake ground motion on seismic demand to natural gas transmission pipelines.
16th World Conference on Earthquake Engineering, Santiago, Chile, 9-13 January., (January).

Parfomak, P. W., Pirog, R., Luther, L., and Vann, A. (2013).
Keystone XL Pipeline Project: Key Issues.
Technical report.

Peletiri, S. P., Rahmanian, N., and Mujtaba, I. M. (2018).
CO2 Pipeline design: A review.
Energies, 11(9).

Perez Rincón, H. (1959).
Estudio geologico del campo petrolero Rodolfo Ogarrio.
Boletín de la Sociedad Geológica Mexicana, 22(3):11–27.

Pickup, G. E. (2013).
CO2 storage capacity calculation using static and dynamic modelling.
Woodhead Publishing Limited.

Pindell, J. and Kennan, L. (2001).
Kinematic Evolution of the Gulf of Mexico and Caribbean.
Petroleum Systems of Deep-Water Basins: Global and Gulf of Mexico Experience: 21st Annual, pages 193–220.

Psarras, P., He, J., Pilorgé, H., McQueen, N., Jensen-Fellows, A., Kian, K., and Wilcox, J. (2020).

Cost Analysis of Carbon Capture and Sequestration from U.S. Natural Gas-Fired Power Plants.
Environmental Science and Technology, 54(10):6272–6280.

Psarras, P. C., Comello, S., Bains, P., Charoensawadpong, P., Reichelstein, S., and Wilcox, J. (2017).
Carbon Capture and Utilization in the Industrial Sector.
Environmental Science and Technology, 51(19):11440–11449.

Raza, A., Rezaee, R., Gholami, R., Bing, C. H., Nagarajan, R., and Hamid, M. A. (2016).
A screening criterion for selection of suitable CO2 storage sites.
Journal of Natural Gas Science and Engineering, 28:317–327.

Ringrose, S., Philip, S., and Andri, I. (2018).
The CCS hub in Norway: some insights from 22 years on of saline aquifer storage.
Energy Procedia, 146:166–172.

Rodriguez Moreno, V. (2020).
Estimación preliminar de la capacidad de almacenamiento geológico de CO 2 de campos maduros de México con oportunidad de Recuperación Mejorada .
PhD thesis, UNAM.

Romero, R. and Bashbush, J. L. (2017).
Análisis de incertidumbre y factibilidad de inyección de fluidos en el campo Ogarrio , bloque A.
Ingeniería Petrolera, 57(6):450–469.

Rudnick, D. A., Ryan, S. J., Beier, P., Cushman, S. A., Dieffenbach, F., Epps, C. W., Gerber, L. R., Hartter, J., Jenness, J. S., Kintsch, J., Merenlender, A. M., Perkl, R. M., Preziosi, D. V., and Trombulak, S. C. (2012).
The role of landscape connectivity in planning and implementing conservation and restoration priorities.
Issues in Ecology, (16):1–23.

Ruiz-Barajas, S., Sharma, N., Convertito, V., Zollo, A., and Benito, B. (2017).
Temporal evolution of a seismic sequence induced by a gas injection in the Eastern coast of Spain.
Scientific Reports, 7(2901):1–15.

Rutqvist, J. (2012).
The Geomechanics of CO 2 Storage in Deep Sedimentary Formations.
Geotech Geol Eng, 30:525–551.

Rutqvist, J. and Tsang, C. F. (2002).

A study of caprock hydromechanical changes associated with CO2-injection into a brine formation.
Environmental Geology, 42(2-3):296–305.

Sanchez, A. (2018).
Factibilidad de la captura y almacenamiento de CO2 en campos de hidrocarburos en México.
PhD thesis, UNAM.

Sanchez Romero, N. (2019).
Modelado de las Princiaples estructuras del campo Cuichapa en la Cuenca Salina del Istmo, Mexico.
PhD thesis, Universidad Central de Venezuela.

Santiago, J., Carrillo, B. J., and Martell, A. B. (1984).
Geología petrolera de México. Evaluación de formaciones en México.
Technical report.

Sarı, F. and Sen, M. (2017).
Least Cost Path Algorithm Design for Highway Route Selection.
International Journal of Engineering and Geosciences, 2(1):1–8.

Satinder, C. and Brown R., A. (2013).
What Is Seismic Interpretation?

SCCS (2021).
Global CCS Map.

Schlumberger (2016).
Neritic | Oilfield Glossary.

Schlumberger (2022).
Oilfield Glossary.

Schultz, R. and Wang, R. (2020).
Newly emerging cases of hydraulic fracturing induced seismicity in the Duvernay East Shale Basin.
Tectonophysics, 779(December 2019):228393.

SEMARNAT (2019).
Registro de Emisiones y Transferencias de Contaminantes.

SENER (2012).
Atlas de almacenamiento geológico de CO2 en México.
Technical report, SENER, CFE.

SENER (2014).
CCUS Technology Roadmap in Mexico.
Technical report, SENER.

SENER (2018a).
Advances in the Implementation of CO2 Capture, Use and Storage in Mexico.
Technical report.

SENER (2018b).
Inventario Nacional de Fuentes de Emisión y Sitios para el Uso y Almacenamiento de CO2 en México.

Serpa, J., Morbee, J., and Tzimas, E. (2011).
Technical and economic characteristics of a CO2 transmission pipeline infrastructure.

Shepherd, M. (2009).
Factors Influencing Recovery from Oil and Gas Fields.
91.

Shi, J. Q. and Durucan, S. (2005).
CO2 storage in caverns and mines.
Oil and Gas Science and Technology, 60(3):569–571.

Shukla, R., Ranjith, P., Haque, A., and Choi, X. (2010).
A review of studies on CO2 sequestration and caprock integrity.
Fuel, 89(10):2651–2664.

Smith, E., Morris, J., Kheshgi, H., Teletzke, G., Herzog, H., and Paltsev, S. (2021).
The cost of CO2 transport and storage in global integrated assessment modeling.
International Journal of Greenhouse Gas Control, 109(March).

Sokama-Neuyam, Y. A., Boakye, P., Aggrey, W. N., Obeng, N. O., Adu-Boahene, F., Woo, S. H., and Ursin, J. R. (2020).
Theoretical Modeling of the Impact of Salt Precipitation on CO2Storage Potential in Fractured Saline Reservoirs.
ACS Omega, 5(24):14776–14785.

Spangler, L. H., Dobeck, L. M., Repasky, K. S., Nehrir, A. R., Humphries, S. D., Barr, J. L., Keith, C. J., Shaw, J. A., Rouse, J. H., Cunningham, A. B., Benson, S. M., Oldenburg, C. M., Lewicki, J. L., Wells, A. W., Diehl, J. R., Strazisar, B. R., Fessenden, J. E., Rahn, T. A., Amonette, J. E., Barr, J. L., Pickles, W. L., Jacobson, J. D., Silver, E. A., Male, E. J., Rauch, H. W., Gullickson, K. S., Trautz, R., Kharaka, Y., Birkholzer, J., and Wielopolski, L. (2010).

A shallow subsurface controlled release facility in Bozeman, Montana, USA, for testing near surface CO2 detection techniques and transport models.
Environmental Earth Sciences, 60(2):227–239.

SSJV MPEP (2020).
Pozos abandonados y pozos inactivos.
Southern San Joaquin Valley Management Practices Evaluation Program.

Stork, A. L., Verdon, J. P., and Kendall, J. (2015).
The microseismic response at the In Salah Carbon Capture and Storage (CCS) site.
International Journal of Greenhouse Gas Control, 32:159–171.

Streit, E. and Hillis, R. R. (2004).
Estimating fault stability and sustainable fluid pressures for underground storage of CO 2 in porous rock.
Energy, 29(9-10):1445–1456.

Svensson, R., Odenberger, M., Johnsson, F., and Strömberg, L. (2004).
Transportation systems for CO2 - Application to carbon capture and storage.
Energy Conversion and Management, 45(15-16):2343–2353.

Sy, S., Fabbri, A., Gravaud, I., and Seyedi, D. (2012).
Evaluation of the CO2 leakage risk along the abandoned wells in the French context.
Energy Procedia, 23:480–486.

Talwani, M. (2011).
The Future of Oil in Mexico.
James A. Barker III Institute for Public Policy.

Thomas, D. and Benson, S. (2005).
Carbon dioxide capture for storage in deep geologic formations-results from the CO2 capture project: Vol 1-capture and separation of carbon dioxide from combustion, Vol 2-geologic storage of carbon dioxide with monitoring and verification.
Elsevier.

Townsend, A. and Gillespie, A. (2020).
Scaling Up the CCS Market to Deliver Net-Zero Emissions.
Technical report, Global CCS Institute.

USDOE, SENER, and NRCAN (2012).
The North American Carbon Storage Atlas.
Technical report.

USDOE/NETL (2015).
Carbon Storage Atlas (5th Edition).

Technical report, National Energy Technology Laboratory.

USGS (2020a).
Earthquake Glossary.

USGS (2020b).
Earthquake Hazards 201 - Technical Q&A.

Usman, M. B. I. and Haris, A. (2019).
Reservoir Characterization Sandstone Reservoir Based on Wireline Log.
IOP Conference Series: Materials Science And Engineering, 546.

van der Meer, L. G. and Yavuz, F. (2009).
CO2 storage capacity calculations for the Dutch subsurface.
Energy Procedia, 1(1):2615–2622.

Van Thienen-Visser, K. and Breunese, J. N. (2015).
Induced seismicity of the Groningen gas field: History and recent developments.
Leading Edge, 34(6):664–671.

Varun Jain, Ramneek Singh Bhamra, Maitreya Mishra, and Rajiv Gupta (2019).
Water Security and Sustainability: Proceedings of Down To Earth 2019 .
Springer Nature Singapore.

Verdon, J. P. (2014).
Significance for secure CO2 storage of earthquakes induced by fluid injection.
Environmental Research Letters, 9(6).

Verdon, J. P. and Bommer, J. J. (2020).
Green, yellow, red, or out of the blue? An assessment of Traffic Light Schemes to mitigate the impact of hydraulic fracturing-induced seismicity.
Journal of Seismology, 25(1):301–326.

Verdon, J. P., Kendall, J., Horleston, A. C., and Stork, A. L. (2016).
Subsurface fluid injection and induced seismicity in southeast Saskatchewan.
International Journal of Greenhouse Gas Control, 54(1750-5836):429–440.

Verdon, J. P., Kendall, J., Stork, A. L., Chadwick, R. A., White, D. J., and Bissell, R. C. (2013).
Comparison of geomechanical deformation induced by megatonne-scale CO2 storage at Sleipner, Weyburn, and In Salah.
Proceedings of the National Academy of Sciences, 110(30):E2762–E2771.

Verdon, J. P., Kendall, J.-M., and White, J. D. (2012).
Monitoring carbon dioxide storage using passive seismic techniques.
Proceedings of the Institute of Civil Engineers - Energy, 165(EN2):85–96.

Vilarrasa, V., De Simone, S., Carrera, J., and Villaseñor, A. (2021).
Unraveling the Causes of the Seismicity Induced by Underground Gas Storage at Castor, Spain.
Geophysical Research Letters, 48(7):1–10.

Walsh, F. R. and Zoback, M. D. (2016).
Probabilistic assessment of potential fault slip related to injection- induced earthquakes : Application to north central Oklahoma , USA.
The Geological Society of America, 44(12):1–4.

White, J. A. and Foxall, W. (2016).
International Journal of Greenhouse Gas Control Assessing induced seismicity risk at CO 2 storage projects : Recent progress and remaining challenges.
49:413–424.

Winter, E. M. and Bergman, P. D. (1993).
Availability of depleted oil and gas reservoirs for disposal of carbon dioxide in the United States.
Energy Conversion and Management, 34(9-11):1177–1187.

Wiprut, D. and Zoback, M. D. (2000).
Fault reactivation and fluid flow along a previously dormant normal fault in the northern North Sea.
Geology, 28(7):595–598.

Worum, G., van Wees, J.-D., Bada, G., van Balen, R. T., Cloetingh, S., and Pagnier, H. (2004).
Slip tendency analysis as a tool to constrain fault reactivation: A numerical approach applied to three-dimensional fault models in the Roer Valley rift system (southeast Netherlands).
Journal of Geophysical Research: Solid Earth, 109(B2):1–16.

Yáñez Angarita, E. E., Núñez-López, V., Ramírez, A. R., Monroy, E. C., and Faaij, A. (2022).
Rapid screening and probabilistic estimation of the potential for CO2-EOR and associated geological CO2 storage in Colombian petroleum basins.
Petroleum Geoscience, 28(1).

Yang, Q., Zhao, W., Dixon, T. H., Amelung, F., Han, W. S., and Li, P. (2015).
InSAR monitoring of ground deformation due to CO2 injection at an enhanced oil recovery site, West Texas.
International Journal of Greenhouse Gas Control, 41:20–28.

Yildirim, V., Yomralioglu, T., and Aydinoglu, A. C. (2007).
GIS Based Pipeline Route Selection by ArcGIS in Turkey.

In *Twenty-Seventh Annual ESRI Intern Seventh Annual ESRI International User Conference*.

Yildirim, V., Yomralioglu, T., Nisanci, R., Çolak, H. E., Bediroğlu, , and Saralioglu, E. (2017).
A spatial multicriteria decision-making method for natural gas transmission pipeline routing.
Structure and Infrastructure Engineering, 13(5):567–580.

Yousefi-sahzabi, A., Sasaki, K., Djamaluddin, I., Yousefi, H., and Yuichi, S. (2011).
Energy Procedia GIS modeling of CO2 emission sources and storage possibilities.
Energy Procedia, 4:2831–2838.

Zegart, D. (2021).
Gassing Satartia: Carbon Dioxide Pipeline Linked To Mass Poisoning | HuffPost UK Environment.

Zhang, X., Liu, W., Chen, J., Jiang, D., Fan, J., Daemen, J. J., and Qiao, W. (2022).
Large-scale CO2 disposal/storage in bedded rock salt caverns of China: An evaluation of safety and suitability.
Energy, 249.

Zoback, M. D. and Gorelick, S. M. (2012).
Earthquake triggering and large-scale geologic storage of carbon dioxide.
Proceedings of the National Academy of Sciences, 109(26):10164–10168.

Zwick, A. A. (2009).
Developing a Routing Priority Map for Geospatial Modeling of CO2 Pipeline Deployment in the People's Republic of China.
Technical report.

APPENDIX A

Supplementary Material for Chapter 3

Well log code

Listing 1: Well log Ogarrio 1483

```
import numpy as np
import matplotlib.pyplot as plt

my_data = np.genfromtxt('C:/Users/Ogarrio/Ogarrio_1483.csv', delimiter=',
    ', skip_header=1)
nfile = str('C:/Users/Ogarrio/Ogarrio 1319.csv') #get name of well to get
     depths of formations from  well database
nfile = nfile[nfile.rfind('/'):]#find '/' in previous line
nfile = nfile[1:-2] #find the name in the last '/'
ndatadh = my_data[:,0] #data from the well csv
ndatagr= my_data[:,1] #matrix to column vector
ndatavs = my_data[:,2]
hln1 = np.array(np.where(my_data[:,2] >= 0.5) and (my_data[:,2] <= 0.499)
    )#find condition in array bolean matrix true/false
hln2 = np.argwhere(np.diff(hln1))#calculates the difference in every
    value and removes the zeros/false from array
hln3 = hln2+1 #add upper limits
hln4 = np.array([[0], [len(hln1)-1]])#add bottom depth
hln5 = np.array(sorted(np.vstack((hln2, hln3, hln4))))#arrange vertically
     all the arrays
hln = my_data[:,0][hln5]#depths where volclay changes
depth1 = np.diff(hln, axis=0)#substract depths to get thickness
diff=depth1[1::2] #substract depths to get  the change in the thickness
depth1 = depth1[::2]#slicing depths eliminating the change in the
    thickness
depth2=diff
if len(depth2)==0: #condition to set up the size of the change of the
    thickness
    depth2=0
    depth1[depth1==0] =depth2
else:
    depth2=diff[0]
    depth1[depth1==0] =depth2
```

```
27
28 sshale=sum(depth1[1::2]) #sum slicing[start,end,step]
29 sstone=sum(depth1[::2]) #sum of all the sandstone in the well
30
31 suma=sshale+sstone
32 pershale= (sshale/suma)*100 #total percentage of shale
33 perstone= (sstone/suma)*100 #total percentage of sandstone
34
35 por= my_data[:,3][hln5] #porosity where volclay changes
36 pshale=sum(por[1::2]) #sum of all the porosity values of shale
37 pstone=sum(por[::2]) #sum of all the porosity values of sandstone
38
39 from depths import depthwell as dw #importing function
40 name = nfile #data to read in the function
41 rule1 = "Upper Concepcion"
42 rule2 = "Lower Concepcion"
43 rule3 = "Encanto"
44 rule4 = "Anhydrite"
45
46 formation= dw(name, rule1, rule2, rule3, rule4) #outputs of the function
47 uc=float(formation['up']) #inputs to find in the fuction
48 lc=float(formation['low'])
49 En=float(formation['en'])
50 An=float(formation['an'])
51
52
53 W= [i for i in range(len(hln)) if hln[i]<uc] #get depths lower than Upper
       Concepcion
54 X= [i for i in range(len(hln)) if hln[i] >= uc and hln[i]<=lc] #condition
       to get UC indexes in relation with depth
55 if X:
56     hln6=np.array(X) #convert X list in array
57     if len(W)>=1: #get upper index if there's any
58         hln6=hln6-1
59     else:
60         hln6=hln6
61     hln7= hln[hln6] # list of depths in relation with UC indexes array
62     depthuc = np.diff(hln7, axis=0) #thicknesses of UC
63     if depthuc[0]==depth2: #condition to slice thicknesess according to
      where the real depth starts
64         depthuc =depthuc[1::2]
65     else:
66         depthuc =depthuc[::2]
67     depthuc[depthuc==0] =depth2
68     poruc=por[hln6] #list of porosity in relation with UC indexes array
69
70     if len(depthuc)>1: #if len of the array of thicknesses is bigger than
       1 then get:
71         ucshale=sum(depthuc[1::2]) #total sum of shale in UC
```

```
72          ucstone=sum(depthuc[::2]) #total sum of sandstone in UC
73          suma1=ucshale+ucstone
74          ucpersh= (ucshale/suma1)*100 #percentage of shale in Upper
    Conception
75          ucperst= (ucstone/suma1)*100
76          avucshale=ucshale/len(depthuc[1::2]) #average of shale in UC
77          avucstone=ucstone/len(depthuc[::2])
78          avpucsh=(sum(poruc[::2])/len(poruc[::2])) #mean porosity of shale
     in UC
79          avpucst=(sum(poruc[1::2])/len(poruc[1::2]))
80          sducsh=np.std(poruc[::2]) #standard deviation of the porosity of
    shale in UC
81          sducst=np.std(poruc[1::2])
82          ucngrsh= ucshale/suma1 #net to gross ratio of porosity of the
    shale in UC
83          ucngrst= ucstone/suma1
84          print ('The percentage of Shale in Upper Concepcion in '+nfile+'
    is',(np.round(ucpersh,2))) #output changing the name of the well
85          print ('The percentage of Sandstone in Upper Concepcion in '+
    nfile+' is', (np.round(ucperst,2)))
86      else:
87          ucpersh= np.nan #otherwise it doesn't have a value
88          ucperst= np.nan
89  else:
90      hln6=np.nan #if hln6  has no values then is nan
91      hln7= np.nan
92      depthuc= np.nan
93
94  Y= [i for i in range(len(hln)) if hln[i] >= lc and hln[i]<=En]#condition
    to get LC indexes in relation with depth
95  if Y:
96      hln8=np.array(Y) #same as X and hln7
97      if hln7 is np.nan and len(W)==0: #get upper index if there's any
98          hln8=hln8
99      else:
100         hln8=hln8-1
101     hln9= hln[hln8] # list of depths in relation with LC indexes array
102     depthlc = np.diff(hln9, axis=0) #thickness of LC
103     if depthlc[0]==depth2:
104         depthlc =depthlc[1::2]
105     else:
106         depthlc =depthlc[::2]
107     depthlc[depthlc==0] =depth2
108     porlc=por[hln8]
109
110     if len(depthlc)>1:
111         lcshale=sum(depthlc[1::2])
112         lcstone=sum(depthlc[::2])
113         suma2=lcshale+lcstone
```

```
114         lcpersh= (lcshale/suma2)*100 #percentage of shale in Lower
    Conception
115         lcperst= (lcstone/suma2)*100 #percentage of sandstone in LC
116         avlcshale=lcshale/len(depthlc[1::2])
117         avlcstone=lcstone/len(depthlc[::2])
118         avplcsh=(sum(porlc[::2])/len(porlc[::2]))
119         avplcst=(sum(porlc[1::2])/len(porlc[1::2]))
120         sdlcsh=np.std(porlc[::2])
121         sdlcst=np.std(porlc[1::2])
122         lcngrsh= lcshale/suma2
123         lcngrst= lcstone/suma2
124         print ('The percentage of Shale in Lower Concepcion in '+nfile+'
    is',(np.round(lcpersh,2)))
125         print ('The percentage of Sandstone in Lower Concepcion in '+
    nfile+' is', (np.round(lcperst,2)))
126     else:
127         lcpersh= np.nan
128         lcperst= np.nan
129 else:
130     hln8 = np.nan #get upper index
131     hln9 = np.nan # list of depths in relation with LC indexes array
132     depthlc = np.nan #thickness of LC
133
134
135 Z= [i for i in range(len(hln)) if hln[i]>=En]
136 if Z:
137     hln10= np.array(Z)
138     if hln9 is np.nan and hln7 is np.nan and len(W)==0: #get upper index
    if there's any
139         hln10=hln10
140     else:
141         hln10=hln10-1
142     hln11= np.append(hln10,[len(hln)-1]) #add the last value of Z/hln
143     hln12= hln[hln11] # list of depths in relation with En indexes array
144     depthen = np.diff(hln12, axis=0) #thickness of En
145     if depthen[0]==depth2:
146         depthen =depthen[1::2]
147     else:
148         depthen =depthen[::2]
149     depthen[depthen==0] =depth2
150     poren=por[hln11]
151
152     if len(depthen)>1:
153         eshale=sum(depthen[::2])
154         estone=sum(depthen[1::2])
155         suma3=eshale+estone
156         epershale= (eshale/suma3)*100 #percentage of shale in Encanto
157         eperstone= (estone/suma3)*100 #percentage of sandstone in Encanto
158         aveshale=eshale/len(depthen[::2])
```

```
159         avestone=estone/len(depthen[1::2])
160         avpensh=(sum(poren[::2])/len(poren[::2]))
161         avpenst=(sum(poren[1::2])/len(poren[1::2]))
162         sdensh=np.std(poren[::2])
163         sdenst=np.std(poren[1::2])
164         enngrsh= eshale/suma3
165         enngrst= estone/suma3
166         print ('The percentage of Shale in Encanto in '+nfile+' is',(np.
    round(epershale,2)))
167         print ('The percentage of Sandstone in Encanto in '+nfile+' is',
    (np.round(eperstone,2)))
168     else:
169         epershale= np.nan
170         eperstone= np.nan
171 else:
172     hln10 = np.nan
173     hln11 = np.nan
174     depthen = np.nan
175
176 #condition that creates a csv with the percentages of sandstone and shale
     values if they meet any of the conditions (if thicknesses has values
    or not)
177 if ((depthuc is not np.nan and len(depthuc)>1) and (depthlc is not np.nan
     and len(depthlc)>1) and (depthen is not  np.nan and len(depthen)>1)):
178     np.savetxt('C:/Users/Ogarrio/'+nfile+'d.csv',
179                (ucpersh,ucperst,lcpersh,lcperst,epershale,eperstone),
180                 fmt="%10.5f",delimiter=",", newline= "," , header="
    percentages")
181 elif ((depthuc is np.nan or len(depthuc)<=1) and (depthlc is not np.nan
    and len(depthlc)>1) and (depthen is not np.nan and len(depthen)>1)):
182     np.savetxt('C:/Users/Ogarrio/'+nfile+'d.csv',
183                (lcpersh,lcperst,epershale,eperstone),
184                fmt="%10.5f",delimiter=",", newline= "," ,header="
    percentages")
185 elif ((depthuc is not np.nan and len(depthuc)>1) and (depthlc is np.nan
    or len(depthlc)<=1) and (depthen is not np.nan and len(depthen)>1)):
186     np.savetxt('C:/Users/Ogarrio/'+nfile+'d.csv',
187                (ucpersh,ucperst,epershale,eperstone),
188                fmt="%10.5f",delimiter=",",newline= ",",header="
    percentages")
189 elif ((depthuc is np.nan or len(depthuc)<=1) and (depthlc is np.nan or
    len(depthlc)<=1) and (depthen is not np.nan and len(depthen)>1)):
190     np.savetxt('C:/Users/Ogarrio/'+nfile+'d.csv',
191                (epershale,eperstone),
192                 fmt="%10.5f",delimiter=",",newline= ",",header="
    percentages")
193 elif ((depthuc is not np.nan and len(depthuc)>1) and (depthlc is np.nan
    or len(depthlc)<=1) and (depthen is np.nan or len(depthen)<=1)):
194     np.savetxt('C:/Users/Ogarrio/'+nfile+'d.csv',
```

```
195                 (ucpersh,ucperst),
196                  fmt="%10.5f",delimiter=",",newline= ",",header="
    percentages")
197
198 #Creates a csv file with the average porosity values
199 if ((depthuc is not np.nan and len(depthuc)>1) and (depthlc is not np.nan
     and len(depthlc)>1) and (depthen is not  np.nan and len(depthen)>1)):
200     np.savetxt('C:/Users/Ogarrio/'+nfile+'p.csv',
201             (avpucsh, avplcsh, avpensh, sducsh , sdlcsh , sdensh ,
    ucngrsh, lcngrsh, enngrsh,
202             avpucst, avplcst , avpenst ,sducst, sdlcst, sdenst, ucngrst,
     lcngrst, enngrst),
203             fmt="%f",delimiter=",",newline= ",",
204             header="AvPorshUC,AvPorshLC,AvPorshEn,SDPshUC,SDPshLC,SDPshEn
    ,NGRshUC,NGRshLC,NGRshEn,AvPorstUC,AvPorstLC,AvPorstEn,SDPstUC,SDPstLC
    ,SDPstEn,NGRstUC,NGRstLC,NGRstEn")
205 elif ((depthuc is np.nan or len(depthuc)<=1) and (depthlc is not np.nan
    and len(depthlc)>1) and (depthen is not np.nan and len(depthen)>1)):
206     np.savetxt('C:/Users/Ogarrio/'+nfile+'p.csv',
207             (avplcsh, avpensh, sdlcsh , sdensh, lcngrsh, enngrsh,avplcst
    , avpenst, sdlcst, sdenst,lcngrst,enngrst),
208             fmt="%f",delimiter=",",newline= ",",
209             header="AvPorshLC,AvPorshEn,SDPshLC,SDPshEn,NGRshLC,NGRshEn,
    AvPorstLC,AvPorstEn,SDPstLC,SDPstEn,NGRstLC,NGRstEn")
210 elif ((depthuc is not np.nan and len(depthuc)>1) and (depthlc is np.nan
    or len(depthlc)<=1) and (depthen is not np.nan and len(depthen)>1)):
211     np.savetxt('C:/Users/Ogarrio/'+nfile+'p.csv',
212             (avpucsh, avpensh, sducsh, sdensh , ucngrsh, enngrsh,avpucst,
     avpenst ,sducst, sdenst, ucngrst,enngrst),
213             fmt="%f",delimiter=",",newline= ",",
214             header="AvPorshUC,AvPorshEn,SDPshUC,SDPshEn,NGRshUC,NGRshEn,
    AvPorstUC,AvPorstEn,SDPstUC,SDPstEn,NGRstUC,NGRstEn")
215 elif ((depthuc is np.nan or len(depthuc)<=1) and (depthlc is np.nan or
    len(depthlc)<=1) and (depthen is not np.nan and len(depthen)>1)):
216     np.savetxt('C:/Users/Ogarrio/'+nfile+'p.csv',
217             (avpensh, sdensh, enngrsh,avpenst ,sdenst, enngrst),
218             fmt="%f",delimiter=",",newline= ",",
219             header="AvPorshEn,SDPshEn,NGRshEn,AvPorstEn,SDPstEn,NGRstEn")
220
221 # creates a csv with the thicknessess of each layer
222 if ((depthuc is not np.nan and len(depthuc)>1) and (depthlc is not np.nan
     and len(depthlc)>1) and (depthen is not  np.nan and len(depthen)>1)):
223     np.savetxt('C:/Users/Ogarrio/'+nfile+'t.csv',
224                 (ucstone,ucshale,lcshale,lcstone,eshale,estone,suma1,
    suma2,suma3,sshale, sstone, suma),
225                 fmt="%10.5f",delimiter=",", newline= "," , header="
    thickness")
226 elif ((depthuc is np.nan) and (depthlc is not np.nan and len(depthlc)>1)
    and (depthen is not np.nan and len(depthen)>1)):
```

```
227     np.savetxt('C:/Users/Ogarrio/'+nfile+'t.csv',
228                (lcshale,lcstone,eshale,estone, suma2, suma3, sshale,
    sstone, suma),
229                fmt="%10.5f",delimiter=",", newline= "," ,header="
    thickness")
230 elif ((depthuc is not np.nan and len(depthuc)>=1) and (depthlc is np.nan)
     and (depthen is not np.nan and len(depthen)>1)):
231     np.savetxt('C:/Users/Ogarrio/'+nfile+'t.csv',
232                (ucshale,ucstone,eshale,estone, suma1, suma3, sshale,
    sstone, suma),
233                fmt="%10.5f",delimiter=",",newline= ",",header="thickness
    ")
234 elif ((depthuc is np.nan) and (depthlc is np.nan) and (depthen is not np.
    nan and len(depthen)>1)):
235     np.savetxt('C:/Users/Ogarrio/'+nfile+'t.csv',
236                (eshale,estone, suma3, sshale, sstone, suma),
237                fmt="%10.5f",delimiter=",",newline= ",",header="thickness
    ")
238
239 #%%
240 fig, axs = plt.subplots(1,2, figsize=(10,20), sharey=True) #creates a
    plot with 2 graphs and set size
241 fig.suptitle(nfile, fontsize=20) #size of the title of the graph
242 fig.subplots_adjust(top=0.95, wspace=0.1) #set place where the title will
     be located
243
244 ax = axs[0] #set up for the first graph
245 ax.invert_yaxis() #from lowest to highest
246 ax.plot(ndatagr, ndatadh, c='tab:red') #choose the data that will be
    plotted
247 ax.set_xlabel('Gamma Ray', color='red', fontsize=10) #costumize the x
    axis label
248 ax.tick_params(axis='x',color='red') #display axes
249 ax.spines['top'].set_position(('outward',1)) # Only show ticks on the top
     and bottom spines
250 [ax.axhline(i, linestyle='-', linewidth=0.5) for i in hln] #depth loop
    list comprehension
251 ax.grid(True) #add grid
252
253 ax = axs[1] #set up for the second graph
254 ax.axvline(0.5, c='r', linewidth=1) #vertical red line
255 ax.plot(ndatavs, ndatadh, c='tab:green')
256 ax.set_xlabel('Volume Clay', color='green', fontsize=10)#X axis label
257 ax.tick_params(axis='x',color='green')
258 ax.spines['top'].set_position(('outward',1))
259 [ax.axhline(i, xmin=-.2, xmax=1, linestyle='dotted',linewidth=1, clip_on=
    False) for i in hln] #depth loop list comprehension with horizontal
    lines
260 ax.grid(True)
```

```
#save plot
plt.savefig('C:/Users/Ogarrio/'+nfile+'.png', dpi=300.0, bbox_inches='
    tight', pad_inches=0.5)
```

Cross plots

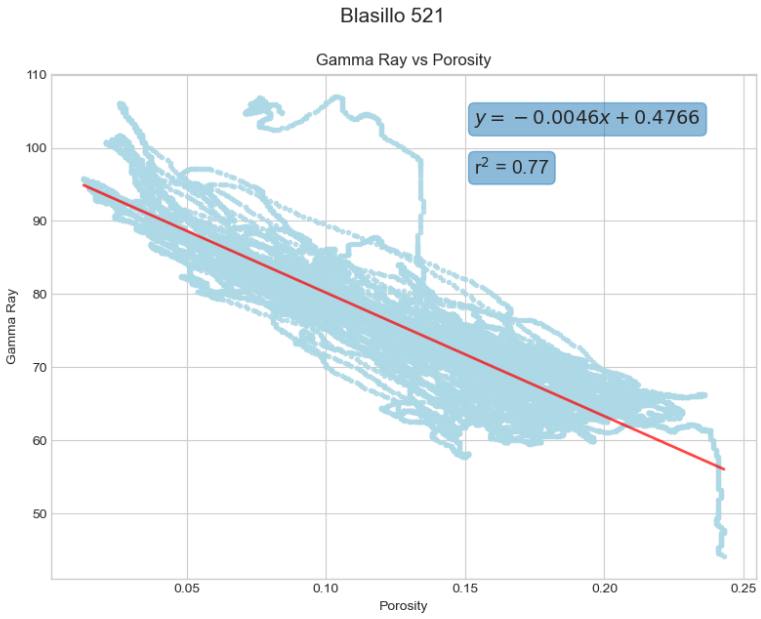

Figure 1: Relationship between GR vs Porosity showing the trend line, the linear regression equation, and r^2 of its values from the well Blasillo 521.

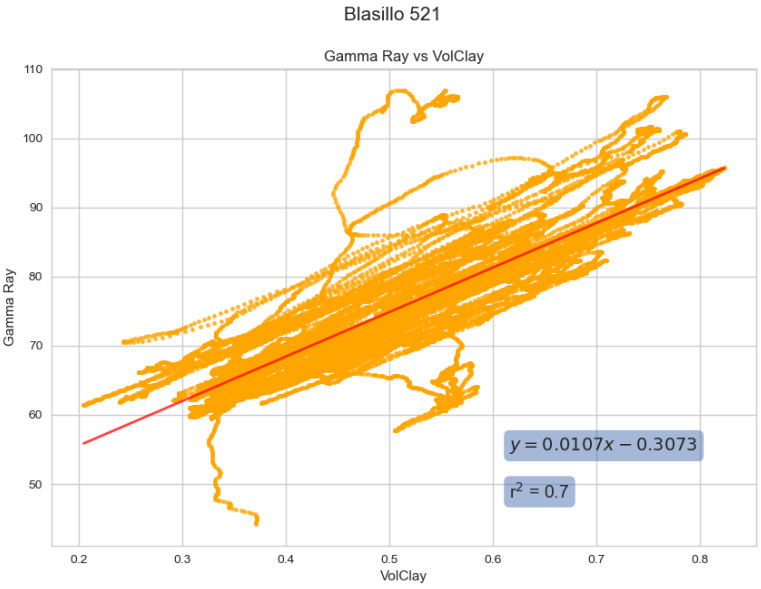

Figure 2: Relationship between GR vs VolClay showing the trend line, the linear regression equation, and r^2 of its values from the well Blasillo 521.

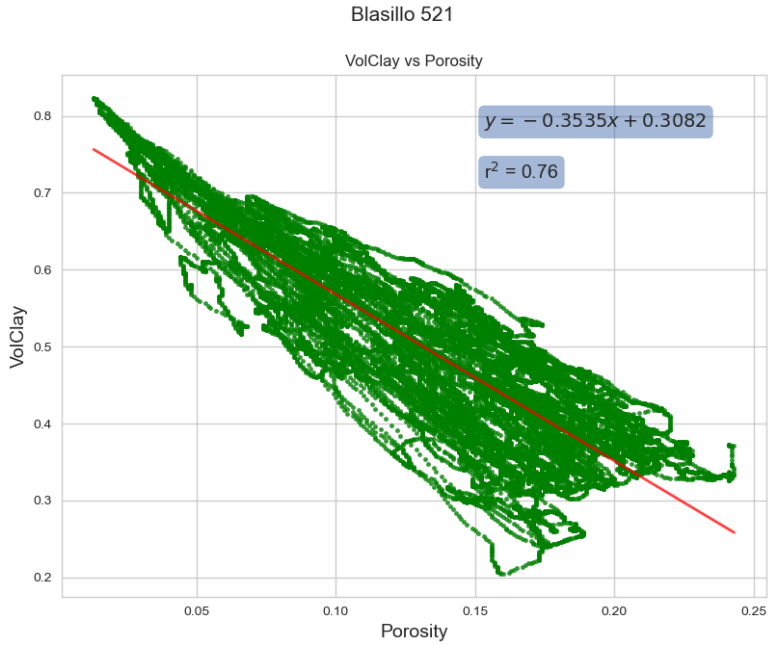

Figure 3: Relationship between VolClay vs Porosity showing the trend line, the linear regression equation, and r^2 of its values from the well Blasillo 521.

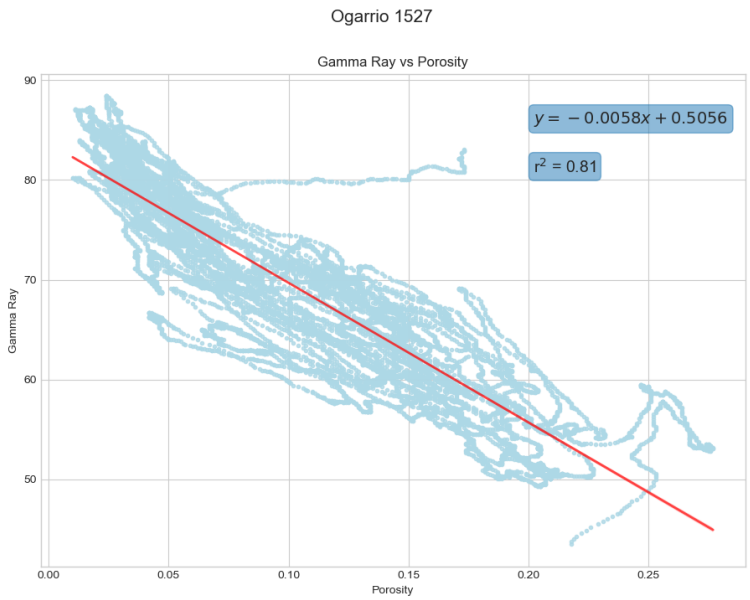

Figure 4: Relationship between GR vs Porosity showing the trend line, the linear regression equation, and r^2 of its values from the well Ogarrio 1527.

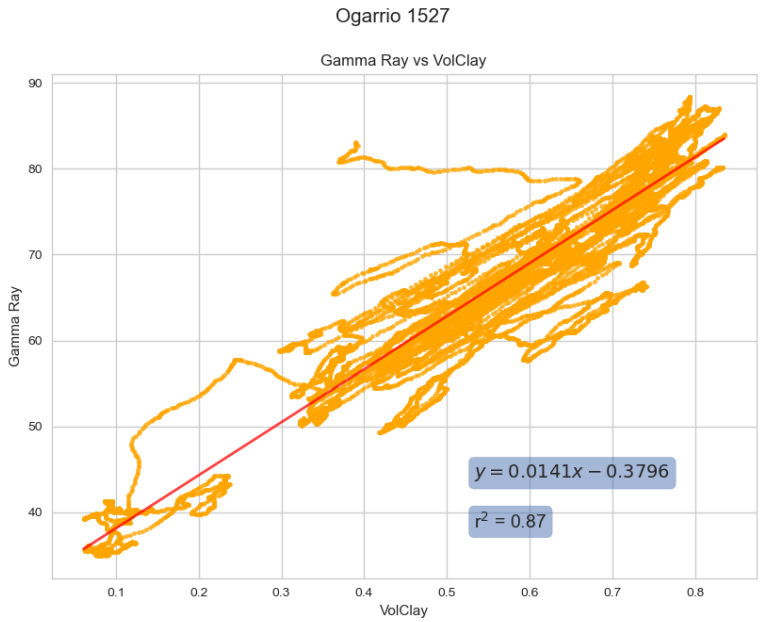

Figure 5: Relationship between GR vs VolClay showing the trend line, the linear regression equation, and r^2 of its values from the well Ogarrio 1527.

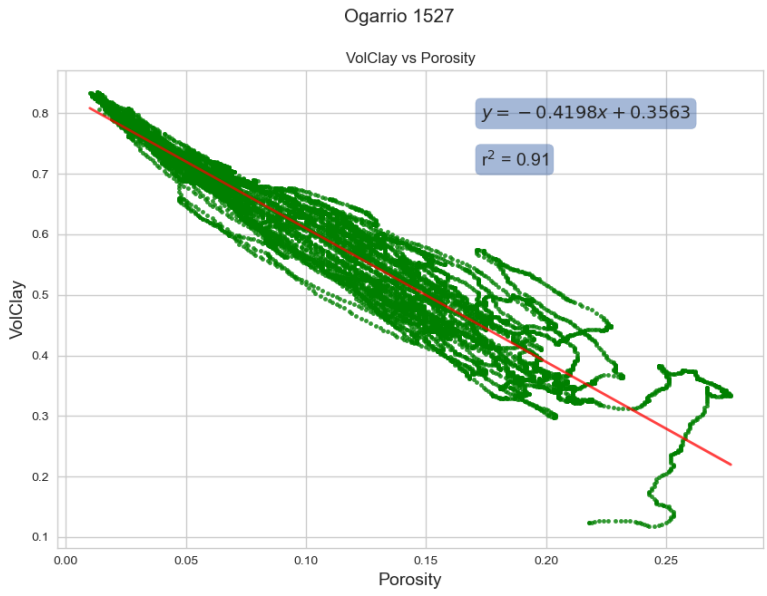

Figure 6: Relationship between VolClay vs Porosity showing the trend line, the linear regression equation, and r^2 of its values from the well Ogarrio 1527.

Average values of the well logs

Average porosity						
Wells	**Upper Concepcion**		**Lower Concepcion**		**Encanto**	
	Shale	**Sandstone**	**Shale**	**Sandstone**	**Shale**	**Sandstone**
Blasillo 521			0.153	0.153	0.122	0.121
Blasillo 525D	0.159	0.162	0.147	0.144	0.127	0.127
Ogarrio 1483	0.146	0.141	0.109	0.103	0.124	0.121
Ogarrio 1483D	0.133	0.129			0.118	0.119
Ogarrio 1527					0.137	0.134
Ogarrio 565					0.033	0.034
Ogarrio 579			0.500	0.500	0.500	0.493
Ogarrio 655					0.195	0.194
Ogarrio 658					0.136	0.137
Ogarrio 678					0.031	0.033
Ogarrio 73D					0.058	0.033
Total average	**0.146**	**0.144**	**0.227**	**0.225**	**0.144**	**0.141**

Table 1: Average porosity values of the available wells.

Average proportion of shale and sandstone of the wells								
Well	**Upper Concepcion**		**Lower Concepcion**		**Encanto**		**Location**	
	Shale	**Sandstone**	**Shale**	**Sandstone**	**Shale**	**Sandstone**	**Lat**	**Long**
Blasillo 521			57.24	42.76	46.62	53.38	-94.0511	18.04662
Blasillo 523					49.48	50.52	-94.048	18.04869
Blasillo 523_1					8.92	91.08	-94.0479	18.04869
Blasillo 525	15.64	84.36	59.69	40.31	66.80	33.20	-94.048	18.04841
Blasillo 525D	95.87	4.13	58.44	41.56	26.32	73.68	-94.0483	18.04674
Magallanes 492						100	-93.8899	18.12252
Magallanes 501	65.46	34.54					-93.9143	18.18742
Magallanes 724					100		-93.8829	18.20231
Magallanes 761					67.93	32.07	-93.8701	18.20206
Magallanes 926					75.42	24.58	-93.8814	18.08963
Ogarrio 101	37.34	62.66	2.04	97.96	84.54	15.46	-93.9114	18.00515
Ogarrio 1303					74.31	25.69	-93.9537	18.02068
Ogarrio 1319					19.62	80.38	-93.9469	18.02044
Ogarrio 1388	65.02	34.98	83.90	16.10	53.29	46.71	-93.9765	18.03619
Ogarrio 1483	72.19	27.81	92.36	7.64	57.97	42.03	-93.9406	17.99851
Ogarrio 1483D	96.27	3.73	71.95	28.05	64.05	35.95	-93.9405	17.99865
Ogarrio 1483D			96.27	3.73	64.05	35.95	-93.9405	17.99865
Ogarrio 1527					78.65	21.35	-93.9526	18.06841
Ogarrio 1528						100	-93.9569	18.02223
Ogarrio 1529	76.00	24.00			97.54	2.46	-93.9468	18.02064
Ogarrio 1529_1	31.59	68.41	51.40	48.60	23.58	76.42	-93.9467	18.0206
Ogarrio 1602					100		-93.9375	18.00719

Ogarrio 1602_1					100		-93.9374	18.0071
Ogarrio 565					68.18	31.82	-93.9308	18.03968
Ogarrio 579			71.90	28.10	32.27	67.73	-93.9442	18.05745
Ogarrio 579_1					80.86	19.14	-93.9441	18.0574
Ogarrio 655					44.39	55.61	-93.9499	18.06233
Ogarrio 658					78.50	21.50	-93.9474	18.05569
Ogarrio 658_1					78.50	21.50	-93.9474	18.0556
Ogarrio 662					65.02	34.98	-93.9101	17.97515
Ogarrio 662 rad					61.13	38.87	-93.91	17.9751
Ogarrio 671					67.70	32.30	-93.9409	18.05204
Ogarrio 676					74.03	25.97	-93.9376	18.05385
Ogarrio 677	88.76	11.24	51.10	48.90	65.96	34.04	-93.9376	18.05386
Ogarrio 678					77.40	22.60	-93.9408	18.05567
Ogarrio 678_2					81.66	18.34	-93.94	18.055
Ogarrio 678_3					74.03	25.97	-93.9408	18.0556
Ogarrio 679	79.65	20.35			34.56	65.44	-93.9442	18.05745
Ogarrio 700			86.01	13.99	54.68	45.32	-93.9731	18.04172
Ogarrio 702					91.06	8.94	-93.9101	17.97877
Ogarrio 736					97.36	2.64	-93.9134	17.98417
Ogarrio 73D					68.53	31.47	-93.9199	18.03058
Ogarrio 73D1					67.27	32.73	-93.919	18.03
Ogarrio 760					94.05	5.95	-93.9068	17.98055
Ogarrio 77A			94.40	5.60	15.01	84.99	-93.9162	18.03052
Ogarrio 802					33.14	66.86	-93.9406	18.00577
Ogarrio 808						100	-93.9438	18.0076
Ogarrio 812					47.90	52.10	-93.934	18.0021
Ogarrio 813					85.89	14.11	-93.934	17.99854
Ogarrio 813D					36.65	63.35	-93.9339	17.9985
Ogarrio 818D	43.41	56.59	73.23	26.77	22.80	77.20	-93.9341	17.99491
Ogarrio 820					69.71	30.29	-93.9371	18.0111
Ogarrio 83						100	-93.9276	18.03866
Ogarrio 89	12.54	87.46			84.87	15.13	-93.9155	18.02915
Ogarrio 94					10.35	89.65	-93.9261	18.03833
Ogarrio 95	49.10	50.90			87.76	12.24	-93.9245	18.03726
Otates 14					100		-93.9529	18.10012
Otates 14_2					91.25	8.75	-93.9528	18.1001
Otates 518					92.82	7.18	-93.934	18.0021
Otates 518_2					90.66	9.34	-93.9339	18.002
Otates 607	100		100		100		-93.9623	18.08781
Total average	**61.92**	**40.79**	**69.99**	**32.14**	**65.80**	**42.09**		

Table 2: Percentage of shale and sandstone in the wells.

Thicknesses of shale and sandstone interbeddings									
	Upper Concepcion			Lower Concepcion			Encanto		
Well	Shale	Sandstone	Total	Shale	Sandstone	Total	Shale	Sandstone	Total
Blasillo 521				189.5	141.56	331.06	843.7	736.82	1580.52
Blasillo 523							118.9	121.4	240.3
Blasillo 523_1							77	786.5	863.5
Blasillo 525	33.19	179	212.19	145.08	97.99	243.07	999.49	496.72	1496.21
Blasillo 525D	241.5	10.4	251.9	150.2	106.8	257	387.7	1085.4	1473.1
Magallanes 501	86.25	45.5	131.75						
Magallanes 761							134.5	63.5	198
Magallanes 926							899	293	1192
Ogarrio 101	325.5	194	519.5	6.25	300.75	307	1435.5	262.5	1698
Ogarrio 1303							384.5	132.9	517.4
Ogarrio 1319							1882.51	214.36	2096.87
Ogarrio 1388	88.75	47.75	136.5	153.75	29.5	183.25	821	719.5	1540.5
Ogarrio 1483	144.38	55.63	200.01	183.58	15.19	198.77	469.1	340.11	809.21
Ogarrio 1483D	154.8	6	160.8				636.2	357.1	993.3
Ogarrio 1527							933.17	251.32	1184.49
Ogarrio 1529	202.69	64	266.69				1202.76	30.32	1233.08
Ogarrio 1529_1	155.14	71.63	226.77	78.02	73.76	151.78	269.1	872.34	1141.44
Ogarrio 565							224.1	104.6	328.7
Ogarrio 568							23.92	6.55	30.47
Ogarrio 579							80.25	19	99.25
Ogarrio 579				62.79	24.54	87.33	192.49	404.05	596.54
Ogarrio 655							4.25	4	8.25
Ogarrio 658							778	272	1050
Ogarrio 658							23.92	6.55	30.47
Ogarrio 662							312.25	168	480.25
Ogarrio 662 rad							307.24	195.38	502.62
Ogarrio 671							887.5	423.5	1311
Ogarrio 676							1042.5	365.75	1408.25
Ogarrio 677	14.25	112.5	126.75	29	27.75	56.75	999.25	515.75	1515
Ogarrio 678							1138	332.25	1470.25
Ogarrio 678_2							161	717	878
Ogarrio 678_3							1096.81	384.79	1481.6
Ogarrio 679	112.5	28.75	141.25				473	895.75	1368.75
Ogarrio 700				195.25	31.75	227	608	504	1112
Ogarrio 702							1724.25	169.25	1893.5
Ogarrio 736							1256.25	34	1290.25
Ogarrio 73D							320.95	147.38	468.33
Ogarrio 73D1							306.25	149	455.25
Ogarrio 760							1639	103.75	1742.75
Ogarrio 760							1639	103.75	1742.75

Ogarrio 77A				400	23.75	423.75	135.5	767	902.5
Ogarrio 802							787.25	390.25	1177.5
Ogarrio 812							190.75	207.5	398.25
Ogarrio 813							441.3	72.5	513.8
Ogarrio 813D							254.2	439.3	693.5
Ogarrio 818D	20.6	15.8	36.4	178.4	65.2	243.6	124.2	420.6	544.8
Ogarrio 820							173.1	75.2	248.3
Ogarrio 89	8.75	61	69.75				839.75	149.75	989.5
Ogarrio 94							86.5	749.5	836
Ogarrio 95	41	42.5	83.5				996.5	139	1135.5
Otates 14_2							163.8	15.7	179.5
Otates 518							231.3	17.9	249.2
Otates 518_2							146.6	15.1	161.7

Table 3: Thicknesses of the shale and sandstone interbeddings in each layer.

Net to gross ratios and standard deviations

	Upper Concepcion			Lower Concepcion			Encanto		
Well	**Sandstone**	**Thickness layer**	**NTG**	**Sandstone**	**Thickness layer**	**NTG**	**Sandstone**	**Thickness layer**	**NTG**
Blasillo 521				141.56	331.06	0.43	843.7	1580.52	0.47
Blasillo 523							118.9	240.3	0.51
Blasillo 523_1							77	863.5	0.91
Blasillo 525	179	212.19	0.84	97.99	243.07	0.40	999.49	1496.21	0.33
Blasillo 525D	10.4	251.9	0.04	106.8	257	0.42	387.7	1473.1	0.74
Magallanes 501	45.5	131.75	0.35						
Magallanes 761							134.5	198	0.32
Magallanes 926							899	1192	0.25
Ogarrio 101	194	519.5	0.37	300.75	307	0.98	1435.5	1698	0.15
Ogarrio 1303							384.5	517.4	0.26
Ogarrio 1319							1882.51	2096.87	0.10
Ogarrio 1388	47.75	136.5	0.35	29.5	183.25	0.16	821	1540.5	0.47
Ogarrio 1483	55.63	200.01	0.28	15.19	198.77	0.08	469.1	809.21	0.42
Ogarrio 1483D	6	160.8	0.04				636.2	993.3	0.36
Ogarrio 1527							933.17	1184.49	0.21
Ogarrio 1529	64	266.69	0.24				1202.76	1233.08	0.02
Ogarrio 1529_1	71.63	226.77	0.32	73.76	151.78	0.49	269.1	1141.44	0.76
Ogarrio 565							224.1	328.7	0.32
Ogarrio 568							23.92	30.47	0.21
Ogarrio 579							80.25	99.25	0.19
Ogarrio 579				24.54	87.33	0.28	192.49	596.54	0.68
Ogarrio 655							4.25	8.25	0.48
Ogarrio 658							778	1050	0.26
Ogarrio 658							23.92	30.47	0.21

Ogarrio 662							312.25	480.25	0.35
Ogarrio 662 rad							307.24	502.62	0.39
Ogarrio 671							887.5	1311	0.32
Ogarrio 676							1042.5	1408.25	0.26
Ogarrio 677	112.5	126.75	0.89	27.75	56.75	0.49	999.25	1515	0.34
Ogarrio 678							1138	1470.25	0.23
Ogarrio 678_2							161	878	0.82
Ogarrio 678_3							1096.81	1481.6	0.26
Ogarrio 679	28.75	141.25	0.20				473	1368.75	0.65
Ogarrio 700				31.75	227	0.14	608	1112	0.45
Ogarrio 702							1724.25	1893.5	0.09
Ogarrio 736							1256.25	1290.25	0.03
Ogarrio 73D							320.95	468.33	0.31
Ogarrio 73D1							306.25	455.25	0.33
Ogarrio 760							1639	1742.75	0.06
Ogarrio 760							1639	1742.75	0.06
Ogarrio 77A				23.75	423.75	0.06	135.5	902.5	0.85
Ogarrio 802							787.25	1177.5	0.33
Ogarrio 812							190.75	398.25	0.52
Ogarrio 813							441.3	513.8	0.14
Ogarrio 813D							254.2	693.5	0.63
Ogarrio 818D	15.8	36.4	0.43	65.2	243.6	0.27	124.2	544.8	0.77
Ogarrio 820							173.1	248.3	0.30
Ogarrio 89	61	69.75	0.87				839.75	989.5	0.15
Ogarrio 94							86.5	836	0.90
Ogarrio 95	42.5	83.5	0.51				996.5	1135.5	0.12
Otates 14_2							163.8	179.5	0.09

Otates 518							231.3	249.2	0.07
Otates 518_2							146.6	161.7	0.09
Average NTG			**0.41**			**0.35**			**0.36**
NTG STD			**0.28**			**0.25**			**0.24**

Table 4: Net to gross ratios and their standard deviations of each layer.
NTG is obtained by dividing the total thickness by the thickness of sandstone interbedding in each layer.

Thickness sandstone in each layer									
	Upper Concepcion			Lower Concepcion			Encanto		
Well	Thickness layer	NTG	T sandstone	Thickness layer	NTG	T sandstone	Thickness layer	NTG	T sandstone
Blasillo 521				331.06	0.43	141.56	1580.52	0.47	736.82
Blasillo 523							240.3	0.51	121.4
Blasillo 523_1							863.5	0.91	786.5
Blasillo 525	212.19	0.84	179	243.07	0.40	97.99	1496.21	0.33	496.72
Blasillo 525D	251.9	0.04	10.4	257	0.42	106.8	1473.1	0.74	1085.4
Magallanes 501	131.75	0.35	45.5						0
Magallanes 761							198	0.32	63.5
Magallanes 926							1192	0.25	293
Ogarrio 101	519.5	0.37	194	307	0.98	300.75	1698	0.15	262.5
Ogarrio 1303							517.4	0.26	132.9
Ogarrio 1319							2096.87	0.10	214.36
Ogarrio 1388	136.5	0.35	47.75	183.25	0.16	29.5	1540.5	0.47	719.5
Ogarrio 1483	200.01	0.28	55.63	198.77	0.08	15.19	809.21	0.42	340.11
Ogarrio 1483D	160.8	0.04	6				993.3	0.36	357.1
Ogarrio 1527							1184.49	0.21	251.32
Ogarrio 1529	266.69	0.24	64				1233.08	0.02	30.32
Ogarrio 1529_1	226.77	0.32	71.63	151.78	0.49	73.76	1141.44	0.76	872.34
Ogarrio 565							328.7	0.32	104.6
Ogarrio 568							30.47	0.21	6.55
Ogarrio 579							99.25	0.19	19
Ogarrio 579				87.33	0.28	24.54	596.54	0.68	404.05
Ogarrio 655							8.25	0.48	4
Ogarrio 658							1050	0.26	272
Ogarrio 658							30.47	0.21	6.55

Ogarrio 662							480.25	0.35	168
Ogarrio 662 rad							502.62	0.39	195.38
Ogarrio 671							1311	0.32	423.5
Ogarrio 676							1408.25	0.26	365.75
Ogarrio 677	126.75	0.89	112.5	56.75	0.49	27.75	1515	0.34	515.75
Ogarrio 678							1470.25	0.23	332.25
Ogarrio 678_2							878	0.82	717
Ogarrio 678_3							1481.6	0.26	384.79
Ogarrio 679	141.25	0.20	28.75				1368.75	0.65	895.75
Ogarrio 700				227	0.14	31.75	1112	0.45	504
Ogarrio 702							1893.5	0.09	169.25
Ogarrio 736							1290.25	0.03	34
Ogarrio 73D							468.33	0.31	147.38
Ogarrio 73D1							455.25	0.33	149
Ogarrio 760							1742.75	0.06	103.75
Ogarrio 760							1742.75	0.06	103.75
Ogarrio 77A				423.75	0.06	23.75	902.5	0.85	767
Ogarrio 802							1177.5	0.33	390.25
Ogarrio 812							398.25	0.52	207.5
Ogarrio 813							513.8	0.14	72.5
Ogarrio 813D							693.5	0.63	439.3
Ogarrio 818D	36.4	0.43	15.8	243.6	0.27	65.2	544.8	0.77	420.6
Ogarrio 820							248.3	0.30	75.2
Ogarrio 89	69.75	0.87	61				989.5	0.15	149.75
Ogarrio 94							836	0.90	749.5
Ogarrio 95	83.5	0.51	42.5				1135.5	0.12	139
Otates 14_2							179.5	0.09	15.7

Otates 518							249.2	0.07	17.9
Otates 518_2							161.7	0.09	15.1
Average thickess			**18.68**			**17.70**			**306.58**

Table 5: Sandstone thicknesses in each layer.
Each thickness is obtained by multiplying the total thickness of the layer by the NTG.

Well logs

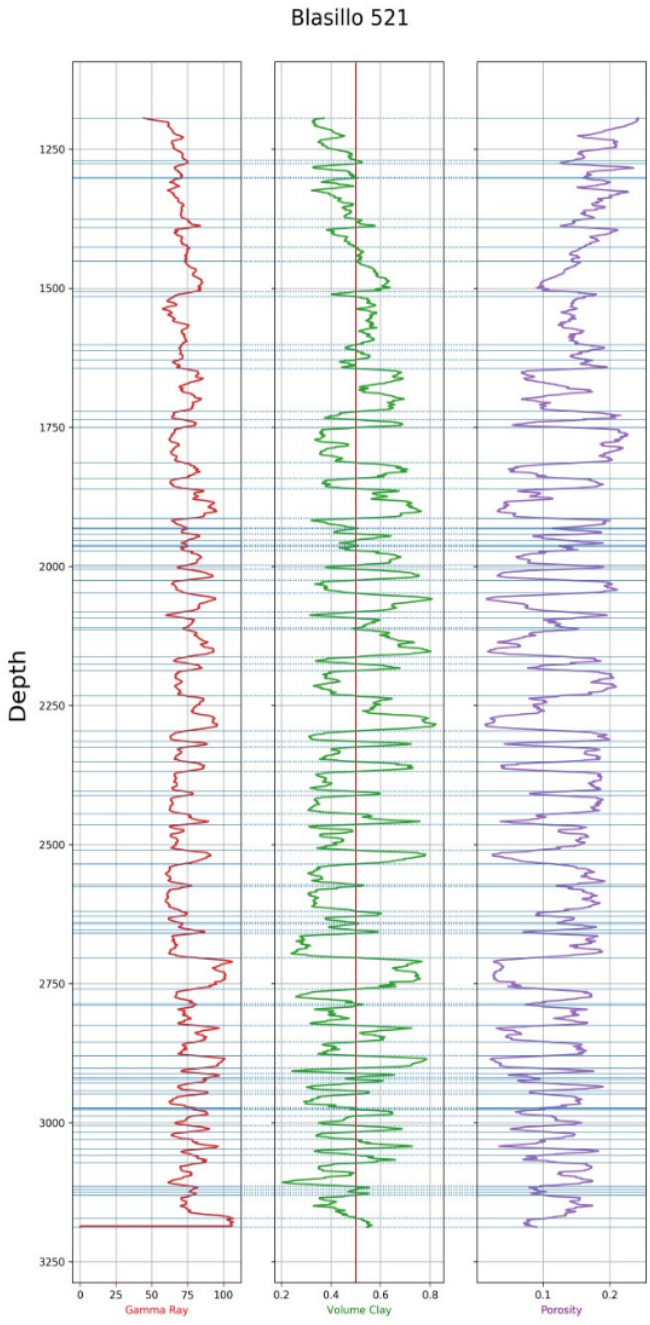

Figure 7: Log curves from Blasillo 521, showing GR, VolClay, and Porosity as a function of depth.The red vertical line on the VolClay log is used to delimit shale versus sandstone. The blue lines show the interbedding between sandstones and shales.

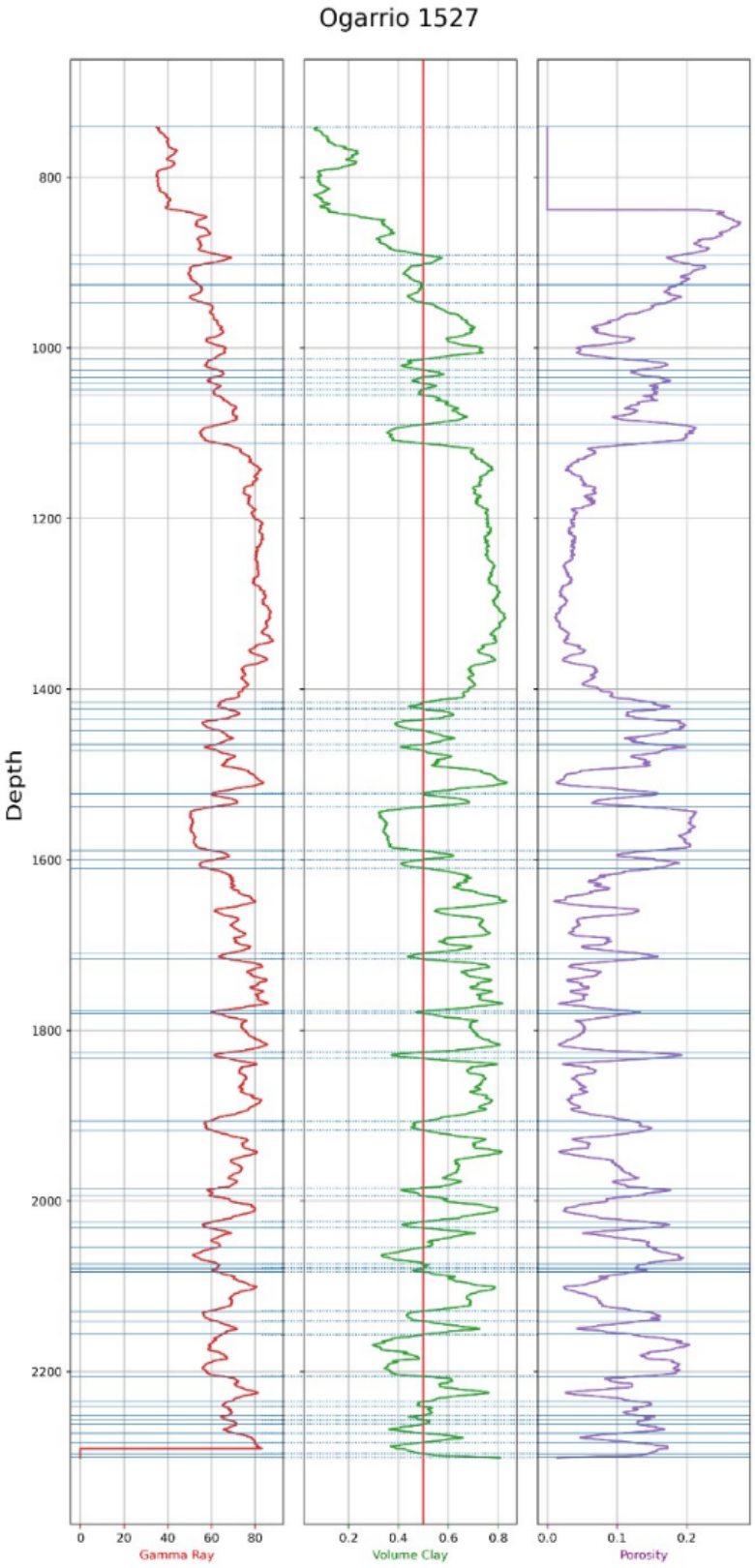

Figure 8: Log curves from Ogarrio 1527, showing GR, VolClay, and Porosity as a function of depth.

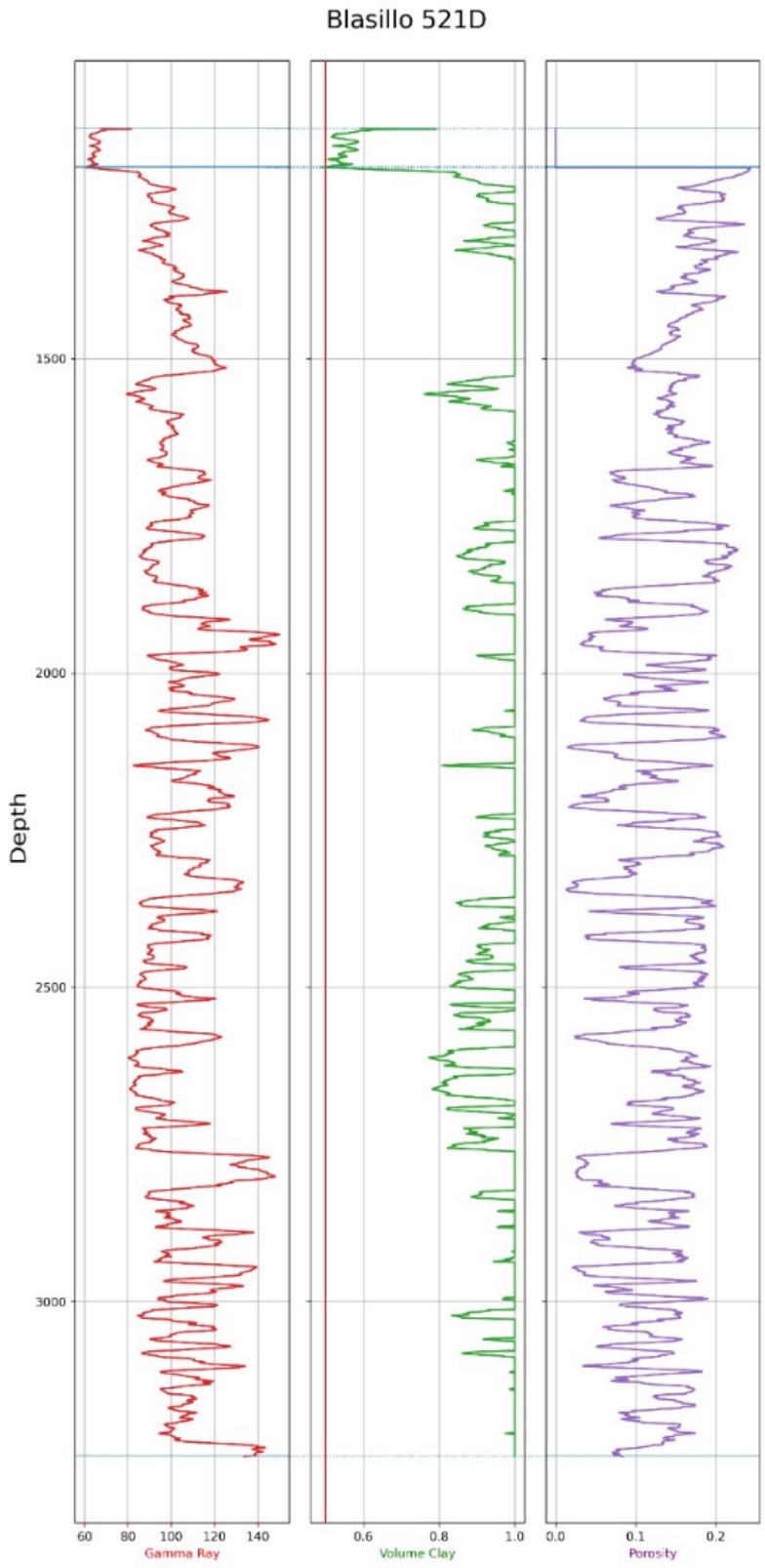

Figure 9: Log curves from Blasillo 521D, showing GR, VolClay, and Porosity as a function of depth.

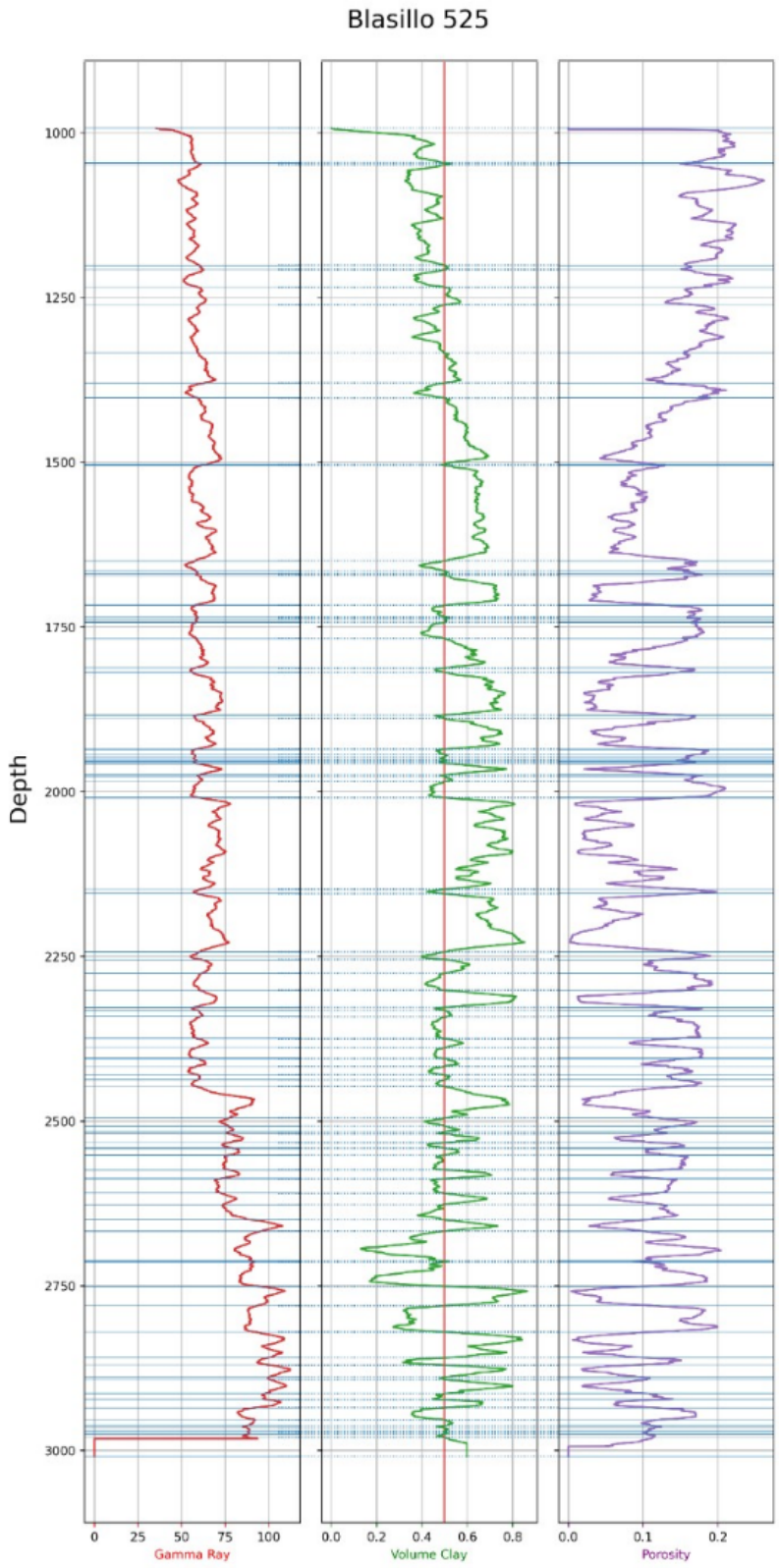

Figure 10: Log curves from Blasillo 525, showing GR, VolClay, and Porosity as a function of depth.

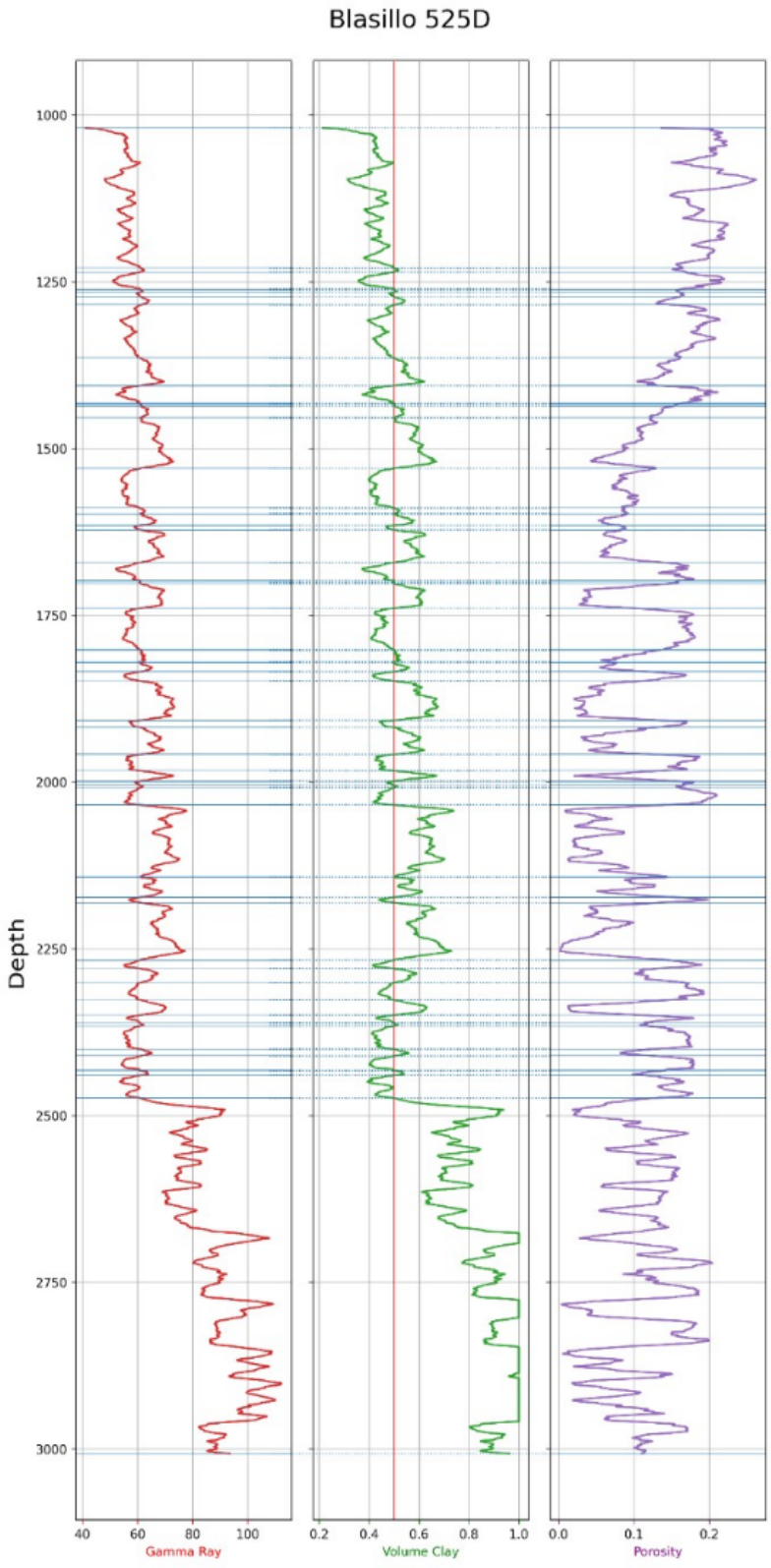

Figure 11: Log curves from Blasillo 525D, showing GR, VolClay, and Porosity as a function of depth.

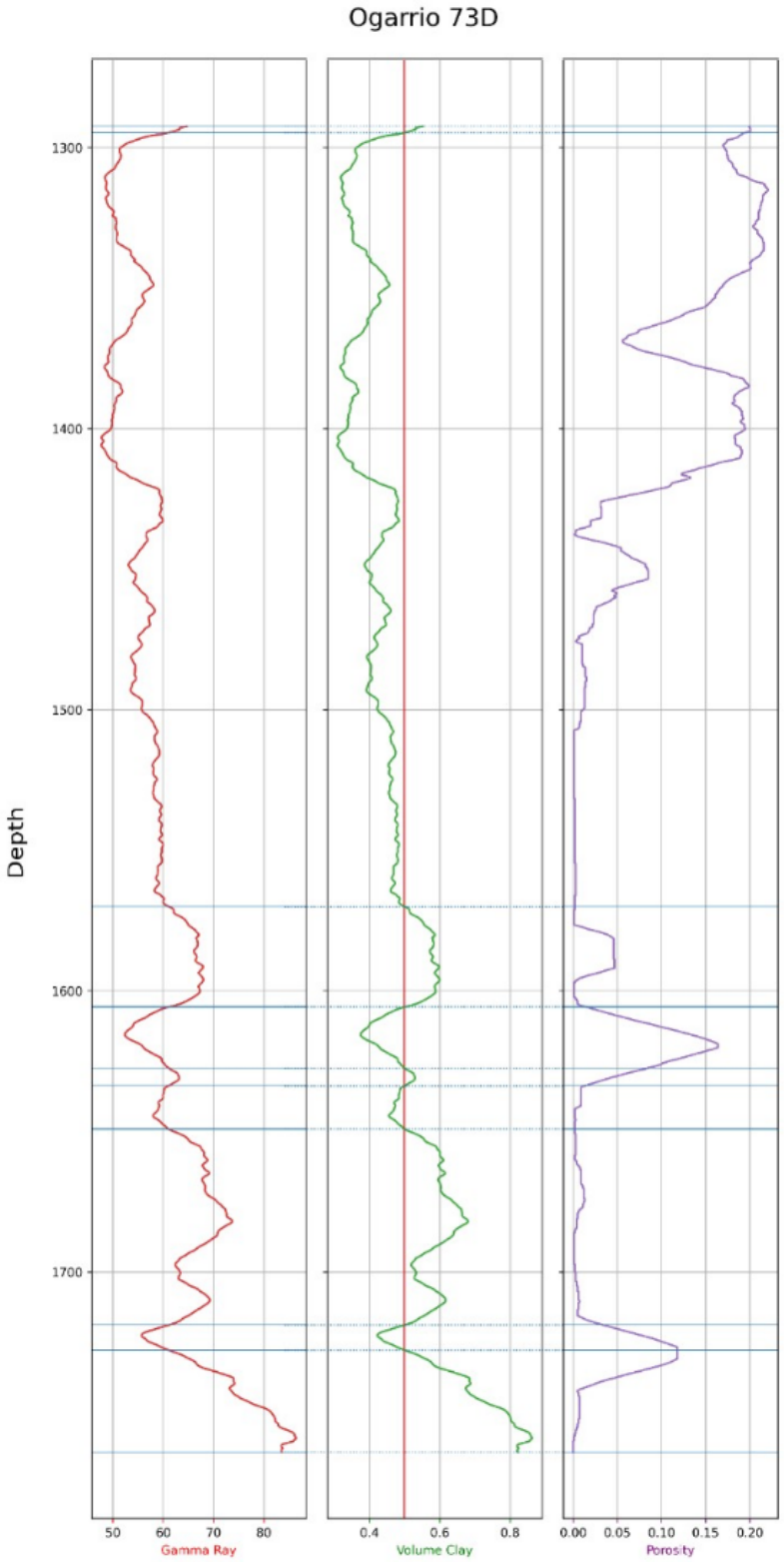

Figure 12: Log curves from Ogarrio 73D, showing GR, VolClay, and Porosity as a function of depth.

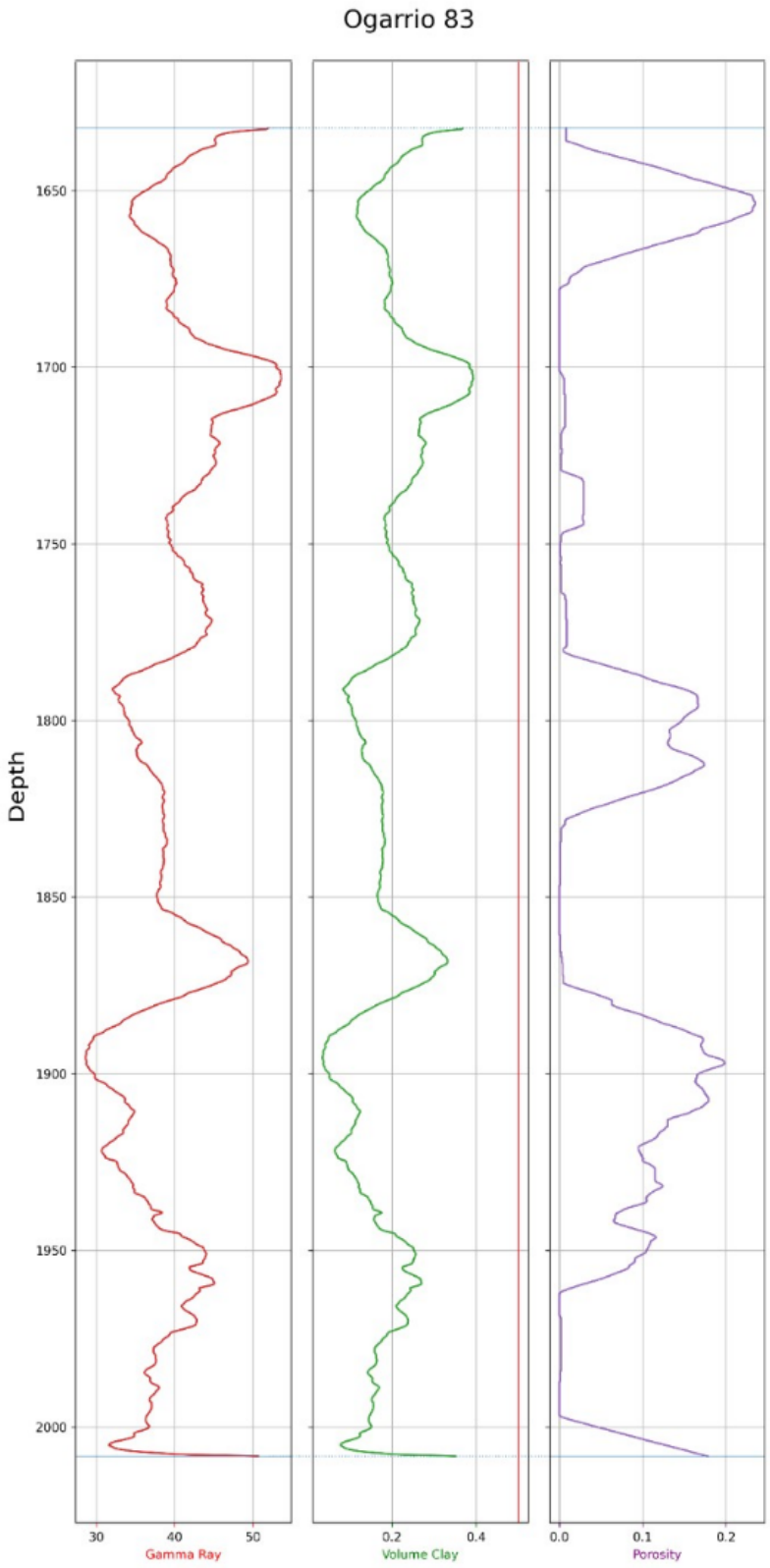

Figure 13: Log curves from Ogarrio 83, showing GR, VolClay, and Porosity as a function of depth.

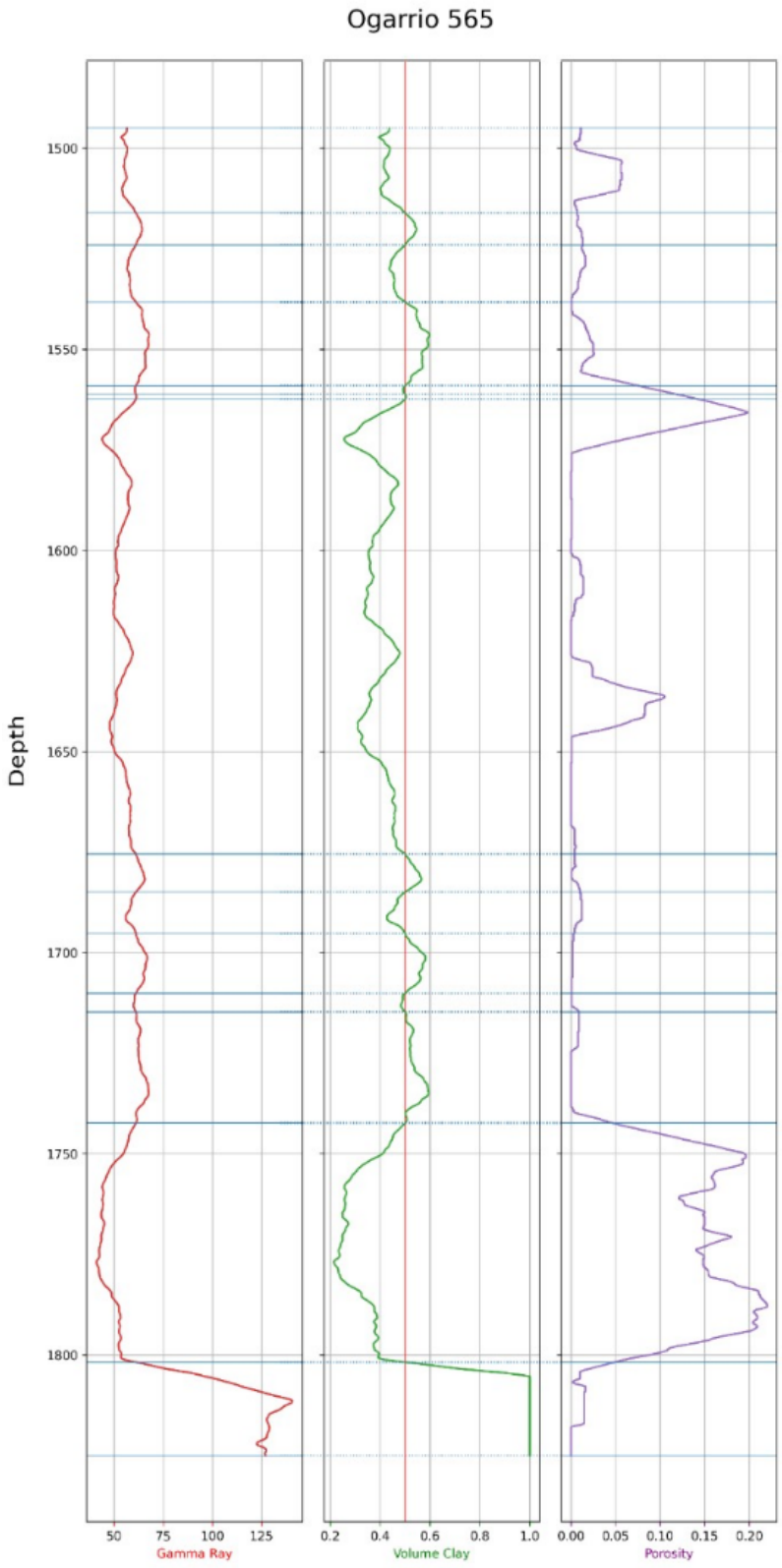

Figure 14: Log curves from Ogarrio 565, showing GR, VolClay, and Porosity as a function of depth.

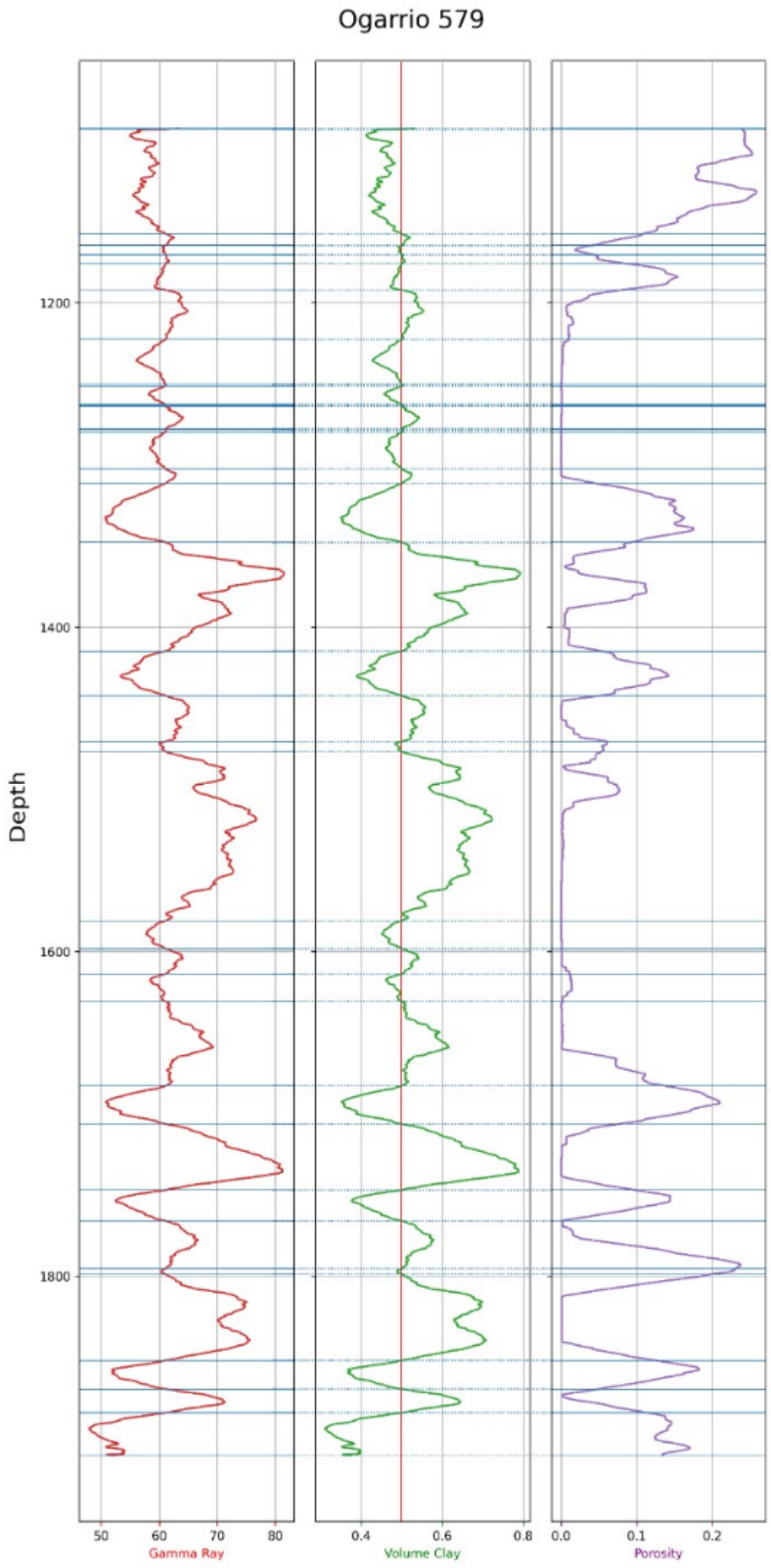

Figure 15: Log curves from Ogarrio 579, showing GR, VolClay, and Porosity as a function of depth.

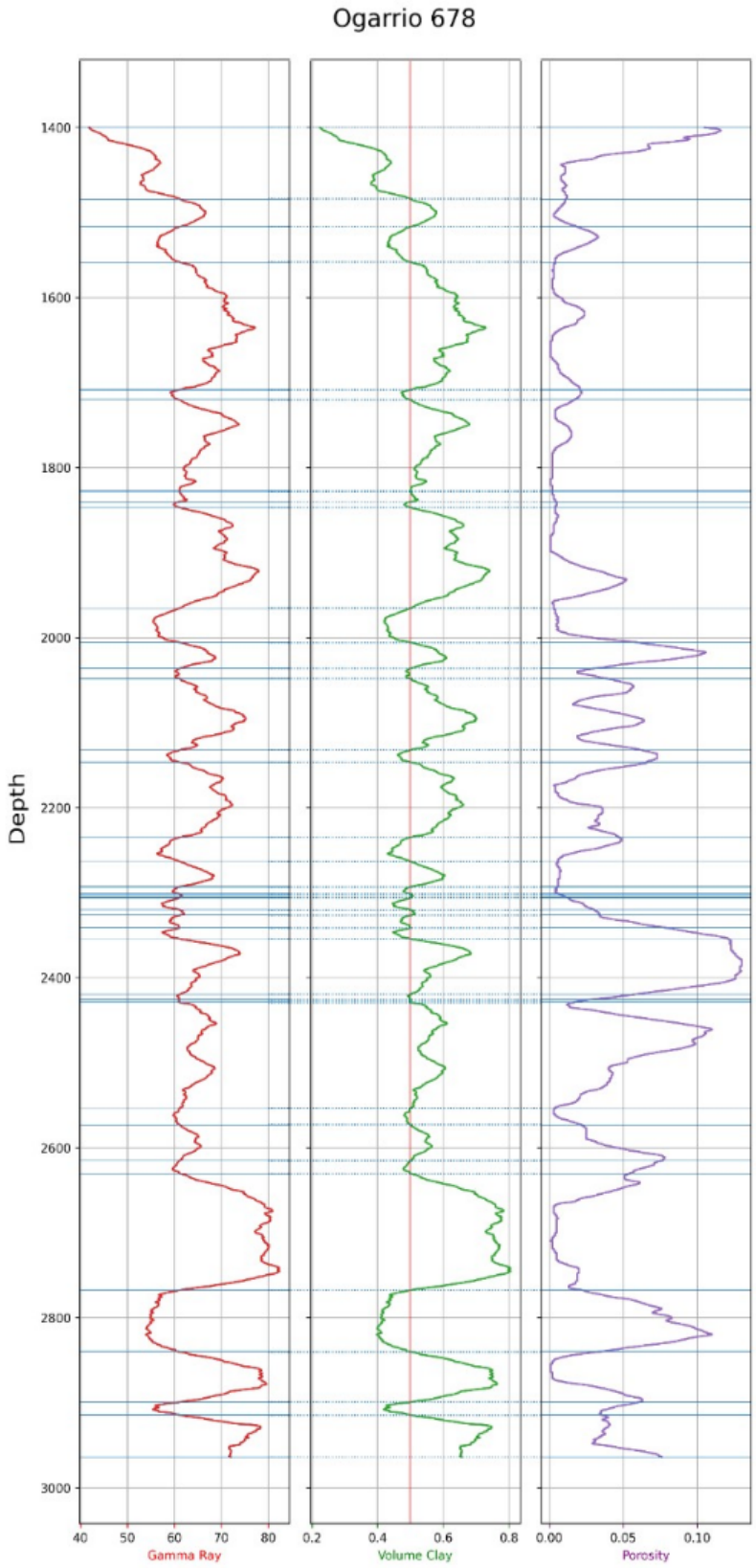

Figure 16: Log curves from Ogarrio 678, showing GR, VolClay, and Porosity as a function of depth.

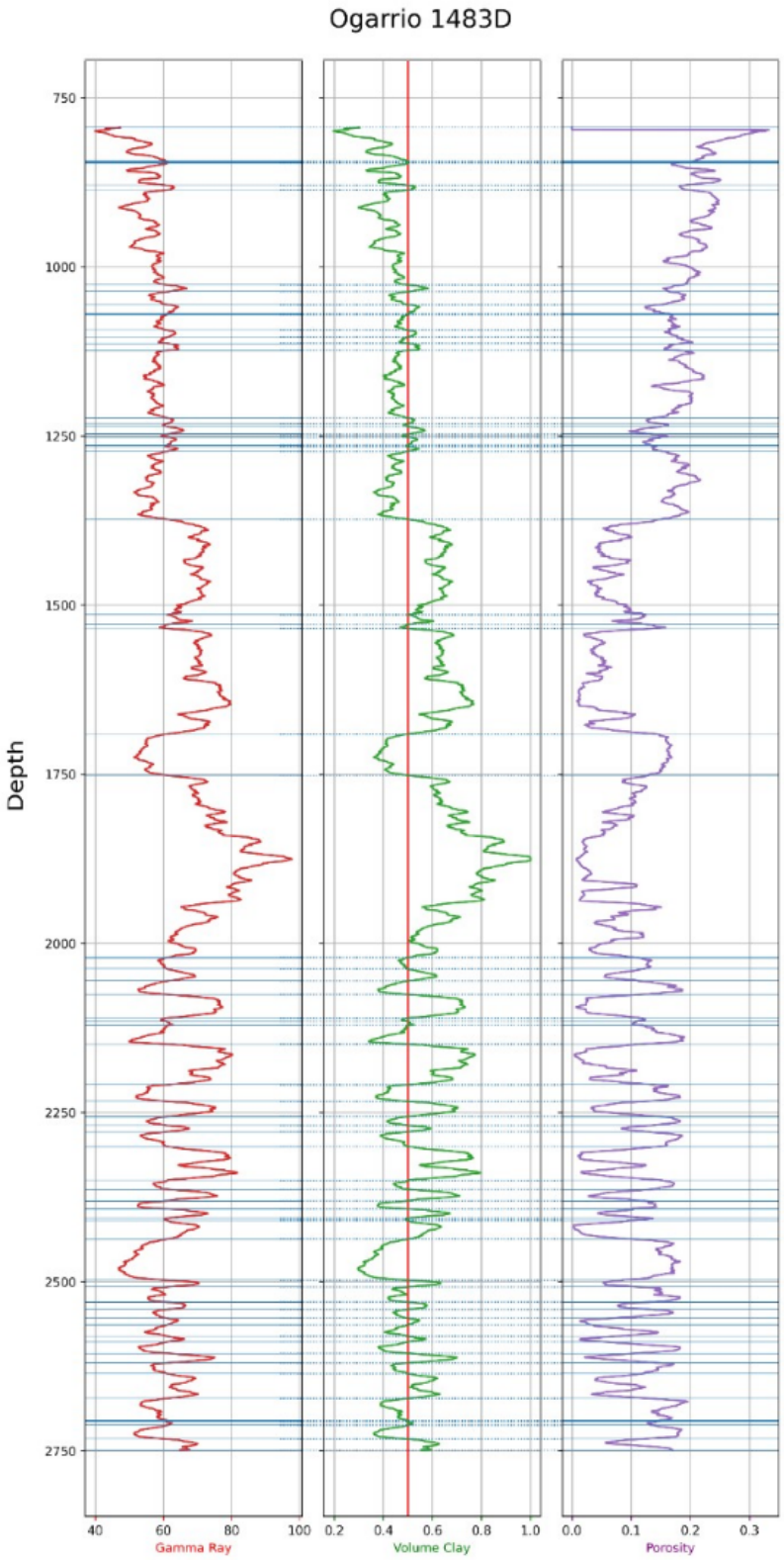

Figure 17: Log curves from Ogarrio 1483D, showing GR, VolClay, and Porosity as a function of depth.

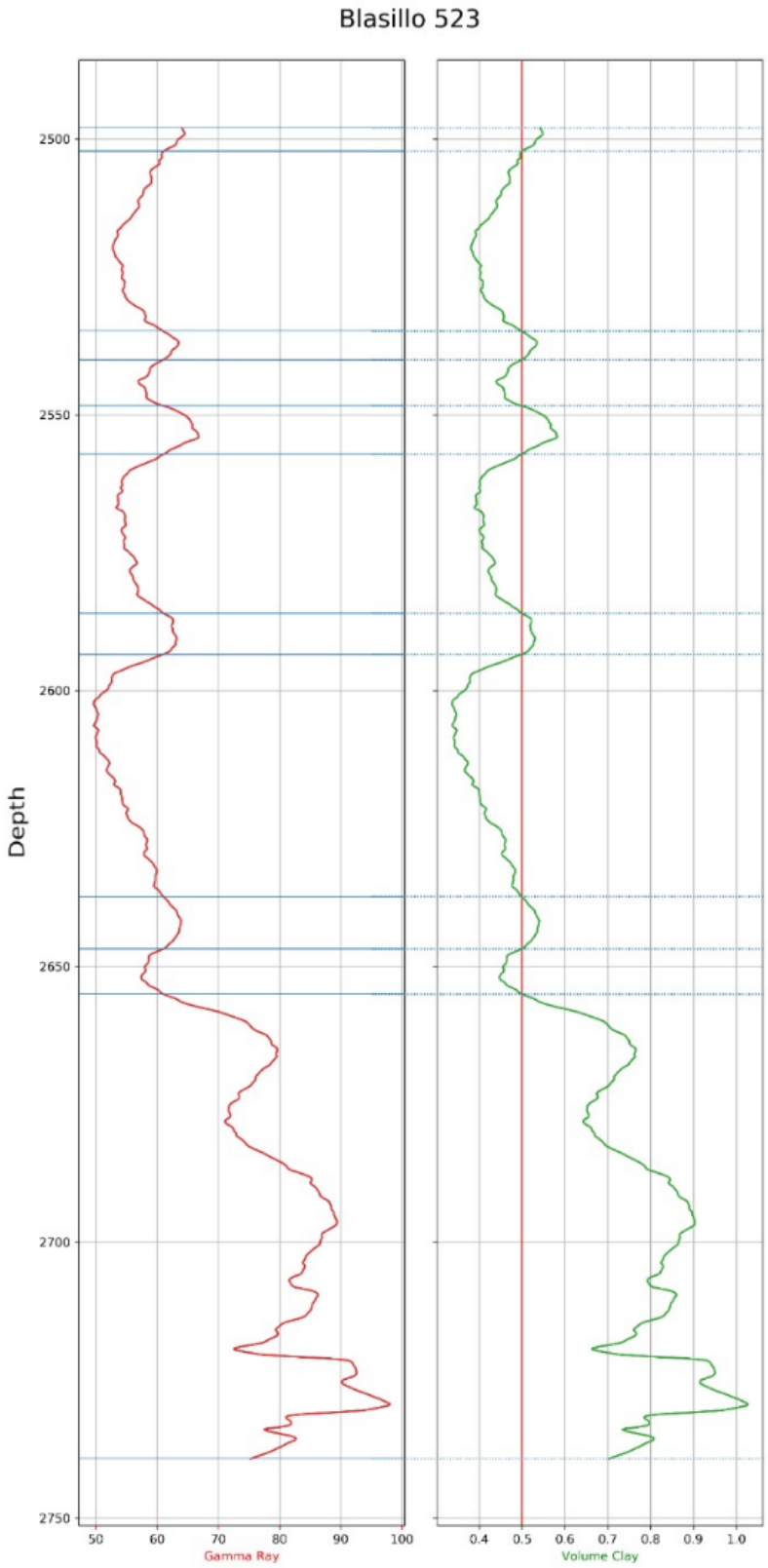

Figure 18: Depth versus GR and VolClay from the well Blasillo 523.

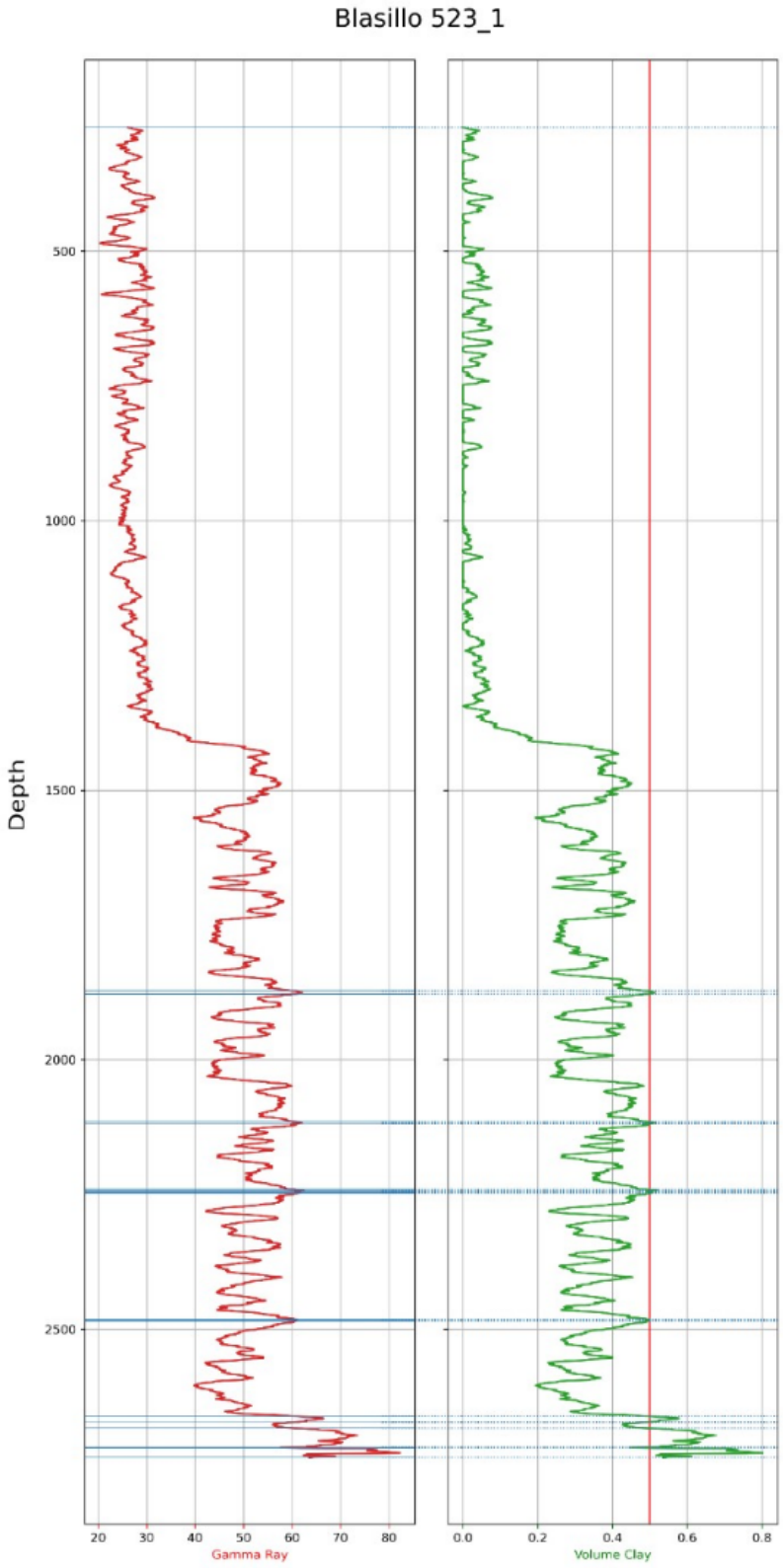

Figure 19: Depth versus GR and VolClay from the well Blasillo 523-1.

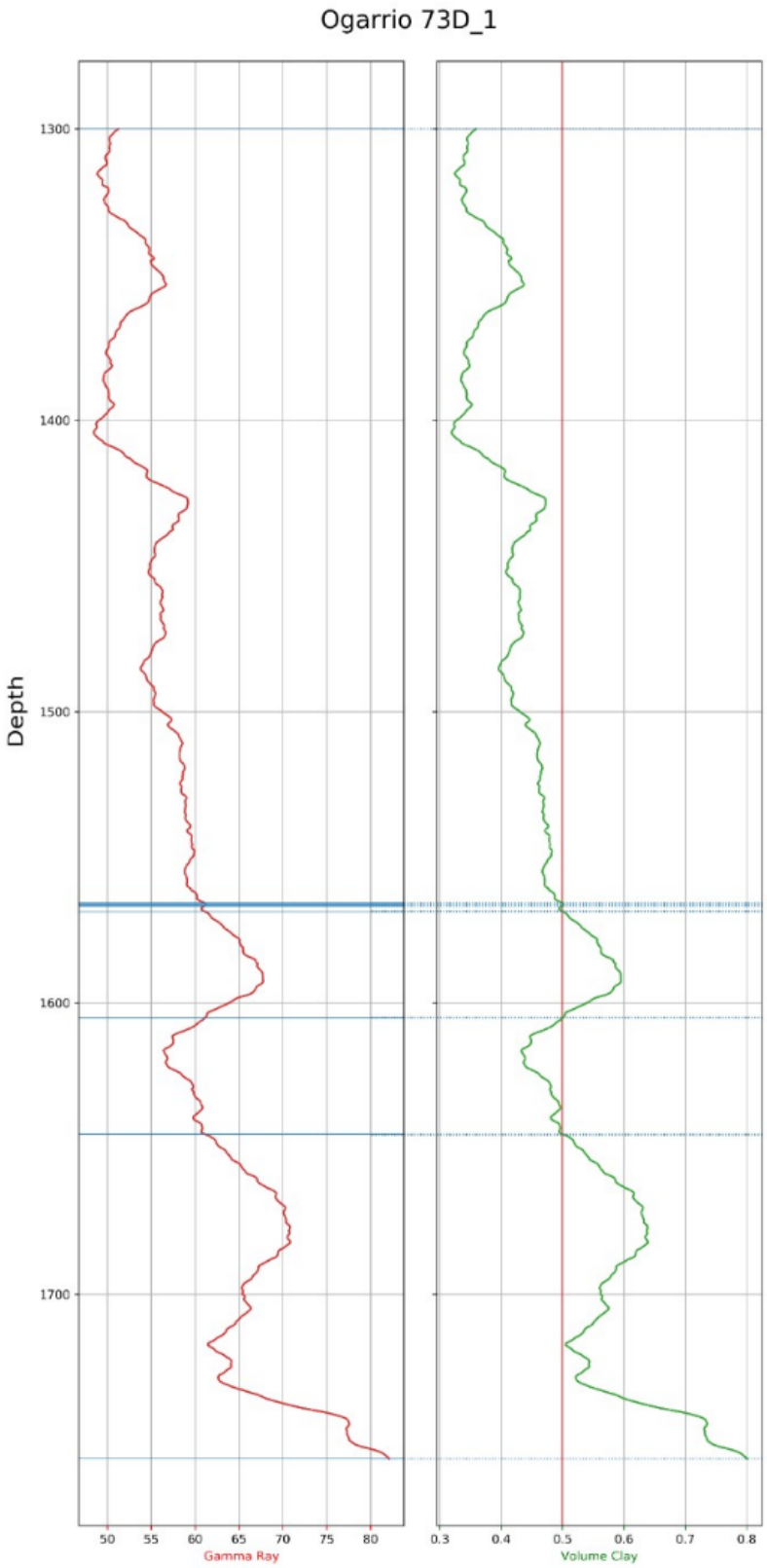

Figure 20: Depth versus GR and VolClay from the well Ogarrio73D-1.

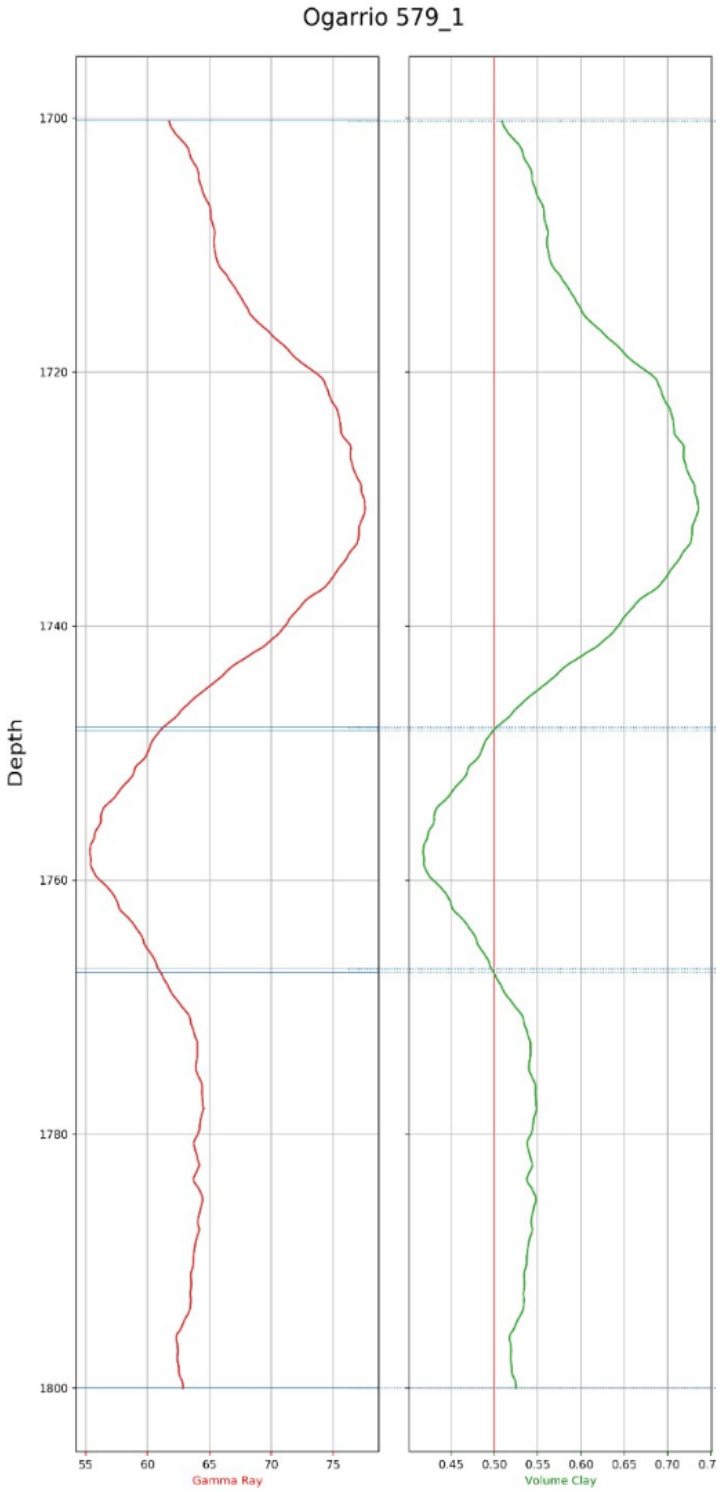

Figure 21: Depth versus GR and VolClay from the well Ogarrio 579-1.

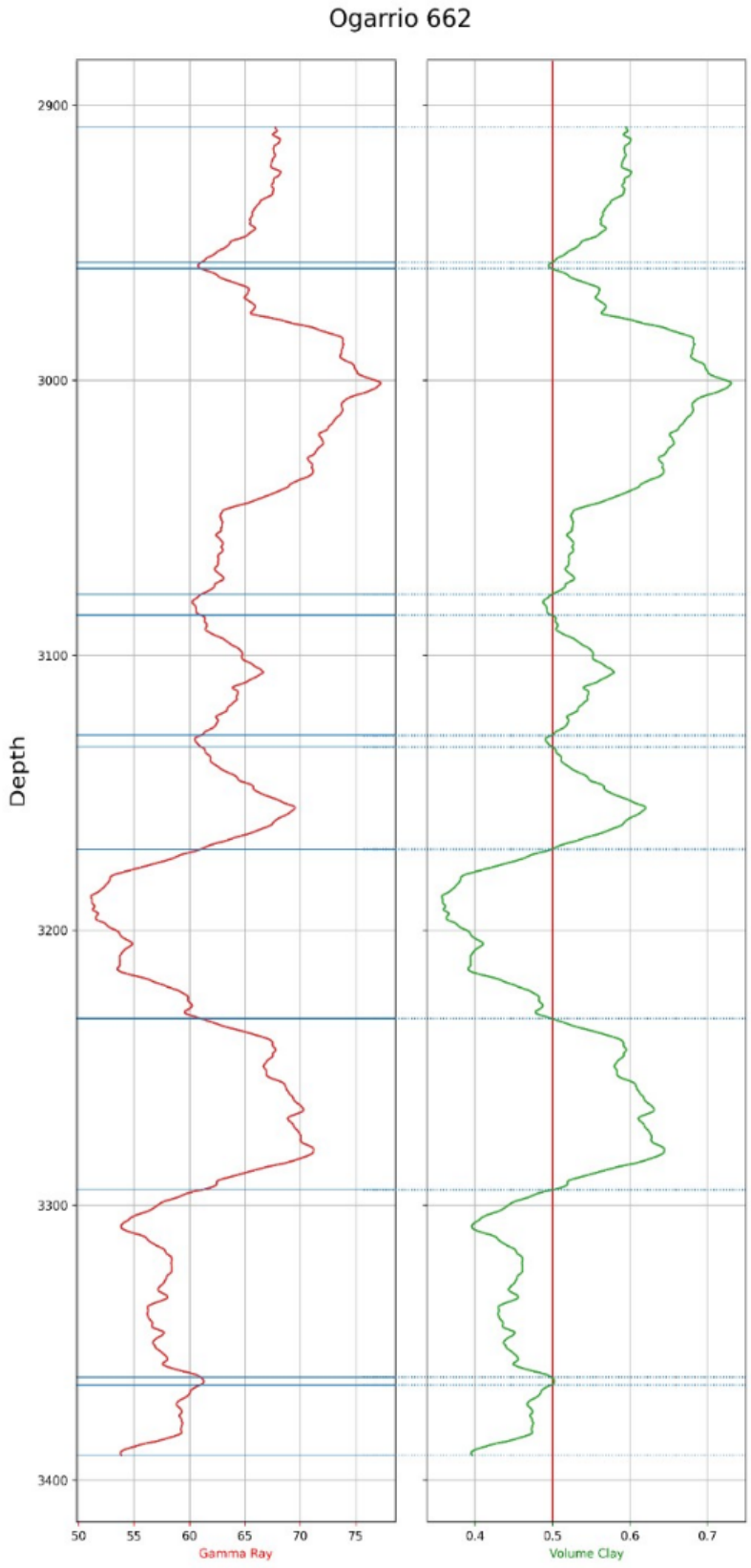

Figure 22: Depth versus GR and VolClay from the well Ogarrio 662.

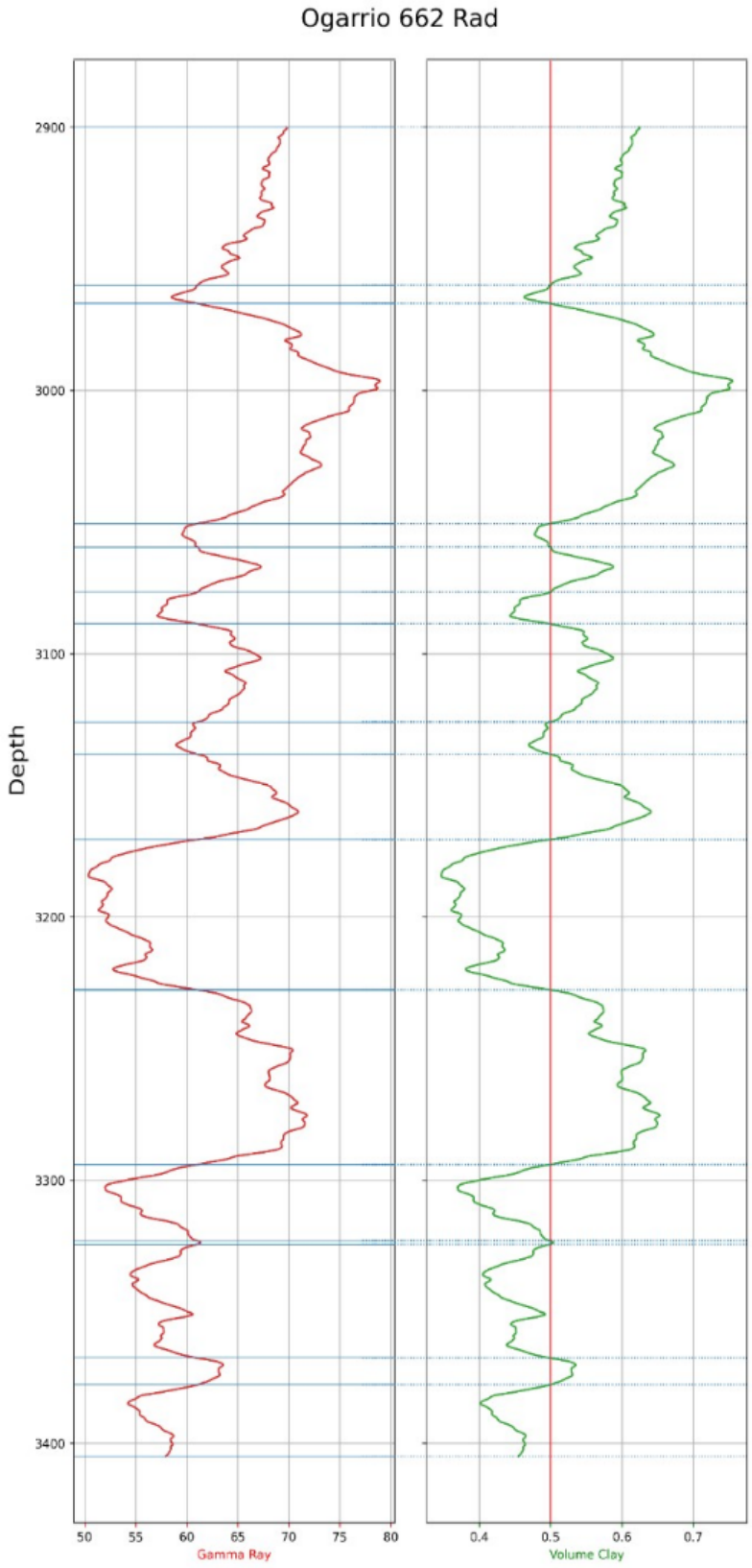

Figure 23: Depth versus GR and VolClay from the well Ogarrio 662 Rad.

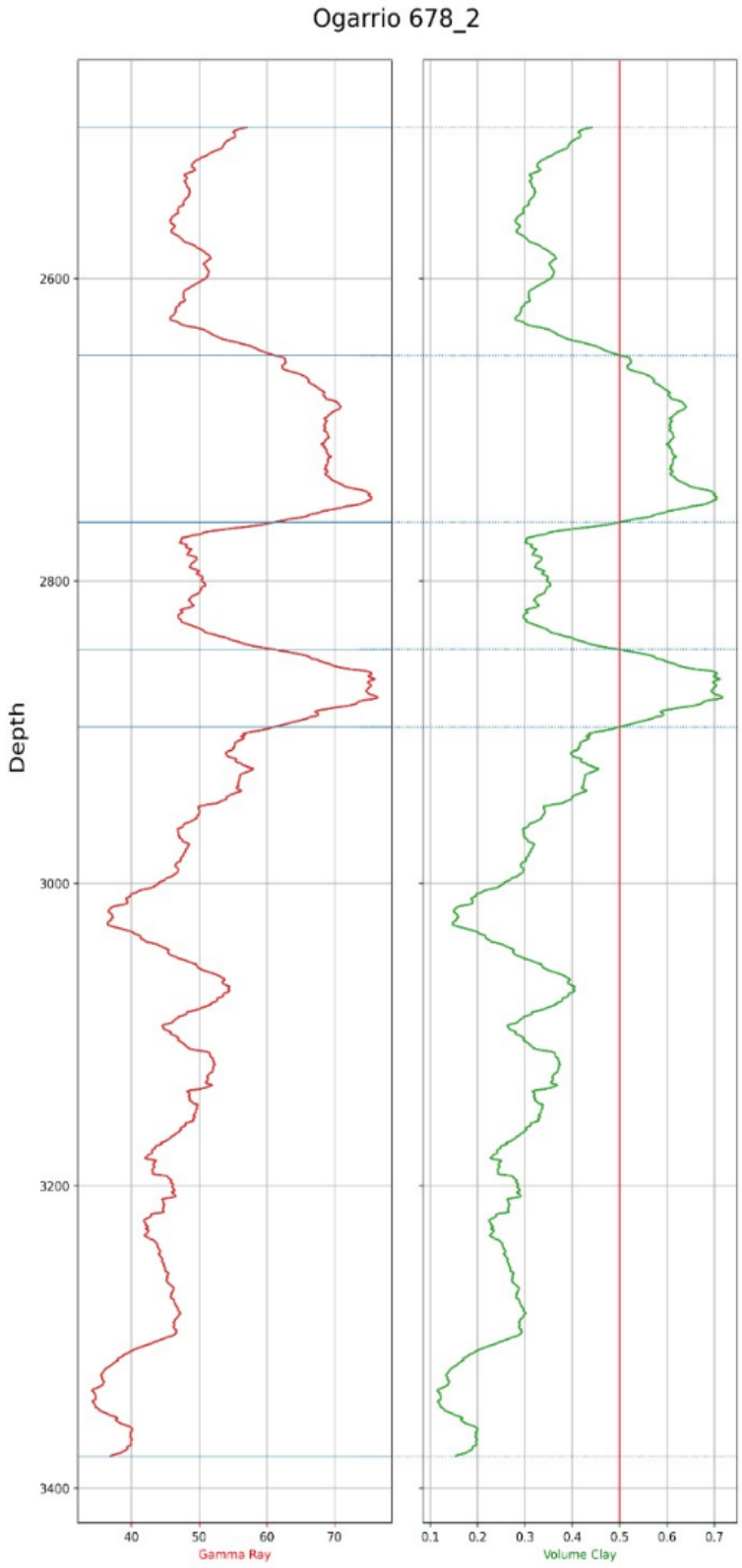

Figure 24: Depth versus GR and VolClay from the well Ogarrio 678-2.

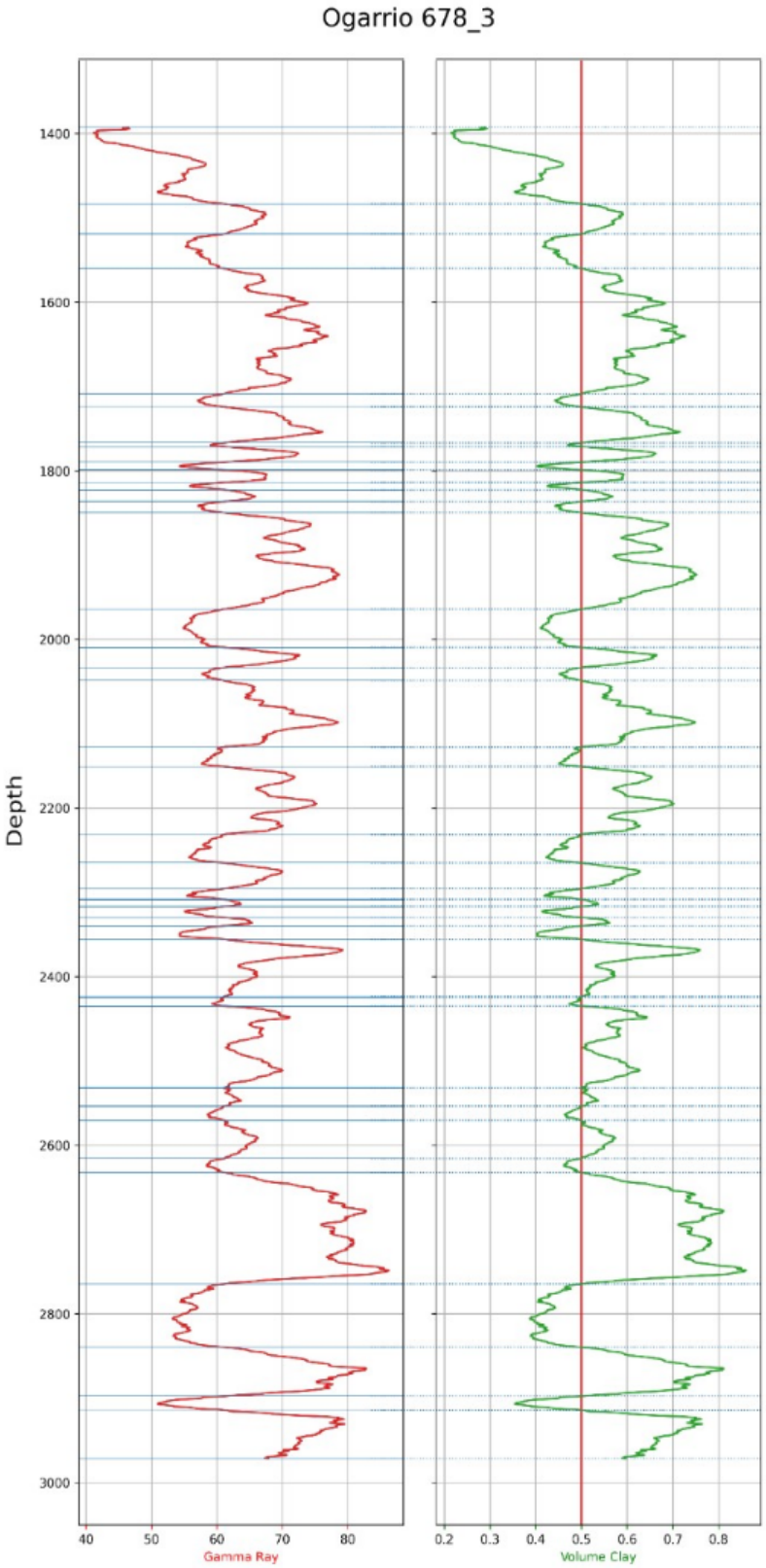

Figure 25: Depth versus GR and VolClay from the well Ogarrio 678-3.

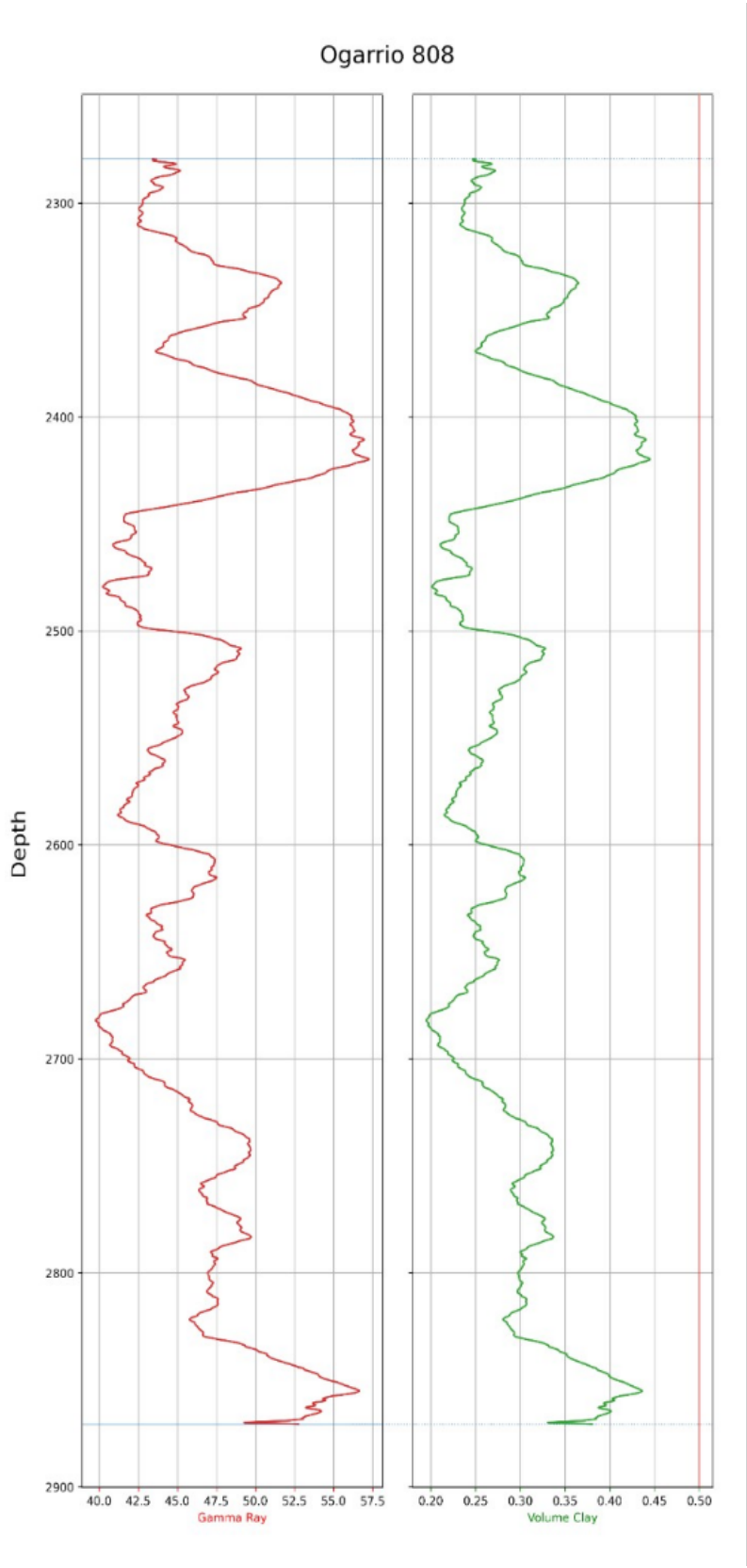

Figure 26: Depth versus GR and VolClay from the well Ogarrio 808.

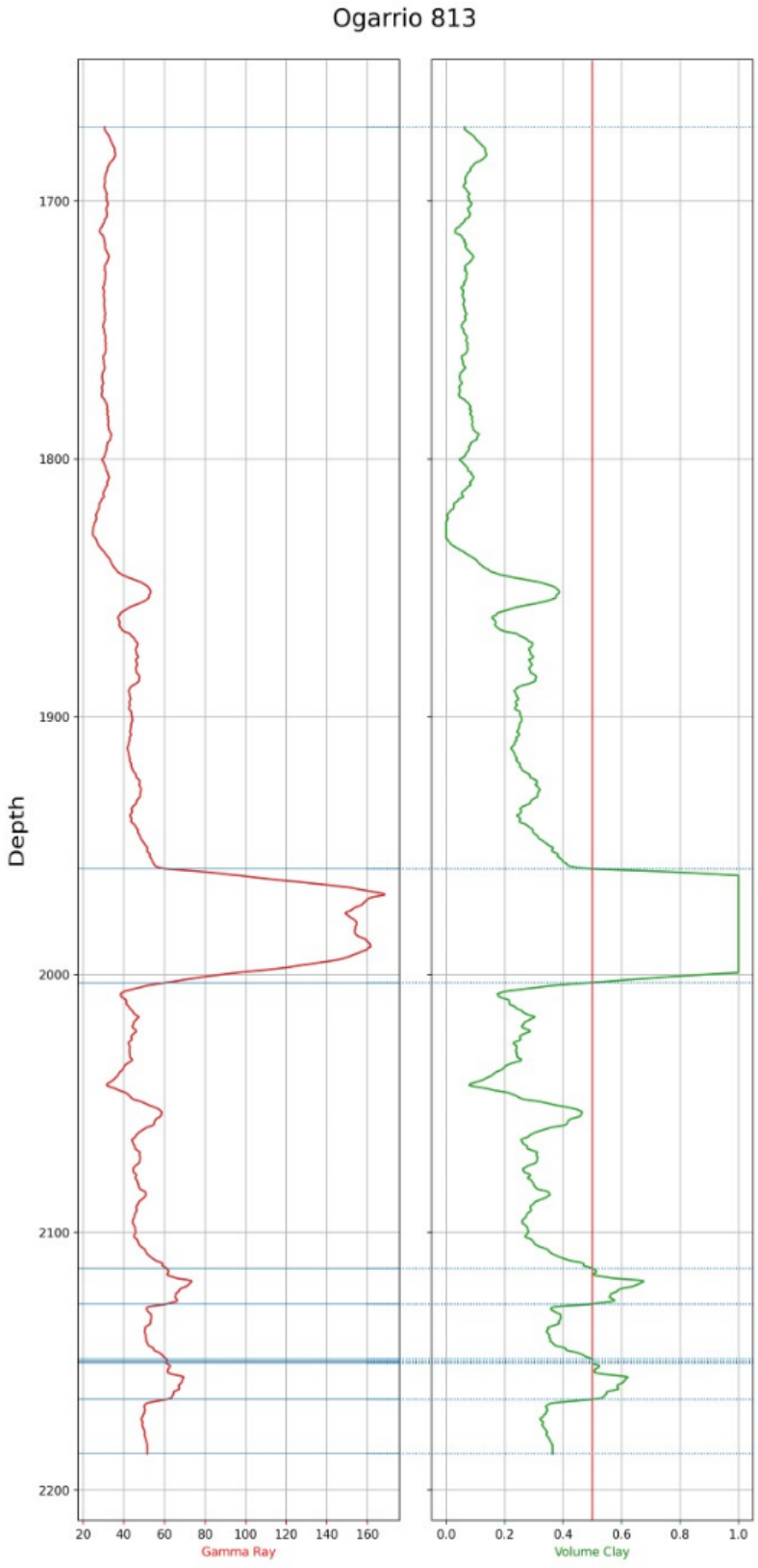

Figure 27: Depth versus GR and VolClay from the well Ogarrio 813.

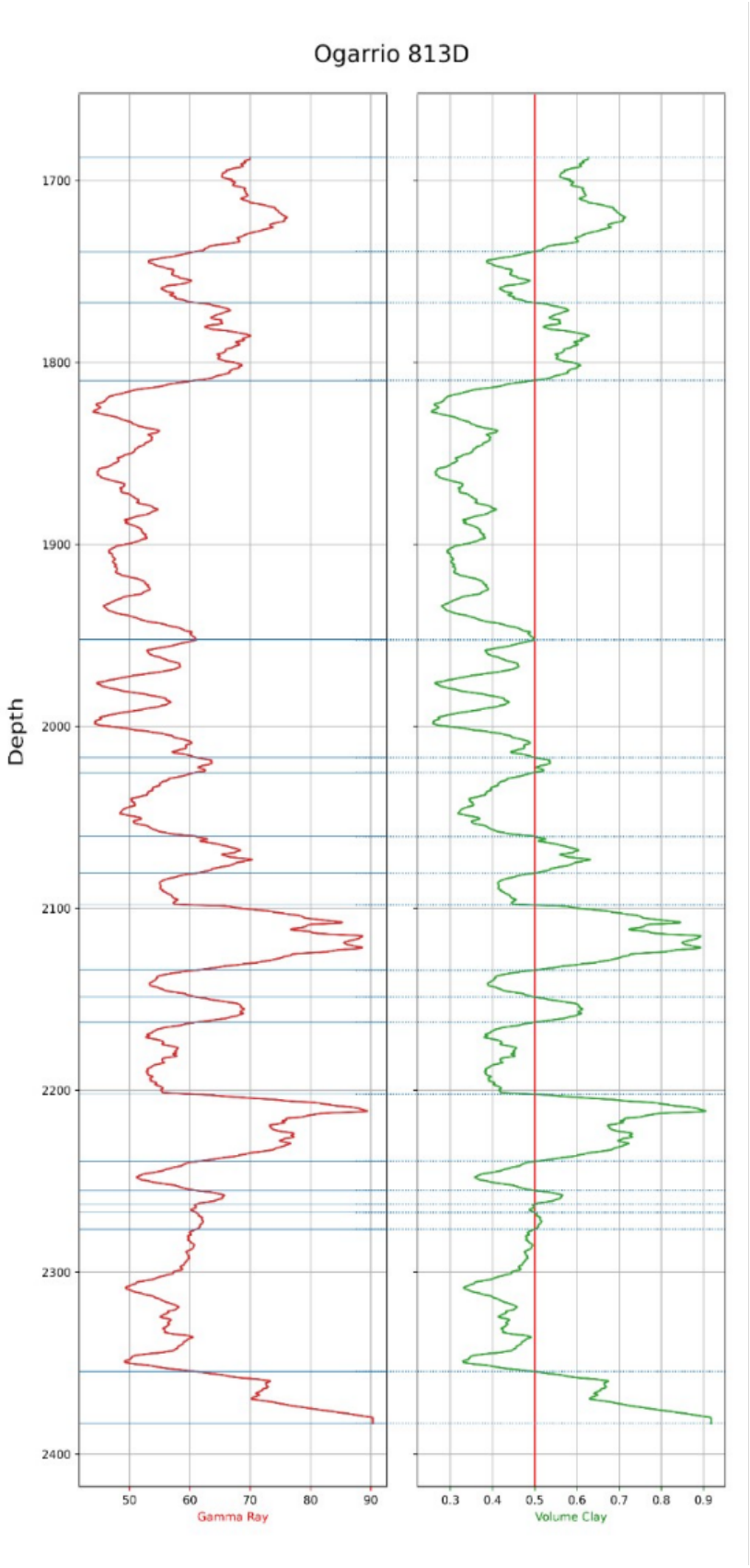

Figure 28: Depth versus GR and VolClay from the well Ogarrio 813D.

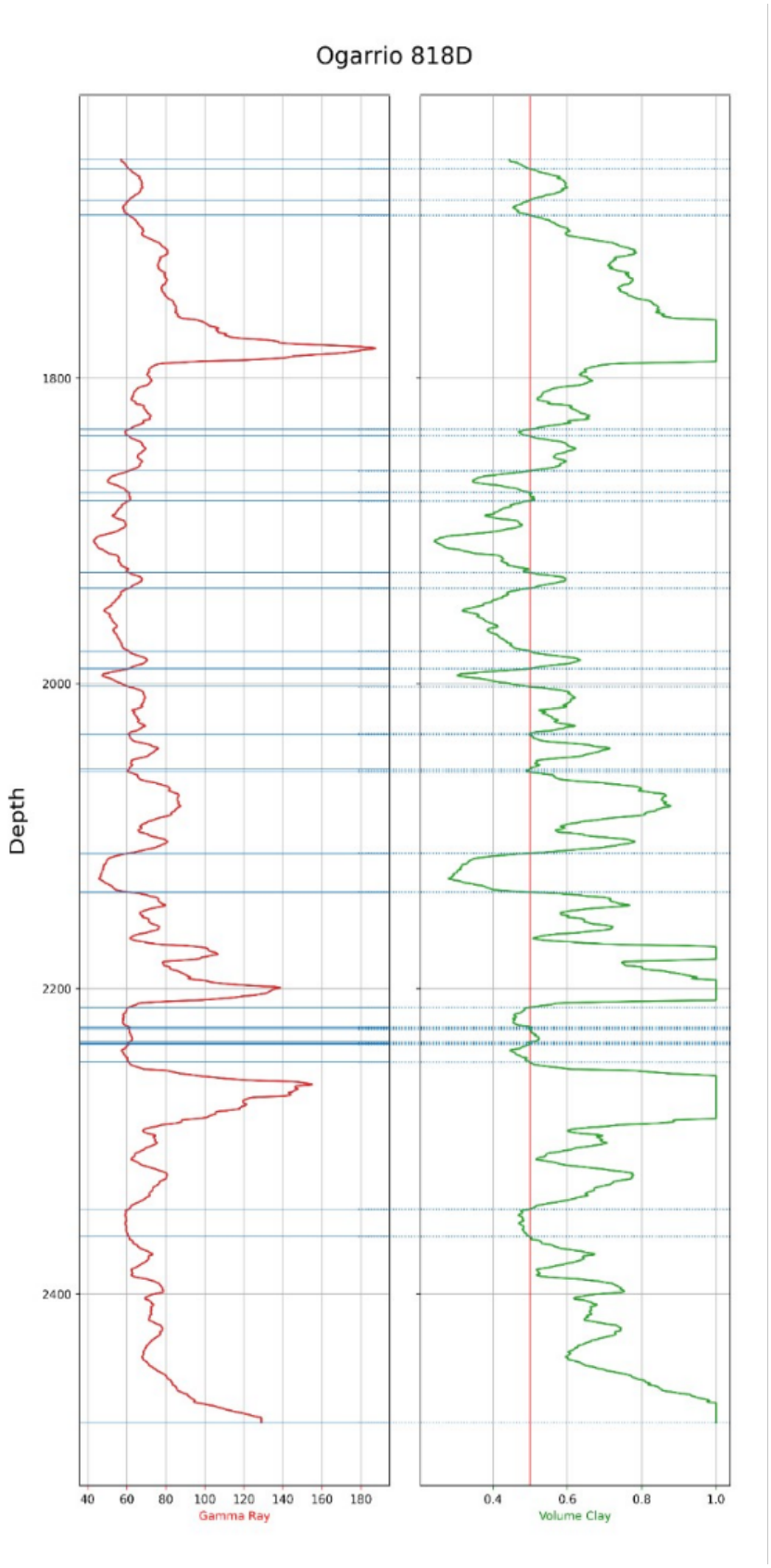

Figure 29: Depth versus GR and VolClay from the well Ogarrio 818D.

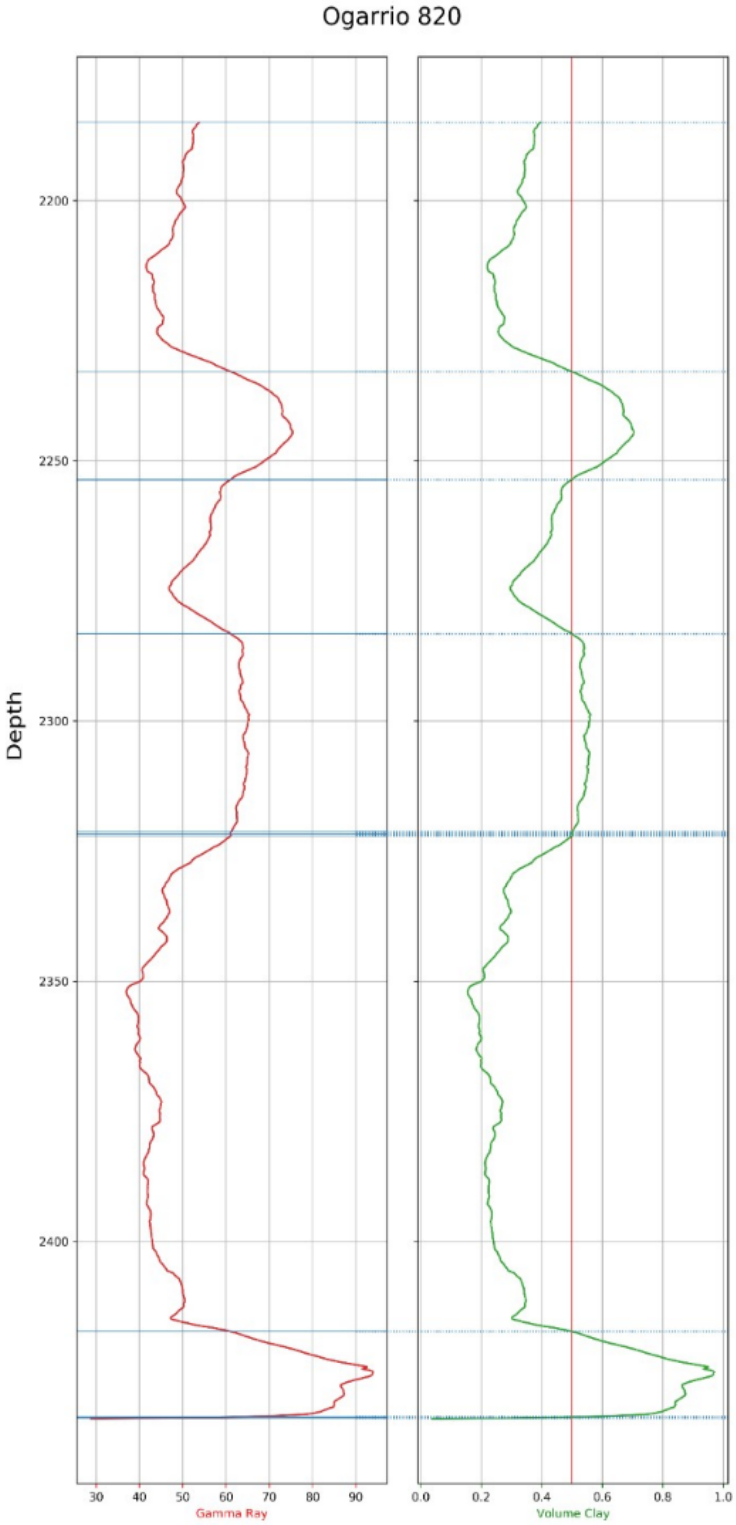

Figure 30: Depth versus GR and VolClay from the well Ogarrio 820.

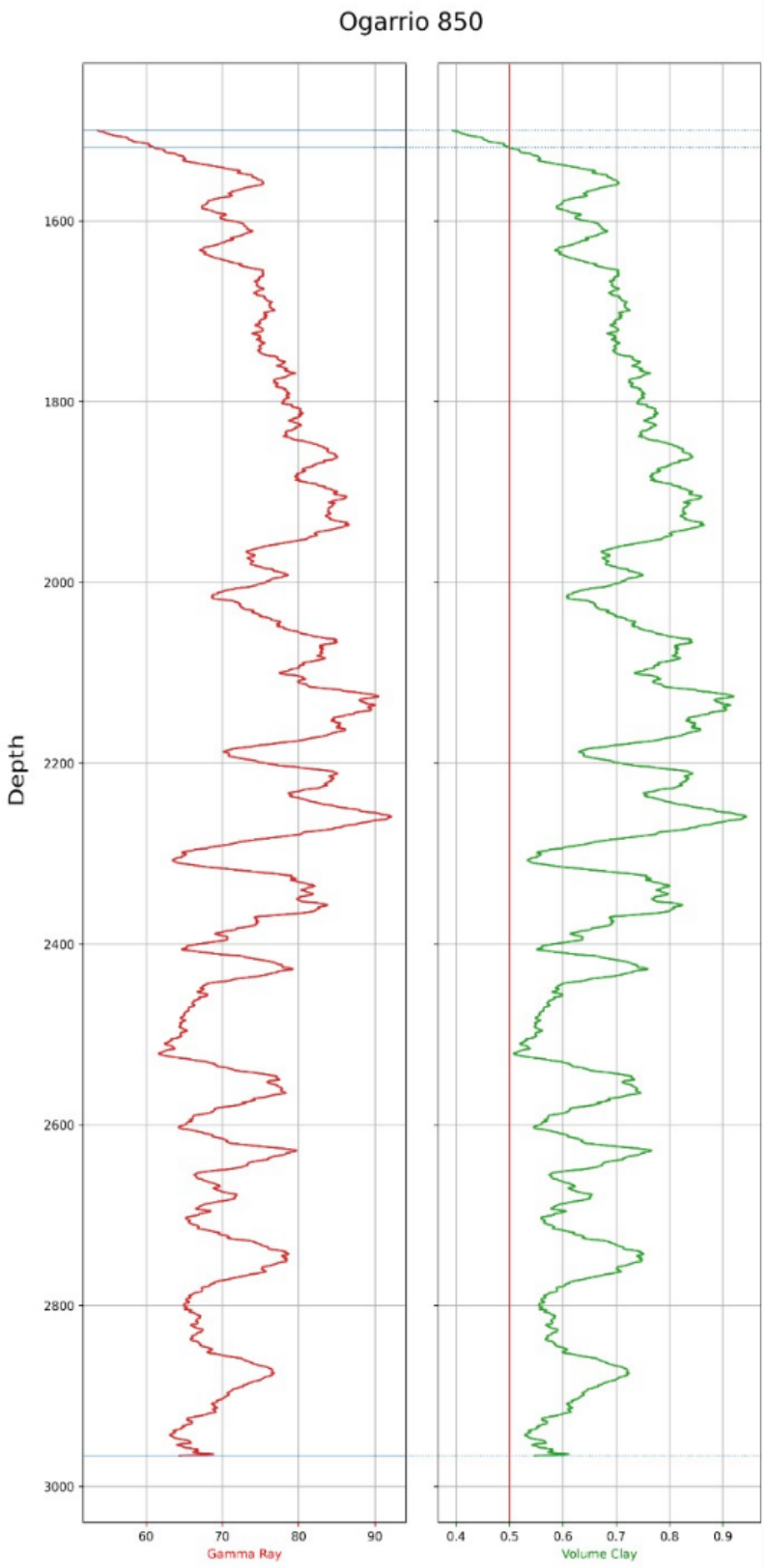

Figure 31: Depth versus GR and VolClay from the well Ogarrio 850.

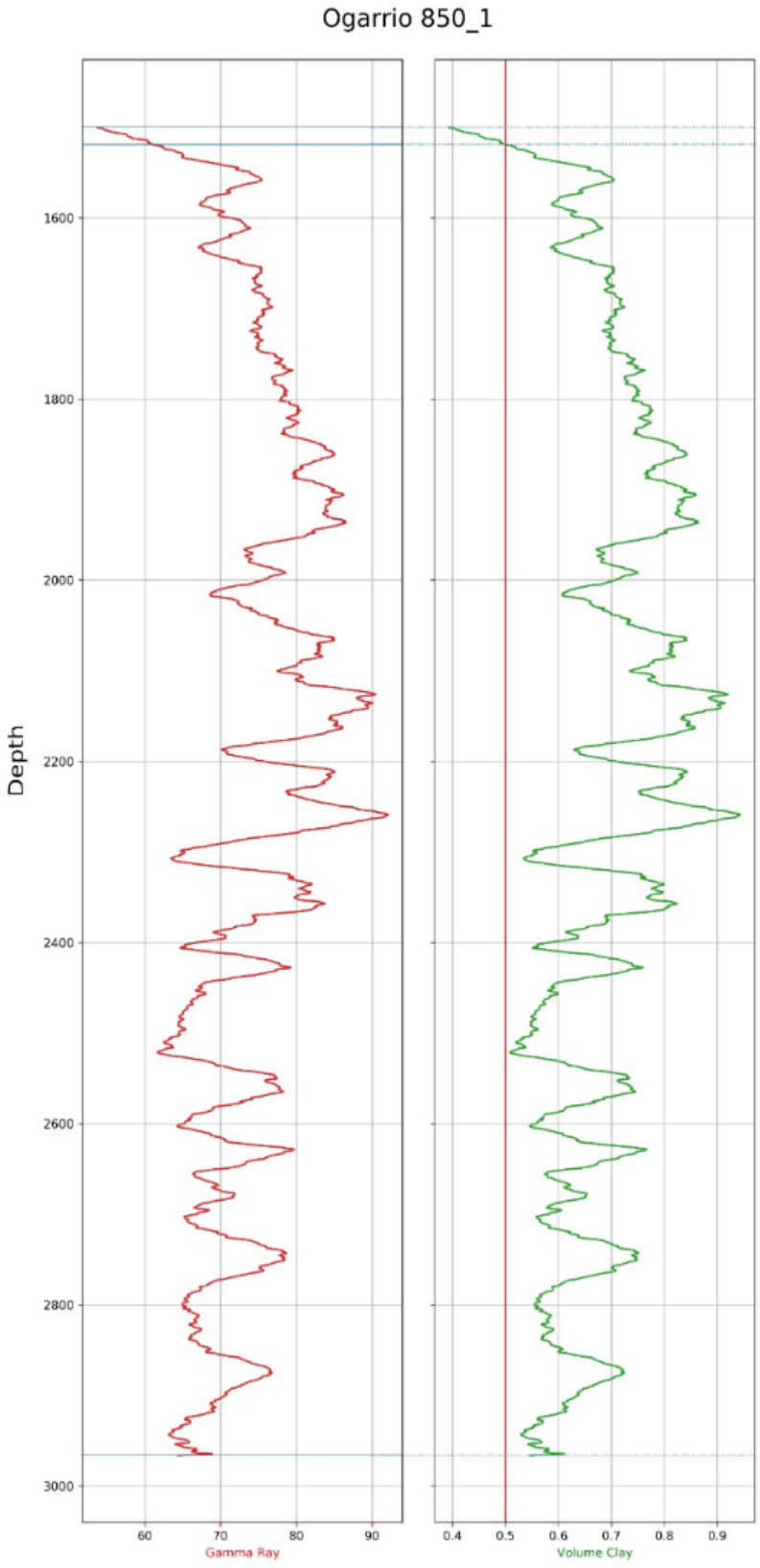

Figure 32: Depth versus GR and VolClay from the well Ogarrio 850-1.

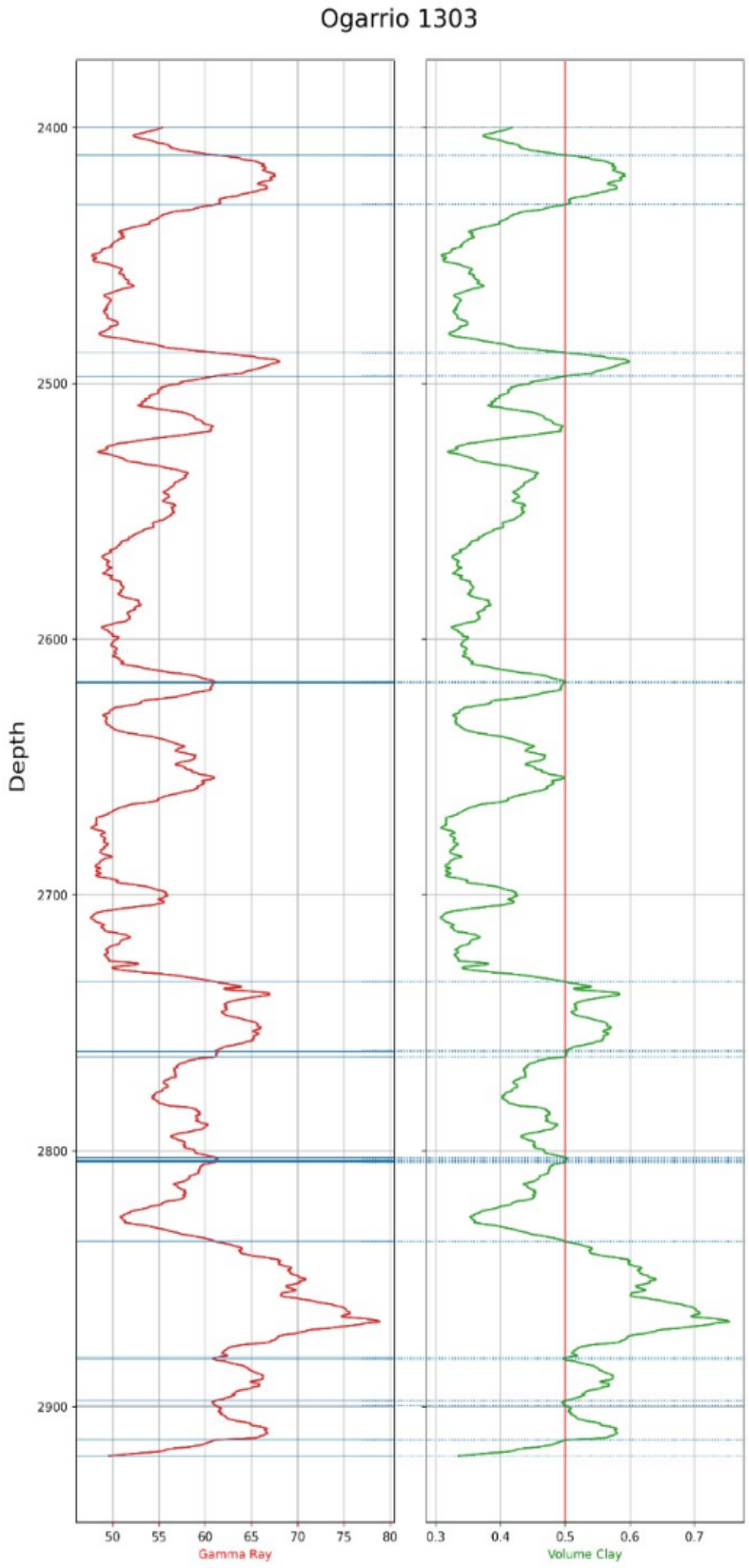

Figure 33: Depth versus GR and VolClay from the well Ogarrio 1303.

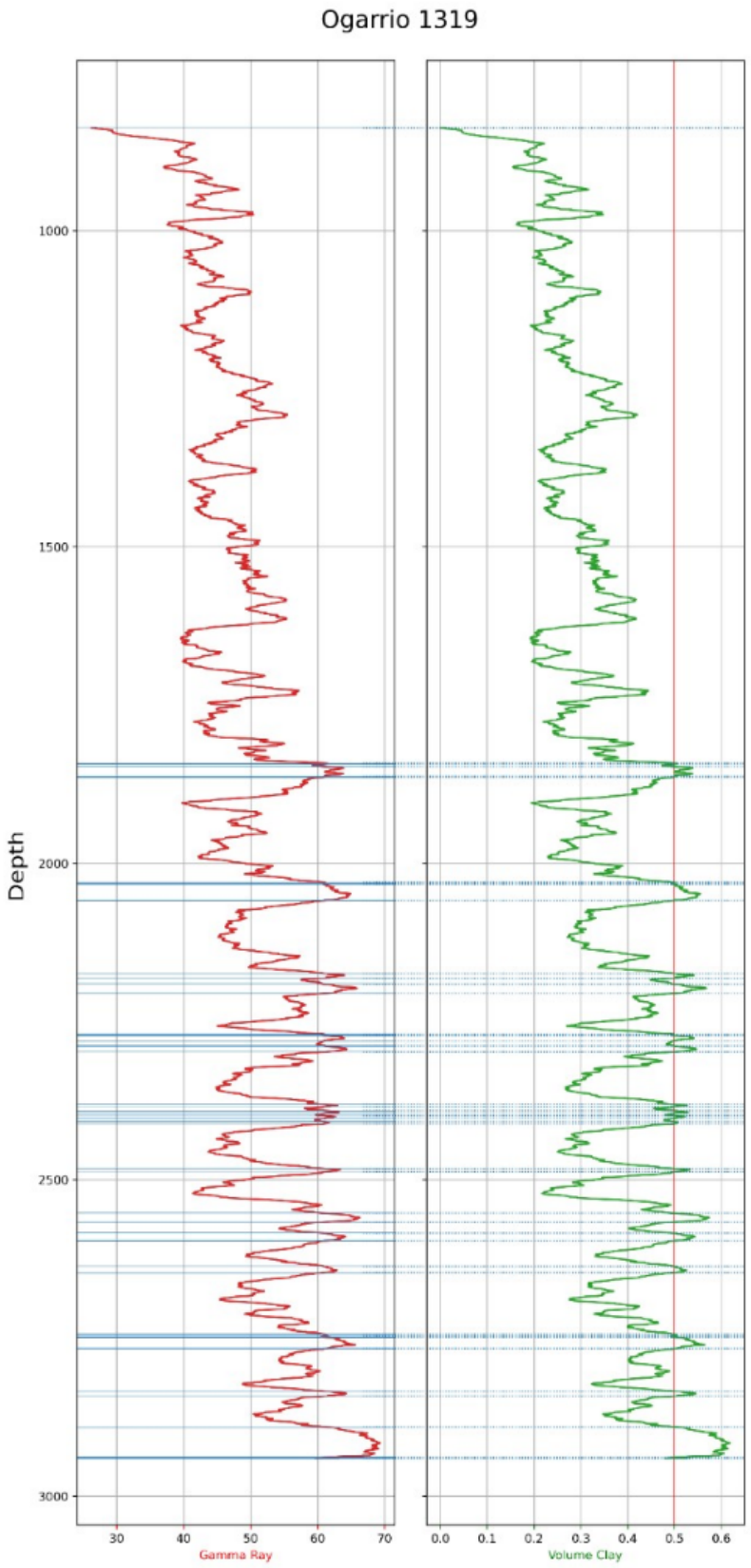

Figure 34: Depth versus GR and VolClay from the well Ogarrio 1319.

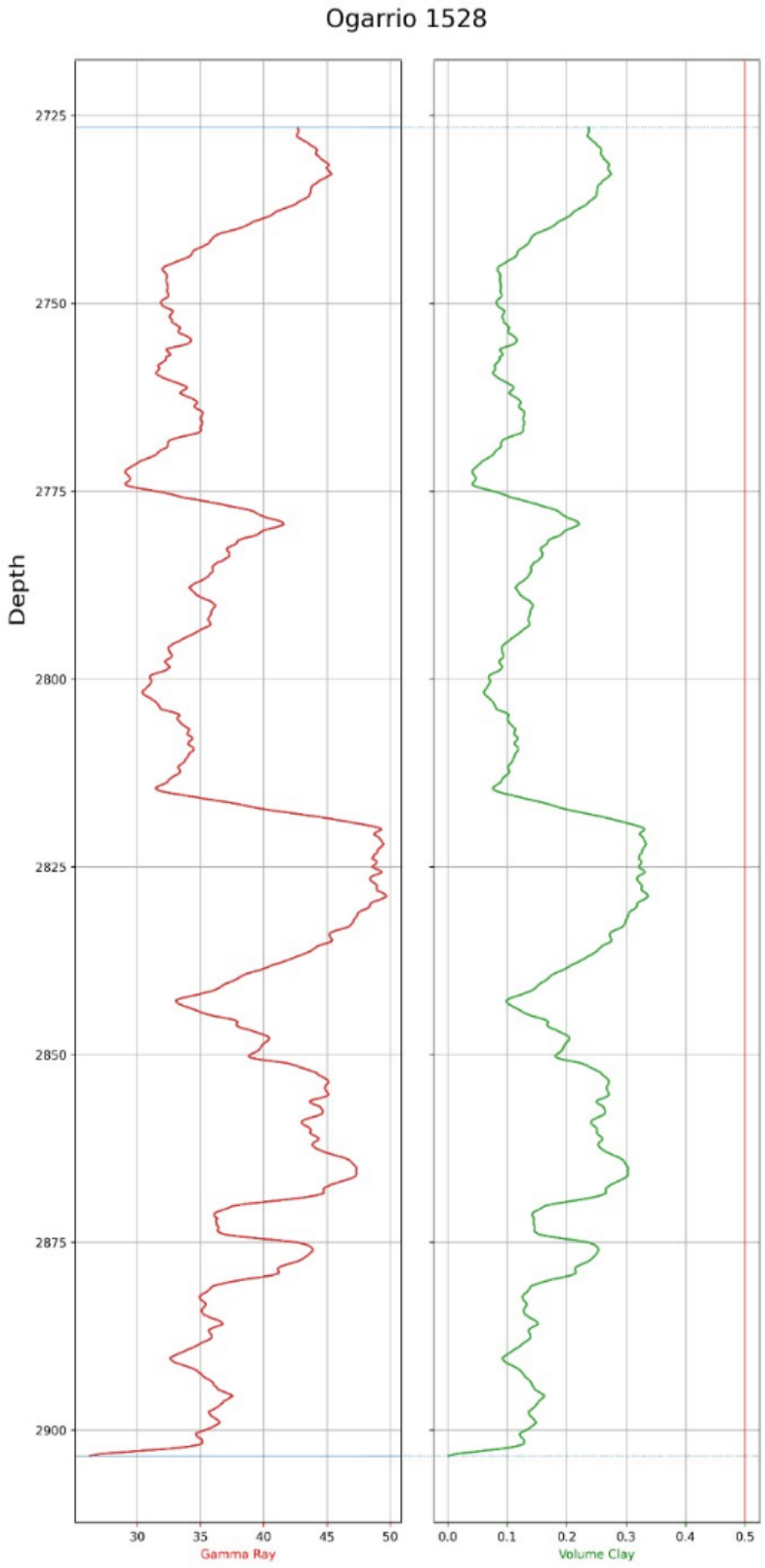

Figure 35: Depth versus GR and VolClay from the well Ogarrio 1528.

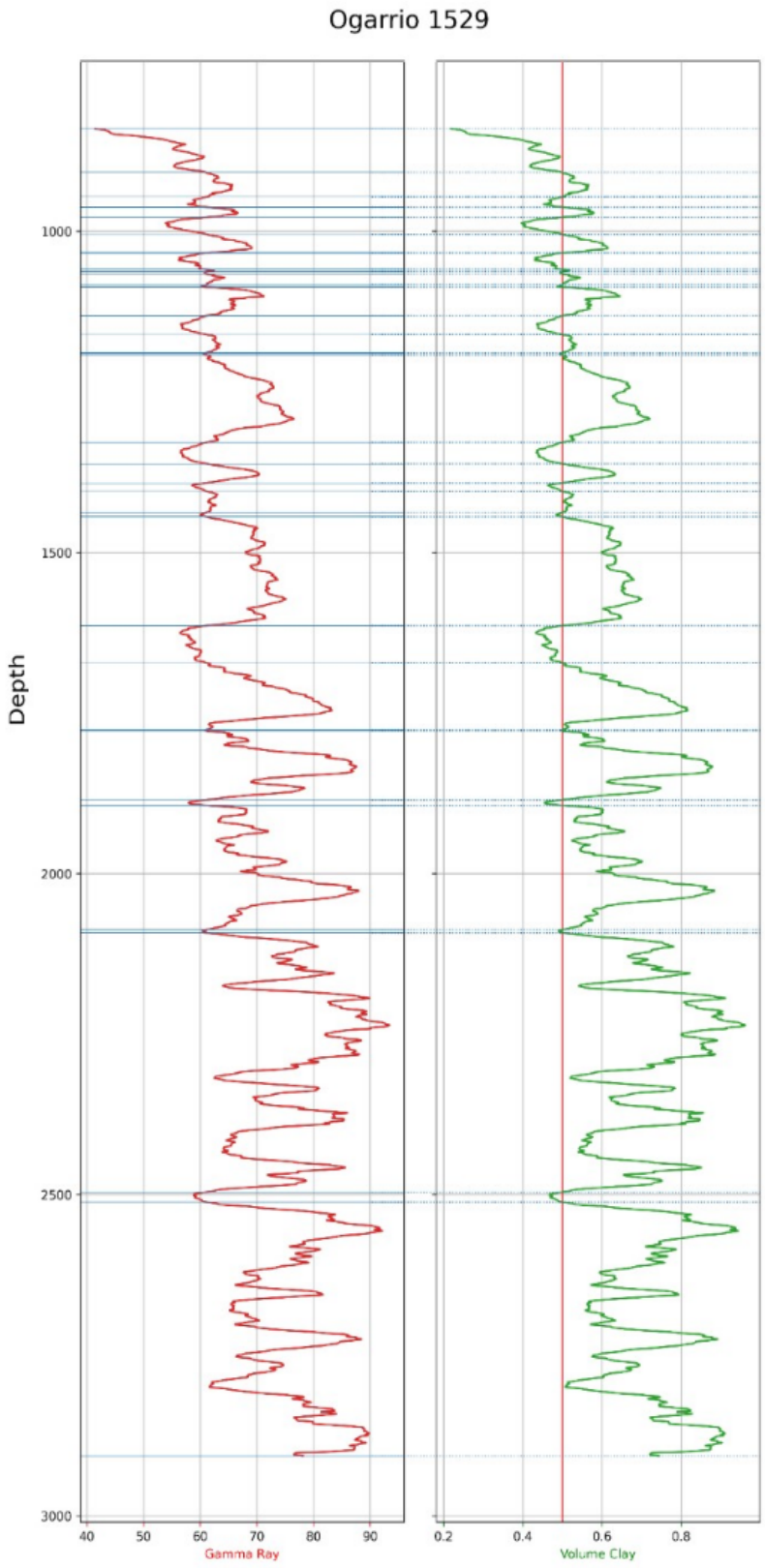

Figure 36: Depth versus GR and VolClay from the well Ogarrio 1529.

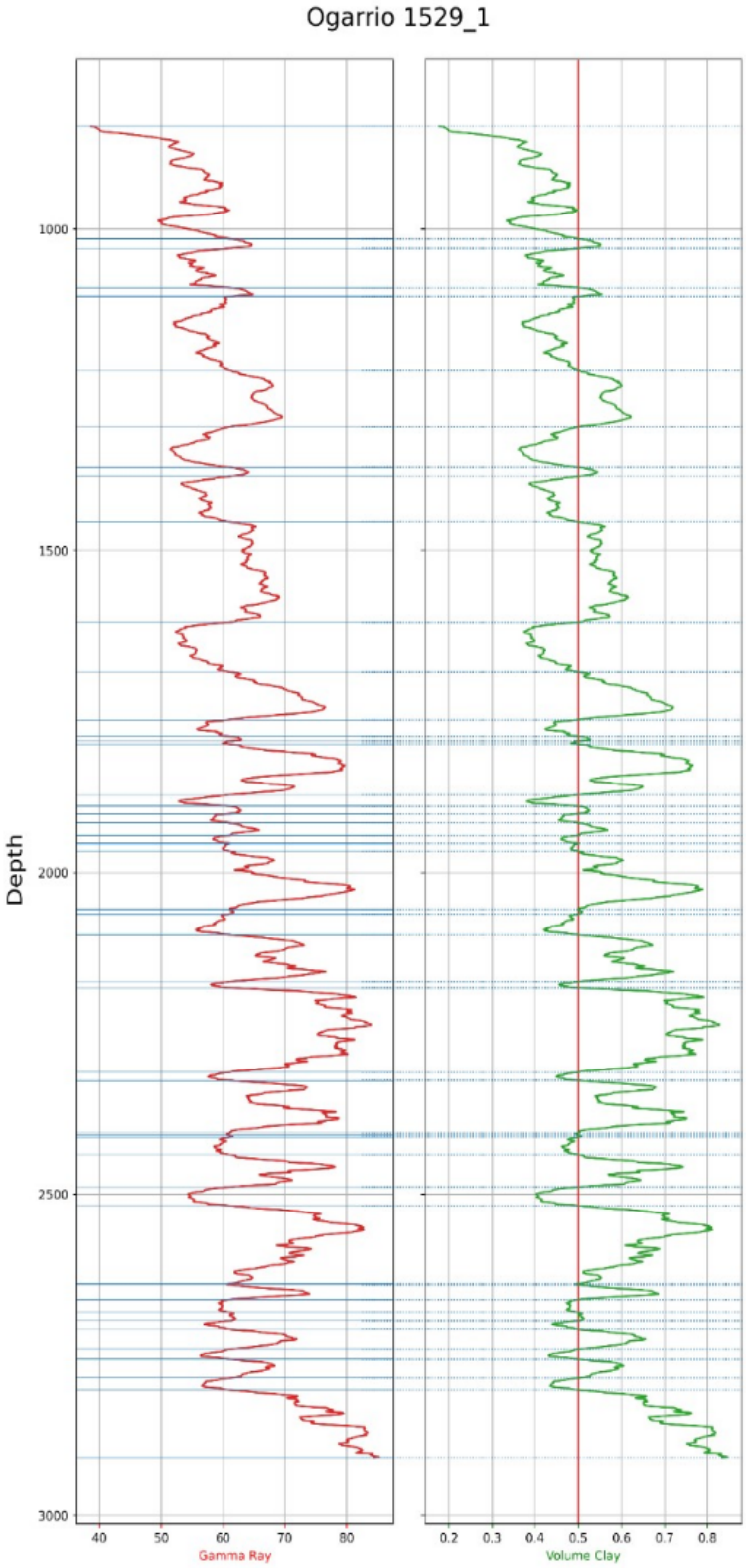

Figure 37: Depth versus GR and VolClay from the well Ogarrio 1529-1.

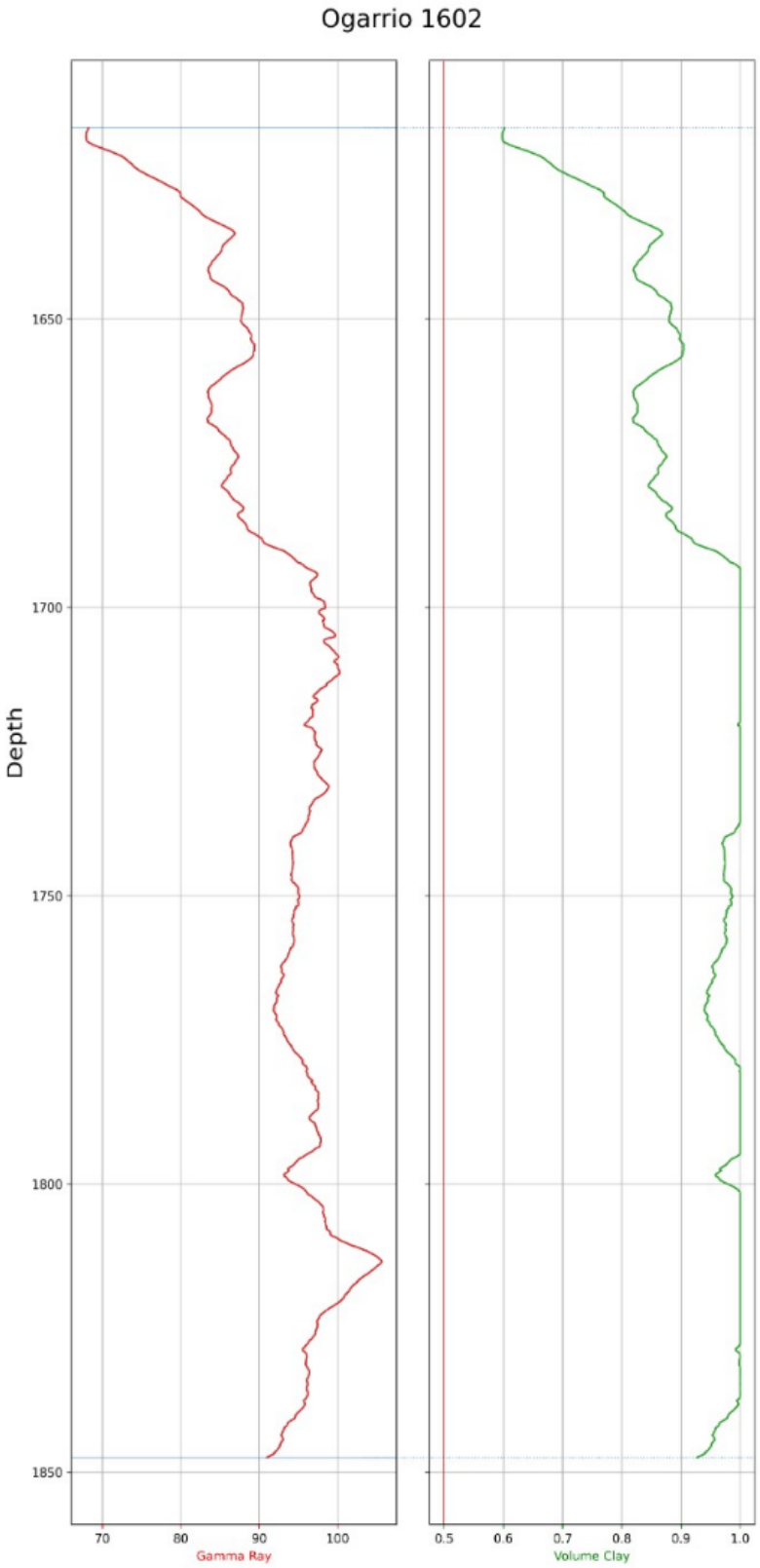

Figure 38: Depth versus GR and VolClay from the well Ogarrio 1602.

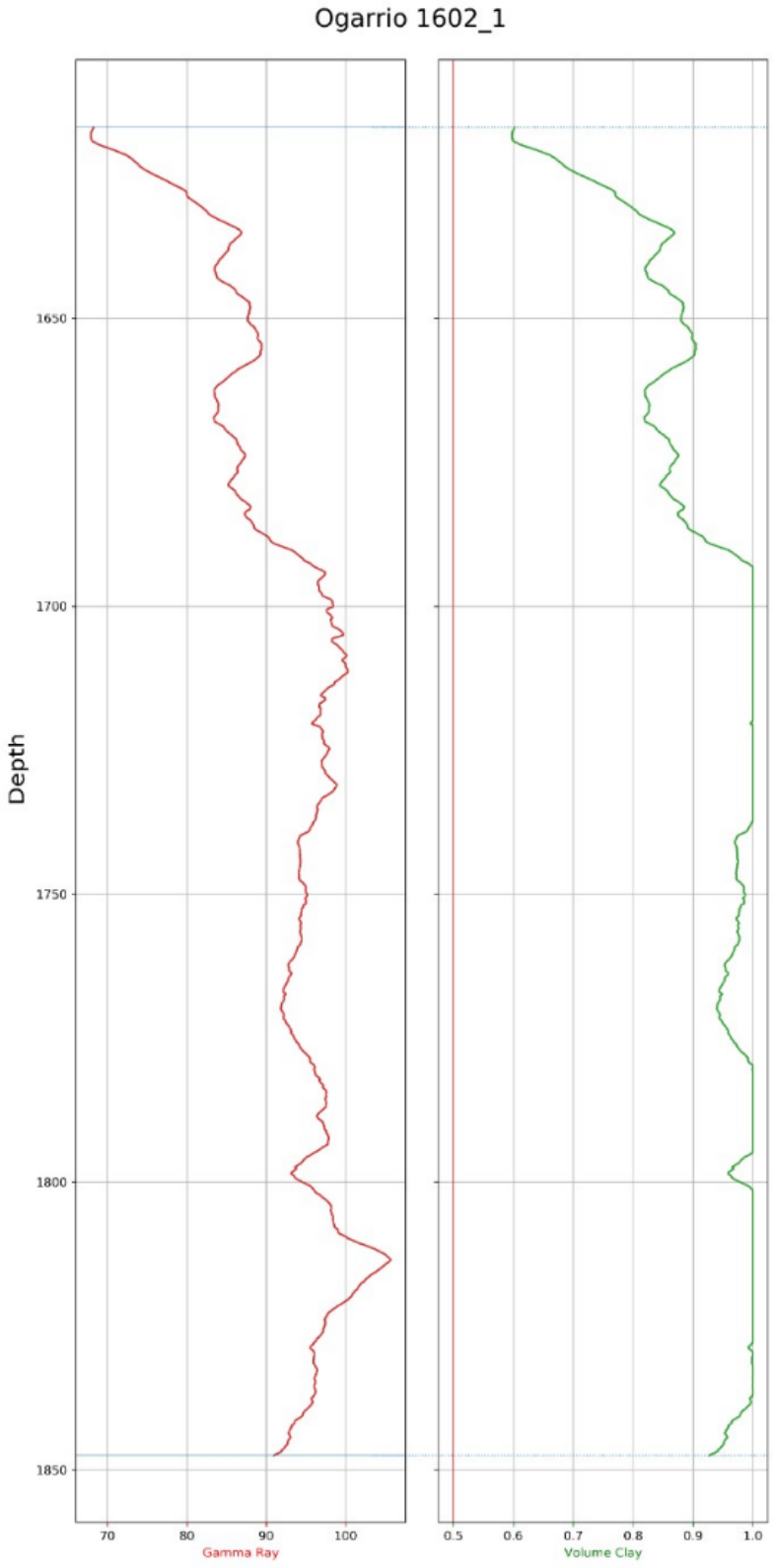

Figure 39: Depth versus GR and VolClay from the well Ogarrio 1602-1.

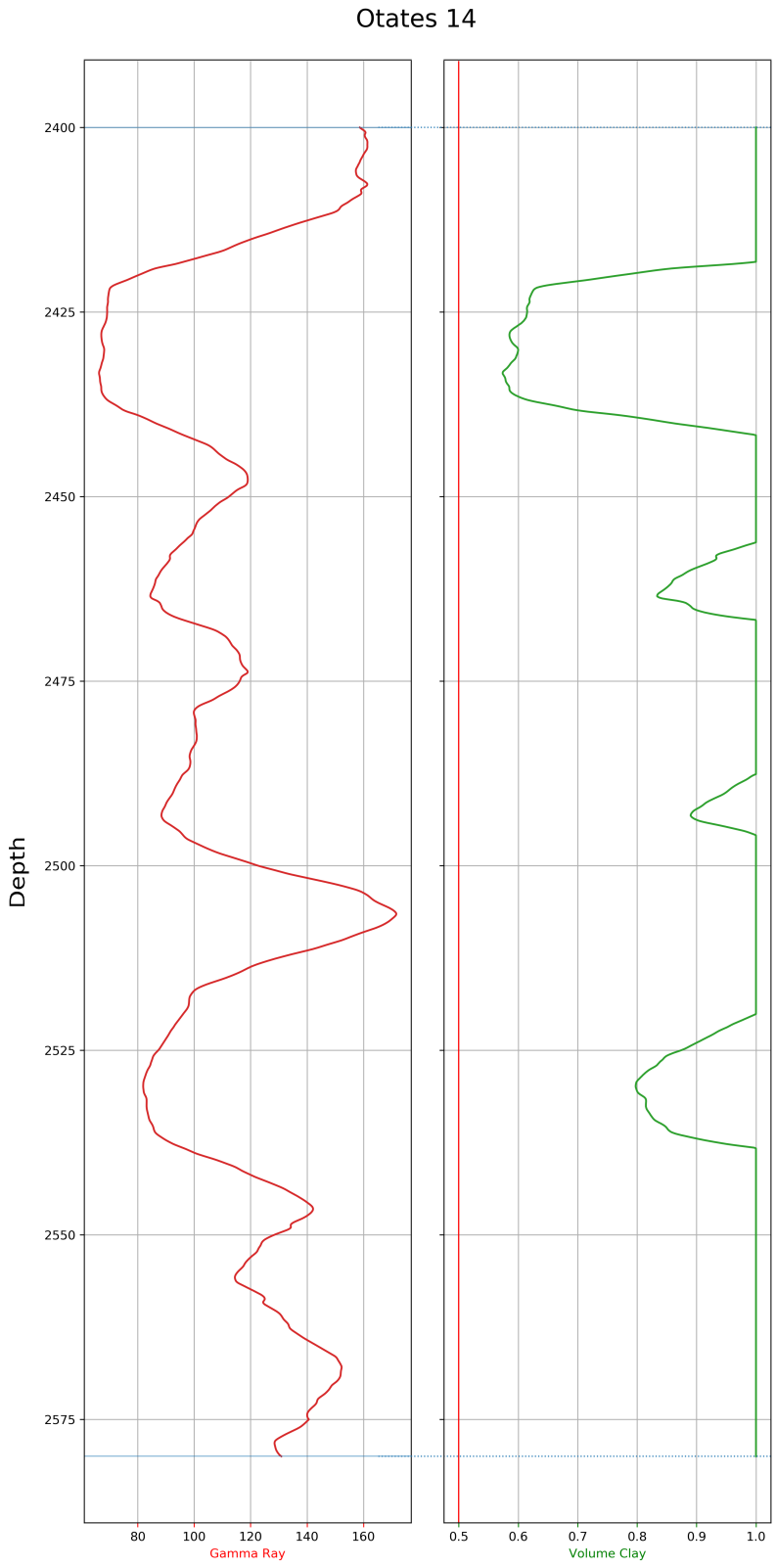

Figure 40: Depth versus GR and VolClay from the well Otates 14.

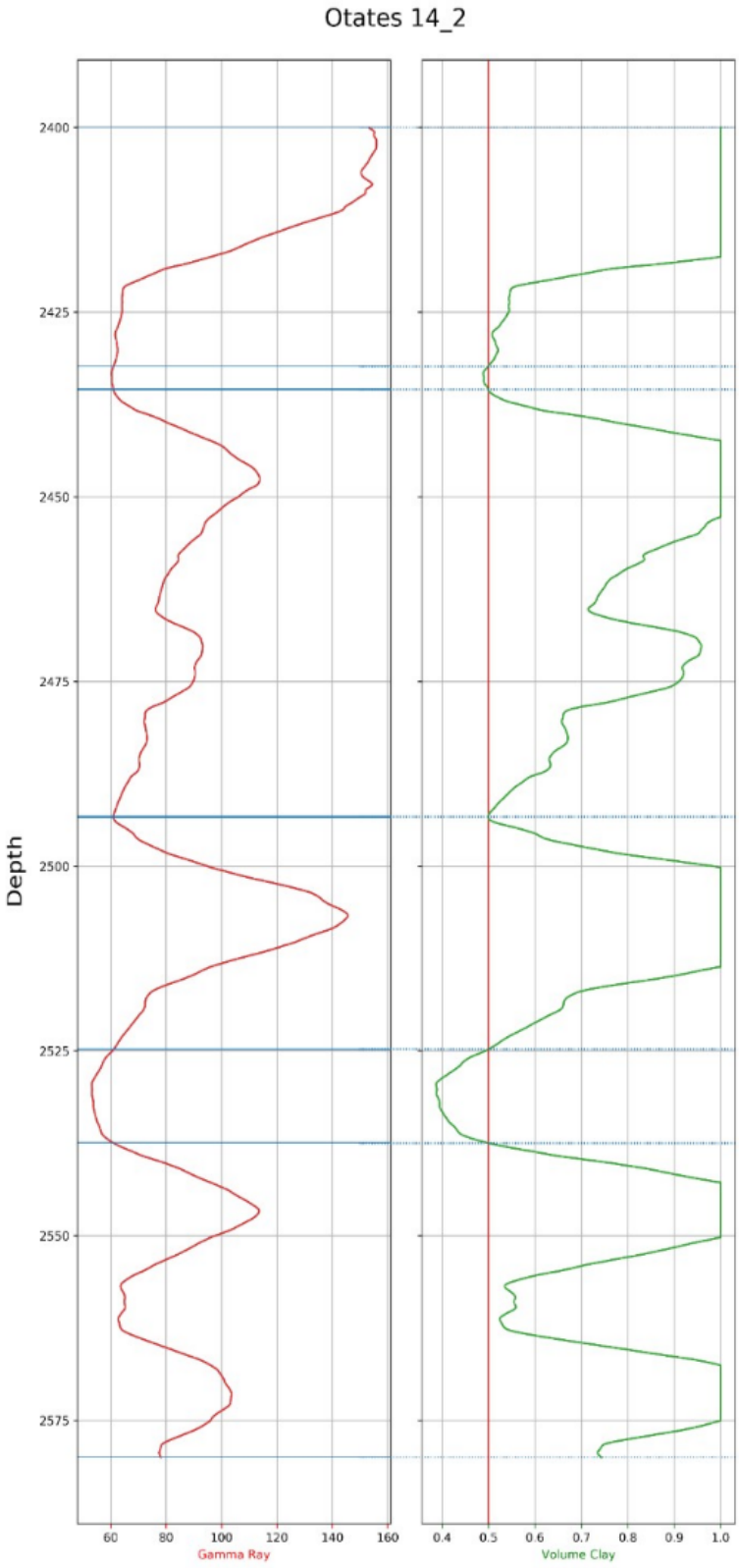

Figure 41: Depth versus GR and VolClay from the well Otates 14-2.

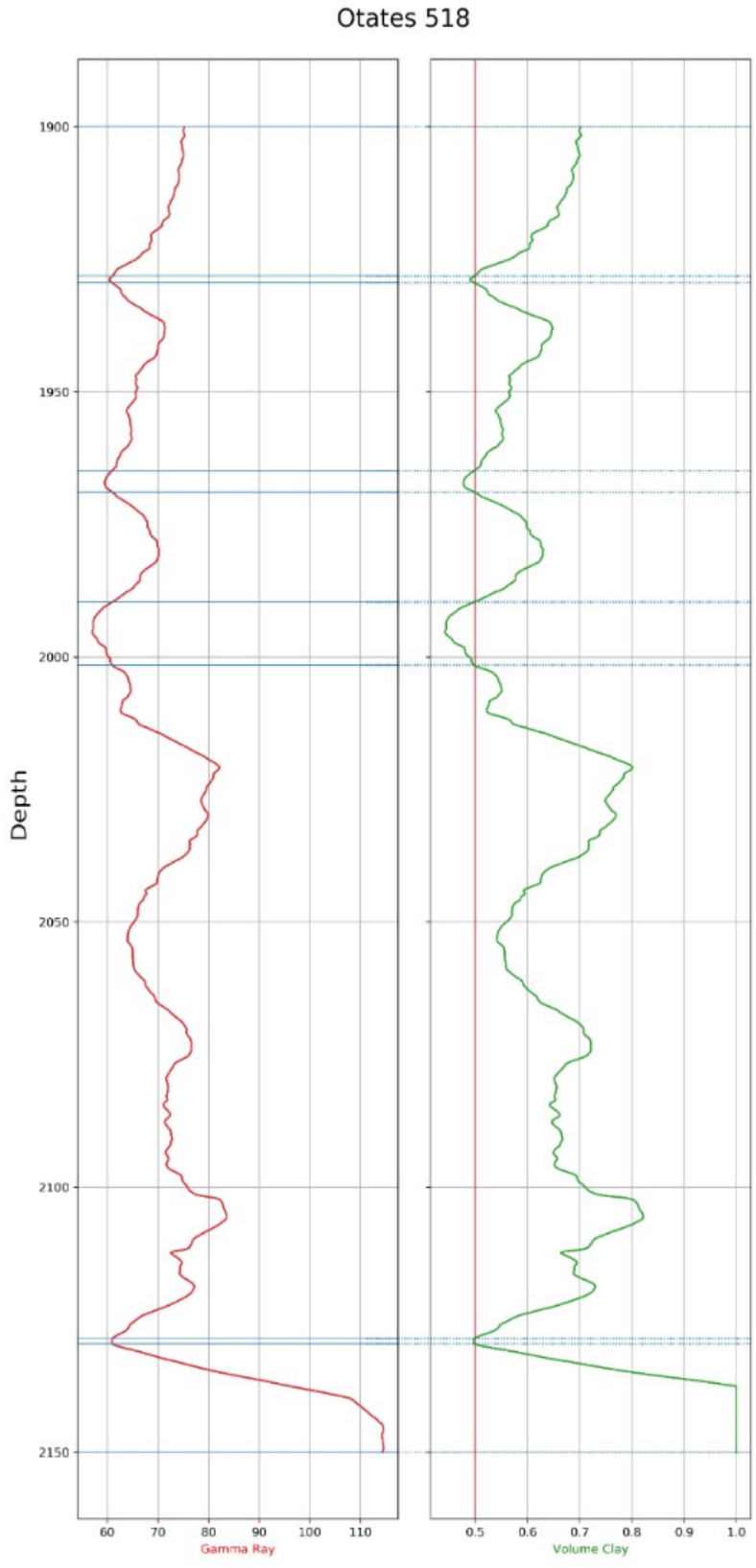

Figure 42: Depth versus GR and VolClay from the well Otates 518.

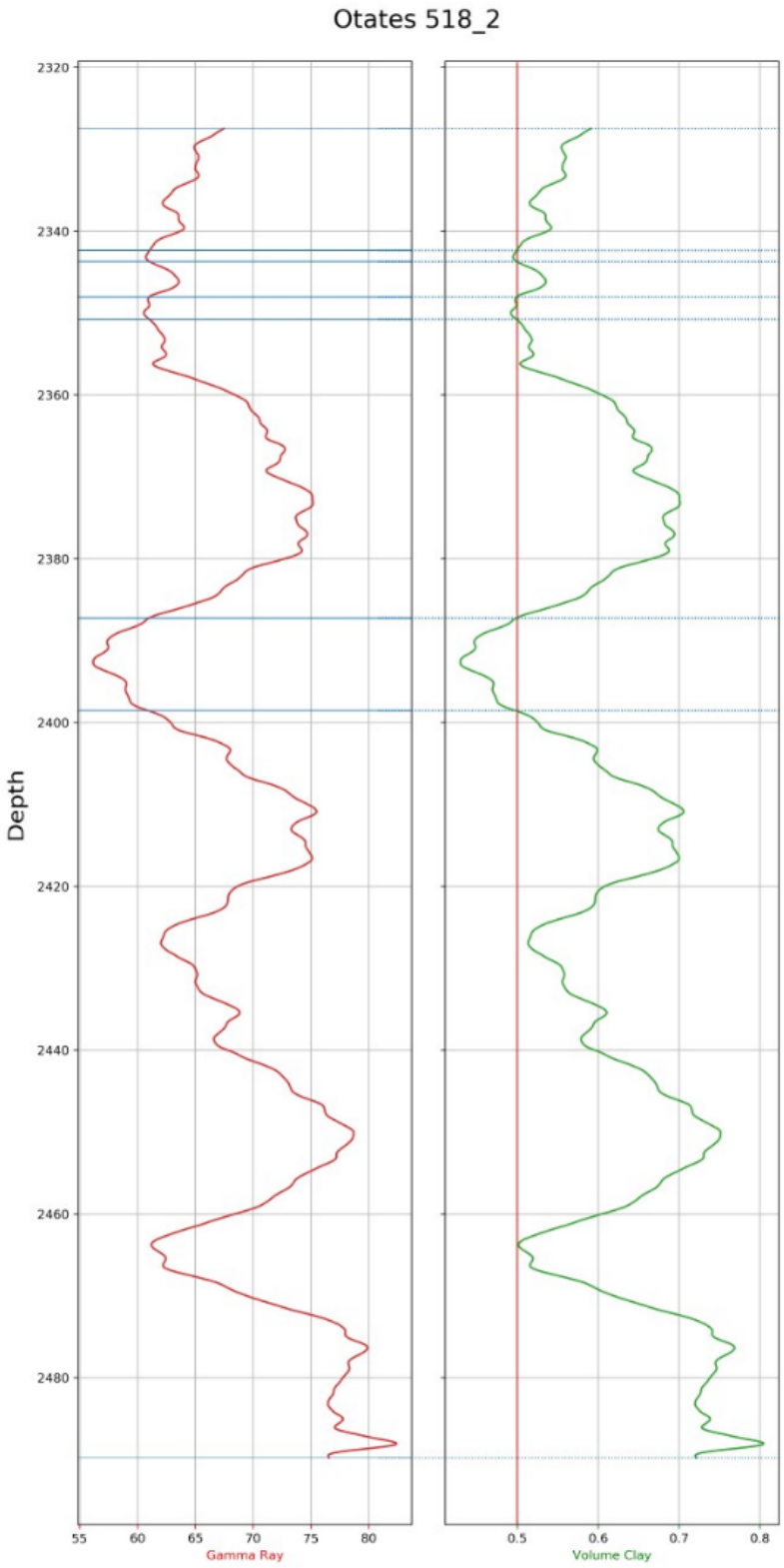

Figure 43: Depth versus GR and VolClay from the well Otates 518-2.

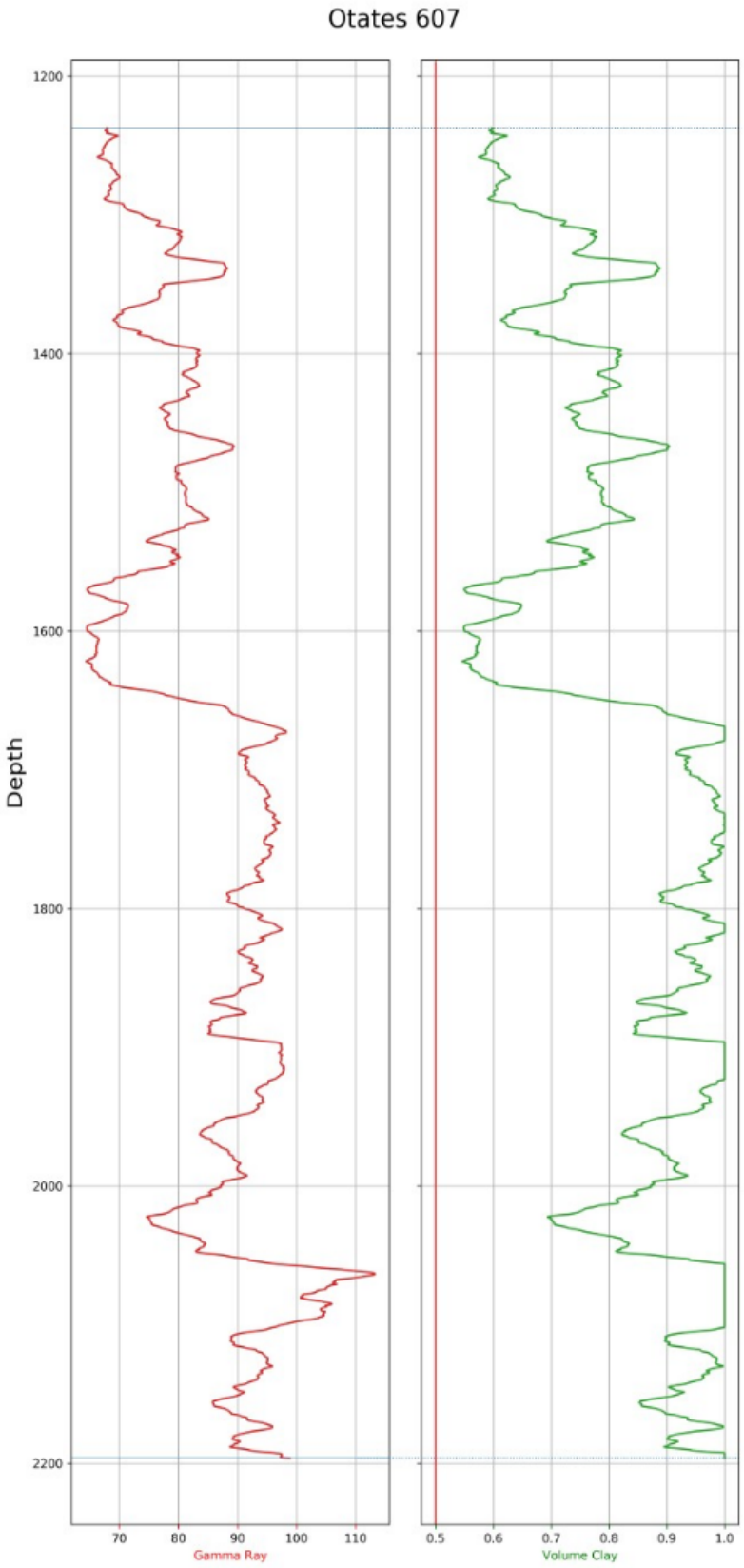

Figure 44: Depth versus GR and VolClay from the well Otates 607.

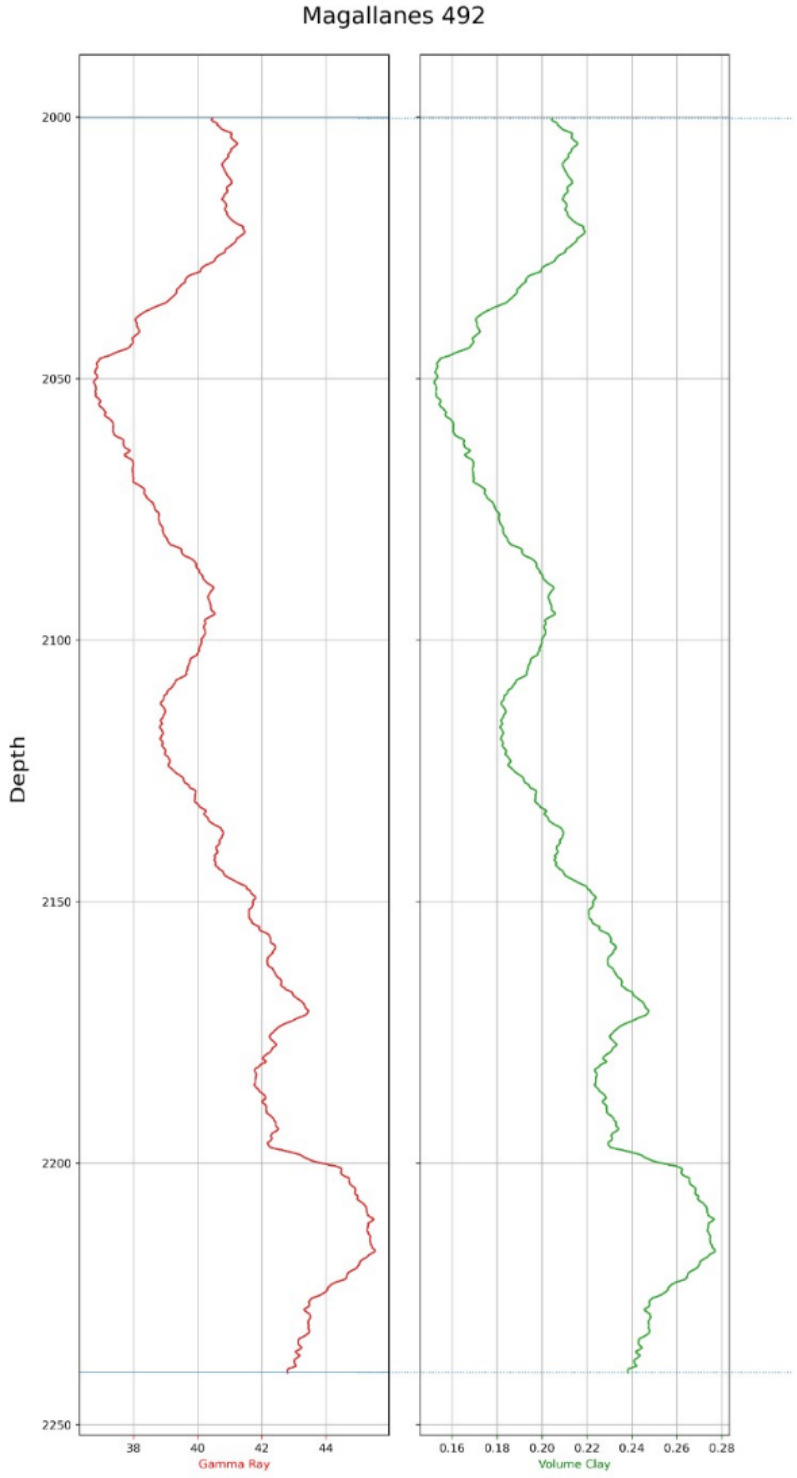

Figure 45: Depth versus GR and VolClay from the well Magallones 492.

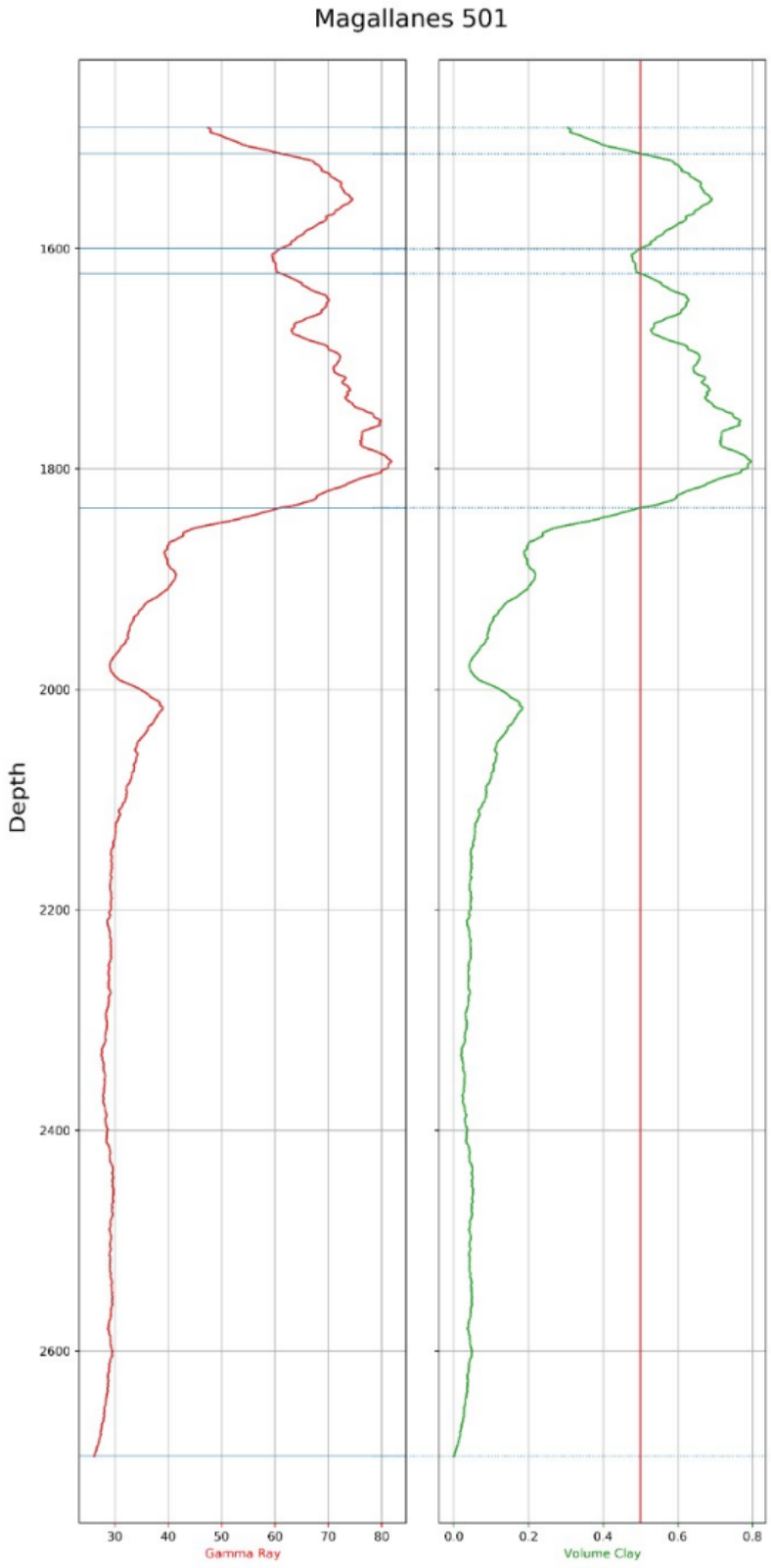

Figure 46: Depth versus GR and VolClay from the well Magallones 501.

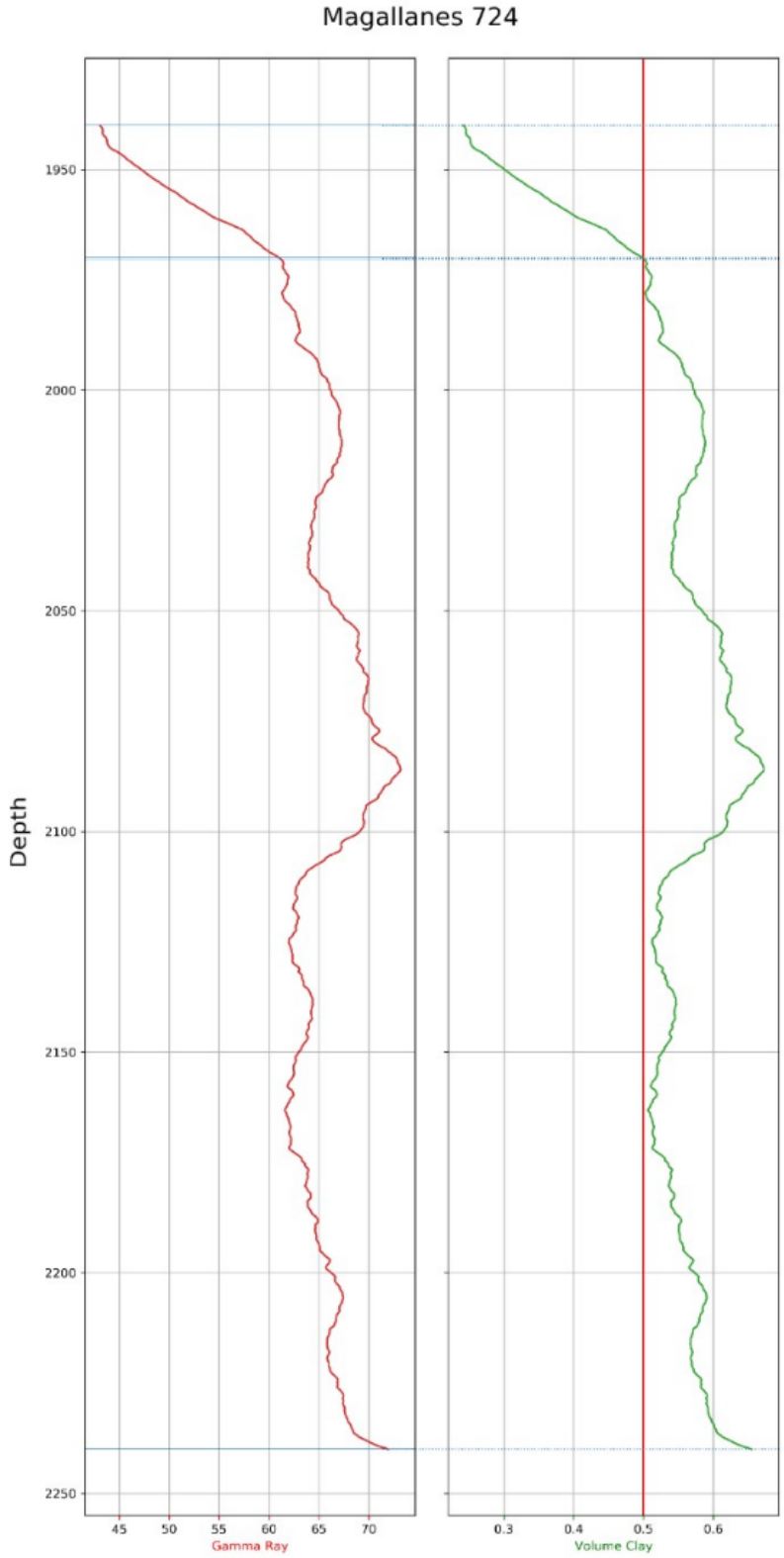

Figure 47: Depth versus GR and VolClay from the well Magallones 724.

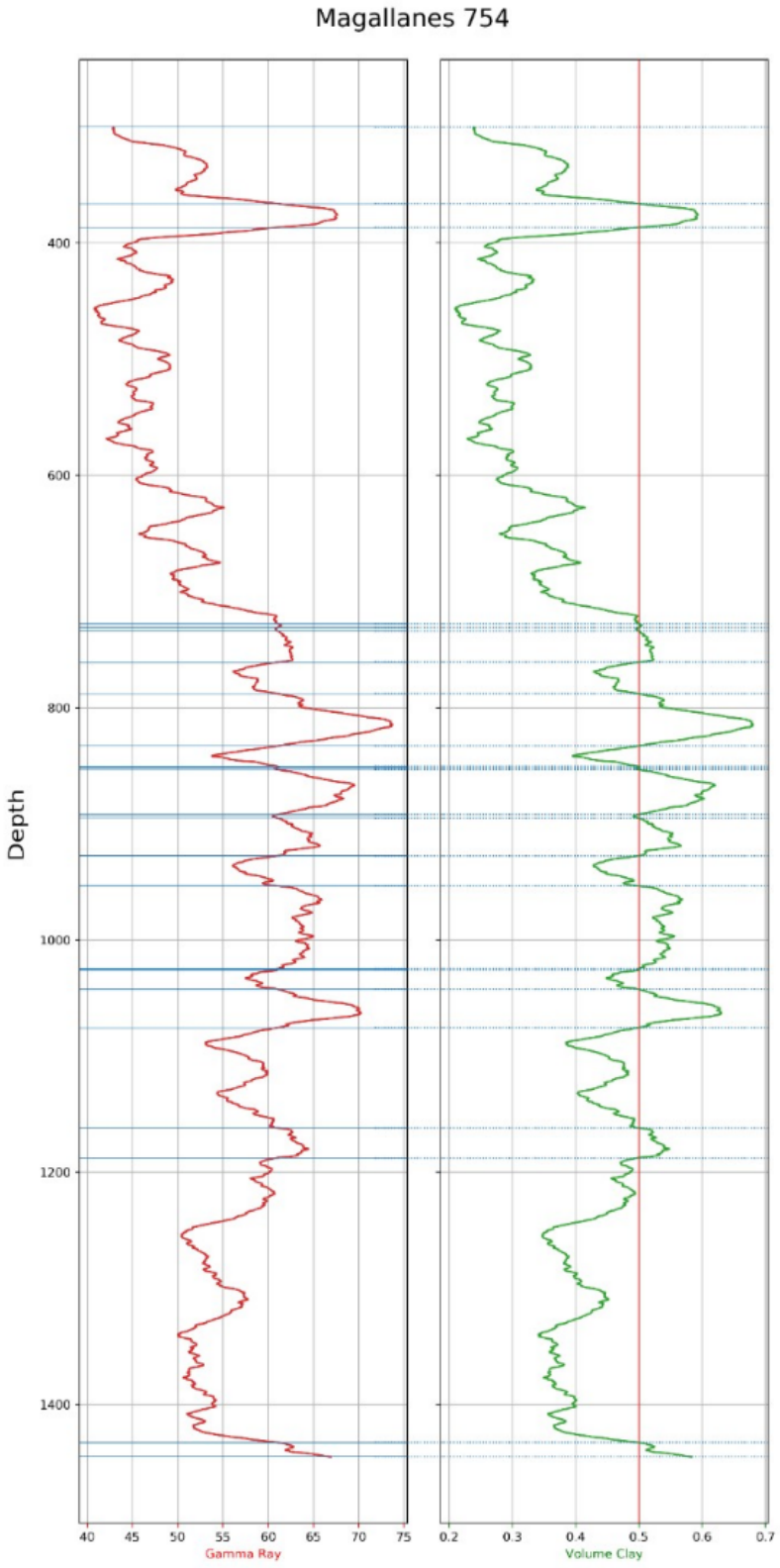

Figure 48: Depth versus GR and VolClay from the well Magallones 754.

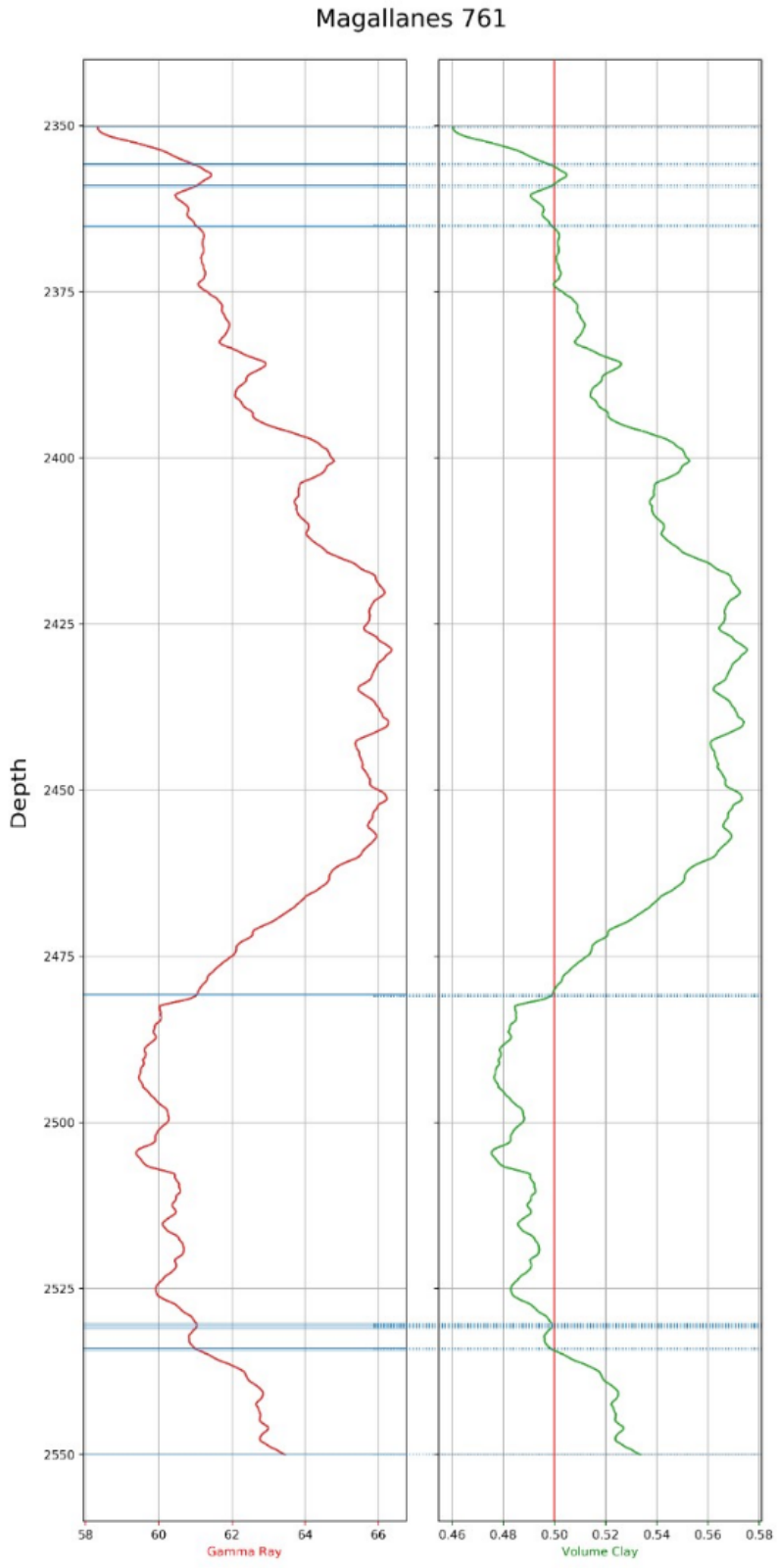

Figure 49: Depth versus GR and VolClay from the well Magallones 761.

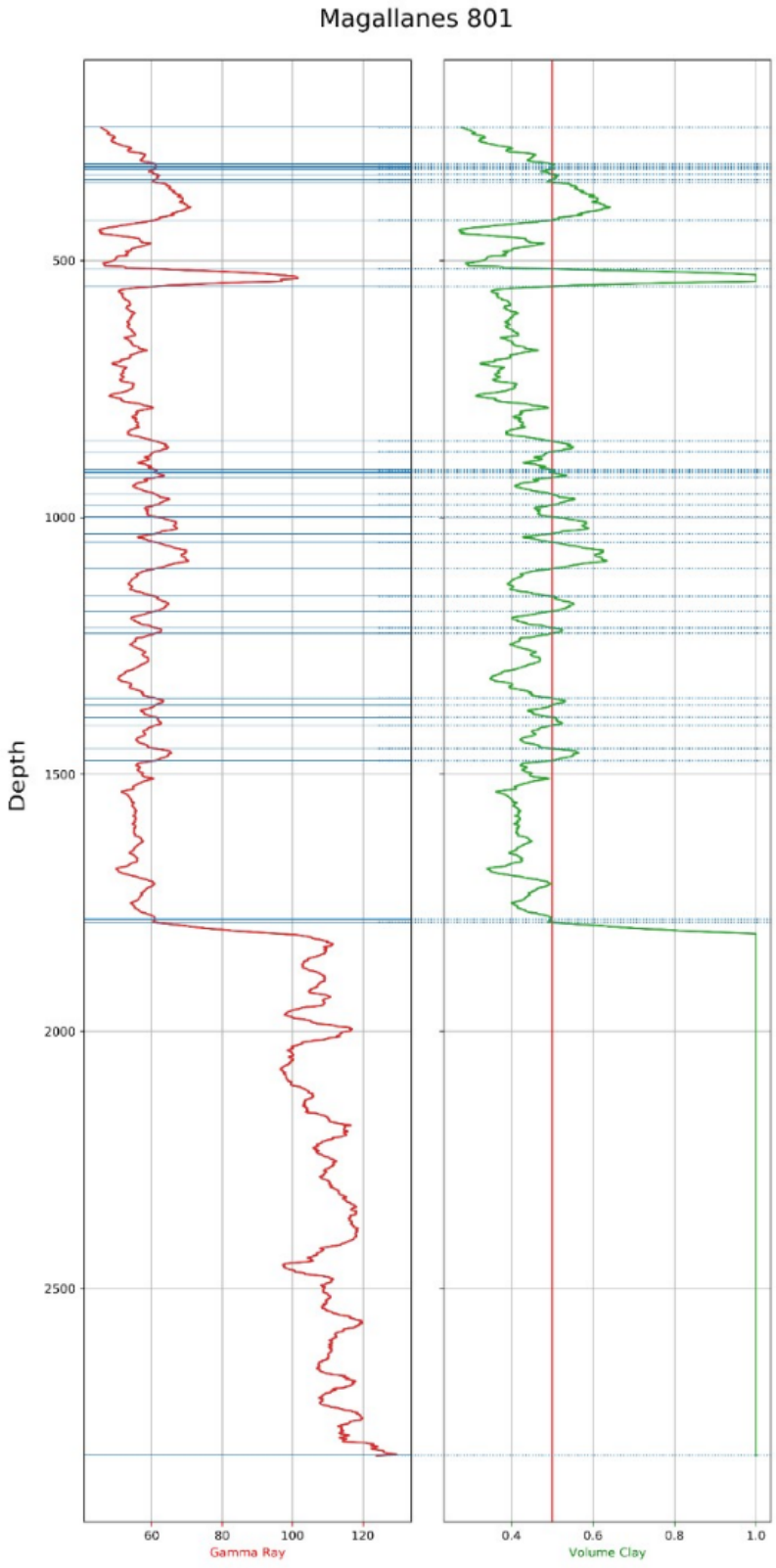

Figure 50: Depth versus GR and VolClay from the well Magallones 801.

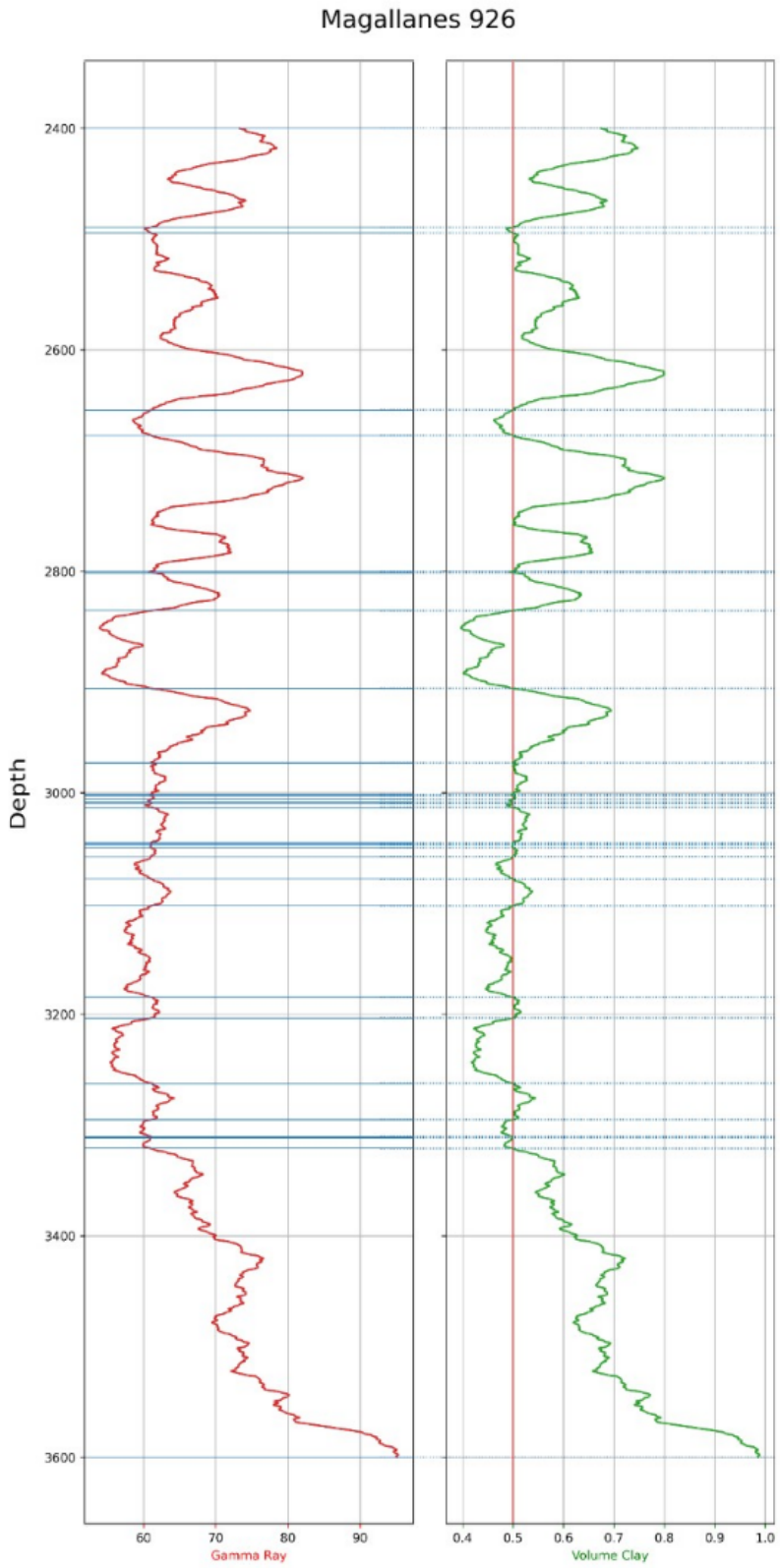

Figure 51: Depth versus GR and VolClay from the well Magallones 926.

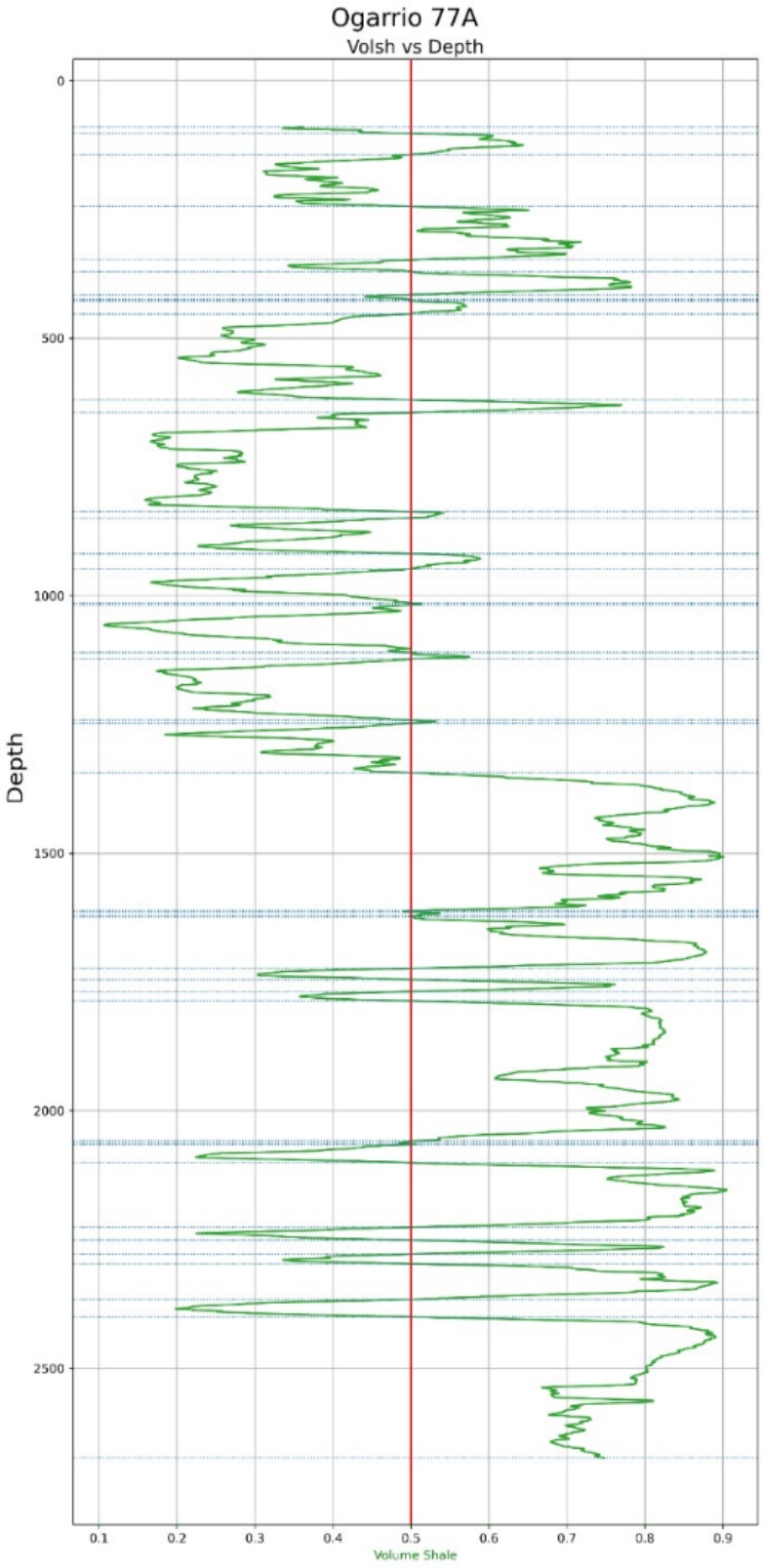

Figure 52: Depth versus VolClay from the well Ogarrio 77A.

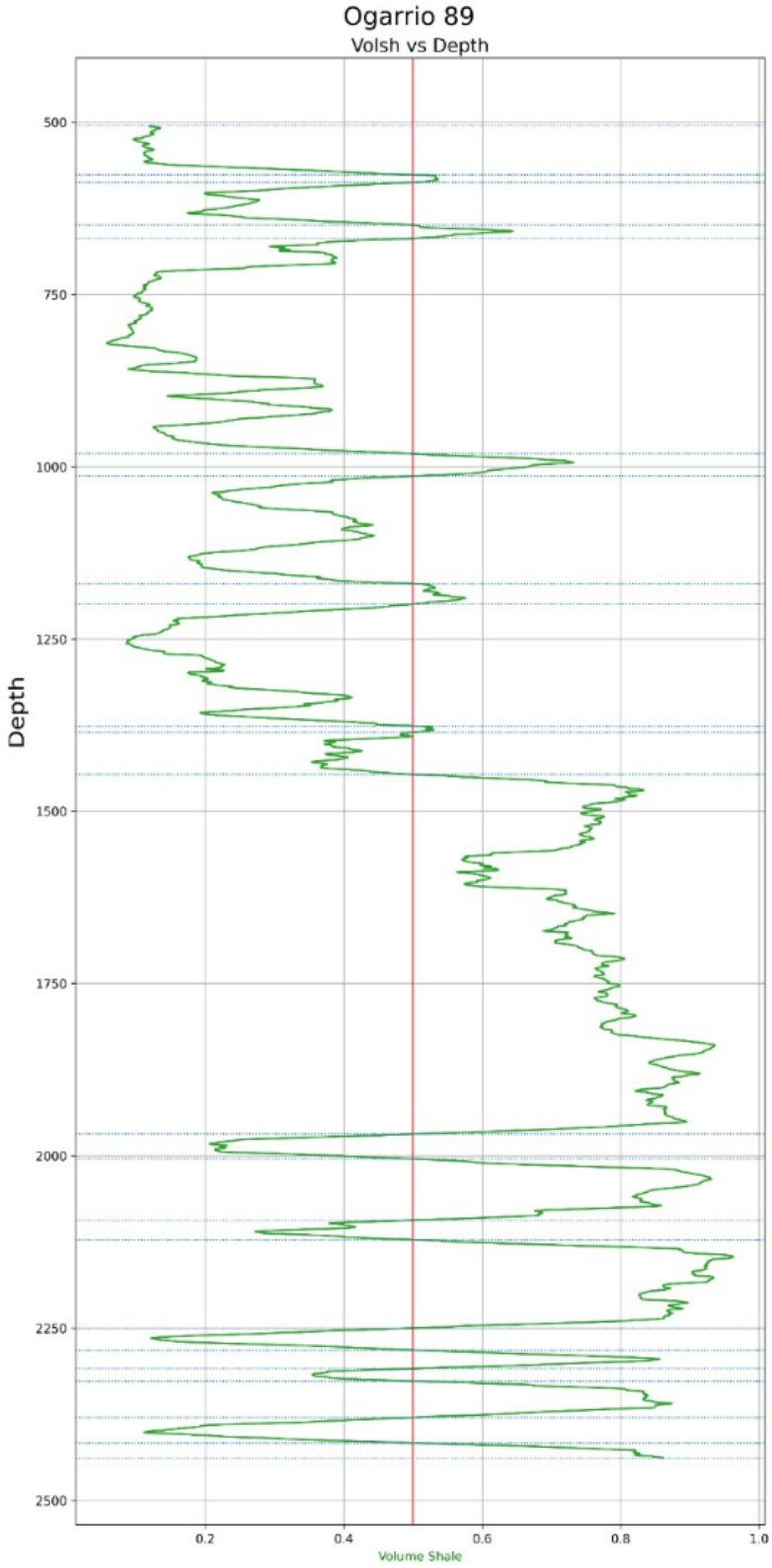

Figure 53: Depth versus VolClay from the well Ogarrio 89.

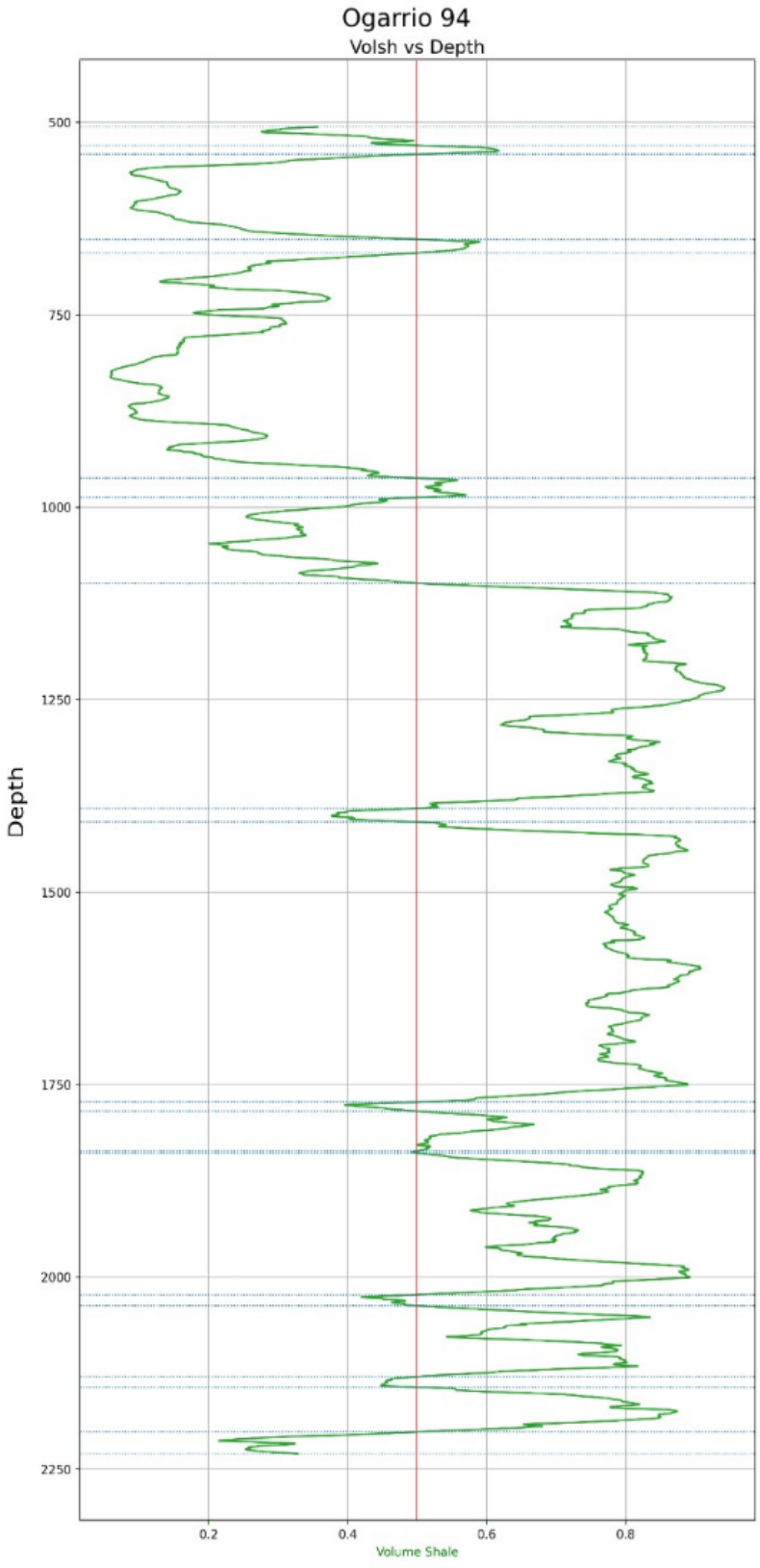

Figure 54: Depth versus VolClay from the well Ogarrio 94.

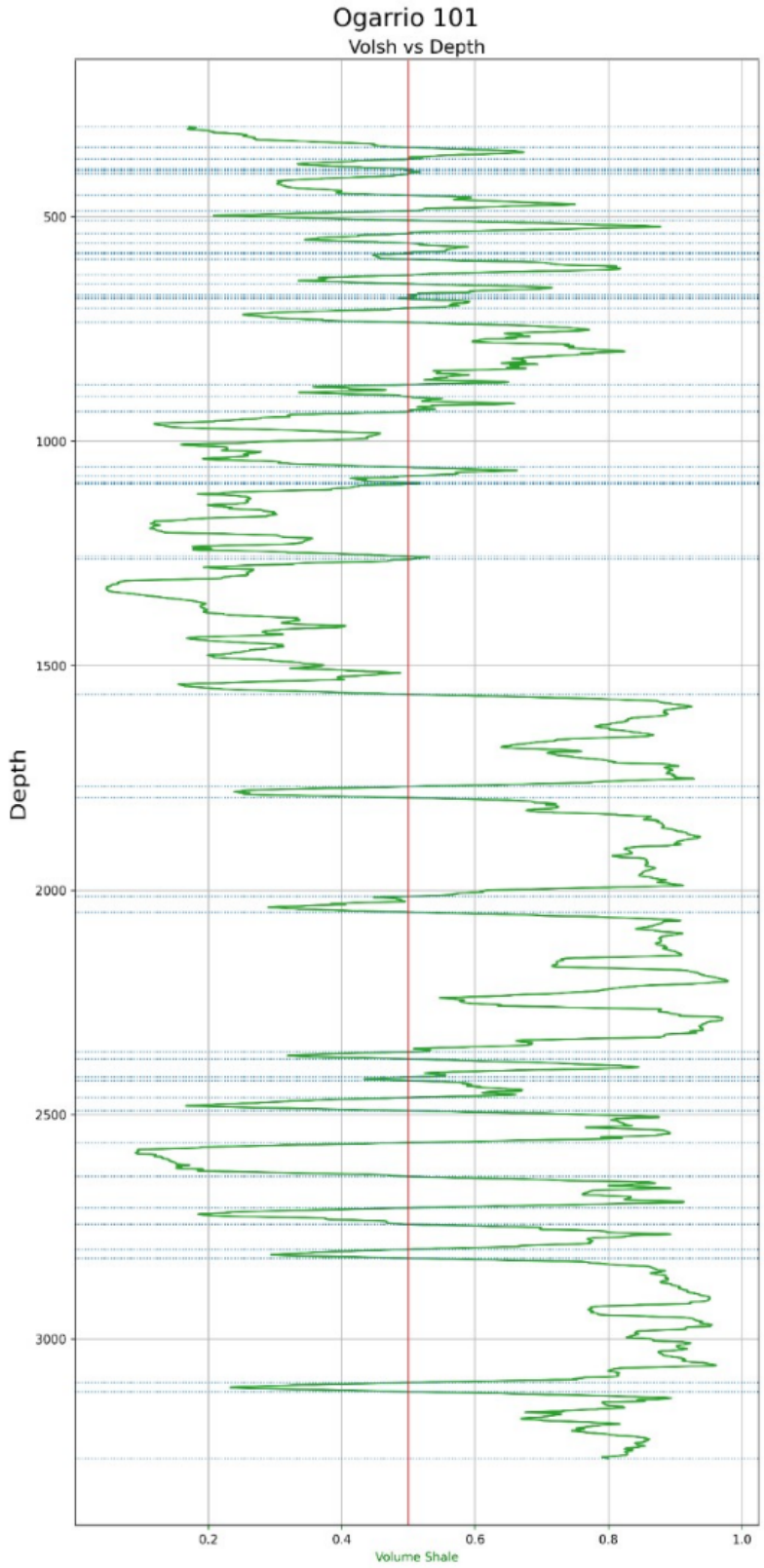

Figure 55: Depth versus VolClay from the well Ogarrio 101.

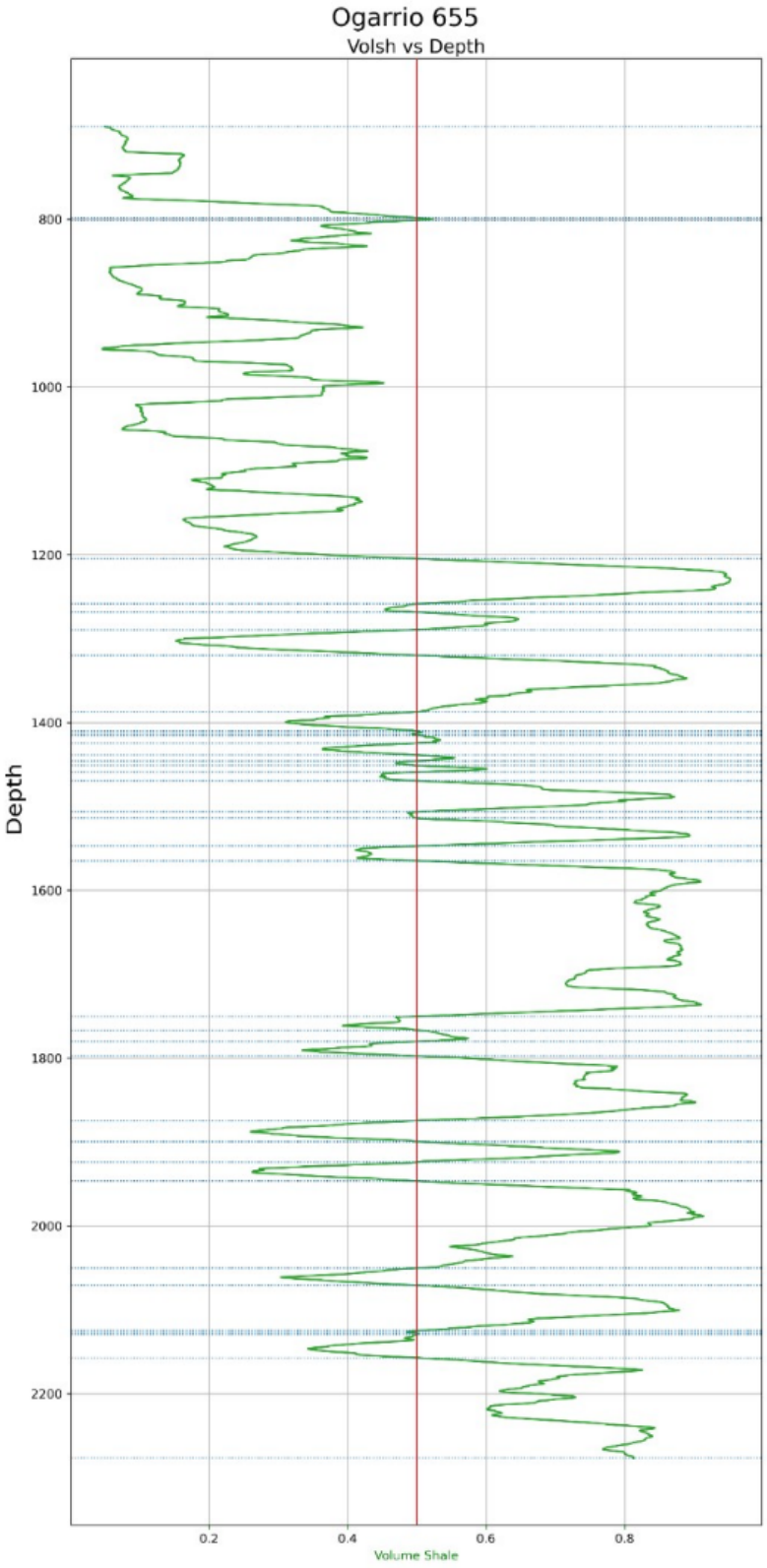

Figure 56: Depth versus VolClay from the well Ogarrio 655.

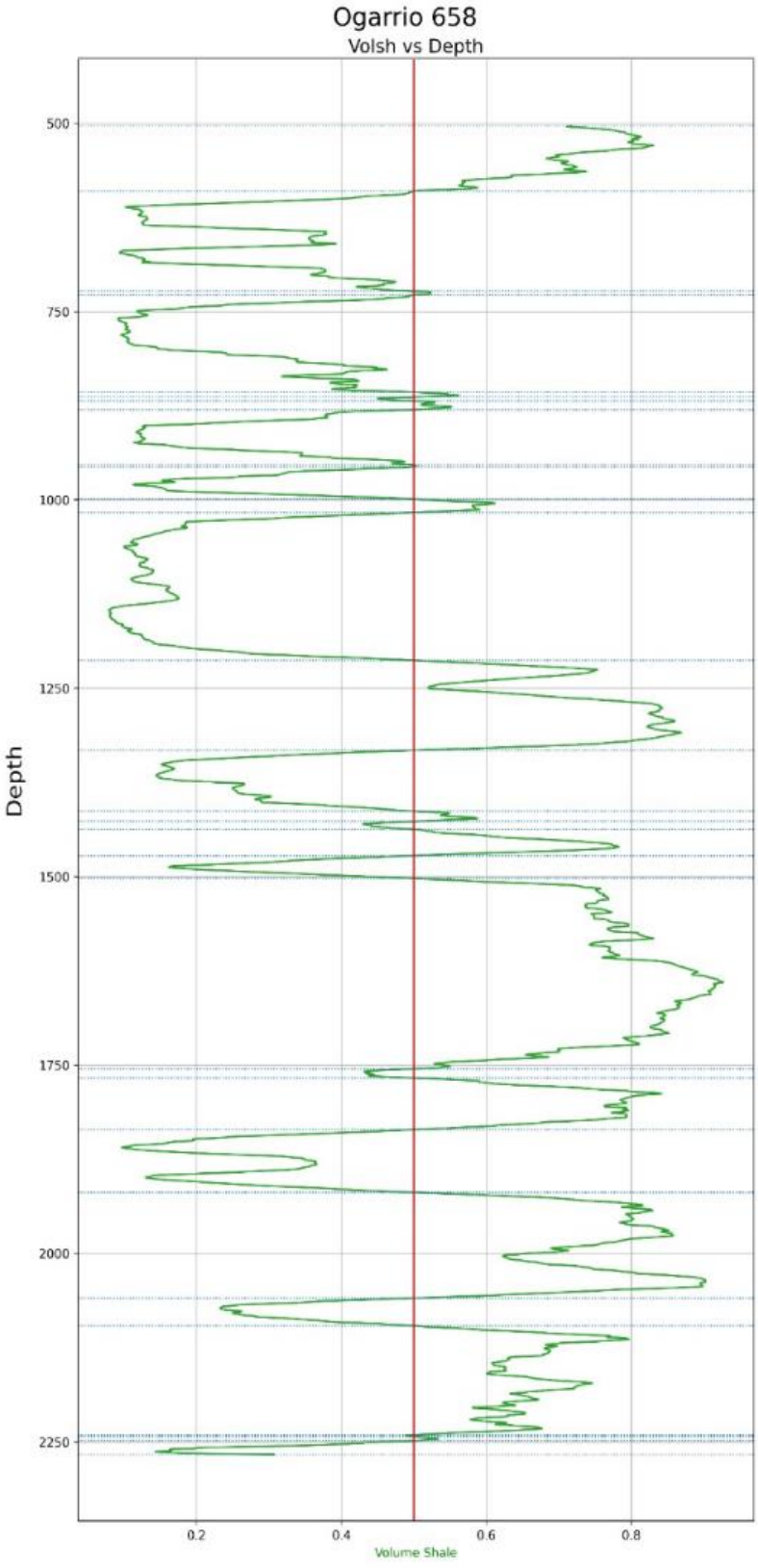

Figure 57: Depth versus VolClay from the well Ogarrio 658.

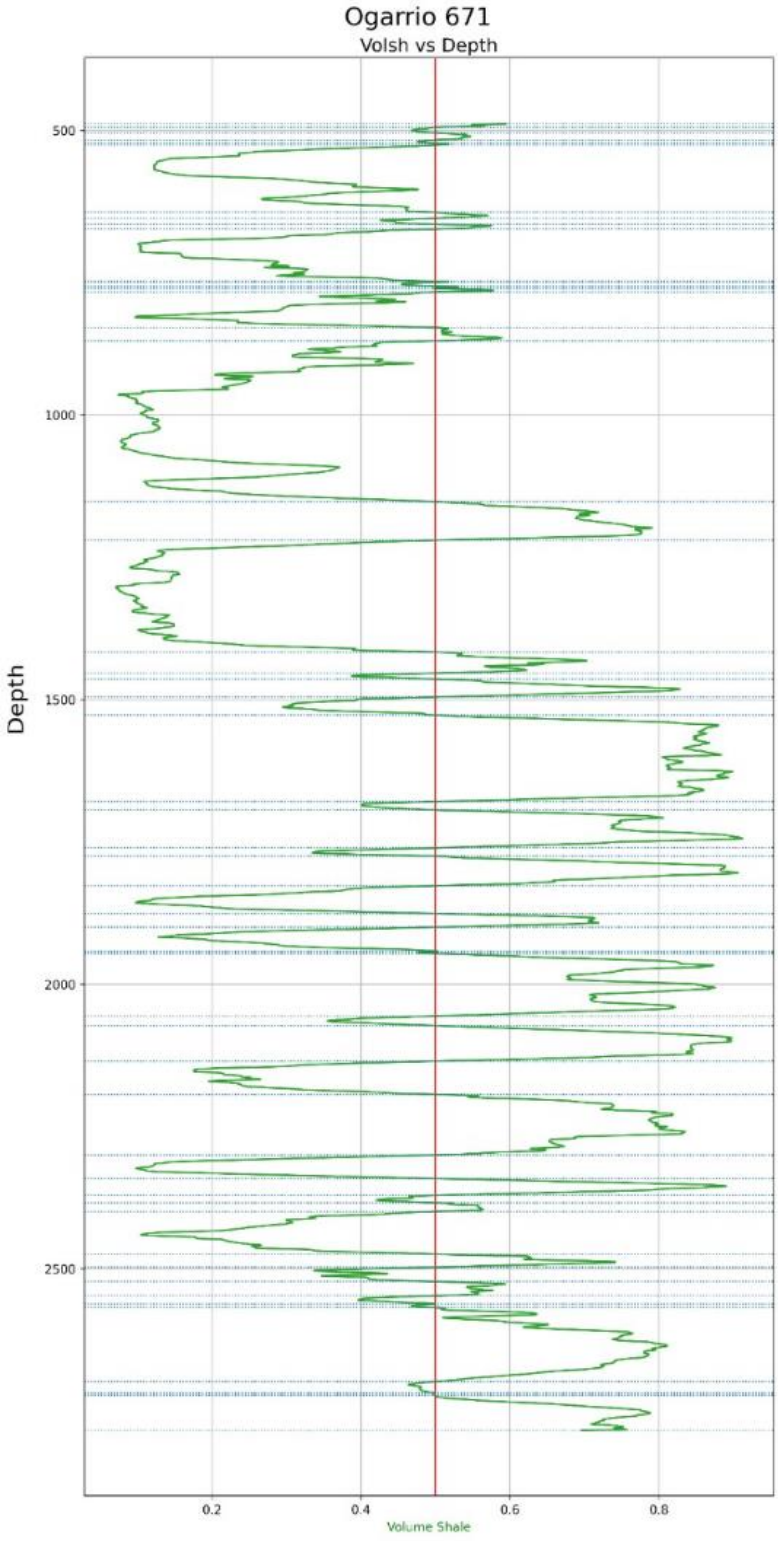

Figure 58: Depth versus VolClay from the well Ogarrio 671.

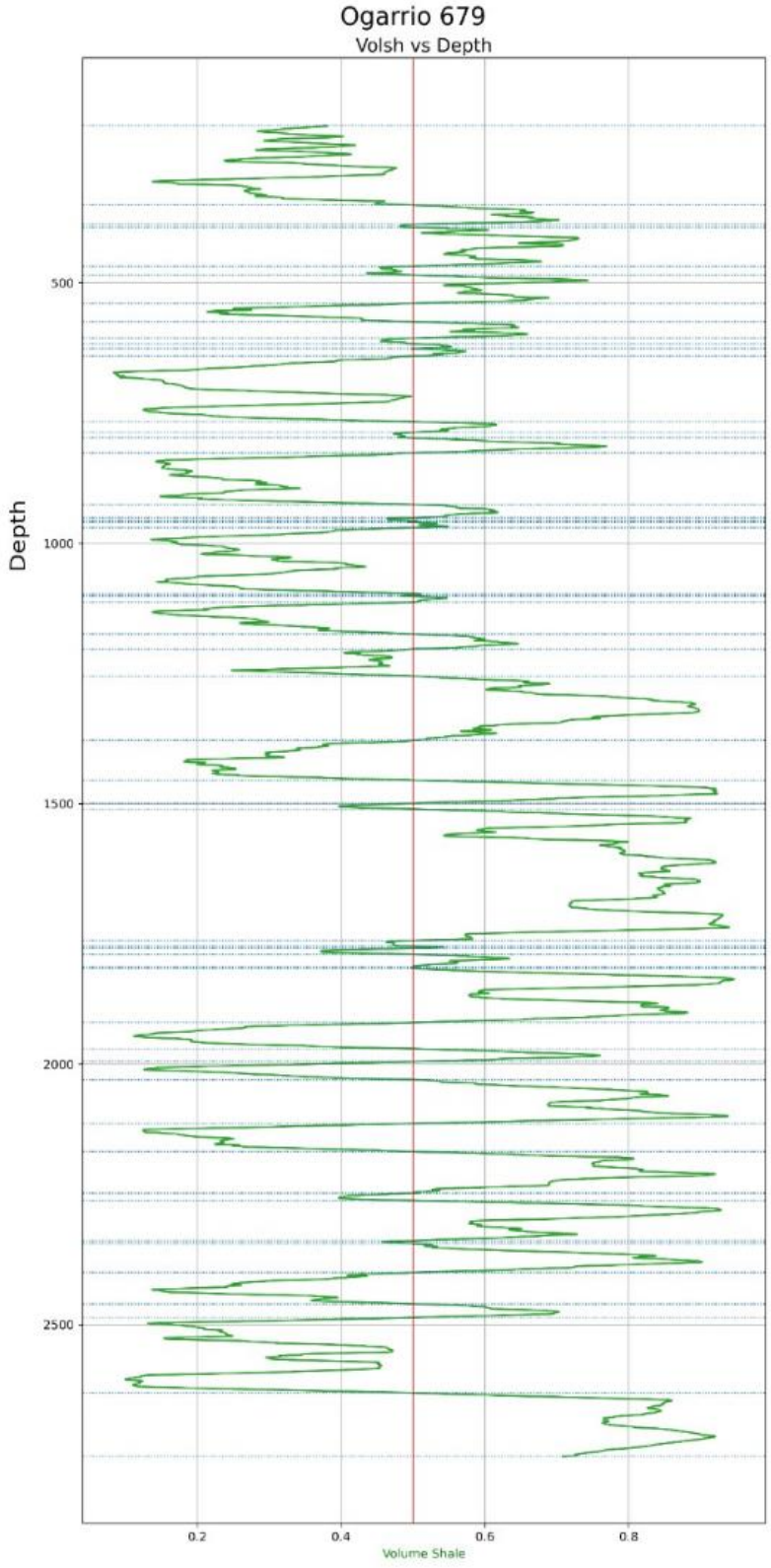

Figure 59: Depth versus VolClay from the well Ogarrio 676.

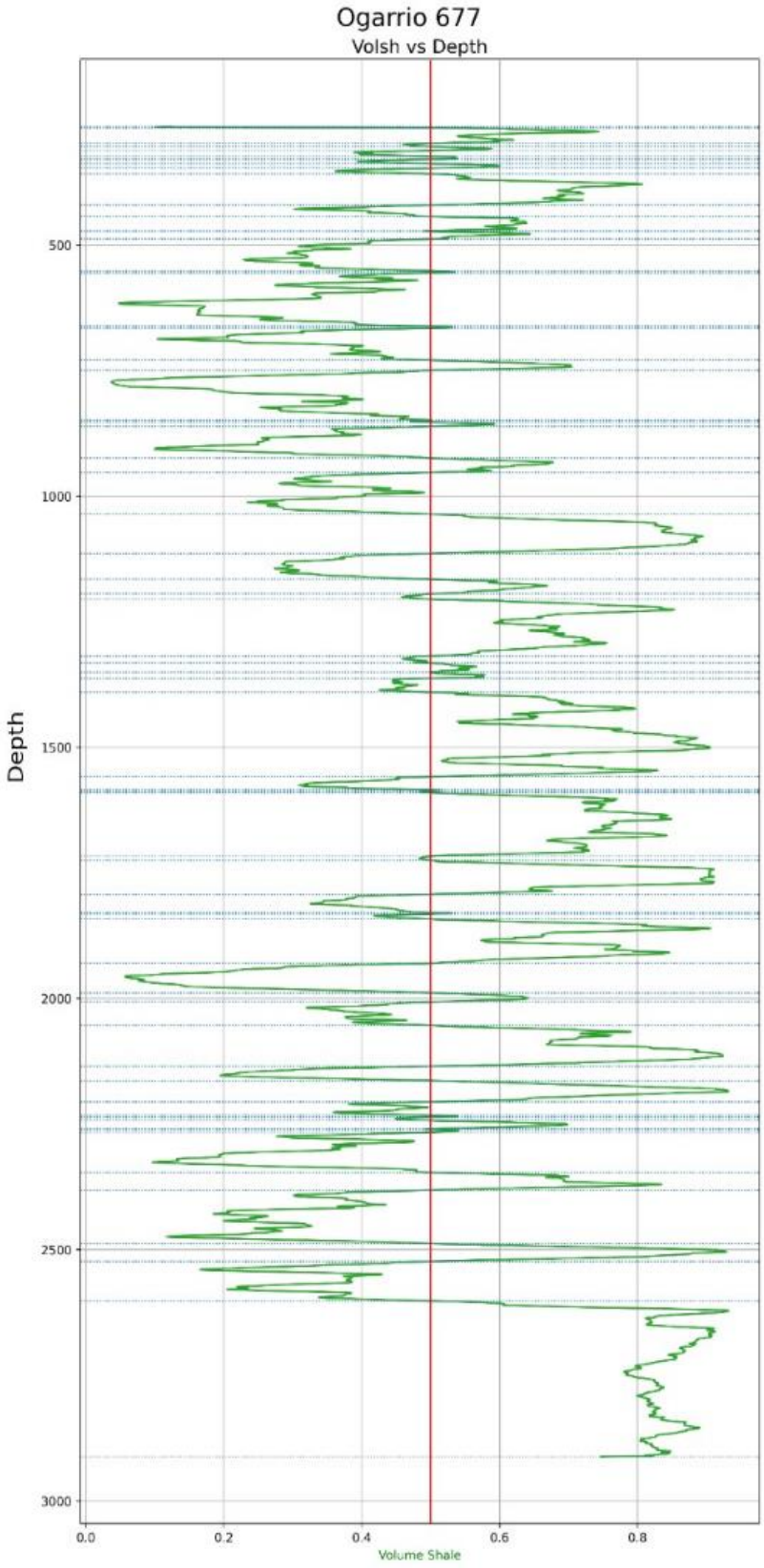

Figure 60: Depth versus VolClay from the well Ogarrio 677.

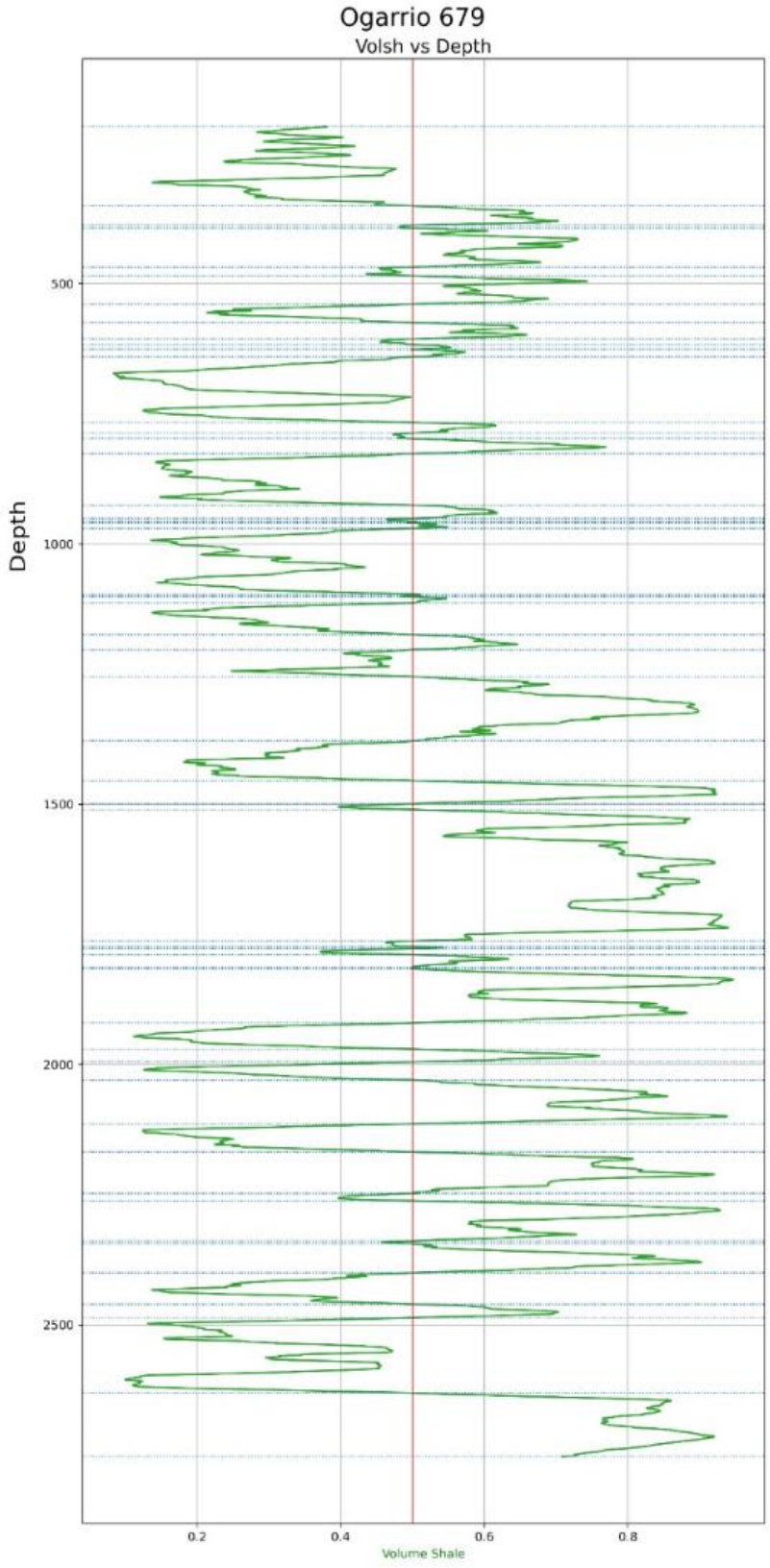

Figure 61: Depth versus VolClay from the well Ogarrio 679.

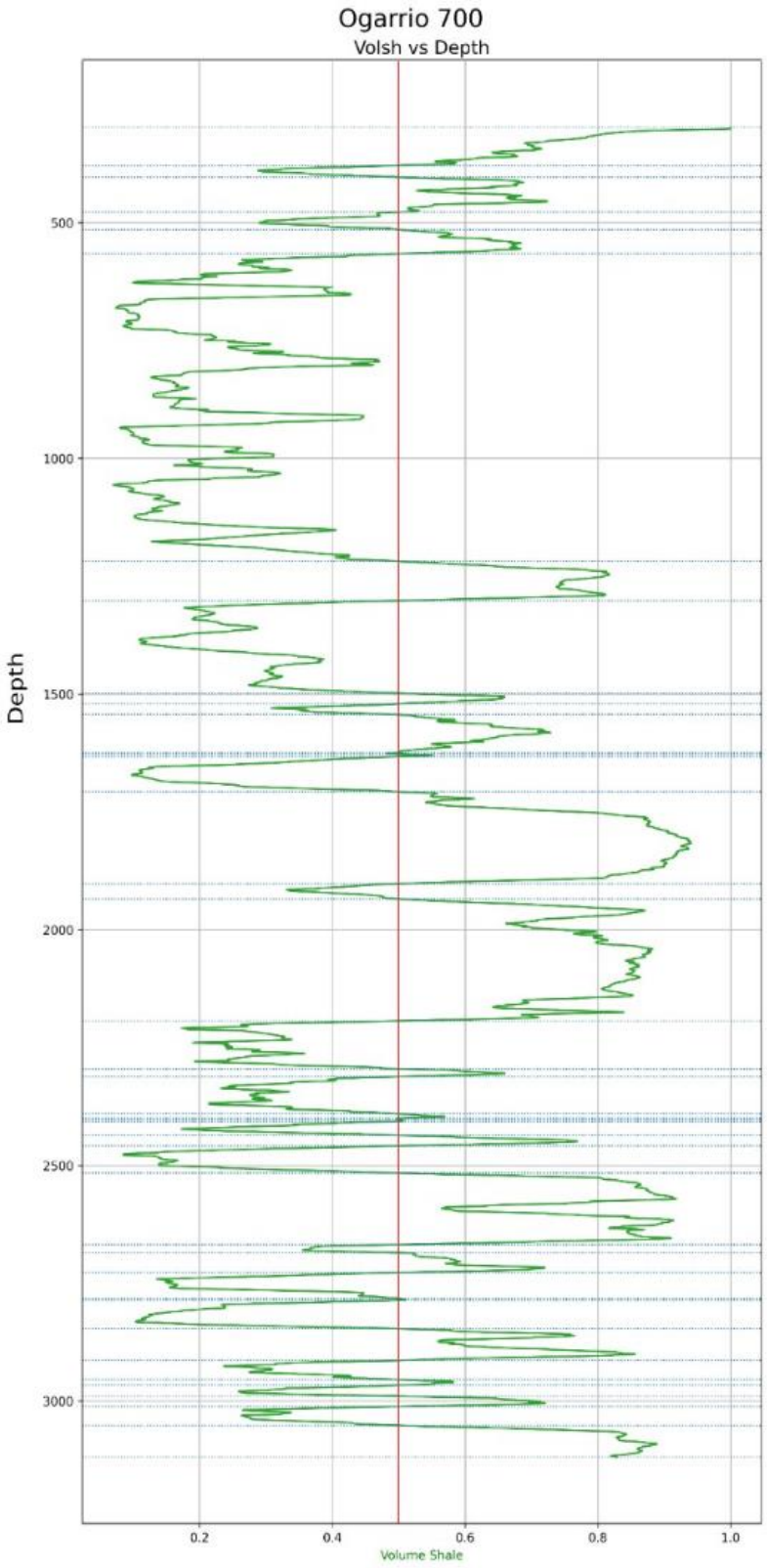

Figure 62: Depth versus VolClay from the well Ogarrio 700.

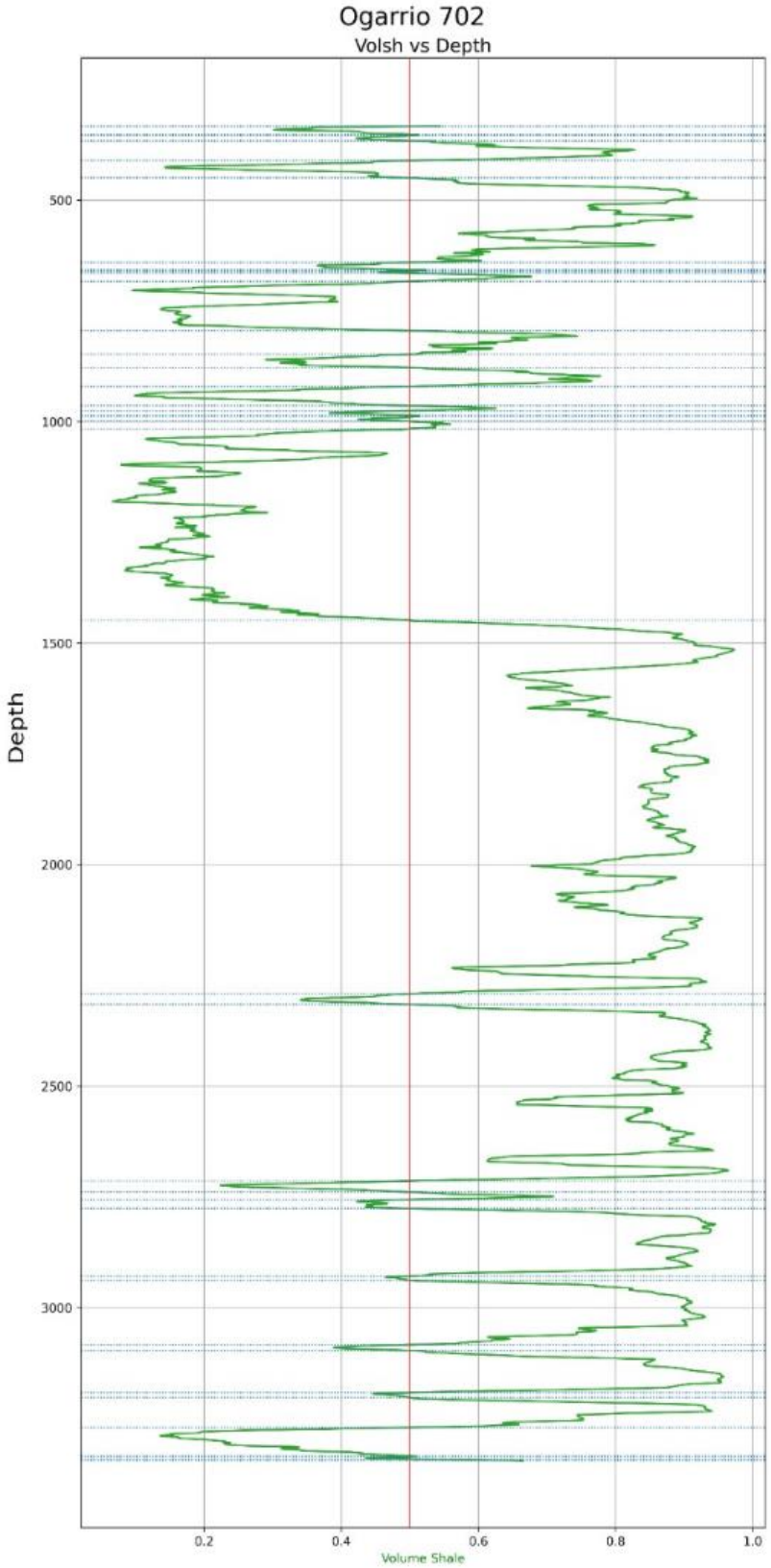

Figure 63: Depth versus VolClay from the well Ogarrio 702.

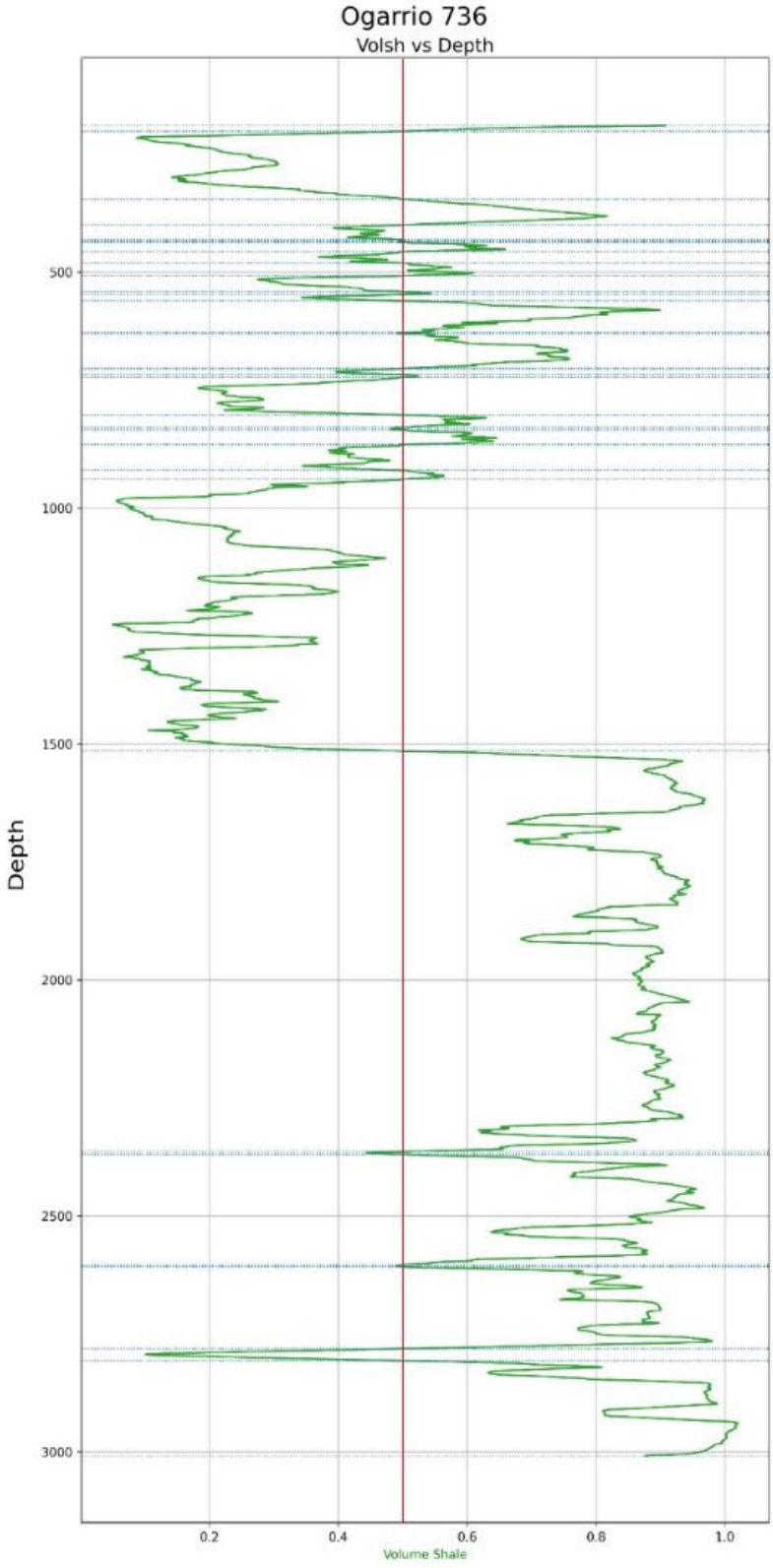

Figure 64: Depth versus VolClay from the well Ogarrio 736.

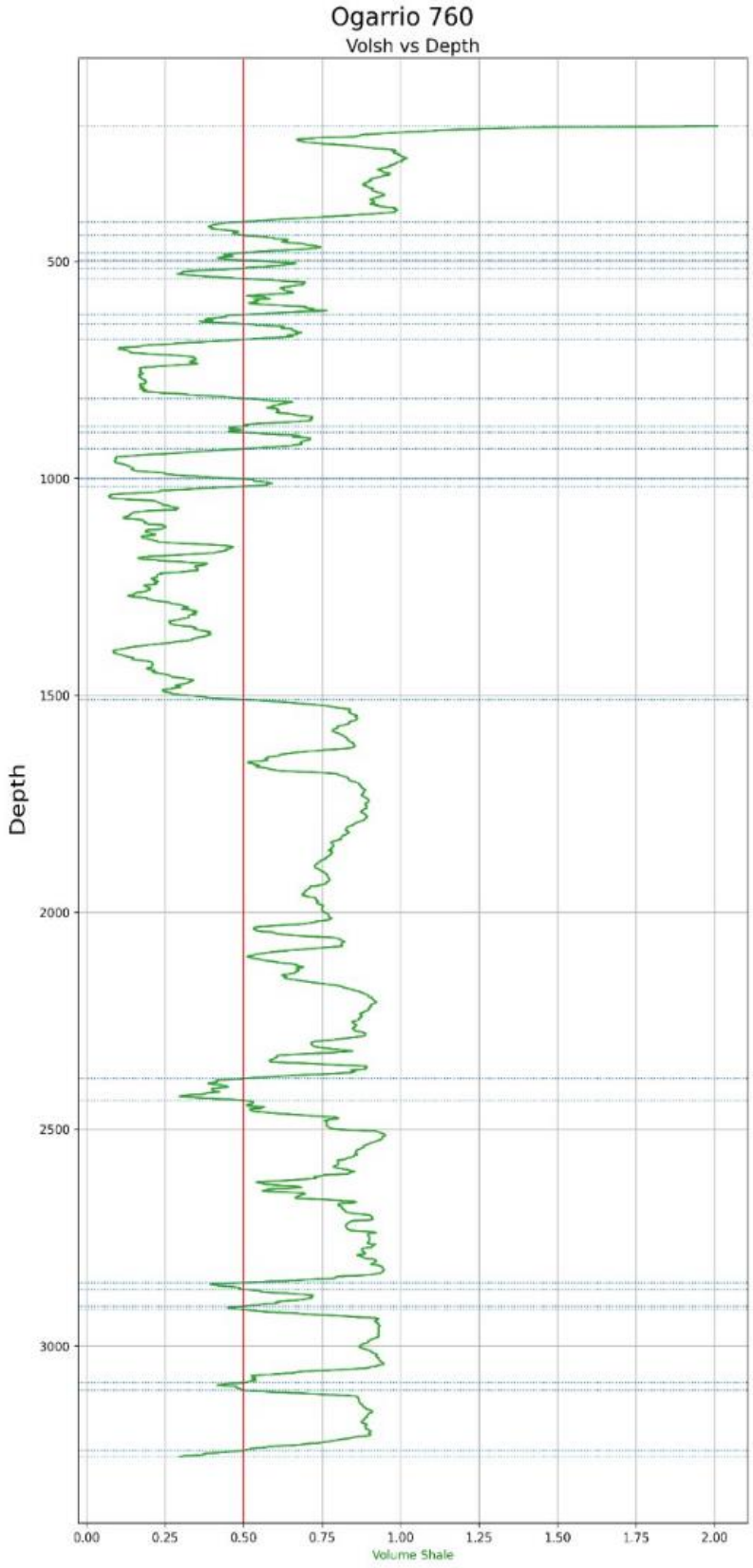

Figure 65: Depth versus VolClay from the well Ogarrio 760.

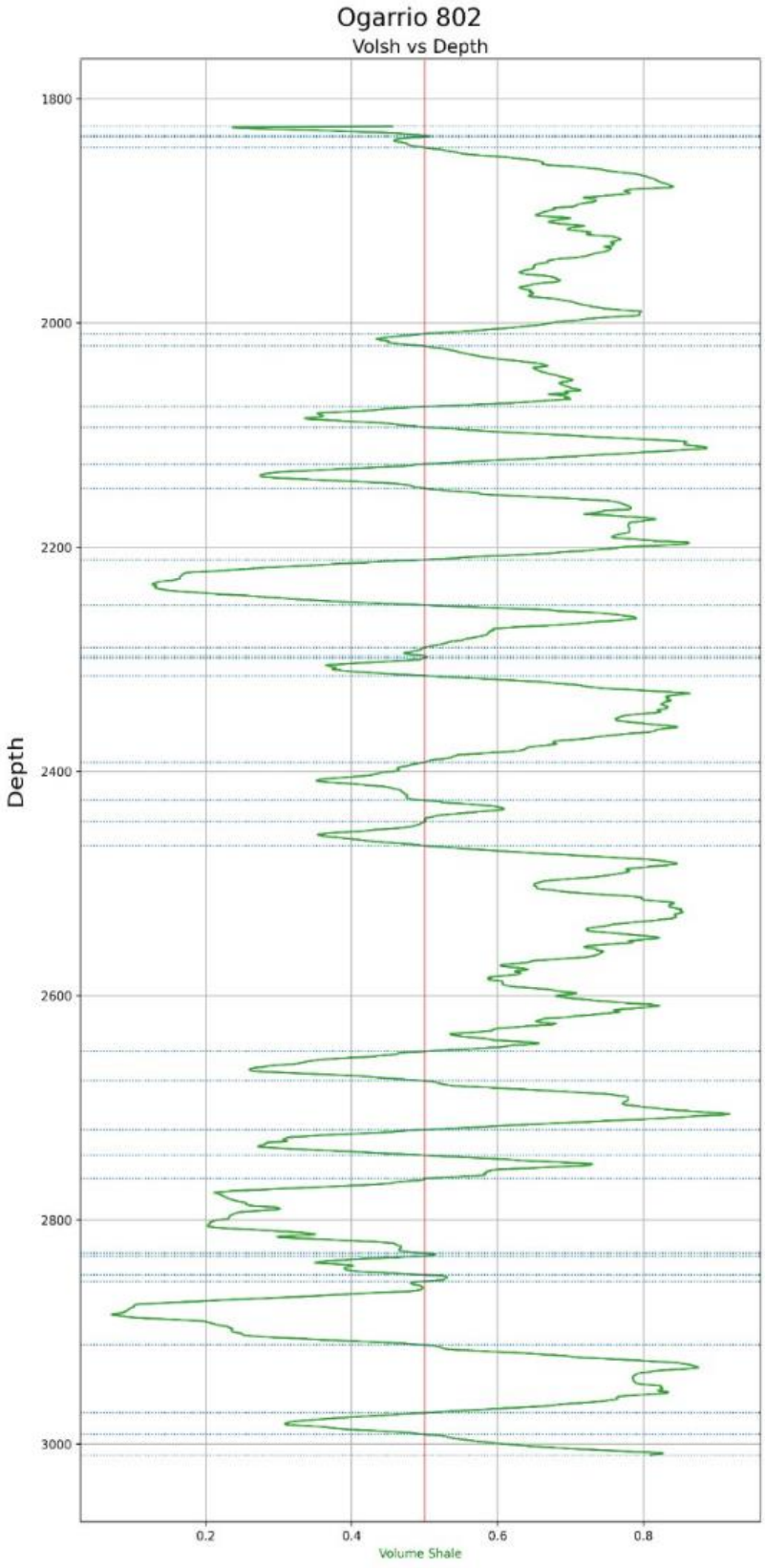

Figure 66: Depth versus VolClay from the well Ogarrio 802.

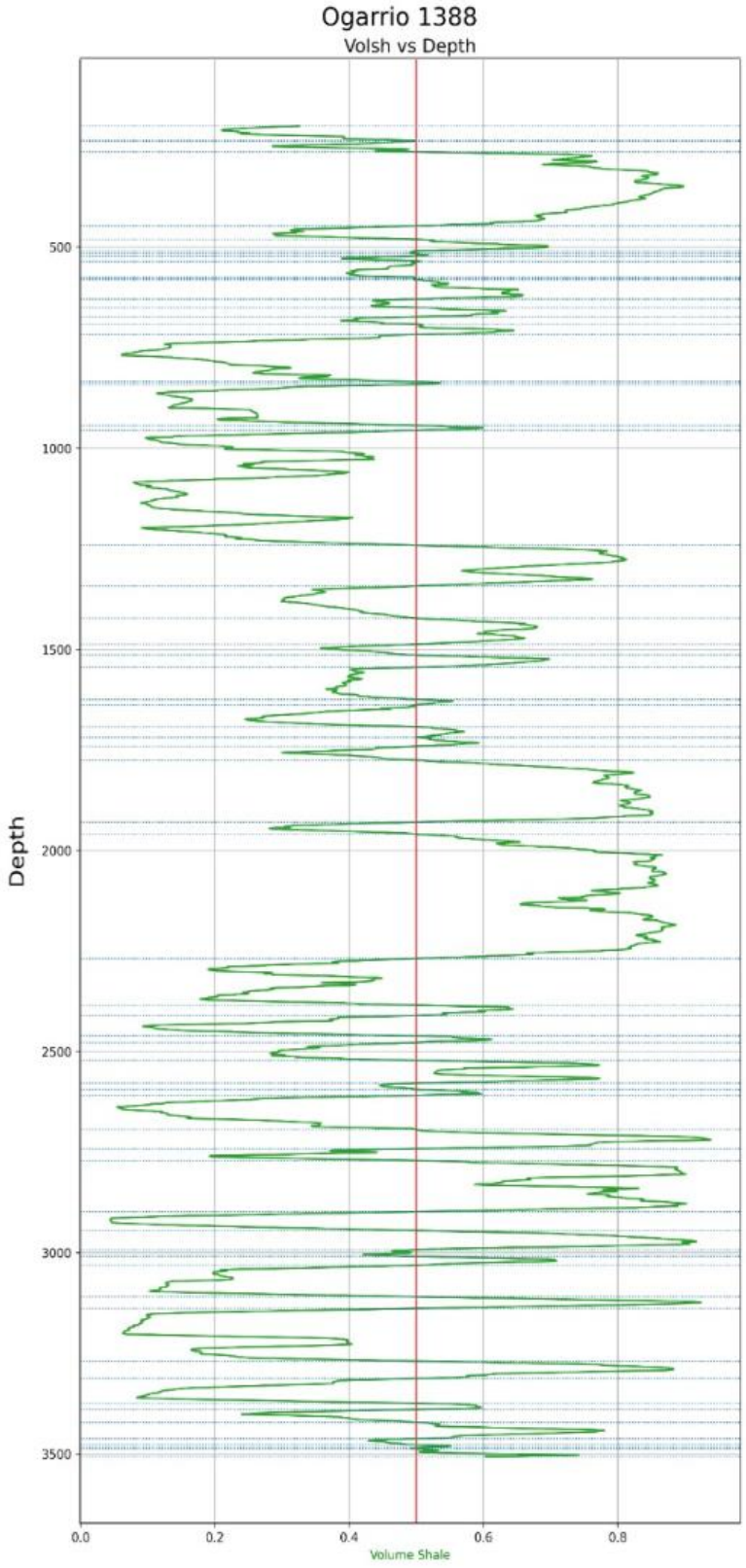

Figure 67: Depth versus VolClay from the well Ogarrio 1388.